MPM study of water wave interaction with porous seawalls

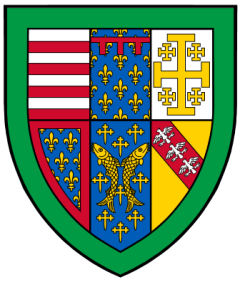

Lucy Harris

Supervisor: Dr. Dongfang Liang

Advisor: Dr. Giovanna Biscontin

Department of Engineering
University of Cambridge

This dissertation is submitted for the degree of
Doctor of Philosophy

Queens' College June 2020

I would like to dedicate this thesis to perseverance in the face of adversity, to the generosity of the collective human spirit, and to the ability of science to solve seemingly impossible problems. The pandemic during which this thesis was written will undoubtedly leave its scar on our psyche, but I believe in our ability to heal and to restore. I believe in community and the ability of the individual to make hard choices for something greater than oneself. I am grateful to all of the frontline NHS staff who put their health at risk daily to save others. I am grateful to all of the scientists and researchers seeking prevention as well as cure. I hope that we can remember the sacrifices of others during this time, and that we can work together to build a better future for all. I believe we are learning as humans to look beyond our self-interest and individual nations. I believe that we have hope.

Declaration

This thesis is the result of my own work and includes nothing which is the outcome of work done in collaboration except as declared in the Preface and specified in the text. It is not substantially the same as any that I have submitted, or, is being concurrently submitted for a degree or diploma or other qualification at the University of Cambridge or any other University or similar institution except as declared in the Preface and specified in the text. I further state that no substantial part of my thesis has already been submitted, or, is being concurrently submitted for any such degree, diploma or other qualification at the University of Cambridge or any other University or similar institution except as declared in the Preface and specified in the text. It does not exceed the prescribed word limit for the relevant Degree Committee. This thesis contains fewer than 65,000 words including appendices, bibliography, footnotes, tables and equations and has fewer than 150 figures.

Lucy Harris
June 2020

Acknowledgements

First and foremost, I would like to express my deepest gratitude to my supervisor, Dr. Dongfang Liang, for his continuous support and guidance throughout the course of my PhD studies. I appreciate his suggestions for the direction of my research, the model applications and the development of this thesis. It is fair to say that his influence has led me to discover a passion for research to the extent of influencing my next steps in life.

I would also like to express appreciation for the assistance given to me by Dr. Xuanyu Zhao, not only his generous help and constructive advice for the whole duration of my PhD studies, but also for his hand in helping me to get acquainted with the material point method, and his advice and support with writing a conference paper. I cannot imagine that I would have been able to produce results using MPM without his encouragement. Moreover, I would like to extend my sincere thanks to the entire Anura3D MPM Research community for their support throughout my PhD study.

I would like to extend a particular thanks to Grace Roberts, with whom I have enjoyed many productive discussions about the material point method, and who has helped me on numerous occasions. I am extremely grateful for your support and friendship. Further, I would like to thank my colleagues from the FIBE CDT for their support, throughout the journey from MRes course to PhD thesis, particularly to Becky Hartwell who has always picked me up when I have fallen.

I would like to add a slightly different note of gratitude to my family, both my parents and my sisters, not only for their extensive support throughout my life, but also particularly for offering a place of refuge during the pandemic when this journey took a different turn, and for your company and moral courage during the lockdown. Without your company and entertainment, I am sure that this thesis would not have been finished. To my partner, Hidde Boekema, thank you for your unrelenting support from both near and far - and the coffee! Finally, to my friends, Omba Kumwenda, Ellie Armstrong, Andy Russell, Emily Marr, and Laura Foster, thank you for tolerating me for so long. I am truly privileged to have such a high calibre of friends and colleagues.

Abstract

Flood defences are becoming increasingly vital for protecting key coastal infrastructure from rising sea levels and storm surge waves. Waves attenuate rapidly as they propagate through porous media, corresponding to significant energy dissipation. The ability of porous armour layers to absorb wave energy is therefore of great interest to hydraulic engineers, as more and more natural and artificial porous structures are constructed to defend vulnerable coastlines or existing flood defences from wave attack.

Design parameters for permeable flood defences include the grain size of the sediment particles that form the barrier and the width of the barrier. Previous studies have demonstrated that the runup height, which determines the risk of overtopping, is primarily dependent on the still water depth, wave amplitude and ground slope. This thesis investigates the effect of manipulating the mean grain size of a permeable barrier on the runup response to a dam-break flood wave and a solitary wave using the Material Point Method (MPM). Traditional methods for ascertaining the stability of protective barriers have used small-scale physical models, however, these are expensive and have been shown to suffer from scaling problems. Numerical methods are therefore gaining popularity in flood risk management applications.

MPM is capable of handling large deformation problems within a Lagrangian framework, allowing for simple application of boundary conditions. MPM has been widely used to solve solid mechanics problems with history-dependent variables, but the application of this method to fluid mechanics has been rare. In MPM, the background mesh is only used to solve the governing equations. The material properties are stored at the material points so that issues arising from mesh distortions such as those exhibited in the classical finite element method (FEM) are easily avoided when coping with large deformations. Although it stores no permanent information, the background mesh allows for simple application of boundary conditions. Boundary conditions can be applied directly at the nodes, unlike in meshfree methods such as SPH where boundary conditions must be applied to a series of "boundary particles", which much first be identified. In single-point MPM, both the liquid and solid velocity fields are tracked by a single material point. The double-point MPM introduces two sets of material points representing the solid phase and liquid phase separately, so that it is capable of capturing the relative acceleration between the water and the soil skeleton. It is

therefore capable of accurately modelling situations where the fluid moves significantly with respect to the soil, such as in wave run-up on structures.

The goal of this research is to determine the effectiveness of sloped and vertical permeable barriers on preventing flooding resulting from storm surges and tsunami waves, and to ascertain the most effective permeability for reducing wave impact, to provide design guidance for coastal flood barriers. To this end, MPM is used to examine the influence of two key design parameters for porous, permeable flood defences, including the grain size of the composition particles and the width of the barrier. The term *porosity* is used to describe the dimensionless ratio of the volume of voids to solid material in the structure, and the term *permeability* is used to describe how resistant the porous structure is to flow, related to the mean grain size forming the material, in accordance with the Ergun equation used to determine the body force between the solid and liquid phases. This equation is presented in Chapter 3. A larger mean grain size results in larger voids in the material, so that there is less resistance to flow and the permeability increases. The multiphase version of the MPM package Anura3D (www.anura3d.com) has been adopted in this study. It is shown that increasing the grain size, and therefore the permeability, of the porous dam effectively reduces the overall runup height. The grain size, rather than the wall width, is shown to be the dominant parameter affecting the runup.

Table of contents

List of figures

List of tables

Nomenclature

Roman Symbols

a	Acceleration [ms^{-2}]
A	Area [m^2], or a constant
b	External body force vector
B	Matrix of shape function gradients
c	Wave celerity [ms^{-1}]
C	Courant number $C = \frac{u_x \Delta t}{\Delta x} + \frac{u_y \Delta t}{\Delta x} \leq C_{\max}$
c_L	Wave celerity in liquid phase [ms^{-1}]
c_S	Wave celerity in solid phase [ms^{-1}]
d	Still water depth [m]
D_p	Mean grain size diameter [m]
E	Young's modulus
E_c	Laterally confined modulus
E_c^u	Undrained constrained modulus
F	Force vector
F	Constant
Fr	Froude number $Fr \equiv \frac{U}{\sqrt{gL}} = \frac{U}{\sqrt{g'H}}$ in the context of the Boussinesq approximation
g	Gravitational field strength [ms^{-2}]

h	Water depth [m]
H	Height [m]
H_1	Initial height of water column [m]
i	Nodal index
$\mathbf{J}$	Jacobian matrix
k	Wave number, Darcy permeability or a constant
K	Bulk modulus [Pa]
K_L	Bulk modulus of liquid phase [Pa]
K_r	Wave reflection coefficient
L	Characteristic length scale [m]
L	Length [m]
l_{min}	Element characteristic length
LX	Domain size in the x direction
LY	Domain size in the y direction
m	Mass [kg]
$\mathbf{m}$	Lumped mass matrix
$\mathbf{M}$	Consistent mass matrix
m_p	Mass carried by a material point
$\mathbf{n}$	Normal outward unit vector on a boundary
n	Soil porosity
N_{el}	Number of elements
$N_{el,i}$	Number of elements connected to node i
n_L	Liquid concentration ratio
n_{max}	Maximum soil porosity

N_n Number of nodes

N_p Number of material points

n_S Solid concentration ratio

N_x Shape function

p Pressure [Pa]

p_L Liquid pressure [Pa]

R Run-up height [m]

R_{cr} Difference between nonlinear and linear run-up [m]

Re Reynolds number $Re \equiv \frac{\rho UL}{\mu} \equiv \frac{UL}{\nu}$

R_s Maximum wave run-up height from linear theory [m]

t Time [s]

$\mathbf{u}$ Displacement vector

U_r Ursell number

$\mathbf{v}$ Velocity vector

w Width [m]

W_k Integration weight factor at point k

$\mathbf{x}$ Shape function

x Horizontal co-ordinate (positive right)

x_p Position of material point

$\mathbf{x}_{pL}$ Shape function of liquid phase

$\mathbf{x}_{pL}$ Shape function of solid phase

y Vertical co-ordinate (positive up)

Greek Symbols

α Aspect ratio

β	Slope angle
δv	Test function
ε	Strain tensor
$\dot{\varepsilon}$	Strain rate tensor
γ	Unit weight of water kgm^{-3}
κ	Soil intrinsic permeability [Pa]
μ	Dynamic viscosity [Pa·s]
ν	Kinematic viscosity $[\mathrm{m}^2\mathrm{s}^{-1}]$
ν	Poisson ratio
Ω	Material domain
Ω_p	Integration weight of point p
Ω_{pL}	Integration weight of liquid point at p
Ω_{pS}	Integration weight of solid point at p
ϕ	Soil internal friction angle
ψ	Dilatancy angle
ρ	Density $[\mathrm{kgm}^{-3}]$
$\bar{\rho}_L$	Liquid phase averaged mass density
$\bar{\rho}_S$	Solid phase averaged mass density
σ	Cauchy stress tensor
σ'	Effective stress
τ	Shear stress or prescribed surface traction vector

Superscripts

0	Initial reference value
ext	External value

int Internal value

Subscripts

0 Initial reference value

dev Deviatoric component

el Elemental value

ext External value

i Nodal index

int Internal value

L Liquid component

p Material point value

q Gauss point value

S Solid component

vol Volumetric component

x Component in x direction

y Component in y direction

Other Symbols

$\partial\Omega_p$ Prescribed pressure boundary

$\partial\Omega_\tau$ Prescribed traction boundary

$\partial\Omega_u$ Prescribed displacement boundary

Acronyms / Abbreviations

ALE Arbitrary Lagrangian-Eulerian formulation

BC Boundary condition

CFD Computational Fluid Dynamics

CFL Courant–Friedrichs–Lewy condition

CISPH Corrected Incompressible Smoothed Particle Hydrodynamics

DCDEM Distributed Contact Discrete Element Method

DEM Discrete Element Method

DNS Direct Numerical Simulation

EFGM Element Free Galerkin Method

FDM Finite Difference Method

FEM Finite Element Method

FLIP Fluid Implicit Particle

FSI Fluid-Structure Interaction

FVM Finite Volume Method

GFDM Generalised Finite Difference Method

GIMP Generalized interpolation material point method

ISPH Incompressible Smoothed Particle Hydrodynamics

LES Large Eddy Simulation

MAC Marker-And-Cell Method

MLPG Meshless Local Petrov-Galerkin Method

MPM Material Point Method

MP Material Point

MPS Moving Particle Semi-implicit Method

NS Navier Stokes

PFEM Particle Finite Element Method

PIC Particle in Cell

PPE Pressure Poisson Equation

RKPM Reproducing Kernel Particle Method

RVE Representative Volume Element

SPH Smoothed Particle Hydrodynamics

SWEs Shallow Water Equations

VOF Volume Of Fluid

WCSPH Weakly Compressible Smoothed Particle Hydrodynamics

Chapter 1

Introduction

Free surface flow problems have long been an area of significant interest in hydrodynamics due to their importance within both the natural and built environment. However, many of these flow problems involve complex dynamics and large surface deformations; this poses a considerable challenge when it comes to the analysis and prediction of such currents. Interactions between these free surface flows and permeable media are of particular interest to engineers who design coastal flood defences and offshore structures.

Flood defences that protect key structures from invading free surface flows are becoming increasingly vital infrastructure due to population growth and climate change, particularly in response to continually rising global sea levels. As sea levels rise and severe storm events occur more frequently, existing flood defences will no longer provide adequate protection. Waves attenuate rapidly as they propagate through permeable media, corresponding to significant energy dissipation. Natural and artificial porous and permeable structures, such as dunes, vegetation, rubble mound breakwaters and armour layers are therefore used as dykes and dams to protect vulnerable infrastructure, or function in conjunction with existing flood defences to defend against wave attack. In this thesis, the term *porosity* is used to describe the dimensionless ratio of the volume of voids to solid material in the structure, and the term *permeability* is used to describe how resistant the porous structure is to flow, related to the mean grain size forming the material in accordance with the Ergun equation used to determine the body force between the solid and liquid phases. The porosity of the material remains constant, but the permeability of the material increases as the mean grain size is increased. A comprehensive understanding of the flow processes arising from wave motion through permeable structures as well as a thorough understanding of the soil-water interaction is key to ensuring the long-term stability and functionality of these structures.

1.1 Background

Whilst the process of long-wave generation and propagation on solid structures is well understood, the wave interaction with permeable media is not. When considering the run-up response to wave attack, the interaction between the fluid and the structure is a key factor in determining how effective the flood defence will be. This is particularly true in the case of permeable barriers that are designed to reduce wave energy by utilising the flow friction that develops through fluid-structure interaction as the wave propagates through the barrier.

Catastrophic failures of man-made structures (dykes, levees, embankments and dams) due to dam-break flows or wave overtopping may cause widespread environmental and economic damage as well as potentially severe injury or loss of life. Traditional methods for ascertaining the stability of protective barriers have used small-scale physical models, however, these are expensive and have been shown to suffer from scaling problems [94]. Numerical methods are therefore gaining popularity in flood risk management applications. When the geometry of the physical problem becomes more complex, analytic methods become unfeasible, requiring a computational approach. However, these hydraulic engineering problems result in large impact forces as well as large rotations and deformations that cause severe numerical problems in traditional, mesh-based computational models. The material point method (MPM) is capable of handling large deformation problems within a Lagrangian framework, allowing for simple application of boundary conditions. MPM has been widely used to solve solid mechanics problems with history-dependent variables, but the application of this method to hydrodynamics has been rare.

Modelling the coupled soil-water behaviour adds significant complexity to the mechanical behaviour of the soil, which is already challenging to model due to the history-dependent and highly nonlinear behaviour of the material. Capturing the response of soil to rapidly invading free surface flows requires a method that can describe both the liquid phase and the soil skeleton with a high level of accuracy. The double-point MPM code uses two layers of material points, for the solid and liquid phases respectively, to better model situations where there is a large relative acceleration between the soil skeleton and the free water.

This thesis focuses on using numerical methods to determine the run-up response for a range of incident waves on permeable vertical walls and steeply sloping beaches of varying permeability. The advantages of the double-point MPM Anura3D are demonstrated through these applications.

1.1.1 Water waves as natural hazards

Water waves are a natural hazard in coastal areas. They can quickly become hydrological or meteorological disasters when substantial wave inundation poses a critical risk to human life or results in significant economic damage. Coastal flooding occurs when normally dry land is flooded by seawater. These coastal floods can be in the form of tsunamis or surges driven by tropical storms, which inundate the coastline in sudden large deluges in the form of solitary waves. The extent of the flood is determined by the volume of flooding and the local topography of the coastal land exposed to the flood. Seawater can inundate the land via three mechanisms:

- Direct inundation — the sea height exceeds the elevation of the land.
- Overtopping of a barrier — Overtopping occurs due to swelling during storm conditions or unusually high (spring) tides. The height of the water exceeds the height of the barrier and water flows over the top of the barrier to flood the land behind it. This can result in high velocity flows that can erode considerable amounts of soil, undermining the existing structure. These barriers may be either engineered (such as traditional sea walls) or natural (dunes and mangrove forests).
- Breaching of a barrier — the barrier is broken down by the impact force of the waves, allowing the seawater to flood inland.

This thesis focuses on preventing flooding due to overtopping of coastal flood defences, by seeking to minimise the maximum run-up height reached by the invading wave.

There are a large number of factors that can affect wave propagation and the subsequent impact on coastal structures in the near-shore region. Only a very few analytical solutions are available, for simple bathymetries and under idealised flow conditions. Consequently, as computational processing power rapidly develops, numerical methods for modelling the interaction between permeable media and free surface flows become crucial for efficiently and accurately predicting and understanding flow behaviour. One major factor that is driving research into coastal flood defence is the impact of global climate change on coastal flooding.

1.1.2 Coastal flooding driven by changing climate

Climate change is defined as a change in the statistical distribution of global or regional weather patterns that lasts for an extended period. There is significant evidence that we are currently undergoing a period of climate change, driven at least in part by human activity [5]. This has affected both ocean water temperature and sea levels.

Although the ocean temperature has seen a slower rise than land temperature due to the high specific heat capacity of water, global ocean temperatures have risen during the 20th century and continue to rise [118].

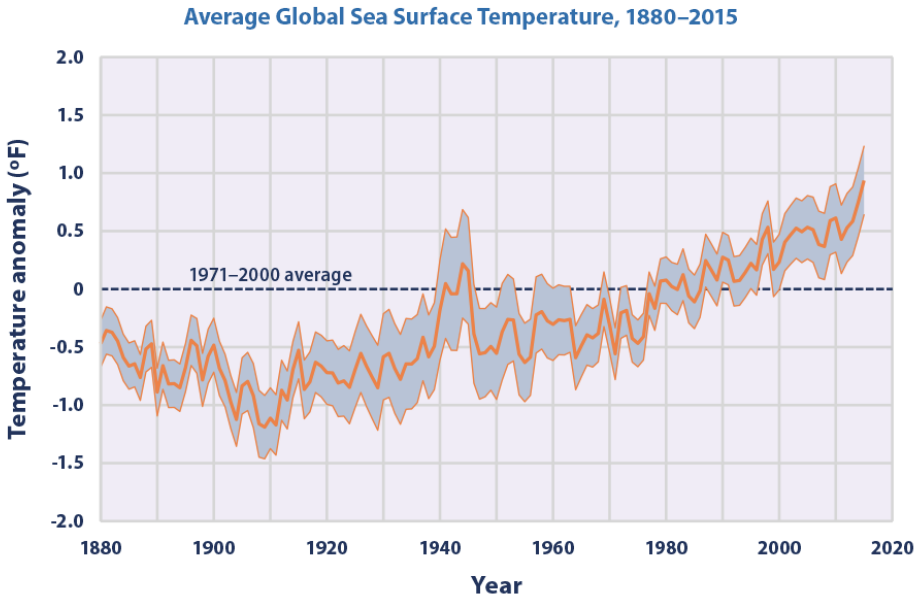

Fig. 1.1 Global average ocean temperature from 1880 [118]

The key points relevant to this thesis are that firstly, from 1901 through 2015, the temperature rose at an average rate of 0.7°C per decade, and secondly, that global sea surface temperature has been consistently higher during the past three decades than at any other time since reliable observations began in 1880 (see Figure 1.1).

This rise in sea temperatures has a direct impact on the frequency and severity of extreme coastal weather events as warmer seas provide more energy to developing storms. Consequently, if sea temperatures continue to rise, we can expect to see floods driven by typhoons, hurricanes and cyclones increase in both frequency and severity.

Global warming is also driving a rise in the global mean sea level. This is a compounded result of two mechanisms: both increasing ocean water volume due to the melting of glaciers and the polar ice caps; and thermal expansion of the water in the ocean due to rising sea temperatures.

Figure 1.2 shows the average absolute sea level change, which refers to the height of the ocean surface, regardless of whether nearby land is rising or falling. The shaded band shows the likely range of values, based on the number of measurements collected and the precision of the methods used. This data is taken from the National Oceanic and Atmospheric Administration

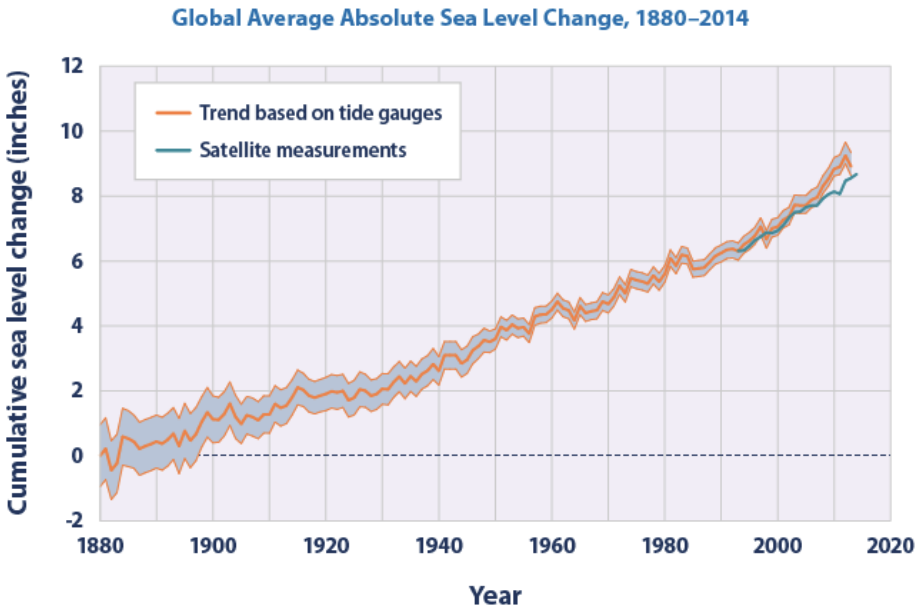

Fig. 1.2 Global average absolute sea level from 1880 [116]

and shows a clear trend in rising sea levels. Global sea levels have risen over the 20th century, and the rate of change has accelerated since approximately 1993.

A January 2017 NOAA report suggests a global mean sea level rise of 0.3 – 2.5 m is possible during the 21st century [117]. This has an obvious and significant effect on the design of coastal flood defences: if a structure is to reach a minimum of 80-year design life, there must be an additional allowance of up to 2.5m of protection *on top of that which has already been designed for*.

1.1.3 Coastal flood defences

Vertical seawalls

A seawall is an onshore coastal defence structure with the primary function of protecting areas of human habitation or activity, or wildlife conservation, from damaging wave action, either as a result of normal tidal processes or from extreme events such as those resulting from storm surges.

Sea walls are built parallel to the coastline to reinforce the existing coastal profile to prevent inundation of the protected area behind the wall. Any overtopping of a sea wall therefore represents a failure of the coastal defence.

Seawalls are typically massive concrete constructions. The simplest design is a vertical seawall that reflects most of the wave energy, as shown in Figure 1.3. The reflected wave

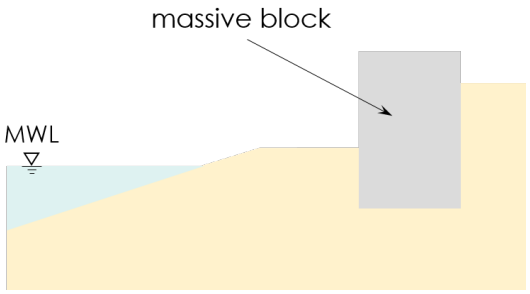

Fig. 1.3 Schematic of a vertical sea wall

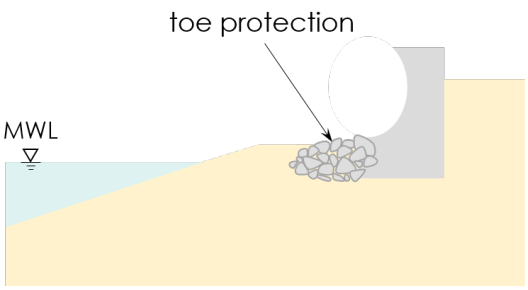

Fig. 1.4 Schematic of a recurved seawall

energy from a vertical impermeable wall is typically 90-100% [101]. The vertical design is easily overtopped and under storm conditions a non-breaking standing wave pattern can form, resulting in a stationary clapotic wave which moves up and down but does not travel horizontally. These circulating currents cause erode material at the base of the wall, reducing stability and potentially leading to catastrophic damage.

More recently, recurved sea walls have been used in place of traditional vertical sea walls. Recurved walls are designed with a concave shape that deflects the wave and then dissipates wave energy via breaking, shown in Figure 1.4. This combination of deflection and breaking re-directs much of the incident energy, resulting in significantly reduced wave reflection and lower turbulence. However, even with protective armour blocks at the toe, the deflected wave energy can cause scour at the base of the seawall that can ultimately lead to undermining.

Natural flood defences

Natural barriers are much less visually intrusive and have been proven to be extremely effective in flood prevention. A report published by the United Nations Environment Programme (UNEP) found that the Boxing Day tsunami in 2004 caused significantly less damage in the areas protected by natural barriers, such as mangroves, coral reefs or coastal vegetation [14].

Studies of the results of the impact of this tsunami in Sri Lanka as a function of different types of trees, identifying natural barriers, such as coral reefs and mangrove forests, that prevented tsunami damage by breaking up the flow of coastal waters, dissipating energy and mitigating the flood surge of the water [14].

Permeable media in flood defences

As well as the typical concrete seawall, permeable coastal flood defences can be constructed. These can range from more obviously engineered structures, such as rubble mounds (figure 1.5),

to a more natural style of flood defence such as dunes and vegetation, particularly mangrove forests.

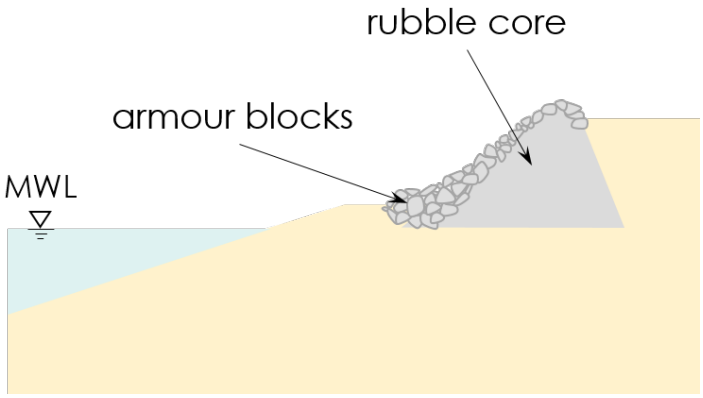

Fig. 1.5 Rubble mound breakwater schematic

Rubble mounds are porous, permeable structures that allow water to flow through once wave energy has been dissipated. However, these too can be damaged by storm waves and can eventually fail by overtopping of broken waves, or by scour and erosion of the underlying seabed.

Permeable structures constructed from porous media have several advantages compared with impermeable ones. The permeable structure is much more effective in decreasing the wave run-up, in reducing reflected wave height, and eventually in reducing pressures acting on it [137].

A permeable structure allows water waves to transmit through it with energy dissipation. Therefore, not only can the resultant force acting on the structure be reduced, but the wave energy is also decreased [58].

The focus of this thesis, therefore, is on permeable media in coastal flood defences, with the aim of describing the effect of changing the material permeability by altering the mean grain size of the constituent porous material on minimising the run-up height reached by attacking flood waves.

Analytical solutions on water-wave diffraction are rare and have only been developed for structures with very simple geometry, and with a flat bottom bed. If the bottom bed is at all uneven or rough, finding an analytical solution becomes more challenging, and besides, the in-situ wave loading on the structure is notoriously difficult to predict.

Experimental studies have also been widely carried out with hydraulic models. However, experimental studies are costly and are heavily limited by the geometry of the flumes and the experimental apparatus available. To assess a wider range of structures and environments, this

thesis exploits computational methods, specifically, the material point method (MPM). The justification for choosing the MPM code is discussed in detail in Chapter 3.1.

1.1.4 Introduction to the Material Point Method

The material point method is a numerical technique used to simulate the behaviour of both solids and fluids and is increasingly being adopted to study soil-water-structure interaction. It is derived from the fluid implicit particle (FLIP) method which was developed to overcome the inherent numerical issues with the early implementations of the particle-in-cell (PIC) method. The FLIP method introduces Lagrangian particles, thus removing the need to discretise the convective term - the largest source of computational diffusion in the PIC method [21]. In the FLIP method, each particle is attributed all of the properties of the fluid, including momentum and energy. This allows material discontinuities to be tracked, making it possible to model highly distorted flows [171].

MPM diverges from the FLIP method in that the governing equations are presented in the weak formulation, consistent with the Finite Element Method (FEM), which, due to its ability to account for the loading history of the material, has been the dominant numerical method used in geotechnical engineering. Where the FLIP method solves for the constitutive equation at the grid nodes, in MPM these are applied at the material points [138].

In MPM, a continuum body is described by small Lagrangian elements referred to as "material points". These material points allow the loading history of the material to be stored. MPM is categorised as a meshless or continuum-based particle method, as is the smoothed particle hydrodynamics (SPH) method. Although the material points are surrounded by a background mesh/grid, this is only used to calculate gradient terms such as the deformation gradient and does not carry any permanent information. Consequently, MPM does not encounter the drawbacks of mesh-based methods (tangling and advection errors when subjected to large deformations), making it a powerful tool in computational geomechanics.

The MPM code has been developed to handle multi-phase problems using two layers of material points ([1], [12], [170]), and this has been applied to landslide run-out, progressive dam failure due to seepage flow, and wave impact on coastal defences.

The formulation of the code is described in detail in Chapter 3.1.

1.1.5 Objectives

We require detailed knowledge of flow behaviour and extensive analyses of wave run-up, breaking and overtopping around porous structures to develop coastal protection methods that are safe, efficient and reliable. This research aims to develop existing numerical models so that

they may be applied the analysis of the interactions between water waves, soil, and structures to investigate wave propagation, run-up and the breaking and run-up of water waves incident on permeable structures.

Ultimately, the interaction between water waves and permeable media will be investigated using the material point method to fully capture fluid-structure interactions. This research project will contribute to a better understanding of fluid flow around permeable media, so that wave impacts on coastal structures can be evaluated to provide design recommendations for coastal flood defences that are capable of withstanding increasingly extreme weather events.

1.2 Thesis structure

The thesis is arranged into seven chapters including this introductory chapter and the contents of each chapter are outlined here:

Chapter 2 presents a literature review of the development of different numerical methods in computational mechanics. Several different mesh-based and meshfree numerical methods together with their advantages and disadvantages are discussed, and the reasons for selecting the method for this research is presented. Relevant material on the development and applications of the material point method is reviewed in detail. Chapter 3 discusses the methodology used in this research, focusing on the mathematical framework of the material point method and how it is applied in this research, exploring the development of the double-point MPM code. Chapter 4 describes parametric studies of dam-break flows using the double-point MPM code including the numerical validation against experimental data and results from other published numerical methods, followed by a study of the interaction of dam-break floods with permeable barriers of different widths and with varying grain sizes. Chapter 5 employs an adapted version of the double-point MPM code to simulate a solitary wave impacting on a permeable vertical barrier, with a parametric study comparing walls with different widths and grain sizes. Chapter 6 demonstrates how the adapted double-point MPM code is further employed to study solitary wave run-up on plane beaches. After the model is validated against experimental observations and comparison with analytical results, the numerical method is employed to simulate the wave run-up on steeply sloped beaches with different permeabilities. Chapter 7 presents the main conclusions drawn from these studies and provides recommendations for future research in this field.

Chapter 2

Literature Review

2.1 Overview

Free-surface hydrodynamics is a topic of significant importance in both industrial and environmental engineering since it governs the mixing that occurs between fluids. It is therefore crucial in fields such as oceanography, ventilation in both residential and industrial buildings, meteorology, aircraft safety, atmospheric pollution and pest control. Initial research into hydrodynamic phenomena has been carried out using physical models to determine empirical coefficients and to provide evidence for the underlying mathematical theory. Coastal defences can be scaled and tested experimentally in flumes to provide a basis and a validation for analytical theory. Whilst these experimental studies can offer great insight into the interaction of free-surface flows with structures, experimental studies such as these are expensive and are limited by the experimental apparatus available. Furthermore, some physical phenomena suffer from scaling issues, largely resulting from the compressibility of air, meaning that we are unable to accurately reproduce fluid-structure interaction on smaller scales.

The rapid advancement of computational power, storage capacity and calculation speed over the last few decades has led to numerical simulations tending to dominate scientific research. Numerical simulations are increasingly used to study the behaviour of systems whose mathematical models are too complex to provide analytical solutions. This is the case for most non-linear systems, which themselves describe most real-world situations. Computer-based simulations are offered as an alternative to physical experimental methods which may be more time consuming and expensive, or in situations where the in-situ conditions are challenging to replicate.

Computational Fluid Dynamics (CFD) simulates the interaction of liquids and gases with surfaces defined by boundary conditions. The fundamental basis of almost all CFD problems is the Navier–Stokes equations. CFD has traditionally utilised mesh-based approaches to discretise

the domain. In mesh-based methods, space containing fluid is divided into a grid, where governing equations are presented in a finite-difference form. Hence, the physical properties of the fluid are stored in each cell. Whilst these computational methods are increasingly being exploited to overcome experimental issues, the moving fluid surfaces that occur in free-surface flows can present a challenge to implement as surface boundary conditions [132].

This thesis uses the numerically-based material point method (MPM) to assess a wider range of structures and environments than would be possible experimentally. The material point method is particularly useful in this field of investigation, since it exploits both Eulerian and Lagrangian frames of motion. The Lagrangian description and the Eulerian description are the two basic descriptions of motion in continuum mechanics [157]; the Lagrangian depiction of the field is a way of looking at fluid motion whereby the observer follows an individual particle as it moves through space and time, and conversely, the Eulerian depiction of the flow field is a way of looking at fluid motion that focuses on specific locations in the space through which the particle flows as time passes. Historically, Lagrangian methods were widely used in solid mechanics and Eulerian methods have been more favoured in fluid mechanics. Consequently, in Lagrangian algorithms, the nodes of the computational mesh deform as the continuum material deforms, whilst in Eulerian algorithms, the material flows through a fixed background mesh. Therefore when modelling large deformations that are easily handled by Eulerian algorithms, the accuracy of Lagrangian methods is significantly compromised by large distortions of the mesh. However, unlike Eulerian methods, Lagrangian methods allow the material interfaces to be captured, and can store the material history, which is of considerable value in soil mechanics where the material typically has history-dependent behaviour. Furthermore, Lagrangian methods do not suffer the same numerical difficulties that arise in calculating the convective term in Eulerian methods. In the material point method, discretised Lagrangian point masses, referred to as material points, are accelerated through an Eulerian background mesh.

Modern computational methods can be classified into two categories, depending on the discretisation approach that they employ: mesh-based methods and meshfree, or particle-based, methods. The development path of these methods is summarised in Figure 2.1. Mesh-based methods are explored in detail in section 2.3, and particle methods are discussed in section 2.5. Since the MPM combines both frames of motion and therefore has the advantages of both meshed and particle methods, it is a logical choice for numerically modelling free-surface flows interacting with porous media. Despite this, there has been little use of the MPM in the field of hydraulic engineering [170]. The material point method was first applied to explore the hydrodynamics of dam-break flows by Xuanyu Zhao and Dongfang Liang in their 2017 paper,

"MPM simulations of dam-break floods". The explicit mathematical basis and the formulation of the material point method are explored in detail in Chapter 3.1.

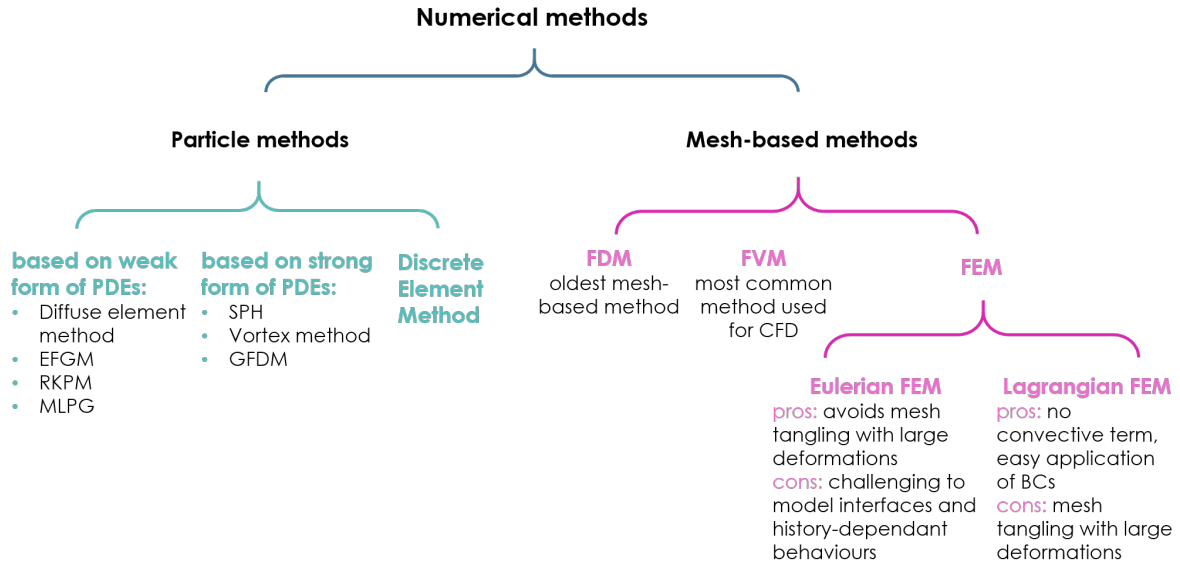

Fig. 2.1 Numerical methods classified by discretisation approach

This chapter provides an overview of the experimental and theoretical basis of existing wave theory and the development of numerical techniques employed to investigate hydrodynamic phenomena in the field of civil engineering. A general review of current mesh-based methods and particle methods is presented, followed by a detailed summary of the material point method. The literature review discusses the advantages and disadvantages of the different computational methods and their relevance to this study.

2.2 Experimental and theoretical investigations

2.2.1 Frictional dissipation of wave energy

One of the first investigations into frictional dissipation of wave energy by porous media was conducted by Savage and Fairchild in 1953 [129]. They used a wave flume equipped with a splitter wall to test wave energy losses by bottom friction and percolation. In their experiments, sands were used to create a permeable bottom layer, and the maximum energy loss reached 60% under the conditions of artificial ripples. The experimental percolation energy losses were far less than the theoretical values; correction factors of 4 to 10 were needed to obtain reasonable agreement. Sand sizes larger than 2 mm resulted in very large percolation losses, while losses for low-permeability sands were insignificant. This demonstrates that porous media can be

very effective at dissipating wave energy, and further that the amount of energy dissipated is heavily influenced by the porosity of the material.

Goda et al. (1975) performed a series of measurements with irregular waves to model seawalls with and without protection by concrete block mounds. They proposed twelve diagrams for overtopping rate estimation from their experimental results to enable quick estimation of the overtopping rate of seawalls at any water depth from the offshore to the foreshore [46]. Özhan and Shi-igai (1977) observed solitary waves of various heights travelling over smooth and rough bottom beds and investigated the effect wave damping. They found that the friction coefficient depends on the instantaneous wave height if the bottom is entirely rough [119].

2.2.2 Wave interaction with porous media

Straub et al. (1957) provided the first comprehensive investigation of the use of permeable materials to absorb wave energy, finding that a material with a high porosity was desirable and that crushed rock was almost as effective as a wire mesh on low-angled bed slopes [136].

Lean (1967) [82] investigated the reflection of waves from simple permeable wave absorbers, finding that some reflection will always take place.

Sollitt and Cross (1972) derived a theoretical solution to predict ocean wave reflection and transmission at a permeable breakwater of rectangular cross-section and compared it experimental results for a rubble mound breakwater [134].

O. S. Madsen (1974) developed empirical relationships for the non-linear flow resistance for long, normally incident waves on a homogenous porous structure [99], and building on that, in 1983, P. A. Madsen developed a theoretical analytical solution for the reflection of linear shallow-water waves from a vertical porous wave absorber on a horizontal bottom [100]. In these studies, the occurrence of a seepage surface is neglected. The results of Sollitt and Cross (1972) and Madsen (1974) are acceptable only for reflected and transmitted wave profiles far away from the porous structure. Since the effects of viscosity are not important for wave profiles, the seepage surface is negligible in this instance.

Sulisz (1985) formulated a theory that predicts wave reflection and transmission at an infinite rubble-mound breakwater if the incident wave is normal to the structure. This showed reasonable agreement with experimental results [137]. Dalrymple et al. (1991) examined linear theory for water waves impinging obliquely on a vertically sided porous structure, adopting an assumption that neglects the evanescent modes of the water wave near the interface with the porous wall to simplify their problem, finding that for the case of oblique wave incidence on a porous structure, the reflection and transmission coefficients are significantly altered, and consequently, the wave mode can swap based on the angle of attack [37].

Huang (1991) extended the study of Chwang (1983) [29] to a finite-thickness porous medium with the inertial effect of flow inside the porous medium included, finding that either assuming constant velocity across the breakwater (Chwang's approach) [29] or neglecting the existence of surface of seepage (Madsen's approach) might cause significant errors [84]. Simplifying Biot's theory of poroelasticity [19] by letting the skeleton of a porous medium be rigid and the fluid be incompressible, Huang (1991) obtained the governing equation of porous media flow. The governing equation given here is very similar to that found in Sollitt and Cross (1972) [134]. Huang (1991) also studied the effect of inertia due to moving porous media on the derivation of Darcy's Law whereby the porous medium is fixed. If the porous medium is also moving, such as in the case of a porous wave-maker, this inertial effect may not be neglected. Huang generalised Darcy's equation by replacing the velocity of the fluid with the relative velocity of the fluid with respect to the matrix,

$$\mathbf{v} = \mathbf{v}_f - \mathbf{v}_s \tag{2.1}$$

where $\mathbf{v}_f$ and $\mathbf{v}_s$ are the velocity of the fluid and the solid with respect to a fixed frame of reference, respectively [84]. Huang and Chao (1992) investigated a small-amplitude water wave acting on a vertical porous breakwater in an infinitely long channel, employing a model whereby homogeneous water follows conventional assumptions of irrotational, inviscid, incompressible fluid flow. The solid skeleton of the porous breakwater is rigid, and the flow inside the porous breakwater is governed by the simplified Biot theory of poro-elasticity (Biot, 1962 [19]). A small "*porous Reynolds number*" [58] was applied to obtain a regular perturbation solution that preserves the seepage surface on the breakwater/channel flow interface, finding that there are dramatic variations of velocity distributions amongst vertical cross-sections inside the porous breakwater. They also found that the reflected wave is of greater amplitude, whilst the transmitted wave is smaller for waves of higher frequency with thicker and less porous breakwaters. However, the thickness of the porous breakwater only has a significant effect on the transmitted wave, and not the reflected wave [58]. Subsequently, by clarifying the boundary conditions for a thin porous wall with both inertial flow reactance and viscous damping, Huang et al. (1993) analysed the wave field of a thin porous wave-maker with a simplified analytical approach [85].

Sakakiyama and Kajima (1992) used a wave flume with a rubble mound breakwater and a caisson breakwater, while Sawaragi and Deguchi (1992) superposed the waves over a flat permeable layer, obtaining the reflection and transmission coefficients. As in Ozhan and Shigai (1977), Sawaragi and Deguchi (1992) found that the wave attenuation could be predicted precisely if the incident wave had strong linearity [130].

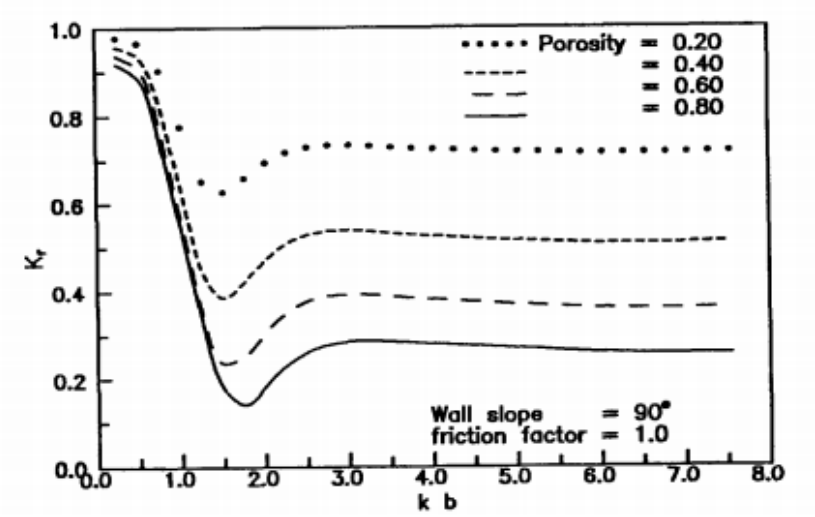

Fig. 2.2 Effect of porosity on reflection coefficient, from Mallayachari and Sundar, 1994

Mallayachari and Sundar (1994) determined the reflection characteristics of permeable vertical seawalls with a numerical model based on the methodology proposed by Ijima et al. (1976) [65]. The variation of the reflection coefficients with the porosity of the wall, its friction factor and the relative wall width were studied and compared with the analytical results of Madsen (1983), showing reasonable agreement [101]. The effect of wall porosity on its reflection characteristics is shown in Figure 2.2 for a constant friction factor of the wall of 1.0, where kb is the product of the wavenumber k and the width b of the porous media at surface water level, and K_r is the absolute value of the complex-valued reflection coefficient, R. The results reveal that the porosity has a negligible effect on K_r for a relative wall width of up to about $kb = 1.20$ for normal range of porosities of rubble materials. Within this range, K_r decreases drastically for a slight increase in kb. Madsen (1983) also has obtained a similar trend with a minimum K_r for porosities of 0.5 and 0.95 [no units] occurring at kb values of about 1.5 and 1.75 respectively.

Yu (1995) studied the diffraction of water waves by porous breakwaters based on linear potential wave theory, including a newly derived relation for the fluid motion through thin porous structures in addition to the conventional governing equation and boundary conditions for small-amplitude waves in ideal fluids. The porous boundary condition, indirectly verified by collected experimental data, demonstrates that neglecting the inertial effect of the porous medium leads to an underestimate of the functional performance of a porous breakwater [160].

Liu et al. (1999) presents a numerical model for simulating wave interaction with porous structures. By using the free-surface-capturing approach together with a novel Cartesian cut cell treatment, the Finite Volume Model calculates the two-phase flows outside porous structure based on the Navier-Stokes equations, while the flow in the porous structure is described by

Navier-Stokes type model equations. The numerical model, based on the computational domain shown in Figure 2.3 is used to simulate the breaking wave overtopping a caisson breakwater, protected by a layer of armour units. The results show that the porous armour layer is effective in reducing the overtopping of the caisson breakwater.

Sakakiyama and Liu (2001) focused on wave behaviour and turbulence flows in front of a caisson breakwater. In their experiments, the breakwater was covered with wave-absorbing blocks and supported by a rubble mound. They concluded that significant turbulence is generated during a wave breaking process and inside the armour layer. The generated turbulence was observed around the caisson breakwater, which considerably affects wave impacts and the scouring process in front of the breakwater [128].

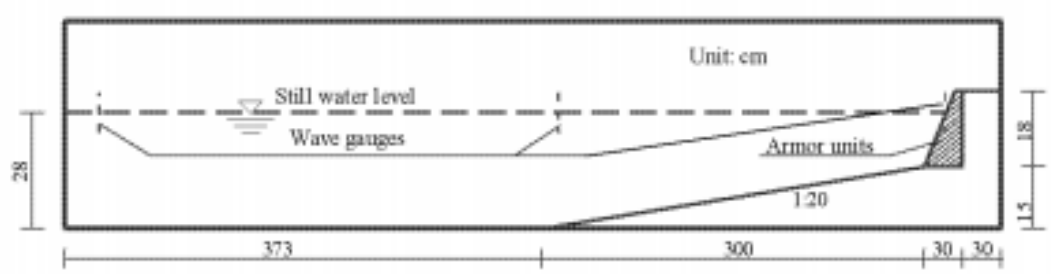

Fig. 2.3 Computational domain used to assess overtopping in Liu, 1999 [94]

Koraim et al. (2014) experimentally investigated the hydrodynamic efficiency of a new type of porous seawall, finding that the run-up and reflection coefficients decrease with increasing porosity: increasing the seawall porosity from n = 0.38 to 0.47, decreases the wave run-up and reflection coefficients by 5–10% [74].

2.2.3 Wave impact

Impact pressures acting on structures are generated by all types of breaking waves, from plunging waves to collapsing breakers in shallow water. It is well known that when a wave breaks directly onto a vertical or inclined wall, impact pressures are produced that can be extremely large in comparison to the pressures exerted by non-breaking waves. Consequently, impact pressures are very relevant to the design of coastal flood defences.

Hattori et al. (1994) performed experiments for wave impact on vertical walls under breaking waves. They found that when a small amount of air is entrapped between the breaking wave and the wall at the collision, the impact pressure increases considerably, so that the highest impact pressure occurs when the smallest air bubble is trapped between the wall and the wave face [53]. Bullock et al. (2007) carried out a detailed investigation into the characteristics of wave impacts against both vertical and inclined walls. They observed that the most substantial

impact pressures occur around the still water level. They also found that whilst nominally identical waves often produce very different pressure distributions, the impulse on the structure during an impact is far less variable and is shown to be broadly proportional to the peak momentum flux of the incident waves [22].

The waves considered for this research project are primarily non-breaking. It is known that regardless of wave height, no wave breaks for slopes steeper than 12° [49]. Consequently, for steeper slopes, the risk of overtopping is a more important factor than the impact pressure, and so the main parameter that is investigated here is the run-up response to different flood conditions.

2.2.4 Summary

Advancements in measurement precision over the last few decades have allowed our understanding of wave motion and impact to be significantly improved. However, whilst many experiments have been performed, only a few analytical models have been developed and validated. One major difficulty with laboratory experiments is the scale effect. Many issues arise from the compressibility of air, particularly in relation to wave impacts. Air compressibility effects are far less significant in a small-scale model than they are in-situ because the relative increases in pressure are much lower. Additionally, most model tests are conducted using freshwater, which tends to hold less entrained air than seawater. Finally, flexibility is a significant limitation of experimental investigations. Wave flumes and laboratory equipment must be set up for each experimental case, which is costly and time-consuming, thus limiting the range of situations and geometries that can realistically be explored. Large wavelengths also require extremely large wave flumes, or a very small scale, thus amplifying the discrepancies that arise from air compressibility. In recent years, researchers investigating problems in the field of hydrodynamics have tended to utilise laboratory experiments to investigate basic physical problems, such as the simple dam-breaking and solitary wave propagation scenarios, and have subsequently used the results of the physical model to compare with results of numerical models. The validated numerical models can then be used to carry out more complex investigations. Numerical studies have therefore rapidly gained traction in recent years as computing power has increased as a method of studying hydrodynamic flow phenomena. Different forms of numerical studies can be split by their discretisation approach into two categories: mesh-based and particle-based. The development of these two approaches is explored in the next section.

2.3 Meshed numerical simulations

2.4 Overview

Computational mechanics is now considered a "third pillar" of scientific investigation, alongside experimental and theoretical studies. All computational analysis (fluid dynamics, solid mechanics, thermodynamics and so on) follows the same basic procedure:

- A mathematical model of the physical phenomenon is developed.
- The continuous mathematical equations are discretised into a form suitable for digital computation.
- The computer program is developed to solve the discretised equations, and the results are processed into useful forms
- The model is verified against benchmark experimental data and refined.

This is an interactive, iterative process and the model is continually refined as processing power increases, new experimental data emerges, and scientific understanding improves.

Computational mechanics methods began with mesh-based simulations. The three classical discretisation methods of computational fluid mechanics are the finite difference method (FDM), the finite volume method (FVM) and the finite element method (FEM).

2.4.1 FDM

The finite difference method is the oldest method, and the most simple. In FDM, the partial derivatives of the function are replaced by the finite differences defined over particular intervals in the coordinate directions. Standard FDM uses regular rectangular grids, creating a major shortcoming of this method when it is applied to any irregular geometries. Furthermore, since derivatives are approximated by finite differences, FDM experiences break down near discontinuities in the solution where the differential equation does not hold [83]. It is now only applied in a few specialist codes which handle complex geometry with high accuracy and efficiency by using embedded boundaries or overlapping grids (with the solution interpolated across each grid) [115]. The finite difference method yields governing equations of the form:

$$\frac{\partial Q}{\partial t}+\frac{\partial F}{\partial x}+\frac{\partial G}{\partial y}+\frac{\partial H}{\partial z}=0 \tag{2.2}$$

where Q is the vector of conserved variables, and F, G and H are the fluxes in the x, y and z directions respectively.

2.4.2 FVM

The finite volume method is now the most common approach used in CFD. It has significant advantages in terms of memory usage and solution speed. It is therefore particularly useful for large problems and high Reynolds number (turbulent) flows. In FVM, volume integrals are converted to surface integrals using the divergence theorem. These terms are then evaluated as fluxes at the surfaces of each finite volume [83]. This discretisation approach guarantees the conservation of fluxes through a particular control volume. FVM can be used in any geometry, using either structured or unstructured grids. The finite volume method yields governing equations of the form:

$$\frac{\partial}{\partial t}\iiint Q\,dV + \iint F\,d\mathbf{A} = 0 \tag{2.3}$$

where Q is the vector of conserved variables, F is the vector of fluxes (see Euler equations or Navier–Stokes equations), V is the volume of the control volume element, and $\mathbf{A}$ is the surface area of the control volume element.

2.4.3 FEM

The finite element method is widely used in the structural analysis of solids, and whilst it is the most commonly applied method in solid mechanics, it may also be applied to fluids. In FEM, the continuum is subdivided into smaller domains, called *elements*. The finite element interpolation functions are then built upon the mesh, which ensures compatibility during interpolation. However, numerical compatibility does not ensure the physical compatibility of a continuum. For instance, in Lagrangian-type computations, mesh distortion may be observed, which can either end the computation altogether or result in a drastic reduction in accuracy [86]. Although FEM must be carefully formulated to be conservative, it is much more stable than the finite volume approach. However, FEM can be computationally expensive, due to a requirement for very fine mesh in problems with high gradients or with distinct local characteristics, and it is slower than the FVM [125] [86]. The Lagrangian formulation of FEM is typically used in solid mechanics, and Eulerian FEM formulations are generally used to solve problems in fluid mechanics [157]. The finite element method yields governing equations of the form:

$$R_i = \iiint W_i Q\,dV^e \tag{2.4}$$

where R_i is the equation residual at an element vertex i, Q is the conservation equation expressed on an element basis, W_i is the weight factor, and V^e is the volume of the element.

2.4.4 ALE

The Arbitrary-Lagrangian-Eulerian (ALE) formulation was developed by Hughes et al. in 1981 to combine the advantages of the Lagrangian and Eulerian depictions of motion [62]. In their formulation, the background mesh can move arbitrarily, it can move with the material as a pure Lagrangian formulation, or it can remain stationary as in the pure Eulerian formulation. The ALE calculation takes place in two steps: first, the governing equations are solved and the new material displacements are calculated, and second, the new mesh is generated and all variables are transferred to the new mesh. The objective is to make the mesh independent of the material so that the mesh distortion can be minimised [86]. The ALE formulation is well suited to cope with modelling large deformations, but the computational cost is correspondingly higher and numerical errors can be generated during the re-meshing process or the transfer of state variables [77]. However, compared to previous mesh-based methods, the ALE formulation is appropriate for modelling fluid-solid interaction problems, and free-surface problems [62]. Significantly, the ALE formulation offers a means of minimising advection errors [103]. However, in simulations with extremely large deformations or high speeds, even with the ALE formulation, a distorted mesh introduces severe errors in numerical computations. Furthermore, the convective transport effects in ALE often lead to spurious oscillation that needs to be stabilised by artificial diffusion or a Petrov-Galerkin stabilisation [86].

2.4.5 MAC

The Marker and Cell (MAC) method was developed by Harlow and Welch (1965) at the Los Alamos National Laboratory [143]. In their first paper, the method was introduced with two sample calculations of the dam-break problem. In MAC, the Navier-Stokes (NS) equations for viscous incompressible flow are used in a finite-difference form. This method uses marker parcels to define a free-surface. A cell without a marker means that there is no fluid, whereas a cell with markers next to an empty cell describes a free-surface. Consequently, boundary conditions must be applied at the surface and the fluid in the rest of the domain must be completely passive. The staggered grid used was a novelty and today any method using a projection-based time integration scheme on a staggered grid is referred to as a "MAC method".

The method was developed further at Los Alamos to be applied to two fluid problems; Chan and Street (1970) improved the original MAC and proposed the Stanford University Modified MAC (SUMMAC) code, making a model suitable for incompressible flows with a free-surface, and subsequently using it to model free-surface waves.

More recently, a solitary wave over porous beds was simulated by Huang et al. (2008) and verified experimentally [57]. Previous work by Huang et al. (2003) had indicated that the fluid

motion near the bottom would cause scour in front of a breakwater. However, this water-soil interaction was not investigated by MAC since it cannot be used to describe soil displacement [56]. Significantly for this thesis, the MAC method requires that more than ten markers are in each cell to track a free-surface accurately, leading to a significant computing time and load.

2.4.6 VOF

The next generation of methods for multi-fluid flow evolved gradually from MAC, largely because of the work done at the Los Alamos laboratories. Since the marker particles could lead to inaccuracies, they were replaced by a marker function. This was the Volume-of-Fluid (VOF) method.

In VOF, a function F is defined, which represents the fractional volume of fluid occupying each cell. For instance, the function F becomes unity if a cell is fully occupied by fluid. A free-surface is represented by an F value between zero and one accordingly. Defining this marker function makes VOF much more efficient than MAC. In first appeared in a journal article by Hirt and Nichols (1981).

The VOF method has been extended widely by a range of authors. It is commonly used in many commercial CFD software packages, including the popular FLOW3D.

2.4.7 Summary

Many numerical models based on a mesh structure exist for wave motion in and around porous structures, and simulations have been performed and validated. However, mesh-based methods often suffer from numerical diffusions since the Navier-Stokes equations are solved in a fixed grid. These diffusions become significant when the free-surface moves violently, causing the accompanying grid distortion. Generally, using classical mesh-based methods such as the finite element method (FEM) to model any behaviour that involves large deformations becomes challenging due to severe mesh distortion resulting in numerical errors. Mesh-based methods are therefore inadequate for simulating complex wave motion; this includes modelling breaking waves.

2.5 Particle methods

The drawbacks associated with mesh-based computational mechanics methods in modelling large deformations prompted the development of meshfree methods. Advances in particle methods that can be derived in continuum mechanics framework allow modelling of large deformation behaviour using conventional geotechnical constitutive models [12], enabling

more accurate modelling of soil behaviour under large deformations, such as those that arise during landslides. These methods can also be applied to fluid mechanics problems; Liu et al. (1999) used the surface capture technique, where a high-resolution shock-capturing solver captures the discontinuous density profile which occurs at the free-surface. In contrast to VOF schemes, no explicit surface reconstruction is required. However, to capture the free-surface, the governing equations must be written in a hyperbolic formulation; requiring the use of a dual time approach to solve the incompressible form of the Navier-Stokes equations [94].

Meshfree methods can be subdivided into those that solve the strong form of PDEs, such as smoothed particle hydrodynamics (SPH), the vortex method, and the generalised finite difference method (GFDM), and those that approximate the weak forms of PDEs, such as the diffuse element method (DEM), the element free Galerkin method (EFGM), and the meshless local Petrov-Galerkin method (MLPG). Other meshfree methods like the particle-in-cell (PIC) method and the reproducing kernel particle method (RKPM), can be used in both strong form and weak form discretisations [86].

The advantages of the meshfree particle methods can be summarised as follows, adapted from Li and Liu (2002) [86]:

- They can easily handle large deformations.
- No mesh generation is required.
- They can easily handle material fracture.
- Accuracy can be controlled easily by adding more particles to important areas.
- Meshfree discretisation can provide more precise representations of geometric objects.

However, despite these advantages over mesh-based methods, entirely meshfree methods suffer from increased computational cost and particular difficulties with applying any boundary conditions.

2.5.1 DEM

The discrete element method has its origins in the distinct element method proposed by Cundall in 1971 [35] to investigate rock system mechanics. Williams, Hocking & Mustoe (1985) developed the generalised discrete element method, showing that DEM could be viewed as a generalised finite element method [155]. DEM is a simple and flexible discrete-element approach, which involves applying Newton's second law of motion to each constituent grain to describe the deformation of the granular assembly [78]. The application of DEM to

geomechanics is described by Williams, Pande and Beer in their book *"Numerical Methods in Rock Mechanics"* (1990) [154].

The primary concept of the DEM is that the material domain is treated as an assembly of rigid or deformable particles, and the contact points amongst these particles are identified and continuously updated during the entire deformation process [68]. Material behaviour is represented by appropriate constitutive models. DEM can be based on both implicit (based on FEM discretisation) and explicit (using FDM/FVM discretisation) formulations. The major difference between the DEM and continuum-based methods is that the contact patterns between components of the system are continuously changing with the deformation process for the former, but are fixed for the latter [68].

Modern versions of DEM are applied to rock mechanics, soil mechanics, structural analysis, granular materials, material processing, fluid mechanics, multi-body systems, robot simulation, computer animation, etc., and DEM is one of most rapidly developing areas of computational mechanics [68]. The drawbacks of this method include the high computational cost and the difficulty in understanding constitutive behaviours associated with DEM simulations [157].

2.5.2 SPH

The Smoothed Particle Hydrodynamics (SPH) method is another method that is widely used in hydrodynamics research. The SPH method is a mesh-free numerical approach particularly suitable for dealing with large free-surface deformations and complex fluid-structure interactions [89]. The use of SPH to model wave interaction with offshore structures is a very active research area in hydrodynamics and coastal engineering. It has been extensively employed in the field of wave propagation and wave-structure interaction [89].

SPH was one of the earliest particle methods in computational mechanics [86]. It was first developed in 1997, simultaneously by Lucy [95] and Gingold and Monaghan [44]. SPH is a fully Lagrangian particle method, in which a continuum material is divided into a set of particles with constant mass, and each particle is assigned a spatial distance called a smoothing length in which the physical properties of each particle is smoothed using a kernel function. Early contributions have been reviewed extensively by various researchers [16, 110, 112]. Although SPH is now used extensively in research areas across the field of geomechanics, it suffers from certain disadvantages for geotechnical problems; many of these involve boundary interfaces (soil-structure interaction). The accuracy of SPH simulations is reduced near boundaries since there are insufficient neighbouring particles, resulting in a loss of consistency; this is currently a widely investigated topic in the SPH research community.

Smoothed particle hydrodynamics was originally developed by Lucy (1977) and Gingold and Monaghan (1977) for use in astrophysics [95, 44]. In SPH, the material is represented by a

series of Lagrangian particles carrying all the physical properties of the continuum. The basic concept of SPH is that the physical properties of each particle can be interpolated from those of neighbour particles. Mass conservation is automatically satisfied. Spatial derivatives are found by analytical differentiation of interpolation formulae. The equations of momentum and energy become sets of ordinary differential equations which are easy to understand in mechanical and thermodynamic terms. Since it is a Lagrangian method, it naturally handles the free-surface breaking and water fragmentation that occurs during wave impact on coastal structures. Monaghan (1992) first extended the SPH formula from astrophysics to incompressible free-surface flows and demonstrated that SPH formulae could also be applied to magnetics, thermal dynamics and hydrodynamics problems, using a weakly compressible assumption to avoid computational complications when modelling fluid flow [112].

Since its initial development for problems in astrophysics, due to the ability of SPH to incorporate complex physics, it has been extended to solve a vast number of problems in fluid mechanics and solid mechanics [92], including areas such as coastal hydrodynamics [32, 36, 70, 90, 113, 111], landslides [10, 24, 26, 27, 59, 121, 120], problems involving fluid-solid interaction [8, 20, 23, 124, 90, 133, 135], interfacial flows [30, 48], and dam-break flows [90, 123].

Monaghan (1994) was the first to apply SPH to free-surface incompressible flows, including application to a breaking dam, a bore, the simulation of a wavemaker, and the propagation of waves towards a beach [113]. Since then, SPH has been widely used in the field of computational fluid dynamics. Monaghan and Kos (1999) demonstrated the capability of SPH to model the run-up of a solitary wave travelling over shallow water with a vertical wall. Their simulation showed good agreement with the experiments, however, they applied SPH for weakly compressible flows to incompressible flow cases [111]. The conventional weakly-compressible SPH (WCSPH) has been found to lead to unphysical pressure fluctuations that arise near solid boundaries. These typically result from the equation of state amplifying small errors in the density and is commonly mitigated by calculating the forces based on the acceleration rather than the pressure [89].

To overcome these drawbacks, incompressible SPH (ISPH) methods have been developed. Cummins and Rudman (1999) first introduced a new formulation for enforcing incompressibility in SPH, based on another popular meshfree method, the Moving Particle Semi-Implicit method (MPS). MPS was developed and used by researchers such as Koshizuka et al. (1998) [76], Gotoh and Sakai (1999) [47], and Hwang et al. (2014) [63]. The incompressible SPH method developed by Cummins and Rudman adopts a fractional step with the velocity field integrated forward in time, without enforcing incompressibility. The resulting intermediate velocity field is then projected onto a divergence-free space by solving a pressure Poisson equation derived

from an approximate pressure projection. Thus, fluid pressure is derived by solving a pressure Poisson equation (PPE) based on a strict incompressibility condition [34]. This method is called incompressible SPH (ISPH). Cummins and Rudman found that simulations using this SPH projection technique showed good agreement with finite-difference solutions for a vortex spin-down and the Rayleigh–Taylor instability. However, their results indicated that using an approximate projection to enforce incompressibility can then lead to error accumulation in the density field [34].

Shao and Lo (2003) also contributed significantly to the development of ISPH, presenting a strictly incompressible SPH for flows with free-surfaces. The incompressible SPH method was tested with typical 2D dam-break problems in which both water and fluid mud were considered and were in good agreement with experimental data [132]. However, the ISPH formulations did not generally preserve angular momentum, which strongly influences computations, particularly for violent free-surface flows. The computational cost of solving the PPE in ISPH is much larger than that of the WCSPH, but the ISPH model allows a much larger time step than the WCSPH method [172, 89].

ISPH was modified by Khayyer et al. (2008) to satisfy the conservation of angular momentum to form the Corrected ISPH (CISPH) [70]. The introduction of corrective terms was found to significantly improve the capability and the accuracy of the ISPH method in the simulation of wave breaking and post-breaking [70]. The incompressible SPH (ISPH) method solves the pressure field using the PPE, rather than relying on the equation of state. It therefore has the advantage of producing more stable and accurate pressure fields and impact forces on structures [89].

Khayyer et al. (2009) improved the CISPH method by applying a higher-order source term to the PPE based on a more accurate differentiation [71], to obtain a less fluctuating and more accurate pressure field. They assessed wave impact pressure on a vertical wall in case of a dam-break and wave propagation over a slope, demonstrating an enhanced performance. However, the improved CISPH method is still based on a single phase. Per Hattori at al. (1994), the pressure is highest when air bubbles are trapped between the wall and a wavefront [53]; two phases should be employed for more accurate simulations. Furthermore, no turbulence model was included in these simulations; turbulence has a significant contribution to wave impact pressure, suggesting that improvements to the method are necessary to ensure the accuracy of the results.

Application of SPH to flows in porous media

Shao (2010) introduced ISPH to flow within porous media [131]. In his model, the flow outside the porous media is solved by the unsteady two-dimensional Navier–Stokes equations, and the

NS-type model equations are solved for the flow inside the porous media. The presence of a porous medium is accounted for by additional friction forces in the equations. The model is validated using the cases of solitary and regular wave damping over a porous bed, and solitary wave interaction with a submerged porous breakwater, thus demonstrating that the ISPH flow model could provide a useful simulation tool in coastal hydrodynamic applications [131]. The assumption for this case was that the turbulence effect should be negligible for the flow outside porous structures, as in Liu et al. (1999) [94] and Huang et al. (2003) [56]; however, Shao concluded that the effect of turbulence should be considered in further work [131].

Rogers et al. (2010) used SPH to simulate the movement of a caisson breakwater in the surf zone, using the open-source code SPHysics with a Rieman solver-based formulation [127]. Although caisson breakwaters consist of caisson blocks and rubble mounds, the mounds were assumed to be impermeable, and thus the permeable flow through the rubble mound was not simulated in their SPHysics model. It was demonstrated that the peak impact forces are captured more accurately using finer resolution and that a Riemann solver-based formulation produces a better agreement with experiment for the predicted caisson displacement than that of conventional SPH [127]. Altomare et al. (2014) extended SPH to model the three-dimensional fluid–structure interaction for waves approaching a rubble mound breakwater is presented [4]. Whilst Rogers et al. (2010) had not been able to reproduce permeable rubble mounds in their model with SPHysics [127], Altomare et al. (2014) investigated the interactions between waves and rubble mound breakwaters, using the open-source code DualSPHysics, and reasonable agreement was obtained for the run-up due to regular waves [4].

Mamouri et al. (2015) proposed an improved ISPH which employs first-order consistent discretisation and by using a wall boundary condition, does not require dummy particles at the boundaries [102]. Gui et al. (2015) investigated the flow motion through porous structures using ISPH, proposing a new boundary treatment that utilised an interface zone, defined between a pure liquid region and porous region [50]. Alongside this, Ren et al. (2016) developed an improved weakly compressible SPH to model wave motions and turbulent flows around porous media. The sub-particle-scale turbulence stresses are calculated using an eddy viscosity type model, and the porosity information is carried by fixed background porosity points. Similarly, this paper proposed an interpolated transition zone between pure liquid and porous areas, in which porosity changes gradually [126].

Iryanto and Gunawan (2016) used the SPH framework to investigate wave mitigation by coastal vegetation [66]. By changing the vegetation resistance to the fluid flow to minimise wave propagation, this paper demonstrates that the inclusion of resistance terms in the Lagrangian SPH model is a viable method for modelling the vegetation resistance to impinging solitary waves on a sloped beach. Furthermore, it is shown that the inclusion of the resistance term

results in mitigation of the water level elevation as the wave propagates inland [66]. Liang et al. (2017) then used ISPH to assess solitary wave propagation and impact on movable impermeable seawalls [89], assessing both wave run-up height and hydrodynamic loading on the vertical seawall in detail and finding good agreement with previous experimental and numerical results.

Recently, Khayyer et al. (2017) developed a novel numerical method, based on ISPH, to simulate the wave interaction with saturated porous media [72]. The numerical method is validated for the case of solitary wave interaction with a submerged porous structure by comparison with the results of Wu and Hsiao, (2013) [156]. Unlike the methods of Gui et al. (2015) [50] and Ren et al. (2016) [126], the presented method does not require any interface or transition zone thanks to the implemented enhanced schemes [72], showing that SPH can accurately model the fluid flow through porous media.

Summary of SPH-based methods

In summary, the meshfree, Lagrangian SPH method is naturally well suited to handling the large free-surface deformations such as wave breaking and wave impacting that arise during the dam-break flows and solitary wave run-up problems considered in this research, when compared to an Eulerian approach [93]. SPH is also able to capture the material history and can be extended with relative ease to three-dimensional cases [92]. However, significant difficulties arise when handling boundary conditions due to the lack of background mesh, creating computational complexities when the porous nature of the structures is considered. Compared to mesh-based methods, the SPH approach to solving geotechnical problems of fluid-structure interactions is much more challenging due to the boundary interfaces. To reproduce the behaviour of the fluid flow within the porous medium, an extremely high resolution of SPH particles would be necessary, resulting in prohibitively high computation costs. Computational costs are further increased by the relatively high number of interacting particles at a given timestep [6]. The inability of the SPH method to account for the effect of run-up is documented in [126, 144]. Arbitrary moving boundaries can be included by modelling the boundaries by particles which repel the fluid particles. The method is explicit, and the time steps are therefore much shorter than required by other less flexible methods, but it is robust and easy to program [113]. However, numerical oscillations of particles can occur since SPH does not require the velocity field to be single valued (it allows particle penetration). Furthermore, the local refining of the spatial resolution remains a current issue. Although it has been addressed by few advanced and complex SPH algorithms, the accuracy is relatively low compared with more established mesh-based methods; accuracy near the boundary is lower due to insufficient neighbouring particles, resulting in a loss of consistency [92]. These problems remain the main challenges in SPH research and significantly improved SPH algorithms are still required to

overcome these issues. SPH was therefore considered to be a less appropriate method than the material point method for this research project.

2.5.3 MPM

MPM is an extension of the fluid implicit particle (FLIP) method [139] which itself is an extension of the particle-in-cell (PIC) method [21]. The FLIP method introduces Lagrangian particles to the PIC method, thus eliminating the need to discretise the convective term, which is a major source of numerical errors in the PIC method [139]. The Lagrangian depiction allows the FLIP method to successfully track material discontinuities and to model highly distorted flows [13, 139]. The development of MPM was motivated by the desire to better model history-dependent materials in solid mechanics. In contrast to the FLIP method, the governing equations of MPM are presented in the weak formulation, allowing for consistency with FEM. Using FEM is currently common practice in soil mechanics research and geotechnical design [122]. In FLIP, the stresses and strains are stored in the centre of the cell, and constitutive equations are solved at the grid nodes [138]. However, in MPM, these variables are carried by the particles themselves. Thus, the material points carry the full physical state of the material including position, mass, velocity, volume, stress, temperature etc., so that the mesh carries no permanent information. In PIC, the particles carry only position and mass. MPM, therefore, combines the advantages of both Lagrangian methods and Eulerian methods, avoiding the drawbacks of both, such as the numerical dissipation problems of Eulerian methods and the mesh distortions and element entanglements of Lagrangian methods [168].

In the material point method, Lagrangian point masses, referred to as material points, are moved through an Eulerian background mesh. Although there is a mesh, it is used only to solve for the governing equations for computational convenience. All the properties of the continuum material are assigned to the material points, and all the information is carried by these material points, so the mesh does not carry permanent information. The major advantage of this method compared to other methods is that application of boundary conditions is straightforward due to the presence of background grid since the boundary conditions can be directly applied to grid nodes as in the FEM [12]. The formulation is dynamic and automatically includes a no-slip contact algorithm. These features make MPM especially useful for solving problems involving large deformations and displacements, velocities and accelerations. The mathematical basis of MPM is explored in detail in the next chapter; here, we focus on the previous applications of this methods and the advantages of selecting this method for the investigations carried out in this thesis.

Sulsky et al. (1995) first developed the MPM for use in solid mechanics problems [139]. Since then, MPM has had a major impact in many engineering fields due to its capability of

simulating large deformations without limitations introduced by the mesh tangling that occurs in mesh-based methods. The single-phase MPM has been applied to several geotechnical problems that involve large deformations, for example, studies of granular flows in Więckowski et al., 1999 [153], modelling anchors in soils [18], landslide run out in Andersen and Andersen, 2010 [7] and Yerro et al., 2014 [158] and retaining walls in Więckowski, 2004 [151]. In these examples, the soil is considered as a single-phase material.

During the last decade, MPM has been widely applied to water-soil interaction problems. Martinelli and Rohe (2015) modelled the fluidisation and sedimentation process in MPM, including simulation of the transition from water to groundwater [106]. Bandara (2013) simulated the column collapse problem with both SPH and MPM, obtaining the same results [11]. However, the SPH simulation required many more particles to obtain an accurate run-out distance and so was more computationally expensive.

More recently, MPM has been extended to solve multi-phase problems in saturated ([1], [170]) and unsaturated porous media [158]. The interaction between the two phases has been formulated in two different manners, either adopting one set of material points (Zabala and Alonso, 2011 [162]; Jassim et al., 2013 [67]) (single-point formulation) or two sets (Więckowski, 2013 [152]; Abe et al., 2014 [1]).

Many problems of interest to engineers involve saturated soils, but the application of MPM to multi-phase problems has been limited. A few exceptions are Zhang et al. (2007, 2008) and Higo et al. (2010). Zhang et al. modelled fluid-saturated soil by using two layers of material points: a solid layer and a fluid layer [166]. This two-point formulation is discussed in section 3.3.4 and allows modelling of coupled soil-water behaviour, such as changes in the location of the phreatic surface with time, by computing the movements of the fluid particles within the soil. This initial formulation assumed only a small deformation of soil; the same interpolation function was used for both the solid and the fluid layers [97].

Zhao and Liang (2016) simulated a seepage flow through embankment using MPM with two sets of material points, representing soil and fluid respectively [170]. Zhao and Liang (2017) then used MPM to investigate collapsing water columns with different initial aspect ratios [171]. Their simulations were validated using experimental data and results of more mature numerical models to establish the accuracy and stability of the material point method. MPM produced reasonable results for the pressure distribution and propagation speed of dam-break flows [171].

Yerro et al. (2017) extended the MPM formulation to model internal erosion problems [159]. Internal erosion refers to the mechanism of detachment and movement of soil grains resulting from water flow through a porous medium; this phenomenon occurs when soil grains are mobilised by seepage flow, detaching from the solid skeleton and leading to internal erosion.

Internal erosion is one of the main failure mechanisms of water retaining structures such as dykes and dams. The model used consists of a mixture of coarse and fine grains: the coarse fraction forms the stable skeleton of the soil, whilst fine grains can be eroded and thus can move freely with seepage flow. Although the presented formulation showed reasonable results, it was noted that mechanical behaviour of the solid skeleton and internal erosion effects should be coupled in future investigations [159].

Subsequent work has been carried out to develop the MPM code further to allow for more precise modelling of partially saturated soil. However, the research interest of this thesis is the effect of changing the porosity of a barrier on the interaction with a water wave, so complex models of partially saturated soils are currently only of limited interest.

Advantages of MPM

MPM offers many advantages over traditional mesh-based and meshfree numerical methods [170]. Of particular relevance in the field of soil mechanics is that history-dependent constitutive models can be incorporated because information such as strains, stresses, and other time-dependent variables are carried by the moving material points, enabling spatial and temporal tracking of the complete history of the material motion. Furthermore, the implementation of a background mesh also gives MPM certain advantages when compared to meshfree methods: the application of boundary conditions is more straightforward, and these can be implemented like that employed in FEM. MPM is also free of the tensile instability that is evident in SPH [90, 96]. MPM is often more computationally efficient than meshfree methods; for example, SPH and EFGM require a time-consuming neighbouring particle search, whereas MPM only requires the identification of particles relative to the background mesh [1]. Perhaps more significantly for geotechnical engineers, since MPM is so similar to traditional FEM, various advanced FEM features can be adopted into MPM with relative ease [169].

Disadvantages of MPM

One major drawback of MPM is a well-known issue with grid crossing errors due to the lack of smoothness in the interpolation function [13]. This issue has been documented by various researchers, such as in [3, 39, 41, 169]. Grid crossing errors arise as a result of the linear shape functions used for spatial discretisation: the gradient of the shape function (used for calculation of internal forces) is discontinuous at the nodes so that when a material point crosses through an element, unphysical imbalanced forces are generated at the node, creating oscillations [42]. The effect of grid-crossing errors become more apparent in simulations with fewer materials points per element, or with a higher mesh resolution, since the migration of material points

through elements speeds up [51]. Measures employed to tackle grid crossing errors include higher-order nodal shape functions or B-spline shape functions to obtain smoother gradients of the shape functions at nodes, as well as modifications to the gradients of the shape functions without changing the shape functions themselves [42]. It is also possible to introduce a particle characteristic function for the material points, that allows material points to partially cross elements [169].

2.5.4 Variants of MPM

In addition to the double-point MPM used in this thesis, other variants of MPM have been developed by various researchers. Bardenhagen and Kober (2004) generalised MPM, obtaining a group of methods called the generalised interpolation material point (GIMP) methods and suggesting that that MPM is a subset of GIMP methods [13]. In GIMP methods, a characteristic function χ_p is selected to represent the particles, and a shape function S_i is chosen as a basis of support on the computational nodes [147]. The effective shape function $\overline{S}_{ip}$ is calculated by the convolution of χ_p and S_i. The traditional MPM formulation can, therefore, be recovered when the Dirac delta function is chosen as the characteristic particle function [13], such that

$$\chi_p(x) = \delta(x - x_p)\Omega_p \tag{2.5}$$

The dual-domain material point method (DDMP) smooths the nodal shape functions, instead of introducing characteristic functions as in GIMP methods [165]. To this end, an auxiliary stress σ_A is added to the stress tensor, representing an addition of viscosity to the system [42]. Other variants on MPM include convected particle domain interpolation methods (CPDI1 and CPDI2), the spline grid shape function, adaptive material point methods and various other methods developed by different researchers for specific applications. More detailed information on alternative forms of MPM that are not employed here can be found in [168] and [42].

2.6 Turbulence modelling

Turbulence modelling was initially approached by researchers employing Reynolds-averaged Navier–Stokes (RANS) equations. In these models, an ensemble version of the governing equations is solved. This introduces new apparent stresses to the equations, known as Reynolds stresses, adding a second-order tensor of unknowns for which various models proposed by different authors can offer some level of closure.

Liu et al. (1999) first proposed a numerical model based on the VOF method for wave interaction with porous structures. The model calculates the mean flow outside of porous

structures based on the Reynolds averaged Navier-Stokes equations. The flow in porous structures is described by the spatially averaged Navier-Stokes equations, and the free-surface was tracked by the VOF method. It was assumed that the turbulence in a pore flow would be relatively little since the maximum intensity of turbulence depends on the mean pore size, and the Navier-Stokes equations are averaged over a length scale that is much larger than the pore size. The mean and average velocity and pressure fields of the outside flow were therefore applied to the inside flow. Good agreements between numerical results and laboratory data were obtained in terms of both free-surface displacement and overtopping rate [94].

Lara et al. (2006) simulated irregular wave interaction with submerged rubble-mound breakwaters based on the model of the Reynolds-averaged Navier Stokes equations presented in Liu et al. (1999), using results from small-scale experiments and numerical results provided by a VOF-type model (COBRAS) based on the Reynolds-Averaged Navier–Stokes (RANS) equations, finding that the overall pattern of the wave interaction with a large-scale submerged breakwater is adequately reproduced by the numerical model [80].

Hsu et al. (2002) developed the model in Liu et al. (1999) to describe surface wave motions around a solid or permeable structure. The improved model was based on a consistent volume averaging process, the Volume-Averaged/Reynolds Averaged Navier-Stokes (VARANS) equations. In the VARANS equations, the volume-averaged Reynolds stress is modelled by adopting the non-linear eddy viscosity assumption. The model equations for the volume-averaged turbulent kinetic energy and its dissipation rate are derived by taking the volume-average of the standard $k-\varepsilon$ equations. Because of the volume-averaging process, the effects of the small-scale turbulence in porous media are introduced [55]. The model was validated by comparing numerical solutions with the experimental data related to a composite breakwater reported by Sakakiyama and Liu (2001).

Karunarathna and Lin (2006) used the numerical model from Liu et al. (1999) as a basis for investigating wave damping by porous sea beds. In their model, the flow outside porous media was described by the Reynolds Averaged NS equations, and the spatially averaged NS equations were implemented for the flow inside the porous media. The comparison between the numerical results and the theoretical results indicated that the omission or linearisation of the non-linear resistance terms in porous flow models can lead to significant errors in estimating wave damping rate [69].

Lara et al. (2011) simulated solitary wave evolution over a shelf including porous damping using the Volume-Averaged Reynolds Averaged Navier–Stokes equations mentioned above. The influence of several parameters such as geometrical configuration (step height and still water level), porous media properties (porosity and nominal diameter) or solitary wave characteristics (wave height) were analysed. A soliton refers to a self-reinforcing solitary wave packet that

maintains its shape while it propagates at a constant velocity. In the absence of breaking, a porous bed is found to trigger faster fission of the incident wave into a second and a third soliton, and both the leading and the second soliton reduce their amplitude whilst propagating. This decrement in amplitude is observed to increase with porosity [81].

del Jesus et al. (2012) extended this model to three-dimensional flows and interactions between waves and porous structures. The model integrates a new set of equations which covers physical processes associated with flow interaction with porous structures. The model considers the multiphase VARANS equations, a volume-averaged version of the traditional RANS (Reynolds-Averaged Navier–Stokes) equations, as in Hsu et al. (2002). Turbulence is modelled using a $k-\varepsilon$ approach, not only at the clear fluid region but also inside the porous media, and a VOF technique is used to track the free-surface. In this paper, the model has been validated using laboratory data of a two-dimensional flow [38].

Following this, Lara et al. (2012) describe how this model is further validated with new experimental data sets, considering porous and solid structures as well as the presence of air. The model predictions present an excellent agreement with the laboratory measurements [79].

In these papers, the numerical resolution is an essential factor for this model. Lower resolutions cause the uncertainty on wave discharge calculations when waves over-top structures. The results also confirm that the theoretical models that have been derived by neglecting the non-linear resistance term can only be used at low *Re* flows. On the other hand, the linearisation of non-linear porous flows may also result in the underestimation or overestimation of wave damping in different ranges of soil permeability [38].

2.7 Summary

This chapter has reviewed various computational and experimental methods that are currently employed to investigate hydrodynamics problems. These methods have been grouped based on their discretisation approach into meshed and meshfree methods. In short, methods employing a mesh are well established, offering computational efficiency and easy application of boundary conditions. On the other hand, meshfree methods are better suited to the modelling of large deformations and situations with complex geometries. Since the problems investigated in this thesis involve large deformations, this review focused on the meshfree technique SPH, and MPM where the mesh exists for computational convenience but does not carry permanent information.

Both MPM and SPH show more promising results than traditional mesh-based methods, which are not generally effective in modelling soil behaviour. MPM has been proven to be useful in modelling large deformations and dealing with moving boundary conditions.

This thesis investigates wave interaction with porous media, and consequently, the soil-water interaction must be considered. As with many geotechnical problems, this involves boundary interfaces and in using SPH, accuracy near the boundaries is reduced, since insufficient neighbouring particles result in a loss of consistency. Numerical oscillations of particles can occur since SPH does not require the velocity field to be single-valued. The single-phase MPM has already been applied to several geotechnical problems that involve large deformations, and the double-point MPM is more developed than two-phase SPH. MPM combines the advantages of both mesh-based methods and meshfree methods, and due to its resemblance of traditional FEM methods, has been widely employed by different research groups and consequently has developed rapidly in recent years. This thesis has therefore chosen MPM as the most suitable method for studying water-wave interaction with porous media. The major drawback of MPM, as previously highlighted, is the grid crossing error. To this end, this research employs a standard form MPM and the MPM-Mixed integration technique detailed in section 3.4.9 is employed to alleviate the associated grid-crossing errors.

Whilst turbulence generated by fluid-structure interaction will affect the flow inside the structure, per Liu et al. (1999), Huang et al. (2003) and Shao et al. (2010), the turbulence effect can be considered negligible for the flow outside porous structures, and since the run-up height is not determined by flow within the porous medium, turbulence can reasonably be neglected in this instance. As Sakakiyama and Liu (2001) observed, there is a significant turbulence intensity inside breakwaters [128]. Turbulence is also crucial when investigating the effects of changing porosity on wave pressures. However, turbulence effects have been found to only be significant if the pore size is comparatively large [55], since the maximum intensity of the turbulence is dependent on the pore size, and the governing Navier-Stokes equations are averaged over a length scale that is much larger than the pore size, so for the investigations carried out during this project, it is reasonable to assume that the turbulent nature of the flow within the porous medium does not affect the overall run-up height. It should be noted, however, that turbulence effects may play an important role in the wave breaking zone [126], [131], [2].

Chapter 3

Methodology

3.1 Overview of the Material Point Method

The material point method (MPM) has its origins in the particle-in-cell (PIC) method that was first developed by Harlow at the Los Angeles National Laboratory in 1957 [52]. The first PIC codes suffered from excessive energy dissipation. This was overcome in 1986 by Brackbill and Ruppel who developed the Fluid Implicit Particle method (FLIP) [21]. FLIP was later modified to form MPM by Sulsky et al. of the University of New Mexico [138] who extended FLIP to look at solid mechanics problems by discretising the equation for the dynamic momentum balance, forming the basis of the material point method. The MPM is built on the two main concepts used in PIC: Lagrangian material points carrying the physical information, and a background Eulerian grid used for the discretisation of the continuum body. Originally, MPM was envisaged as a way of modelling fluid flow as a set of material points moving through a fixed background mesh [139]. The success of the method led to its application to other problems; MPM was subsequently applied to dry granular materials by Więckowski in the late 90s [150, 153, 151].

In 2012, the material point method was extended to handle saturated soils (coupled, dynamic, two-phase problems) [67], with a numerical approach which uses the velocities of both the solid and fluid phase as the primary variables. This code was applied to several small and large deformation problems and was able to capture the physical response of saturated soil under dynamic loading, including examples such as the physics of wave propagation, consolidation and wave attack on a sea dyke. However, only one set of material points is used to encapsulate both the solid and the liquid phase; therefore, groundwater flow and the transition between free surface water and groundwater cannot be captured [107]. Recently, a formulation with two sets of material points has been proposed ([11], [12]) to overcome this. Extensions to the double-point formulation were first presented by Martinelli and Rohe in 2015 ([106]) and then

extended by Martinelli in 2016 ([105]). In the Anura3D code, this is achieved by the use of two sets of material points to handle a separate velocity field for the solid and liquid phases, for example, to investigate the case of seepage flow through dams. The two-phase approach with two sets of material points is explored in detail in section 3.3.4. The history and applications of MPM are explored in greater detail in section 2.5.3 in the previous chapter; here, we focus on the mathematical framework of the different formulations used in this research.

This study has not explicitly considered the effect of turbulence. Although turbulence is generated when the incoming flow interacts with porous media, these effects are not directly resolved. Turbulence effects of flow inside the structure could also be considered. As Sakakiyama and Liu (2001) observed, there is a significant turbulence intensity inside breakwaters [128]. Turbulence is also crucial when investigating the effects of changing porosity on wave pressures. However, turbulence effects have been found to only be significant if the pore size is comparatively large [55], since the maximum intensity of the turbulence is dependent on the pore size, and the governing Navier-Stokes equations are averaged over a length scale that is much larger than the pore size, so for the investigations carried out during this project, it is reasonable to assume that the turbulent nature of the flow within the structure does not affect the overall run-up height. Additionally, per Liu et al. (1999), Huang et al. (2003) and Shao et al. (2010), the turbulence effect can be considered negligible for the flow outside these permeable structures, and since the run-up height is not directly determined by flow within the structure, turbulence can reasonably be neglected in this instance. It should be noted, however, that turbulence effects may play an important role in the wave breaking zone [126], [131], [2]. If the study were extended to much larger pore sizes, it would, therefore, be recommended to consider the turbulent effects. It may also be useful to consider wave pressure and impact force, as well as run-up height, for which the turbulence would certainly need to be considered.

3.2 Framework of the Material Point Method

Within the MPM, there are two fundamental frames to describe motion:

- Lagrangian: A mesh is embedded in, and deforms with, the material domain. There are no convective effects: the boundary conditions at the free surface, moving boundaries, and material interfaces are automatically imposed. This is ideal for a history-dependent material, however, if the deformation is very large, mesh distortion and element entanglement become limiting factors. Meshfree methods use a set of discrete points to construct trial functions so mesh distortion difficulties can be completely avoided. However, there is a high computational cost and the accuracy is, to some extent, dependant on the regularity of the nodes.

- Eulerian: A material flows through a fixed background grid. This completely avoids numerical issues relating to element distortion, but difficulties arise in dealing with the deformation history of the material and in tracking the material interface.

To achieve this, the material domain is discretised into material points. These are Lagrangian points that carry all the material information and track the deformation history of the body. The momentum equations are solved on a predefined background grid, providing an Eulerian description of the domain. Figure 3.1 shows the space discretisation: how the material points are generated within a background mesh.

This combines both Lagrangian and Eulerian depictions of motions for an optimal description of large deformation so that MPM is considered to be in-between particle-based methods such as SPH, and the Finite Element Method (FEM).

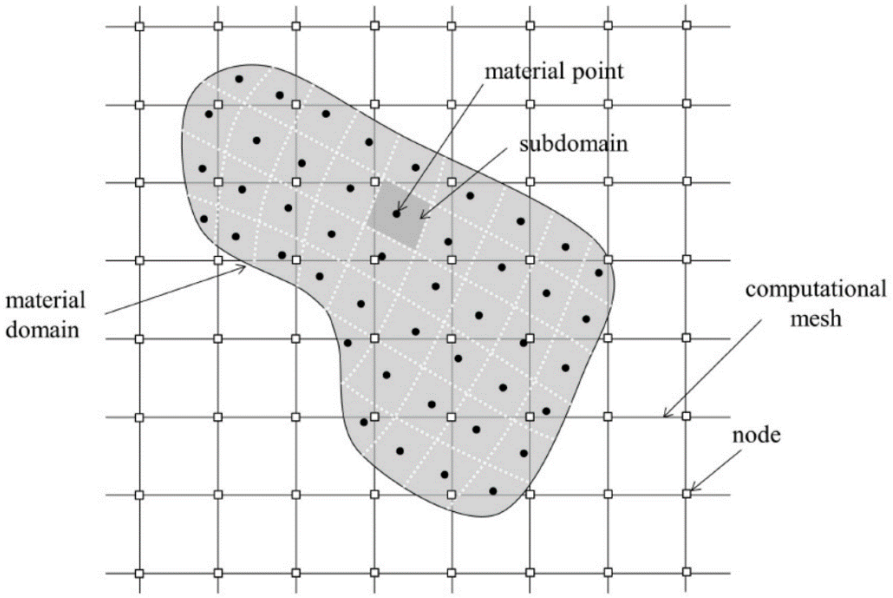

Fig. 3.1 Two sets of material points [157]

During the computation cycle, each material point moves with the deformation of the body, as shown in Figure 3.2. In the classical MPM used in this thesis, the mass of the sub-domain is considered to be concentrated at each material point, thus ensuring mass conservation. Velocities, strains and stresses are also initialised and carried by the material points.

The computational mesh is derived directly from FEM and spans the entire domain of the problem. The discrete governing equations are solved at the nodes of the computational mesh [114]. Figure 3.2 shows how during the computation cycle, the variables required to solve the governing equations at the mesh nodes are transferred using mapping functions from the material points. The variables carried by the material points are updated using the same

mapping functions via interpolation of the results produced by the mesh. The shape functions used to map information between the material points and the grid nodes are explored in detail in Section 3.4.3. Since the information held by the grid is no longer required, it can be discarded. Grid distortion is therefore inherently avoided, by virtue of the grid carrying no permanent information.

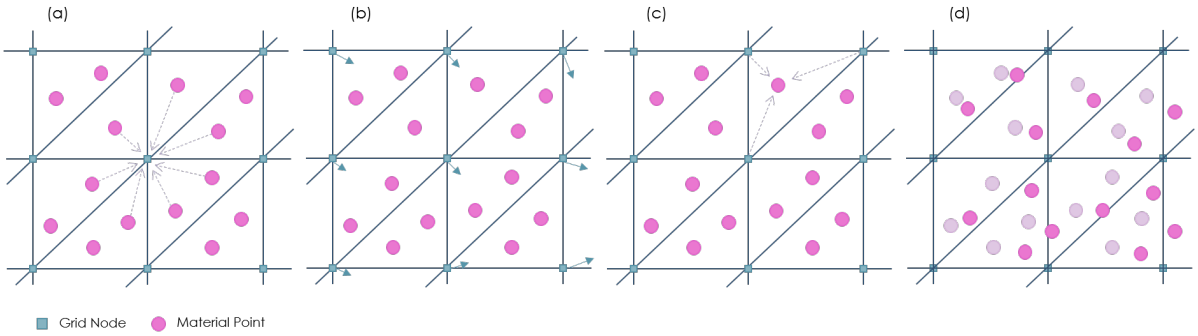

Fig. 3.2 MPM computation scheme: (a) map information from MPs to grid nodes; (b) solve equations of motion at nodes; (c) update MP information; (d) update MP position. After the Anura3D scientific manual (2019) [114]

At the beginning of each time step, interpolation functions are used to map information from the material points to the computational mesh nodes (Figure 3.2a). The discretised governing equations of motion are then used to solve for the primary unknown variables, such as the nodal velocities (Figure 3.2b). The unknown variables are summarised in Table 3.1 These nodal values are then used to update the acceleration, velocity and position of the material points and to calculate stresses and strains (Figure 3.2c). Since no permanent information is stored in the mesh, it could freely be redefined after each time step to improve computational efficiency, however, in this thesis the mesh remains fixed for simplicity. Once the mesh has been adjusted, the assignment of the material points to the finite elements is updated (Figure 3.2d), per the Anura3D Scientific Manual (2019) [114].

Table 3.1 Primary and derived unknowns for liquid and solid phases

Primary unknowns		
v_S	v_L	velocity fields
Derived unknowns		
σ_S	p	stress fields
n	ρ_L	porosity and density fields
$\dot{\varepsilon}_S$	ε_L	strain rate fields

3.3 Mathematical formulation of the Material Point Method

3.3.1 Introduction

This section presents the mathematical equations that form the basis of the MPM code for the dynamic equilibrium of the solid body and of porous media in the context of continuum mechanics. The equations presented for single-phase MPM can be considered an extension of the FEM procedure. The following section is adapted from the Anura3D Scientific Manual, version 2019.1, Tinctorius ([114]). The governing equations are developed for the single point, single-phase analysis of both solid (dry soil) and liquid (free water only, such as the collapsing water column in the dam-break flow problem) phases, then for the single-point two-phase analysis (saturated soils), and then for the double-point two- or three-phase analysis (such as partially saturated soils, like the solitary wave impact problem). Figure 3.3 shows an overview of the different formulations of MPM. This thesis mostly uses the double-point two-phase analysis to investigate water wave impact on a dry porous barrier.

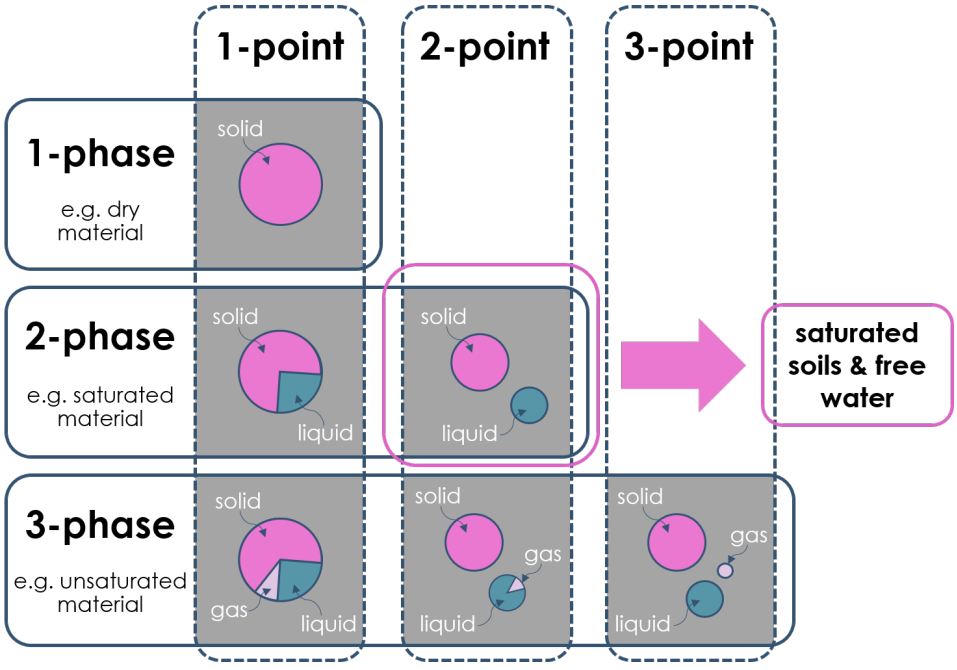

Fig. 3.3 MPM formulations and their specific uses after Yerro (2015) [157]

3.3.2 Governing equations for single-phase solid analysis using MPM

The continuum can be described mathematically by a set of differential governing equations: conservation of momentum, conservation of mass, energy balance and boundary conditions. To

solve these, constitutive equations that are characteristic of the material forming the continuum are needed, such a stress-strain relationship.

In single-phase, one-point MPM, the balance equations are applied to the liquid phase, which is assumed to represent a continuum. The trajectory of each material point is followed through time, corresponding to the Lagrangian depiction of motion. Since MPM is codified as an updated Lagrangian formulation, the current instantaneous configuration is considered as the reference configuration at the beginning of each timestep. The governing equations are therefore always solved in the current configuration, thus supporting the modelling of large deformations.

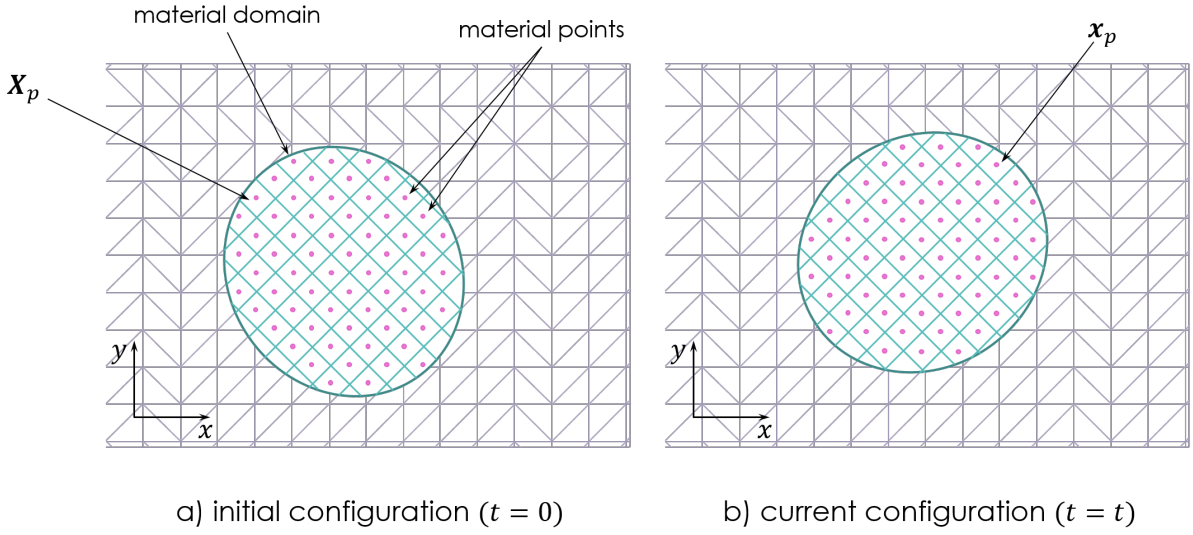

Fig. 3.4 The MPM computational grid and the movement of material points, after Zhao (2019) [169]

Figure 3.4 shows a sketch of material movement across a timestep in MPM. The material domain Ω is represented by a number of material points N_p and x_p denotes the position of the material point at the current instant (time t). The same material point at the initial time ($t = 0$) is denoted X_p. Each material point carries a fixed amount of mass m_p throughout the calculation, and the density $\rho(\mathbf{x},t)$ at an arbitrary point $\mathbf{x}$ can be expressed as:

$$\rho(\mathbf{x},t) = \sum_{p=1}^{N_p} m_p \delta(\mathbf{x} - \mathbf{x}_p) \tag{3.1}$$

where δ is the Dirac delta function.

The displacement $\mathbf{u}(\mathbf{x},t)$, velocity $\mathbf{v}(\mathbf{x},t)$ and acceleration $\mathbf{a}(\mathbf{x},t)$ of the continuum at any location $\mathbf{x}$ are defined as:

$$\mathbf{u}(\mathbf{x},t) = \mathbf{x} - \mathbf{X} \tag{3.2}$$

$$\mathbf{v}(\mathbf{x},t) = \frac{d\mathbf{u}(\mathbf{x},t)}{dt} \tag{3.3}$$

$$\mathbf{a}(\mathbf{x},t) = \frac{d\mathbf{v}(\mathbf{x},t)}{dt} \tag{3.4}$$

where

$$\frac{d}{dt} = \frac{\partial}{\partial t} + \mathbf{v} \cdot \nabla \tag{3.5}$$

is the material derivative with respect to time.

The compatibility equations therefore take the form

$$\varepsilon = \frac{1}{2}\left[\nabla \mathbf{u} + (\nabla \mathbf{u})^T\right] \tag{3.6}$$

where ε is the strain tensor, and the strain rate is given by

$$\dot{\varepsilon} = \frac{1}{2}\left[\nabla \mathbf{u} + (\nabla \mathbf{u})^T\right] \tag{3.7}$$

The governing equations that describe the motion of the continuum body Ω are the standard conservation equations: mass (equation 3.8) and momentum (equation 3.9) [138, 139].

Conservation of mass

Each material point carries the field variables, mass M_p, density $\rho_p(\mathbf{x},t)$, velocity $v_p(\mathbf{x},t)$ and the Cauchy stress $\sigma_p(\mathbf{x},t)$, where $p = 1,2,3....N_p$. For a single-phase material, there are no sources or sinks in the domain occupied by the material, so the change in mass with time is zero [3, 169] and the mass M_p is constant throughout the calculation. The conservation of mass equation can be written in Lagrangian form such that:

$$\frac{\partial \rho}{\partial t} + \rho \nabla \cdot \mathbf{v}_S = 0 \tag{3.8}$$

where $\rho(\mathbf{x},t)$ is the density of the continuum body, and the acceleration $\mathbf{a}(\mathbf{x},t)$ is the material derivative of the solid phase velocity, $\mathbf{v}_S(\mathbf{x},t)$. Since in single-phase, single-point MPM the mass is carried by each material point and remains unchanged throughout the calculation, the mass balance equation is automatically satisfied, i.e., mass is inherently conserved.

Conservation of momentum

The conservation of momentum of the continuum can be written in differential form such that

$$\rho \mathbf{a}_S = \nabla \cdot \sigma_{\mathbf{S}} + \rho \mathbf{b} \tag{3.9}$$

where $\mathbf{b}(\mathbf{x},t)$ is a specific body force vector and σ is the stress tensor, which can be divided into a hydrostatic component $\mathbf{p}$ and a deviatoric component σ_{dev}. Since MPM is written in an explicit-dynamic formulation (see section 3.4), the dynamic formulation of the momentum balance equation means that the acceleration term is accounted for.

The Lagrangian framework eliminates the need for a non-linear convective term. Instead, the positions of each material point are updated with every timestep.

Two types of boundary conditions can be defined: prescribed traction (Equation 3.10) and prescribed displacement (Equation 3.11), which are applied to the corresponding domains $\partial\Omega^{\sigma}$ and $\partial\Omega^{\mathbf{u}}$ respectively. The boundary condition along $\partial\Omega^{\sigma}$ is defined as

$$\sigma_S(\mathbf{x},t) \cdot \mathbf{n} = \hat{\mathbf{t}}_S(t) \tag{3.10}$$

and the boundary condition along $\partial\Omega^{\mathbf{u}}$ is defined as

$$u_S(\mathbf{x},t) \cdot \mathbf{n} = \hat{\mathbf{u}}_S(t) \tag{3.11}$$

where $\sigma_S(\mathbf{x},t)$ is the stress tensor, $\mathbf{n}$ is the outward unit vector normal to the free surface, $\hat{\mathbf{t}}_S(t)$ is the surface traction vector, $\mathbf{x}$ is the position vector, $\hat{\mathbf{u}}_S$ is the displacement vector and t is time.

Weak form of the momentum equations

In continuum mechanics, conservation of momentum is a key governing equation since it represents the equation of motion of the continuum. So that this equation can be discretised, it must be transformed into the *weak form* or *virtual work equation*, in which the momentum balance equation is multiplied by a *test function* or *virtual velocity*, δv, and is integrated over the domain Ω currently occupied by the continuum such that

$$\int_{\Omega} \delta \mathbf{v}_S \rho \mathbf{a}_S \, d\Omega = \int_{\Omega} \delta \mathbf{v}_S (\nabla \cdot \sigma_S) \, d\Omega + \int_{\Omega} \delta \mathbf{v}_S \rho \mathbf{g} \, d\Omega \tag{3.12}$$

where $\delta \mathbf{v} = 0$ on the domain $\partial\Omega^{\mathbf{u}}$, so that the weak form is solved on average.

The first term on the right hand side of Equation 3.12 can be expanded so that

$$\int_{\Omega} \delta \mathbf{v}_S (\nabla \cdot \sigma_S)\, d\Omega = \int_{\Omega} (\nabla \cdot \delta \mathbf{v}_S \sigma_S)\, d\Omega - \int_{\Omega} (\nabla \cdot \delta \mathbf{v}_S) \sigma_S\, d\Omega \tag{3.13}$$

Applying the divergence theorem to Equation 3.13 allows us to rewrite the first term on the right hand side so that

$$\int_{\Omega} (\nabla \cdot \delta \mathbf{v}_S \sigma_S)\, d\Omega = \int_{\partial\Omega_\sigma} \delta \mathbf{v}_S \tau_S\, d\partial\Omega \tag{3.14}$$

and we can then substitute Equations 3.14 and 3.13 into Equation 3.12 so that

$$\int_{\Omega} \delta \mathbf{v}_S \rho \mathbf{a}_S\, d\Omega = \int_{\partial\Omega_\sigma} \delta \mathbf{v}_S \tau_S\, d\partial\Omega - \int_{\Omega} (\nabla \cdot \delta \mathbf{v}_S) \sigma_S\, d\Omega + \int_{\Omega} \delta \mathbf{v}_S \rho \mathbf{g}\, d\Omega \tag{3.15}$$

which can then be used to form the discretised equations.

Constitutive equations

The general form of the constitutive equations that characterise the stress-strain relationship of the material can be written as [157]:

$$\dot{\sigma} = \mathbf{D} \cdot \dot{\varepsilon} \tag{3.16}$$

where $\mathbf{D}$ is the tangent matrix defined by the specific material constitutive model, and $\dot{\sigma}$ and $\dot{\varepsilon}$ are the rate of stress and strain tensors, respectively:

$$\dot{\sigma} = \frac{d}{dt}\sigma(\mathbf{x}, t) \tag{3.17}$$

and

$$\dot{\varepsilon} = \frac{d}{dt}\varepsilon(\mathbf{x}, t) \tag{3.18}$$

These stress and strain tensors can be written in vector form as

$$\sigma(\mathbf{x}, t) = \begin{bmatrix} \sigma_{xx} & \sigma_{yy} & \sigma_{zz} & \sigma_{xy} & \sigma_{yz} & \sigma_{zx} \end{bmatrix}^T \tag{3.19}$$

$$\varepsilon(\mathbf{x}, t) = \begin{bmatrix} \varepsilon_{xx} & \varepsilon_{yy} & \varepsilon_{zz} & 2\varepsilon_{xy} & 2\varepsilon_{yz} & 2\varepsilon_{zx} \end{bmatrix}^T \tag{3.20}$$

where ε_{xx}, ε_{yy} and ε_{zz} are the normal strains in the x, y and z directions, respectively; and $2\varepsilon_{xy}$, ε_{yz}, and ε_{zx} are the shear strains in the xy, yz and zx planes, respectively. This tensor

notation is also referred to as *Voigt notation*. This representation is frequently used since it allows efficient storage and computation in numerical calculations [3].

3.3.3 Governing equations for single-phase liquid analysis using MPM

To understand the basis of liquid analysis using the material point method, the equations of conservation of both mass and linear momentum are rewritten with respect to the liquid phase.

Conservation of mass

The conservation of mass of the liquid phase is expressed in Lagrangian form as

$$\frac{\partial \rho_L}{\partial t} + \rho_L \, \nabla \cdot \mathbf{v}_L = 0 \tag{3.21}$$

where $\mathbf{v}_L$ is the velocity vector of the liquid phase. As with the solid phase, the mass M_p is constant throughout the calculation, so that mass is inherently conserved throughout the calculation.

Conservation of momentum

The conservation of momentum of the liquid phase can be written in differential form such that

$$\rho \mathbf{a}_L = \nabla \cdot \sigma_\mathbf{L} + \rho_L \mathbf{b} \tag{3.22}$$

where ρ_L is the density of the liquid phase, $\mathbf{a}_L$ is the liquid acceleration vector, σ_L is the liquid Cauchy stress tensor and $\mathbf{b}$ is the body force. As with the solid phase, a dynamic formulation is considered so that the acceleration is accounted for.

As with the solid phase, there are two types of boundary conditions which can be defined: prescribed traction (Equation 3.23) and prescribed displacement (Equation 3.24), which are applied to the corresponding domains $\partial\Omega^\sigma$ and $\partial\Omega^\mathbf{u}$ respectively. The boundary condition along $\partial\Omega^\sigma$ is defined as

$$\sigma_L(\mathbf{x},t) \cdot \mathbf{n} = \hat{\mathbf{t}}(t) \tag{3.23}$$

and the boundary condition along $\partial\Omega^\mathbf{u}$ is defined as

$$u_L(\mathbf{x},t) \cdot \mathbf{n} = \hat{\mathbf{u}}(t) \tag{3.24}$$

where $\sigma_L(\mathbf{x},t)$ is the liquid stress tensor, $\mathbf{n}$ is the outward unit vector normal to the free surface, $\hat{\mathbf{t}}(\mathbf{x},t)$ is the surface traction vector, $\mathbf{x}$ is the position vector, $\hat{\mathbf{u}}$ is the displacement vector and t is time.

The boundary between the liquid phase and gas phase is the *free surface* and is modelled as a boundary condition applied on $\partial\Omega^{\sigma}$. For the case where the surface tension and atmospheric pressure are zero, the boundary condition is set so that $\hat{\mathbf{t}}(\mathbf{x},t) = p(\mathbf{x},t) = 0$.

Weak form of the momentum equations

For the discretisation of the momentum conservation equation, the weak form is developed from the strong form by multiplication with a test function (or virtual velocity δv) and integrated over the current domain occupied by the continuum Ω to form the virtual work equation such that

$$\int_{\Omega} \delta\mathbf{v}_L \rho \mathbf{a}_L \, d\Omega = \int_{\Omega} \delta\mathbf{v}_L (\nabla \cdot \sigma_L) \, d\Omega + \int_{\Omega} \delta\mathbf{v}_L \rho \mathbf{g} \, d\Omega \tag{3.25}$$

where $\delta\mathbf{v} = 0$ on the domain $\partial\Omega^{\mathbf{u}}$. The analysis can be carried out in the same manner as the solid phase so that we arrive at the equation

$$\int_{\Omega} \delta\mathbf{v}_L \rho \mathbf{a}_L \, d\Omega = \int_{\partial\Omega_{\sigma}} \delta\mathbf{v}_L \tau_L \, d\partial\Omega - \int_{\Omega} (\nabla \cdot \delta\mathbf{v}_L) \sigma_L \, d\Omega + \int_{\Omega} \delta\mathbf{v}_L \rho \mathbf{g} \, d\Omega \tag{3.26}$$

which can then be used to form the discretised equations.

3.3.4 Governing equations for two-phase coupled analysis: double point formulation

This thesis investigates situations where the water can flow through the solid skeleton, i.e., the calculated water velocity is significantly different from that of the solid skeleton. It is therefore inappropriate to describe the solid and liquid phases with the same velocity field. The MPM code may also be constructed with two sets of material points to soil and liquid phases separately, in order to better to capture the fluid-structure interaction where there is a large difference in velocity between the solid and liquid phases [1, 11, 105, 152, 169]. Figure 3.3 shows the situations in which the different formulations are employed. The double-point formulation is necessary for cases where there is significant fluid flow, as in both the dam-break and solitary wave simulations presented in this thesis. To allow for this, two sets of material points are introduced, such that a set of material points are assigned to both the solid and the liquid phases, where each set of material points represents the velocity fields of each of the

two phases, respectively. This is indicated in Figure 3.5. The two phases interact with each other via a drag force term. Depending on the porosity of the soil, the soil skeleton may either be regarded as a porous medium surrounded by a fluid, or as soil particles floating within a fluid. We need, therefore, to determine the *state* of the material, characterised by the porosity parameter n, shown in Figure 3.7. The porosity parameter of the soil remains constant in this thesis, however, the permeability of the soil increases as the mean grain size is increased. Within the double-point formulation, the space may be occupied by the solid and liquid material points at the same time, and three domains can be distinguished depending on the constituent particles: saturated soil (elements containing both solid and liquid material points), dry soil (elements containing only solid material points) and pure liquid (elements containing only liquid material points), as in Figure 3.5 [42]. Since the number of material points doubles, the computational and storage costs of double-point MPM are considerably higher than the single-point version of the code. A detailed comparison of two-phase analyses employing both double-point and single-point formulations has been presented by Ceccato et al. (2018) [28].

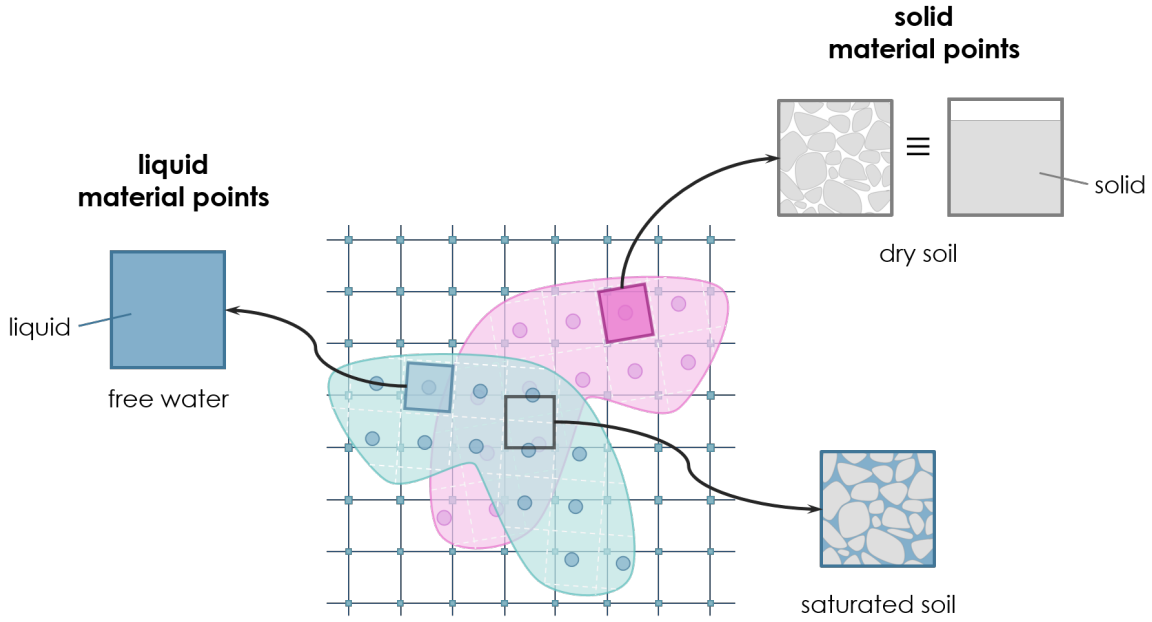

Fig. 3.5 Scheme of the two-phase double-point MPM approach, after Fern, Rohe and Soga (2019) [42]

The two-point MPM is based on the following assumptions [11, 105, 169]:

1. Soil skeleton and liquid phase are described in a Lagrangian formulation under the assumption that each constituent can be represented as a continuous medium.

2. Solid grains are incompressible, i.e., $\rho_S \approx$ const.

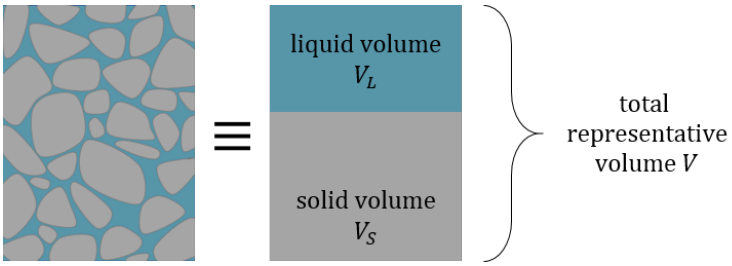

Fig. 3.6 Porosity of the soil skeleton is expressed as a function of the volume of void space compared to the overall volume

3. There is no mass transfer between the solid and liquid phases.
4. The spatial variability of the fluid density is negligible, i.e., $\nabla \rho_L \approx 0$
5. The soil may either be dry or saturated, i.e., partially saturated soil is not considered. Whilst the soil may in reality become partially saturated, this would not affect the flow outside the structure and therefore has no bearing on the run-up height reached.

State determination

When two sets of material points are used, the mixture must be identified by its *state*, characterised by the dominant material. This is shown in Figure 3.7. On the left side, the mixture is characterised by a low porosity: the grains of the solid skeleton are in contact and the behaviour can be described by constitutive models designed for granular materials: it is a porous medium surrounded by a fluid. In this condition, the *state* is defined as *solid*.

Conversely, on the right-hand side, the mixture has a high porosity, the grains are not in contact and flow with the liquid phase: it consists of soil grains floating within a liquid. In this condition, the effective stresses are equal to zero ($\sigma_s = 0$) and the response of the mixture is described by the Navier-Stokes equation. In this condition, the *state* is defined as *liquid*.

The variable n representing the porosity of the mixture is introduced where

$$n = \frac{V_L}{V} \tag{3.27}$$

where V_L is the volume of the fluid in the pore space of the soil skeleton, and V is the total representative volume of the soil, as shown in Figure 3.6.

To determine which state is appropriate, an additional parameter n_{max} is defined, representing the maximum porosity. A mixture with an initially solid state that undergoes fluidisation is characterised by two aspects: the mean effective stress decreases and the porosity increases. The mean effective stresses become zero when there are no longer contact forces between the

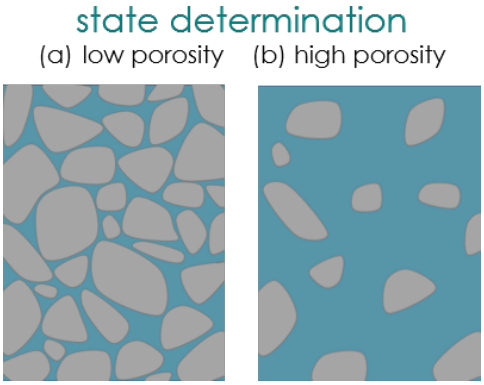

Fig. 3.7 (a) Solid-liquid mixture with low porosity and grains in contact (*solid state*); (b) Solid-liquid mixture with high porosity and no grain contact (*liquid state*)

grains so that $\sigma_{ij} = 0$ when $n > n_{max}$. Fluidisation only occurs if the grains are significantly separated so that the porosity is larger than n_{max} and the state becomes liquid. The mixture behaves as a Navier-Stokes flow with viscosity. In the reverse process, sedimentation, the porosity decreases as the solid grains become closer to each other. However, the effective stresses arise only if the porosity is smaller than n_{max}, i.e. the grains are close enough to be in contact and the *state* is *solid* so that $\sigma_{ij} > 0$ when $n \leq n_{max}$. The soil skeleton now behaves according to mixture theory, as in the case of seepage flow.

Conservation of mass

The mass balance equations for the two layers of material points are presented by separate velocity fields, first for the solid phase as

$$\frac{d^S(n_S\,\rho_S)}{dt} + n_S\rho_S(\nabla\cdot\mathbf{v}_S) = 0 \tag{3.28}$$

and then for the liquid phase as

$$\frac{d^L(n_L\,\rho_L)}{dt} + n_L\rho_L(\nabla\cdot\mathbf{v}_L) = 0 \tag{3.29}$$

in which $\mathbf{v}_L$ and $\mathbf{v}_S$ are the velocity vectors of the liquid phase and of the solid phase, respectively; n_L is the liquid concentration ratio defined as the ratio between the macroscopic partial density of liquid $\overline{\rho}_L$ and the liquid density ρ_L. The macroscopic partial densities $\overline{\rho}_L$ and $\overline{\rho}_S$ represent the partial densities of the solid and liquid constituent, respectively, defined as the ratio of the mass with respect to the reference volume. Similarly, n_S is the solid concentration ratio, which is defined as the ratio between the macroscopic solid partial density $\overline{\rho}_S$ and the solid density ρ_S [106].

The double-point MPM assumes that the spatial variability of the liquid density is negligible ($\nabla\rho_L \approx 0$), the soil grains are incompressible ($\rho_s \approx constant$), the medium is saturated ($n_L = n$ and $n_s = 1-n$). Based on these assumptions, the volumetric strain rate of the weakly compressible liquid $\frac{d^L\varepsilon_{vol,L}}{dt}$ can be derived from the mass conservation equations as

$$\frac{d^L\varepsilon_{vol,L}}{dt} = \frac{1}{n}\left[(1-n)\nabla\cdot\mathbf{v}_S + n\nabla\cdot\mathbf{v}_L + \nabla n\cdot(\mathbf{v}_L-\mathbf{v}_S)\right] \tag{3.30}$$

Conservation of momentum

The momentum balance equations for the two layers of material points are presented by separate velocity fields for the two phases as follows:

$$(1-n)\rho_s\dot{\mathbf{v}}_S = \nabla\cdot\sigma' + (1-n)\nabla\cdot\sigma_L + (1-n)\rho_s\mathbf{g} + \mathbf{F}_d \tag{3.31}$$

for the solid phase and

$$n\rho_L\dot{\mathbf{v}}_L = n\nabla\cdot\sigma_L + n\rho_L\cdot\mathbf{g} - \mathbf{F}_d \tag{3.32}$$

for the liquid phase, where σ' is effective stress tensor, σ_L is the stress tensor of the liquid phase (equivalent to the pore pressure tensor $\mathbf{p}_L$ in saturated porous media), and $\mathbf{f}_d$ represents the interaction force exerted by the liquid on the soil skeleton, calculated from Ergun's Law [40] as follows:

$$\mathbf{F}_d = n^2\left[\frac{\mu}{\kappa} + n\rho_L\frac{F}{\sqrt{\kappa}}|\mathbf{v}_L-\mathbf{v}_S|\right](\mathbf{v}_L-\mathbf{v}_s) + \sigma_L\nabla n \tag{3.33}$$

with the first two terms representing a viscous force related to the permeability of the soil skeleton k, the liquid viscosity μ and the relative velocity between the liquid and solid phases $(\mathbf{v}_L-\mathbf{v}_s)$. The final term is contributed by the gradient of the porosity ∇n. F is a coefficient and κ is the intrinsic soil permeability, calculated from the Kozeny-Carman formula [15] such that

$$F = \frac{B}{\sqrt{A}n^{1.5}} \tag{3.34}$$

where B is a constant set to 1.75 according to Ergun [40] and

$$\kappa = \frac{D_p^2}{A}\frac{n^3}{(1-n)^2} \tag{3.35}$$

where D_p is the mean effective grain size diameter and n is the soil porosity. A is a constant and has been determined to be in the range 150 - 180, and for the situations explored here the value of 150 will be used, after Ergun 1952 [40].

Constitutive equations

The constitutive equations for the liquid and solid phases, respectively, are shown below:

$$\Delta p_L = K_L \Delta \varepsilon_{vol,L} \tag{3.36}$$

$$\Delta \sigma_S = \mathbf{D} \cdot \Delta \varepsilon_S \tag{3.37}$$

where Δp_L is the pressure increment; K_L is the bulk modulus of the liquid, $\Delta \varepsilon_{vol,L}$ is the incremental volumetric strain of the liquid, $\mathbf{D}$ is the tangent matrix defined by means of the constitutive model. For cases of either liquid or fluidised solid material, the deviatoric part of the stress tensor $\sigma_{dev,L}$ is calculated as

$$\sigma_{dev,L} = 2\mu \dot{\varepsilon}_{dev,L} \tag{3.38}$$

where $\dot{\varepsilon}_{dev,L}$ is the deviatoric component of the liquid strain rate.

A summary of the governing equations and how they are applied using single-point two-phase MPM is shown in Figure 3.8.

3.4 Explicit-dynamic formulation

3.4.1 Introduction

MPM was developed using an explicit solver, since it was originally developed to solve transient impact solid mechanics problems [138], and for these problems explicit solvers are more efficient. For problems with low rates of loading, implicit solvers are more suitable. However, these simulations involve fast transient loading, so an explicit formulation is appropriate.

This section presents the dynamic explicit implementation of Anura3D and how the governing equations are assembled into a computation scheme. The system of solving the equations within the MPM framework and the main steps of the solution procedure are shown.

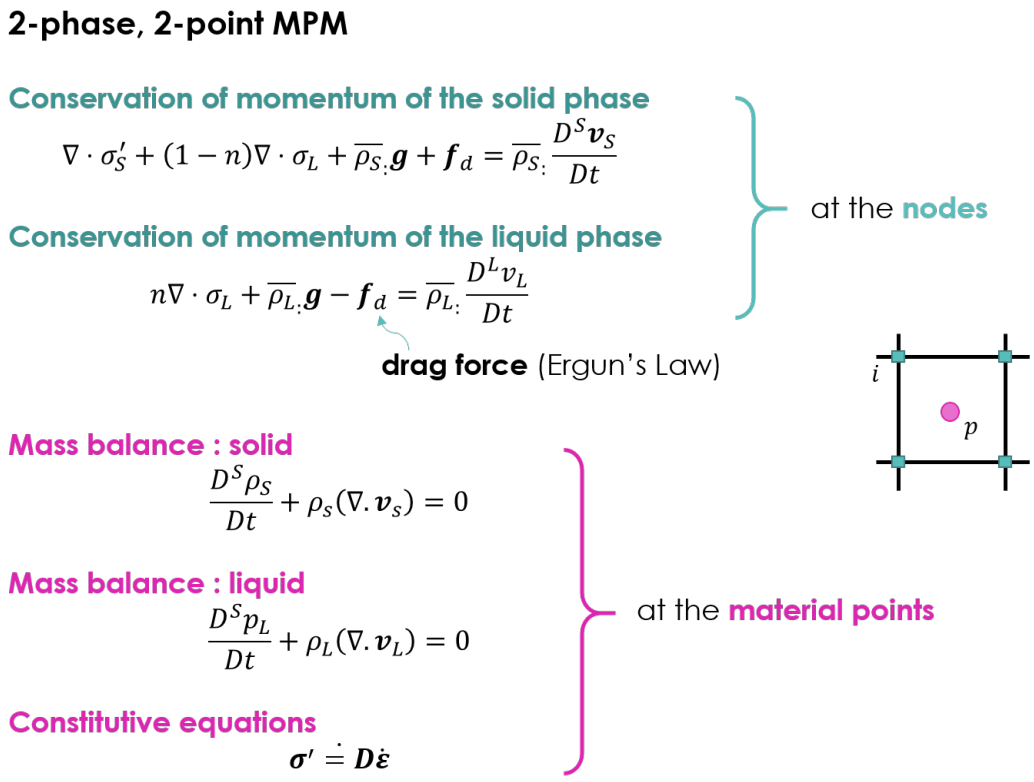

Fig. 3.8 Schematic showing the governing equations of double-point MPM

3.4.2 Notation and variables

The stress and strain tensors are written here in vector form, exploiting the symmetry of each such that

$$\varepsilon(\mathbf{x},t) = [\varepsilon_{11}\ \varepsilon_{22}\ \varepsilon_{33}\ 2\varepsilon_{12}\ 2\varepsilon_{23}\ 2\varepsilon_{31}]^T \tag{3.39}$$

$$\sigma(\mathbf{x},t) = [\sigma_{11}\ \sigma_{22}\ \sigma_{33}\ 2\sigma_{12}\ 2\sigma_{23}\ 2\sigma_{31}]^T \tag{3.40}$$

where the first three terms in each vector(i.e. σ_{ij} and ε_{ij} where $i = j$) are the normal components, along the axis x_{ij} of the coordinate system, and the remaining three terms in each vector represent the shear terms, acting on the $x_i x_j$ planes. This representation of the stress and strain tensors is known as the *Voigt* notation, and is particularly useful since it reduces the order of the symmetric tensors.

In the Voigt notation, the representation of strain is different to that of stress; the last three terms in the strain vector are represented by $\gamma_{ij} = 2\varepsilon_{ij}$. This is to ensure that the energy is preserved and that different expressions of energy using these tensors are equal, i.e.

$$\varepsilon_{ij}\sigma_{ij} = \varepsilon^T \sigma \tag{3.41}$$

3.4.3 Spatial discretisation

The spatial discretisation of the momentum balance equation is the main focus in MPM, and for the MPM formulation utilised in this study, the FEM with an updated Lagrangian formulation is adopted to obtain a discrete equation for the momentum balance on the background mesh [157]. This mesh is divided into N_{el} tetrahedral elements Ω_{el} where $(el = 1,2,3,...,N_{el})$ in three dimensions, with N_n mesh nodes $\mathbf{x}_i$ where $(i = 1,2,3,...,N_n)$. Similarly to the FEM, the displacement, velocity and acceleration fields are approximated by interpolation of the nodal values using shape functions $N_i(\mathbf{x})$. The location of a point $\mathbf{x}$ can therefore be obtained as:

$$\mathbf{x} = \sum_{i=1}^{N_n} \mathbf{x}_i\, N_i(\mathbf{x}) \tag{3.42}$$

The discrete displacement field, velocity field and acceleration field can therefore be approximated as:

$$\mathbf{u}(\mathbf{x},t) = \mathbf{x} - \mathbf{X} = \sum_{i=1}^{N_n} (\mathbf{x}_i - \mathbf{X}_i) N_i(\mathbf{x}) = \sum_{i=1}^{N_n} \mathbf{u}_i\, N_i(\mathbf{x}) \tag{3.43}$$

$$\mathbf{v}(\mathbf{x},t) = \dot{\mathbf{u}}(\mathbf{x},t) = \sum_{i=1}^{N_n} \dot{\mathbf{u}}_i(t)\, N_i(\mathbf{x}) = \sum_{i=1}^{N_n} \mathbf{v}_i(t)\, N_i(\mathbf{x}) \tag{3.44}$$

$$\mathbf{a}(\mathbf{x},t) = \dot{\mathbf{v}}(\mathbf{x},t) = \sum_{i=1}^{N_n} \dot{\mathbf{v}}_i(t)\, N_i(\mathbf{x}) = \sum_{i=1}^{N_n} \mathbf{a}_i(t)\, N_i(\mathbf{x}) \tag{3.45}$$

where $\mathbf{X}$ is the location of the material point at the initial time $t = 0$, per Figure 3.4.

We can apply the technique of virtual work employing a test function $\mathbf{w}(\mathbf{x},\mathbf{t})$ as detailed in section 3.3.2 to obtain the weak form of the momentum balance equation. With a test function defined as:

$$\mathbf{w}(\mathbf{x}) = \sum_{i=1}^{N_n} \mathbf{w}_i\, N_i(\mathbf{x}) \tag{3.46}$$

If we multiply the momentum balance equation (Equation 3.9) with the test function and integrate over a domain Ω, the weak form of the momentum balance equation is now expressed as:

$$\int_\Omega \rho \mathbf{w} \cdot \mathbf{a}\, d\Omega = \int_\Omega \mathbf{w} \nabla \cdot \sigma\, d\Omega + \int_\Omega \rho \mathbf{w} \cdot \mathbf{b}\, d\Omega \tag{3.47}$$

where $\mathbf{w} = 0$ on $\partial\Omega_u$; and $d\Omega$ represents the differentiated volume of the current domain. Integrating the first term on the right hand side yields

$$\int_\Omega \mathbf{w} \nabla \cdot \sigma\, d\Omega = \int_\Omega \nabla(\mathbf{w} \cdot \sigma)\, d\Omega - \int_\Omega \nabla \mathbf{w} \cdot \sigma\, d\Omega \tag{3.48}$$

Applying the divergence theorem to the first term on the right-hand side of this equation yields

$$\int_\Omega \nabla(\mathbf{w} \cdot \sigma)\, d\Omega = \int_{\partial\Omega_\tau} \mathbf{w} \cdot \tau\, dS \tag{3.49}$$

where $\tau = \sigma \cdot \mathbf{n}$ is a prescribed surface traction vector, $\mathbf{n}$ is the unit normal to the boundary and dS represents the differential surface which is only non-zero at the traction boundary $\partial\Omega_\tau$.

Substituting Equations 3.48 and 3.49 back into the momentum balance equation (Equation 3.47), yields the weak form of the momentum equation:

$$\int_\Omega \rho \mathbf{w} \cdot \mathbf{a}\, d\Omega = -\int_\Omega \nabla \mathbf{w} \cdot \sigma\, d\Omega + \int_{\partial\Omega_\tau} \mathbf{w} \cdot \tau dS + \int_\Omega \rho \mathbf{w} \cdot \mathbf{b}\, d\Omega \tag{3.50}$$

Substituting Equations 3.44 and 3.45 into each component of Equation 3.50 yields:

$$\int_\Omega \rho \mathbf{w}\cdot\mathbf{a}\, d\Omega = \sum_{i=1}^{N_n} \mathbf{w}_i \cdot \sum_{j=1}^{N_n} \int_\Omega \rho\, N_i N_j\, \mathbf{a}_j\, d\Omega = \sum_{i=1}^{N_n} \mathbf{w}_i \cdot \sum_{j=1}^{N_n} \mathbf{M}_{ij}\, \mathbf{a}_j \tag{3.51}$$

$$-\int_\Omega \nabla\mathbf{w}\cdot\sigma d\Omega = -\sum_{i=1}^{N_n} \mathbf{w}_i \int_\Omega \nabla N_i \cdot \sigma\, d\Omega \tag{3.52}$$

$$\int_{\partial\Omega_\tau} \mathbf{w}\cdot\tau dS = \sum_{i=1}^{N_n} \mathbf{w}_i \int_{\partial\Omega_\tau} \tau N_i\, dS \tag{3.53}$$

$$\int_\Omega \rho\mathbf{w}\cdot\mathbf{b}\, d\Omega = \sum_{i=1}^{N_n} \mathbf{w}_i \int_\Omega \rho\mathbf{b} N_i\, d\Omega \tag{3.54}$$

Since the components of $\mathbf{w}_i$ are arbitrary, except where the components of the displacement are prescribed, we can substitute Equations 3.51, 3.52, 3.53, and 3.54 back into Equations 3.50, and divide by a factor of $\sum_{i=1}^{N_n} \mathbf{w}_i$ to yield

$$\sum_{j=1}^{N_n} \mathbf{M}_{ij}\, \mathbf{a}_j = -\int_\Omega \nabla N_i \cdot \sigma\, d\Omega + \int_{\partial\Omega_\tau} \tau N_i\, dS + \int_\Omega \rho\mathbf{b} N_i\, d\Omega \tag{3.55}$$

where $\mathbf{M}_{ij}$ is the consistent mass matrix

$$\mathbf{M}_{ij} = \int_\Omega \rho\, N_i N_j\, d\Omega \tag{3.56}$$

The spatial discretisation is continued by considering the material points as the integration points; and the integrals thus become sums over the material points. The inertial term of Equation 3.51 can be discretised using the consistent mass matrix, such that:

$$\begin{aligned} \mathbf{M}_{ij} = \int_\Omega \rho\, N_i N_j\, d\Omega &\approx \sum_{p=1}^{N_p} \rho(\mathbf{x}_p) N_i(\mathbf{x}_p) N_j(\mathbf{x}_p) \Omega_p \\ &= \sum_{p=1}^{N_p} m_p N_i(\mathbf{x}_p) N_j(\mathbf{x}_p) \end{aligned} \tag{3.57}$$

where m_p is the material point mass, which remains unchanged throughout the calculation, and Ω_p is the material point integration weight.

The internal and external nodal forces can be obtained as:

$$\begin{aligned}\mathbf{F}_i^{int} &= -\int_\Omega \nabla N_i \cdot \boldsymbol{\sigma}\, d\Omega \\ &\approx -\sum_{p=1}^{N_p} \nabla N_i(\mathbf{x}_p) \cdot \boldsymbol{\sigma}_p(\mathbf{x}_p, t)\, \Omega_p\end{aligned} \tag{3.58}$$

$$\begin{aligned}\mathbf{F}_i^{ext} &= \int_\Omega \rho \mathbf{b} N_i\, d\Omega + \int_{\partial\Omega_\tau} \tau N_i\, dS \\ &\approx -\sum_{p=1}^{N_p} m_p \mathbf{b}_p N_i(\mathbf{x}_p) + \int_{\partial\Omega_\tau} \tau N_i\, dS\end{aligned} \tag{3.59}$$

Finally, substituting Equations 3.57, 3.58 and 3.59 back into Equation 3.55 yields the semi-discrete momentum balance equation for the continuum:

$$\sum_{j=1}^{N_n} \mathbf{M}_{ij}\, \mathbf{a}_j = \mathbf{F}_i^{int} + \mathbf{F}_i^{ext} \tag{3.60}$$

which is computed to arrive at the nodal accelerations $\mathbf{a}_j$.

3.4.4 Time discretisation

The numerical solution of the momentum balance equation is obtained at a discrete set of times, t [11], and the general solution scheme is summarised as follows:

1. Calculate nodal acceleration $\mathbf{a}_i^t$ using the momentum balance equation:

$$\mathbf{m}_i^t \mathbf{a}_i^t = \mathbf{F}_i^{int,t} + \mathbf{F}_i^{ext,t} \tag{3.61}$$

   where t is the time at the beginning of the timestep. The consistent mass matrix $\mathbf{M}_{ij}$ in Equation 3.60 is replaced with the lumped mass matrix of the node at time t $\mathbf{m}_i^t$ which is computed using

$$\mathbf{m}_i^t = \sum_{p=1}^{N_p} m_p\, N_i\, (\mathbf{x}_p^t) \tag{3.62}$$

   to reduce the computational cost, as discussed in section 3.4.5.

2. Compute the nodal velocity $\mathbf{v}_i^t$ at the beginning of the timestep from the material point velocity, and update the particle velocity using the nodal acceleration obtained from the

previous step:

$$\mathbf{m}_i^t \mathbf{v}_i^t = \sum_{p=1}^{N_p} m_p \, \mathbf{v}_p^t \, N_i \, (\mathbf{x}_p^t) \tag{3.63}$$

$$\mathbf{v}_p^{t+\Delta t} = \mathbf{v}_p^t + \Delta t \sum_{i=1}^{N_n} \mathbf{a}_i^t \, N_i \, (\mathbf{x}_p^t) \tag{3.64}$$

where Δt is the timestep of the calculation.

3. Map the momentum from the material points to the nodes and determine the updated nodal velocity $\mathbf{v}_i^{t+\Delta t}$

$$\mathbf{m}_i^t \mathbf{v}_i^{t+\Delta t} = \sum_{p=1}^{N_p} m_p \mathbf{v}_p^{t+\Delta t} N_i(\mathbf{x}_p^t) \tag{3.65}$$

4. Update the particle location $\mathbf{x}_p^{t+\Delta t}$ using the nodal velocity $\mathbf{v}_i^{t+\Delta t}$

$$\mathbf{x}_p^{t+\Delta t} = \mathbf{x}_p^t + \Delta t \sum_{i=1}^{N_n} \mathbf{v}_i^t \, N_i \, (\mathbf{x}_p^t) \tag{3.66}$$

3.4.5 Single-phase solid analysis

Discretised momentum balance equation

The weak form of the linear conservation of momentum equation is developed in section 3.3.2 as

$$\int_\Omega \delta \mathbf{v}_S \rho \mathbf{a}_S \, d\Omega = \int_{\partial\Omega_\sigma} \delta \mathbf{v}_S \tau_S \, d\partial\Omega - \int_\Omega (\nabla \cdot \delta \mathbf{v}_S) \sigma_S \, d\Omega + \int_\Omega \delta \mathbf{v}_S \rho \mathbf{g} \, d\Omega \tag{3.67}$$

The domain Ω is decomposed into finite subdomains Ω_{el} called *finite elements*. The union of these subdomains comprises the total domain

$$\Omega = \cup_{el=1}^{n_{elm}} \Omega_{el} \tag{3.68}$$

where n_{elm} denotes the total number of finite elements in the mesh. Each element is connected to its surrounding elements via points called *nodes*. The state variable has a pre-defined interpolation function *within* the element, and the solution is obtained at the nodes. Equilibrium is therefore satisfied at the nodes.

Typically, in the finite element method, matrix notation is used in the discretisation of the virtual work equation. The discrete form is obtained by approximating the displacement and thus subsequently the velocity and acceleration as

$$\mathbf{u}(\mathbf{x},t) \approx \overline{\mathbf{N}}(\mathbf{x})\hat{\mathbf{u}}(t) \tag{3.69}$$

$$\mathbf{v}(\mathbf{x},t) \approx \overline{\mathbf{N}}(\mathbf{x})\hat{\mathbf{v}}(t) \tag{3.70}$$

$$\mathbf{a}(\mathbf{x},t) \approx \overline{\mathbf{N}}(\mathbf{x})\hat{\mathbf{a}}(t) \tag{3.71}$$

respectively. The corresponding virtual quantities are approximated in the same way so that

$$\delta\mathbf{u}(\mathbf{x},t) \approx \overline{\mathbf{N}}(\mathbf{x})\delta\hat{\mathbf{u}}(t) \tag{3.72}$$

$$\delta\mathbf{v}(\mathbf{x},t) \approx \overline{\mathbf{N}}(\mathbf{x})\delta\hat{\mathbf{v}}(t) \tag{3.73}$$

$$\delta\mathbf{a}(\mathbf{x},t) \approx \overline{\mathbf{N}}(\mathbf{x})\delta\hat{\mathbf{a}}(t) \tag{3.74}$$

The interpolation function or shape matrix $\overline{\mathbf{N}}$ takes the form

$$\overline{\mathbf{N}}(\mathbf{x}) = \left[\overline{\mathbf{N}}_1(\mathbf{x})\ \overline{\mathbf{N}}_2(\mathbf{x})\ \ldots\ \overline{\mathbf{N}}_{nT}(\mathbf{x})\right] \tag{3.75}$$

with

$$\overline{\mathbf{N}}_i(\mathbf{x}) = \begin{bmatrix} \overline{N}_i(x) & 0 & 0 \\ 0 & \overline{N}_i(x) & 0 \\ 0 & 0 & \overline{N}_i(x) \end{bmatrix} \tag{3.76}$$

where nT denotes the total number of nodes in the mesh. The *bar* superscript indicates that the quantity (in this case, shape function), is written in terms of the *global* coordinate system. The nodal displacement, velocity and acceleration vectors are denoted $\hat{\mathbf{u}}$, $\hat{\mathbf{v}}$ and $\hat{\mathbf{a}}$ respectively. These vectors, in full, are written

$$\hat{\mathbf{u}}(t) = \left[\hat{u}_{11}\ \hat{u}_{12}\ \hat{u}_{13}\ \ldots\ \ldots\ \ldots\ \hat{u}_{nT^1}\ \hat{u}_{nT^2}\ \hat{u}_{nT^3}\right]^T \tag{3.77}$$

$$\hat{\mathbf{v}}(t) = \left[\hat{v}_{11}\ \hat{v}_{12}\ \hat{v}_{13}\ \ldots\ \ldots\ \ldots\ \hat{v}_{nT^1}\ \hat{v}_{nT^2}\ \hat{v}_{nT^3}\right]^T \tag{3.78}$$

$$\hat{\mathbf{a}}(t) = \left[\hat{a}_{11}\ \hat{a}_{12}\ \hat{a}_{13}\ \ldots\ \ldots\ \ldots\ \hat{a}_{nT^1}\ \hat{a}_{nT^2}\ \hat{a}_{nT^3}\right]^T \tag{3.79}$$

where v_{12} indicates the velocity at node 1 in the direction of coordinate x_2.
The kinematic relation is expressed using matrix notation as

$$\dot{\varepsilon}(\mathbf{x},t) = \mathbf{L}\mathbf{v}(\mathbf{x},t) \tag{3.80}$$

where L is a linear differential operator that takes the form

$$\begin{bmatrix} \frac{\partial}{\partial x_1} & 0 & 0 \\ 0 & \frac{\partial}{\partial x_2} & 0 \\ 0 & 0 & \frac{\partial}{\partial x_3} \\ \frac{\partial}{\partial x_2} & \frac{\partial}{\partial x_1} & 0 \\ 0 & \frac{\partial}{\partial x_3} & \frac{\partial}{\partial x_2} \\ \frac{\partial}{\partial x_3} & 0 & \frac{\partial}{\partial x_1} \end{bmatrix} \tag{3.81}$$

We can substitute Equation 3.70 into Equation 3.80 such that

$$\dot{\varepsilon}(\mathbf{x},t) = \mathbf{L}\overline{\mathbf{N}}(\mathbf{x})\hat{\mathbf{v}}(t) = \mathbf{B}(\mathbf{x})\hat{\mathbf{v}}(t) \tag{3.82}$$

where $\mathbf{B}$ is the strain-displacement matrix

$$\left[\mathbf{B}(\mathbf{x}) = \left[\mathbf{B}_1(\mathbf{x})\ \mathbf{B}_2(\mathbf{x})\ \mathbf{B}_3(\mathbf{x})\ \ldots\ \ldots\ \ldots\ \mathbf{B}_{nT}(\mathbf{x})\right]\right] \tag{3.83}$$

with

$$\overline{\mathbf{B}}_i(\mathbf{x}) = \begin{bmatrix} \frac{\partial \overline{N}_i(x)}{\partial x_1} & 0 & 0 \\ 0 & \frac{\partial \overline{N}_i(x)}{\partial x_2} & 0 \\ 0 & 0 & \frac{\partial \overline{N}_i(x)}{\partial x_3} \\ \frac{\partial \overline{N}_i(x)}{\partial x_2} & \frac{\partial \overline{N}_i(x)}{\partial x_1} & 0 \\ 0 & \frac{\partial \overline{N}_i(x)}{\partial x_3} & \frac{\partial \overline{N}_i(x)}{\partial x_2} \\ \frac{\partial \overline{N}_i(x)}{\partial x_3} & 0 & \frac{\partial \overline{N}_i(x)}{\partial x_1} \end{bmatrix} \tag{3.84}$$

The weak form then yields

$$\delta\hat{\mathbf{v}}^T \int_{\partial\Omega} \overline{\mathbf{N}}^T \mathbf{t}\cdot\mathbf{n}\, d\partial\Omega - \delta\hat{\mathbf{v}}^T \int_{\Omega} \mathbf{B}^T \sigma\, d\Omega + \delta\hat{\mathbf{v}}^T \int_{\Omega} \overline{\mathbf{N}}^T \rho\mathbf{g}\, d\Omega - \delta\hat{\mathbf{v}}^T \left[\int_{\Omega} \overline{\mathbf{N}}^T \rho\overline{\mathbf{N}}\, d\Omega\right]\hat{\mathbf{a}} = 0 \tag{3.85}$$

where $\mathbf{n}$ is the unit vector that is normal to the domain boundary.

The discretised form yields

$$\mathbf{f}^{ext} - \mathbf{f}^{int} = \mathbf{M}\hat{\mathbf{a}} \tag{3.86}$$

with

$$\mathbf{f}^{ext} = \int_{\partial\Omega} \overline{\mathbf{N}}^T \mathbf{t} \cdot \mathbf{n} \, d\partial\Omega + \int_{\Omega} \rho \overline{\mathbf{N}}^T \mathbf{g} \, d\Omega \tag{3.87}$$

$$\mathbf{f}^{int} = \int_{\Omega} \mathbf{B}^T \sigma' \, d\Omega \tag{3.88}$$

$$\mathbf{M} = \int_{\Omega} \rho \overline{\mathbf{N}}^T \overline{\mathbf{N}} \, d\Omega \tag{3.89}$$

where $\mathbf{f}^{ext}$ is the vector of external nodal forces, $\mathbf{f}^{int}$ is the vector of internal nodal forces and $\mathbf{M}$ is the nodal mass matrix.

Initialisation of material points

The material points carry all the information associated with the continuum. This section discusses the initialisation of the material points within the background mesh, including the association of mass, body forces, traction and other properties of the continuum to the material point. Elements within the mesh that contain any material points are called *active elements* and their nodes contribute to solving the system of equations; empty elements are ignored to reduce computation cost.

If we consider a single, tetrahedral element: each material point is initially positioned at a predefined local position inside the parent element. Thus, the *local* position vector ξ_{MP} is initialised. The *global* position vector $\mathbf{x}_{MP}$ is then obtained as

$$\mathbf{x}_{MP}(\xi_{MP}) \approx \sum_{i=1}^{n_{nodes}} N_i(\xi_{MP}^t)\mathbf{x}_i \tag{3.90}$$

where n_{nodes} denotes the number of nodes per element, $N_i(\xi_{MP}^t)$ is the shape function of node i evaluated at the local position of the material point MP and $\mathbf{x}_i$ are the nodal coordinates.

The volumes associated with each material point are calculated so that all material points inside an element have the same initial volume i.e.

$$\Omega_{MP} = \frac{a}{n_{MP,el}} \int_{\Omega_e} d\Omega \approx \frac{a}{n_{MP,el}} \sum_{q=1}^{n_{q,el}} w_{MP} \, |\mathbf{J}(\xi_{MP})| \tag{3.91}$$

where Ω_{MP} is the volume associated with the material point MP, $n_{MP,el}$ denotes the number of material points in the element, $n_{q,el}$ is the number of Gauss points in the element, w_{MP} is the local integration weight associated with the Gauss point MP and $\mathbf{J}$ is the Jacobian matrix.

This implies that, at the beginning of the calculation, all active elements are assumed to be fully filled by the continuum body. An element is partially filled if the sum of the volumes of the material points within the element is less than the element volume.

The mass m_{MP} is calculated as

$$m_{MP} = \Omega_{MP}\rho_{MP} \tag{3.92}$$

where ρ is the density of the material assigned to the material point MP.

The gravitational force $\mathbf{f}_{MP}^{grav}$ is calculated using the material point mass m_{MP} and the gravitational acceleration vector $\mathbf{g}$ such that

$$\mathbf{f}_{MP}^{grav} = m_{MP}\mathbf{g} \tag{3.93}$$

Any external forces applied at the boundary are mapped to the material point located nearest to the element border, known as the *boundary material point*. These material points carry surface traction throughout the calculation. If we consider a tetrahedral element, the traction vector τ_e applied to the surface is interpolated from each of the three nodes that form the surface to the boundary material point. The traction at boundary material point p is therefore

$$\tau_e(\mathbf{x}_p) \approx \sum_{i=1}^{n_{tri}} N_i(\xi_q)\tau_e(\mathbf{x}_i) \tag{3.94}$$

where N_i is the shape function of node i of the triangular surface element within the tetrahedral element with n_{tri} triangular surfaces and ξ_q are the coordinates of the boundary material point p inside the parent triangular element. Together, these coordinates represent the projection of the material point onto the triangular surface element of the tetrahedral node.

The traction force vector $\mathbf{f}_p^{trac}$ is

$$\mathbf{f}_p^{trac} = \tau_e(\mathbf{x}_{MP})\frac{S_e}{n_{eb,MP}} = \frac{S_e}{n_{eb,MP}}\sum_{i=1}^{n_{tri}}(\xi_{MP})\tau_e(\mathbf{x}_i) \tag{3.95}$$

where $n_{eb,MP}$ is the number of boundary material points located adjacent to the surface under loading, and S_e is the area of the corresponding loaded surface of the element e.

As the material points are initialised, they are assigned initial conditions, material parameters and constitutive variables. "Book-keeping" is also initialised at this point, tracking information such as the element to which each material point initially belongs, and the initial number of material points per active element.

Calculation of internal forces

In the finite element formulation, the numerical integration of all above integrals is not performed in the global coordinate system $(\mathbf{x})$, but rather each element is transformed into a reference or *parent* element system (ξ) via a mapping procedure that utilises the Jacobian matrix, as in Equation 3.91. The mapping procedure is explored in Section 3.4.11. If we choose a 4-node tetrahedron with linear shape functions as a reference element, the internal force becomes

$$\mathbf{f}^{int} = \sum_{el=1}^{n_{el}} \int_{\Omega_{el}} \mathbf{B}^T \sigma \, d\Omega = \sum_{el=1}^{n_{el}} \int_{V} \mathbf{B}^T \sigma |J| dV \tag{3.96}$$

where Ω_{el} is the volume of the element el in the global coordinate system, n_{el} is the number of active elements, V is the volume of the parent element, $dV = d\xi_1 \, d\xi_2 \, d\xi_3$ is the infinitesimal volume in the parent element system, $|J|$ is the determinant of the Jacobian matrix, and $\mathbf{B}$ is the matrix of the shape function gradients calculated at location ξ with respect to the parent coordinate system. We can integrate Equation 3.96 so that

$$\mathbf{f}^{int} = \sum_{el=1}^{n_{elm}} \sum_{i=1}^{n_{nodes,el}} \sum_{k=1}^{n_{int,el}} \mathbf{B}_i^T(\xi_k) \sigma_k |J_k| W_k \tag{3.97}$$

where $n_{nodes,el}$ and $n_{int,el}$ are the number of nodes and the number of integration points inside the element el respectively and W_k is the *integration weight*, or *weight factor*, of the integration point k.

Since, in the material point method, the material points carry all of the information of the continuum body, including the stresses, the internal forces take the form

$$\mathbf{f}^{int} = \sum_{el=1}^{n_{elm}} \sum_{i=1}^{n_{nodes,el}} \sum_{k=1}^{n_{MP,el}} \mathbf{B}_i^T(\xi_{MP}) \, \sigma_{MP} \, \Omega_{MP} \tag{3.98}$$

where $n_{MP,el}$ is the number of material points in element el.

Calculation of external forces

The external forces can be split into two parts: the body force (due to gravitational acceleration), and the external loading.

The body force can be calculated by

$$\mathbf{f}^{ext,grav} = \sum_{el=1}^{n_{el}} \int_{\Omega_{el}} \rho \bar{\mathbf{N}}^T \mathbf{g} \, d\Omega = \sum_{el=1}^{n_{el}} \int_{V} \rho \mathbf{N}^T \mathbf{g} |J| \, dV \tag{3.99}$$

where Ω_{el} is the volume of the element el in the global coordinate system, n_{el} is the number of active elements, V is the volume of the parent element, $|J|$ is the determinant of the Jacobian matrix, and $\mathbf{B}$ is the matrix of the shape function gradients calculated at location ξ with respect to the parent coordinate system, as before.

Integrating over material points, we see that

$$\mathbf{f}^{ext,grav} = \sum_{el=1}^{n_{elm}} \sum_{i=1}^{n_{nodes,el}} \sum_{MP=1}^{n_{MP,el}} m_{MP} \mathbf{N}_i^T(\xi_{MP}) \mathbf{g} \Omega_{MP} \tag{3.100}$$

where $n_{nodes,el}$ and $n_{MP,el}$ are the nuber of nodes and the number of material points in element el, respectively.

The external forces due to traction can be calculated by

$$\mathbf{f}^{ext,trac} = \sum_{el=1}^{n_{el}} \int_{\partial\Omega_{el}} \bar{\mathbf{N}}^T \mathbf{t} \cdot \mathbf{n} \, d\partial\Omega = \sum_{el=1}^{n_{elm}} \sum_{i=1}^{n_{nodes,el}} \sum_{MP=1}^{n_{MP,el}} \mathbf{N}^T(\xi_{MP}) \mathbf{f}_{MP}^{ext} \tag{3.101}$$

where $\mathbf{f}_{MP}^{ext}$ is the force stored at each material point due to distributed external forces applied at the boundary of the continuum body.

The complete form of the external force is therefore

$$\mathbf{f}^{ext} = \sum_{el=1}^{n_{elm}} \sum_{i=1}^{n_{nodes,el}} \sum_{MP=1}^{n_{MP,el}} \mathbf{N}^T(\xi_{MP}) \, \mathbf{f}_{MP}^{ext,trac} + \sum_{el=1}^{n_{elm}} \sum_{i=1}^{n_{nodes,el}} \sum_{MP=1}^{n_{MP,el}} m_{MP} \mathbf{N}_i^T(\xi_{MP}) \, \mathbf{g} \, \Omega_{MP} \tag{3.102}$$

Mass matrix

The mass matrix must be inverted to solve Equation 3.86. To simplify the calculation, and reduce the computational cost, a *lumped mass matrix* may be used. This is a diagonal matrix in which each entry m_i is the sum the corresponding row of the consistent mass matrix. Matrix inversions then become trivial, although some dissipation of kinetic energy occurs, summarised by Brackbill et al. in *"FLIP: A low-dissipation, particle-in-cell method for fluid flow"* (1988) [21]. We can use the property $\sum^{N_{j=1}^n} N_j^P = 1$ so that the mass matrix becomes

$$\mathbf{M}^{lump} = sum_{el=1}^{n_{elm}} \sum_{i=1}^{n_{nodes,el}} \sum_{MP=1}^{n_{MP,el}} \mathbf{N}^T(\xi_{MP}) m_{MP} \tag{3.103}$$

From here, the superscript lump is removed from the lumped mass matrix $\mathbf{M}_{lump}$ and *mass matrix* will always refer to a lumped matrix, for simplicity. In this study, the 4-node tetrahedral element is used and the lumping procedure gives

$$\mathbf{M} = \sum_{el=1}^{n_{el}} \mathbf{M}_{el} \tag{3.104}$$

$$\sum_{el=1}^{n_{el}} \mathbf{M}_{el} = \begin{bmatrix} \mathbf{m}_1 & \mathbf{0} & \mathbf{0} & \dots & \mathbf{0} \\ \mathbf{0} & \mathbf{m}_2 & \mathbf{0} & \dots & \mathbf{0} \\ \mathbf{0} & \dots & \dots & \mathbf{m}_i & \mathbf{0} \\ \mathbf{0} & \mathbf{0} & \mathbf{0} & \dots & \mathbf{m}_{NodeEl} \end{bmatrix} \tag{3.105}$$

$$\mathbf{m}_i = \begin{bmatrix} m_i & 0 & 0 \\ 0 & m_i & 0 \\ 0 & 0 & m_i \end{bmatrix}; \ \mathbf{0} = \begin{bmatrix} 0 & 0 & 0 \\ 0 & 0 & 0 \\ 0 & 0 & 0 \end{bmatrix} \tag{3.106}$$

$$m_i = \sum_{MP=1}^{n_{MP,el}} m_{MP} N_i(\xi_{MP}) \tag{3.107}$$

Time discretisation

For these calculations, time is discretised into instants: k, so that $t^{k+1} = t^k + \Delta t$, where Δt is the time step size.

If the general system of equations (Equation 3.86) is posed at time instant t^k, it can be rewritten

$$\mathbf{M}^k \cdot \hat{\mathbf{a}}^k = \mathbf{f}^{int^k} + \mathbf{f}^{ext^k} \tag{3.108}$$

where the acceleration a^k is the unknown. An explicit Euler time integration scheme is used to update the velocity. For velocity v^k at time t^k, the velocity at the next time step t^{k+1} is calculated using the acceleration at time t^k as

$$\hat{\mathbf{v}}^{k+1} = \hat{\mathbf{v}}^k + \Delta t \ \hat{\mathbf{a}}^k \tag{3.109}$$

The displacements at time t^{k+1} are calculated using the updated velocity v^{k+1}:

$$\hat{\mathbf{u}}^{k+1} = \hat{\mathbf{u}}^k + \Delta t \ \hat{\mathbf{v}}^k \tag{3.110}$$

Solution algorithm for a single timestep

The algorithm presented here is based on the work presented by Sulsky et al., in *Application of a particle-in-cell method to solid mechanics* (1995) [139], which was itself an improved version by the same author of the algorithm presented in *A particle method for history-dependent*

materials (1995) [138]. The key here is to work with momentum instead of velocity as much as possible, thus avoiding divisions by nodal masses. In each time step, the MPM computational cycle can be listed as follows:

1. The nodal mass is calculated using the shape functions and the lumped mass matrix at time t^k is formed (Eq. 3.102). The internal and external forces are evaluated in the nodes (Eqs 3.103 and 3.98).

2. The momentum balance equation (Eq. 3.108) is solved and the nodal accelerations $\mathbf{a}_i^k$ are determined.
$$\hat{\mathbf{a}}_i^k = [\mathbf{M}_i^k]^{-1}(\mathbf{f}_i^{ext,k} - \mathbf{f}_i^{int,k}) \tag{3.111}$$

3. The velocity at the material points is updated according to Eq. 3.109
$$\mathbf{v}_{MP}^{k+1} = \mathbf{v}_{MP}^k + \Delta t \sum_{i=1}^{n_{Nodes}} N_i(\xi_{MP}^k)\hat{\mathbf{a}}_i^k \tag{3.112}$$

4. The nodal momentum is updated.
$$\mathbf{P}_i^{k+1} = \sum_{el=1}^{n_{el}} \sum_{MP=1}^{n_{MP,el}} m_{MP} N_j(\xi_{MP}^k)\mathbf{v}_{MP}^{k+1} \tag{3.113}$$

5. Nodal velocities are updated.
$$\mathbf{v}_i^{k+1} = \frac{\mathbf{P}_i^{k+1}}{\mathbf{M}_i^k} \tag{3.114}$$

6. The incremental nodal displacement is computed.
$$\Delta\mathbf{u}_i^{k+1} = \Delta t \mathbf{v}_i^{k+1} \tag{3.115}$$

7. The strain increment is computed.
$$\Delta\varepsilon_{MP}^{k+1} = \mathbf{B}(\mathbf{x}_{MP})\Delta\mathbf{u}_i^{k+1} \tag{3.116}$$

8. The stresses are updated according to the material constitutive model

9. The volume and density of the material point are updated.
$$\Omega_{MP}^{k+1} = \Omega_{MP}^k(1+\varepsilon_{vol,MP}) \quad \text{and} \quad \rho_{MP}^{k+1} = \frac{\rho_{MP}^k}{(1+\Delta\varepsilon_{vol,MP})} \tag{3.117}$$

10. Particle positions are updated according to Eq. 3.110

$$\mathbf{x}_{MP}^{k+1} = \mathbf{x}_{MP}^{k} + \sum_{i=1}^{n_{Nodes}} N_i(\xi_{MP}^{k})\Delta\mathbf{u}_i^{k} \tag{3.118}$$

11. The computational grid is initialised for the next step, nodal values are discarded, and the material points carry all the updated information.

3.4.6 Single-phase liquid analysis

The weak form of the linear conservation of momentum equation is developed in section 3.3.3 as

$$\int_{\Omega} \delta\mathbf{v}_L \rho \mathbf{a}_L \, d\Omega = \int_{\partial\Omega_\sigma} \delta\mathbf{v}_L \tau_L \, d\partial\Omega - \int_{\Omega} (\nabla \cdot \delta\mathbf{v}_L)\sigma_L \, d\Omega + \int_{\Omega} \delta\mathbf{v}_L \rho \mathbf{g} \, d\Omega \tag{3.119}$$

We can treat this in a similar way as the single-phase solid analysis described in Section 3.4.5 such that the solution for a single time step is as described in Section 3.4.6.

Solution for single timestep

In each time step, the MPM computational cycle for a single-phase liquid analysis can be listed as follows:

1. The nodal mass is calculated using the shape functions and the lumped mass matrix at time t^k is formed. The internal and external forces are evaluated in the nodes.

2. The momentum balance equation is solved and the nodal accelerations $\mathbf{a}_{L,i}^{k}$ are determined:

$$\hat{\mathbf{a}}_{L,i}^{k} = [\mathbf{M}_{L,i}^{k}]^{-1}(\mathbf{f}_{L,i}^{ext,k} - \mathbf{f}_{L,i}^{int,k}) \tag{3.120}$$

3. The velocity at the material points is updated.

$$\mathbf{v}_{MP}^{k+1} = \mathbf{v}_{MP}^{k} + \Delta t \sum_{i=1}^{n_{Nodes}} N_i(\xi_{MP}^{k})\hat{\mathbf{a}}_{L,i}^{k} \tag{3.121}$$

4. The nodal momentum is updated.

$$\mathbf{P}_{L,i}^{k+1} = \sum_{el=1}^{n_{el}} \sum_{MP=1}^{n_{MP,el}} m_{MP} N_j(\xi_{MP}^{k})\mathbf{v}_{MP}^{k+1} \tag{3.122}$$

5. Nodal velocities are updated.

$$\mathbf{v}_{L,i}^{k+1} = \frac{\mathbf{P}_{L,i}^{k+1}}{\mathbf{M}_{L,i}^{k}} \tag{3.123}$$

6. The incremental nodal displacement is computed.

$$\Delta\mathbf{u}_{L,i}^{k+1} = \Delta t\,\mathbf{v}_{L,i}^{k+1} \tag{3.124}$$

7. The strain increment is computed.

$$\Delta\boldsymbol{\varepsilon}_{MP}^{k+1} = \mathbf{B}(\mathbf{x}_{MP})\Delta\mathbf{u}_{L,i}^{k+1} \tag{3.125}$$

8. The stresses are updated according to the material constitutive model

9. The volume and density of the material point are updated.

$$\Omega_{MP}^{k+1} = \Omega_{MP}^{k}(1+\varepsilon_{vol,MP}) \;\text{ and }\; \rho_{MP}^{k+1} = \frac{\rho_{MP}^{k}}{(1+\Delta\varepsilon_{vol,MP})} \tag{3.126}$$

10. Particle positions are updated according to Eq. 3.110

$$\mathbf{x}_{MP}^{k+1} = \mathbf{x}_{MP}^{k} + \sum_{i=1}^{n_{Nodes}} N_i(\xi_{MP}^{k})\Delta\mathbf{u}_{L,i}^{k} \tag{3.127}$$

11. The computational grid is initialised for the next step, nodal values are discarded, and the material points carry all the updated information.

3.4.7 Two-phase double-point analysis

The double-point analysis treats the solid and liquid phases separately. We define a parameter n_{max}. This is a maximum porosity above which the soil-water mixture is determined to be fluidised, and below which the soil-water mixture is determined to be in a solid state, or non-fluidised.

Spatial discretisation

Based on the discretisation method, the momentum balance equations can be discretised onto the background mesh and integrated at the material points as follows:

$$\mathbf{M}_{iL}\mathbf{a}_{iL} = \mathbf{F}_{iL}^{ext} - \mathbf{F}_{iL}^{int} - \mathbf{F}_{id} \tag{3.128}$$

$$\mathbf{M}_{iS}\mathbf{a}_{iS} = \mathbf{F}_{iS}^{ext} - \mathbf{F}_{iS}^{int} - \mathbf{F}_{id} \tag{3.129}$$

where $\mathbf{a}_{iL}$ and $\mathbf{a}_{iS}$ are liquid and solid nodal accelerations, respectively; and $\mathbf{M}_{iL}$ and $\mathbf{M}_{iS}$ are liquid and solid lumped mass matrices, respectively:

$$\mathbf{M}_{iL} \approx \sum_{p=1}^{N_{Lp}} m_{pL} N(\mathbf{x}_{pL}) \tag{3.130}$$

$$\mathbf{M}_{iS} \approx \sum_{p=1}^{N_{Sp}} m_{pS} N(\mathbf{x}_{pS}) \tag{3.131}$$

where N_{Lp} and N_{Sp} are the number of liquid and solid material points, respectively, m_{pL} and m_{pS} are the masses of the liquid and solid material points, respectively, and $\mathbf{x}_{pL}$ and $\mathbf{x}_{pS}$ are the shape functions for each phase. $\mathbf{F}_{iL}^{ext}$ and $\mathbf{F}_{iS}^{ext}$ are external nodal force vectors of the two phases:

$$\mathbf{F}_{iL}^{ext} \approx \int_{\partial\Omega_p} N(\mathbf{x})\mathbf{p}_L \, dS + \sum_{p=1}^{N_{Lp}} m_{pL} N(\mathbf{x}_{pL})\mathbf{g} \tag{3.132}$$

$$\mathbf{F}_{iS}^{ext} \approx \int_{\partial\Omega_\tau} N(\mathbf{x})[\tau + (1-n)\mathbf{p}_L] dS + \sum_{p=1}^{N_{Sp}} m_{pS} N(\mathbf{x}_{pS})\mathbf{g} \tag{3.133}$$

where τ is the prescribed traction vector, $\mathbf{p}_L$ is the prescribed liquid pressure, and $\mathbf{F}_{iL}^{int}$ and $\mathbf{F}_{iS}^{int}$ are internal force vectors of the liquid and solid phases:

$$\mathbf{F}_{iS}^{int} \approx \sum_{p=1}^{N_{Sp}} \nabla N(\mathbf{x}_{pS})[\sigma' - (1-n)\sigma_L] \, \Omega_{pS} \tag{3.134}$$

$$\mathbf{F}_{iL}^{int} \approx \sum_{p=1}^{N_{Lp}} \nabla N(\mathbf{x}_{pL}) n_p \, \sigma_{Lp} \, \Omega_{pL} \tag{3.135}$$

where Ω_{pL} and Ω_{pS} are the integration weight of the liquid material point and solid material point, respectively.

$\mathbf{F}_{id}$ is the nodal drag force:

$$\mathbf{F}_{id} \approx (\mathbf{v}_L - \mathbf{v}_S) \sum_{p=1}^{N_{Lp}} N(\mathbf{x}_{pL}) \left[n_p^2 \frac{\mu_p}{\kappa_{Lp}} + n_p^2 \rho_L \frac{F}{\sqrt{\kappa_{Lp}}} |\mathbf{v}_L - \mathbf{v}_S| \right] N(\mathbf{x}_{pL}) \Omega_p + \sum_{p=1}^{N_{Lp}} N(\mathbf{x}_{pL}) \nabla n_p \, \sigma_{Lp} \, \Omega_p \tag{3.136}$$

Free surface detection

The free surface develops at an interface between two fluids of different densities. In most cases involving a single fluid, the free surface occurs where the fluid is exposed to atmospheric pressure. The shape of the free surface is unknown as it depends on the developing flow. In MPM, the mass density field can be evaluated at the nodes during each time step. The density field at the nodes is

$$\rho_{L,i} = \frac{\sum_{el=1}^{n_{el,i}} \sum_{MP=1}^{n_{MP,el}} N_i(\xi_{MP}) m_{MP}}{\sum_{el=1}^{n_{el,i}} \frac{\Omega_{el}}{n_{nodes,el}}} \tag{3.137}$$

The denominator in Equation 3.137 only involves the active elements. Consequently, the density at any location $\mathbf{x}$ can be interpolated using

$$\bar{\rho}_{L,MP} = \sum_{i=1}^{n_{nodes,el}} N_i(\xi_{MP}) \rho_{L,i} \tag{3.138}$$

where $\bar{\rho}_{L,MP}$ is the interpolated liquid density field. The interpolated density is evaluated for all material points and this is used to capture the free surface:

$$\bar{\rho}_{L,MP} \leq F_{FreeSurf}\ \rho_{L,0} \tag{3.139}$$

where $\rho_{L,0}$ is the reference value of the liquid density ($\rho_{L,0} = 1000\ kgm^{-3}$) and $0 < F_{FreeSurf} < 1$ is a factor that controls the continuity of the free surface. A greater value of $F_{FreeSurf}$ means a greater number of particles are detected. This parameter is mesh dependant and should be set accordingly. The suggested value is 0.7.

3.4.8 Solution algorithm for double-point MPM

Time discretisation

The numerical solution of the double-point MPM code follows these steps:

1. Calculate nodal accelerations for solid and liquid constituents:

$$\mathbf{a}_{iL} = (\mathbf{F}_{iL}^{ext,t} - \mathbf{F}_{iL}^{int,t} - \mathbf{F}_{id}^{t})/\mathbf{M}_{iL}^{t} \tag{3.140}$$

$$\mathbf{a}_{iS} = (\mathbf{F}_{iS}^{ext,t} - \mathbf{F}_{iS}^{int,t} - \mathbf{F}_{id}^{t})/\mathbf{M}_{iS}^{t} \tag{3.141}$$

where t is the time at the beginning of the time step.

2. Update nodal velocities using the nodal accelerations.

$$\mathbf{v}_{iL}^{t+\Delta t} = \mathbf{v}_{iL}^{t} + \Delta t\ \mathbf{a}_{iL}^{t} \tag{3.142}$$

$$\mathbf{v}_{iS}^{t+\Delta t} = \mathbf{v}_{iS}^{t} + \Delta t\ \mathbf{a}_{iS}^{t} \tag{3.143}$$

where Δt is the time increment and $\mathbf{v}_{iL}^{t}$, $\mathbf{v}_{iS}^{t}$ and $\mathbf{v}_{iL}^{t+\Delta t}$, $\mathbf{v}_{iS}^{t+\Delta t}$ are the nodal velocities for the liquid and solid phases, at the beginning and end of the time step, respectively.

3. Determine the nodal displacements

$$\mathbf{u}_{iL}^{t+\Delta t} = \mathbf{u}_{iL}^{t} + \Delta t \mathbf{v}_{iL}^{t} \tag{3.144}$$

$$\mathbf{u}_{iS}^{t+\Delta t} = \mathbf{u}_{iS}^{t} + \Delta t \mathbf{v}_{iS}^{t} \tag{3.145}$$

4. Update strains ($\varepsilon_{L}^{t+\Delta t}$ and $\varepsilon_{S}^{t+\Delta t}$) and stresses ($p^{t+\Delta t}$, $\sigma_{dev,L}^{t+\Delta t}$ amd $\sigma_{S}^{t+\Delta t}$) for both constituents.

5. Update densities and integration weights. Since the mass remains constant within the system, the densities and the integration weights change as functions of the incremental volumetric strains $\Delta\varepsilon_{p,\,vol,\,L}^{t+\Delta t}$ and $\Delta\varepsilon_{p,\,vol,\,S}^{t+\Delta t}$ of the material point p as follows:

$$\rho_{iL}^{t+\Delta t} = \rho_{iL}^{t} \frac{1}{1+\Delta\varepsilon_{p,\,vol,\,L}^{t+\Delta t}} \tag{3.146}$$

$$\rho_{iS}^{t+\Delta t} = \rho_{iS}^{t} \frac{1}{1+\Delta\varepsilon_{p,\,vol,\,S}^{t+\Delta t}} \tag{3.147}$$

$$\Omega_{iL}^{t+\Delta t} = \Omega_{iL}^{t}(1+\Delta\varepsilon_{p,\,vol,\,L}^{t+\Delta t}) \tag{3.148}$$

$$\Omega_{iS}^{t+\Delta t} = \Omega_{iS}^{t}(1+\Delta\varepsilon_{p,\,vol,\,S}^{t+\Delta t}) \tag{3.149}$$

A summary of the modified computation scheme for the double-point formulation is shown in Figure 3.9.

The MPM computational cycle for a double-point two-phase analysis requires the liquid free surface to be identified. This is explained in detail in Section 3.4.7.

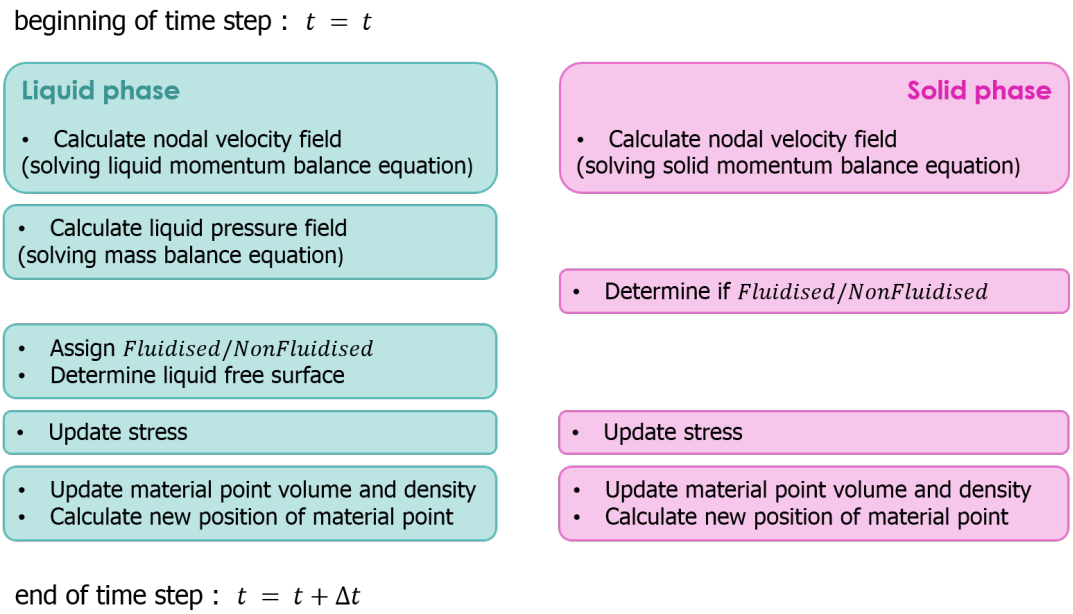

Fig. 3.9 Summary of the double-point MPM computation scheme, adapted from Martinelli (2016) [105]

3.4.9 Mixed integration scheme

In the Anura3D code, a procedure called MPM-Mixed integration is employed to mitigate the grid-crossing instability detailed in section 2.5.3. It is based on the research carried out by Beuth (2012) [17] and Al-Kafaji (2013) [3]. In this simple procedure, a distinction between the fully filled elements and partially filled elements is made based on

$$\sum_{p=1}^{N_{p,el}} \Omega_p \geq F_{fill}\, \Omega_{el} \tag{3.150}$$

in which $N_{p,el}$ is the number of material points within the element el, Ω_{el} and Ω_p are the integration weights of the element el and material point p, respectively. A factor F_{fill} is set to 0.9 to determine the threshold, per the recommendation in Beuth (2012) [17], and each element is checked by Equation 3.150 during each timestep.

If the condition is fulfilled, the element is considered a fully filled element. Otherwise, the element is determined to be as a partially filled element. For partially filled elements, the internal force is calculated with the classic MPM procedure, but for fully filled elements, the internal force is determined by Gauss point integration, and as in FEM, a Gauss point with an averaged stress σ_{av} is considered. The averaged stress σ_{av} is calculated as follows:

$$\sigma_{av} = \frac{\sum_{p=1}^{N_{p,el}} \sigma_p \Omega_p}{\sum_{p=1}^{N_{p,el}} \Omega_p} \tag{3.151}$$

where σ_p is the stress in the material point p and Ω_p is the integration weight of the Gauss point q obtained by:

$$\Omega_p = \frac{1}{N_{p,el}} \sum_{p=1}^{N_{p,el}} \Omega_p \tag{3.152}$$

so that the equation for the internal forces becomes:

$$\mathbf{F}_i^{int} = \sum_{el=1}^{N_{el,i}} \sum_{q=1}^{N_{q,el}} \nabla N_i(\mathbf{x}_q) \sigma_{av} \Omega_q \tag{3.153}$$

where $N_{q,el}$ denotes the number of Gauss points in element el, which is set as 1 in Anura3D [169], and $\mathbf{x}_q$ is the position of the Gauss point.

This is a mixed approach which adopts both material points and Gauss points to calculate the internal forces. This procedure can be summarised in the following four steps [3]:

1. Identify fully filled and partially filled elements using Equation 3.150
2. Average the stress σ and other state variables per Equation 3.151, and assign these to Gauss points of fully filled elements
3. Calculate the internal nodal forces using Gaussian integration for fully filled elements using Equation 3.153 and standard material point integration for other elements
4. Apply the constitutive equations at Gauss point of fully filled elements, and assign the obtained stresses σ and state variables to all particles in the element.

3.4.10 Stability criteria

The stability of a numerical algorithm depends on the integration scheme. This analysis uses an explicit time integration scheme, which is conditionally stable. The Courant-Friedrichs-Levy condition [31] is used to obtain the critical time interval required to achieve a stable solution.

Single-phase solid analysis

$$\Delta t_{cr} = \frac{l_{min}}{c};\ c = \sqrt{\frac{E_c}{\rho}} \tag{3.154}$$

where E_c is the constrained modulus of the solid media and l_{min} is the minimum length of the element. The example of a tetrahedral element (used for 3D simulations) is shown in Figure 3.10.

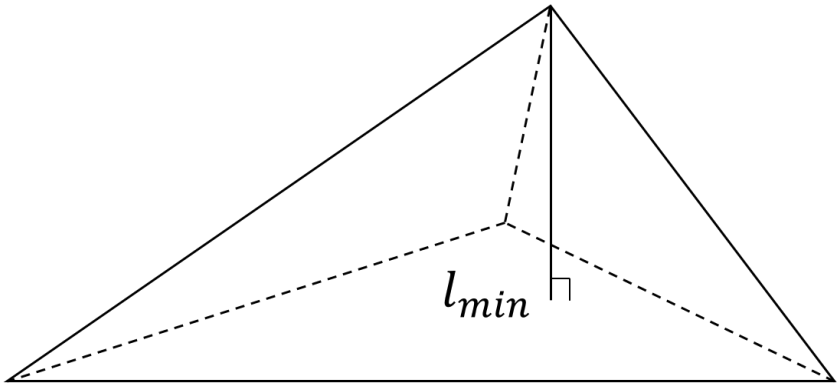

Fig. 3.10 Minimum length l_{min} for a tetrahedral element [114]

Single-phase liquid analysis

$$\Delta t_{cr} = \frac{l_{min}}{c_L};\ c_L = \sqrt{\frac{K_L}{\rho_L}} \tag{3.155}$$

where K_L is the liquid bulk modulus.

Two-phase coupled analysis

The stability analysis of the 2-phase-coupled formulation is described as *onerous* [114]; for this reason, a first simplified analysis was performed in by Mieremet (2015) [109] on a simplified formulation that is derived by assuming an incompressible pore fluid. Based on the eigenvalue analyses of a single linear finite element, it is observed that in addition to the CFL stability condition, the influence of the permeability must be included [109]. The full stability criterion for the 2-phase-coupled formulation is represented by the following:

$$\Delta t_{cr} = \min\{\Delta t_{cr,1};\ \Delta t_{cr,2}\} \tag{3.156}$$

where

$$\Delta t_{cr,1} = \frac{l_{min}}{c_1} \tag{3.157}$$

and

$$\Delta t_{cr,2} = \frac{2\tilde{\rho}k}{\rho_L g} \tag{3.158}$$

with l_{min} defined as the minimum length of the tetrahedral element, as before, and

$$c_1 = \sqrt{\frac{E_c^u}{\rho_{sat}}} \tag{3.159}$$

$$E_u^c = E_c + \frac{K_L}{n} \tag{3.160}$$

$$\rho_{sat} = (1-n)\rho_s + n\rho_L \tag{3.161}$$

$$\tilde{\rho} = \rho + \left(\frac{1}{n} - 2\right)\rho_L \tag{3.162}$$

where E_c^u is the undrained constrained modulus of the saturated soil, E_c is the laterally confined modulus of the soil skeleton, and K_L is the bulk modulus of the liquid.

$\Delta t_{cr,1}$ is a function of the size of the mesh, the stiffness, the porosity and the density of the material, whilst $\Delta t_{cr,2}$ is a function of the permeability, the porosity and the density. In many cases, the time step required to ensure stability in low permeability soils is smaller than that required for highly permeable soils, i.e. $\Delta t_{cr,2} < \Delta t_{cr,1}$.

Equation 3.156 can therefore be reformulated into a single equation:

$$\Delta t_{cr} = \frac{-2a + \sqrt{4a^2 + 8(b^2 - 4ac)}}{b + \sqrt{b^2 - 4c}} \tag{3.163}$$

where

$$a = \frac{n\rho g}{(1-n)\rho_s k} \tag{3.164}$$

$$b = \frac{4(n\rho K_L + (1-2n)\rho_L K_L + n\rho_L E_c)}{n(1-n)\rho_S \rho_L L_{min}} \tag{3.165}$$

and

$$c = \frac{16 E_c K_L}{(1-n)\rho_s \rho_L L_{min}} \tag{3.166}$$

Double-point analysis

To ensure the numerical stability of the explicit integration method, the critical time step Δt_{cr} must satisfy the Courant-Friedrichs-Levy (CFL) condition. According to Verruijt (2010) [146], the critical timestep $\Delta t_{cr,1}$, in a saturated medium, is:

$$\Delta t_{cr,1} = \min\left\{\frac{l_{min}}{c_1};\ \frac{l_{min}}{c_2}\right\} \tag{3.167}$$

where l_{min} is the characteristic length of the tetrahedral element, as before (see Figure 3.10), c_1 and c_2 are the *undrained wave speed* and the *damped wave speed* in the saturated medium, given by

$$c_1 = \sqrt{\frac{E_u^c}{\rho_{sat}}} \tag{3.168}$$

as in Equation 3.159 and

$$c_2 = \beta_S c_L \tag{3.169}$$

where E_u^c is the undrained constrained modulus of the saturated soil,as before, ρ_{sat} is the density of the saturated medium, β_S is a dimensionless factor, and c_L is the speed of the compression wave in water, as given in Equation 3.155. These parameters are obtained per Equations 3.160 and 3.161, and:

$$\beta_S = \sqrt{\frac{n\frac{E_c}{K_L}}{1-n+n\frac{E_c}{K_L}}} \tag{3.170}$$

where E_c is the constrained modulus of the soil skeleton, as before.

In addition to these criteria, Mieremet (2015) [109] suggests an additional criterion that depends on the soil permeability is necessary to restrict the critical time step to ensure complete stability. This additional criterion takes the form:

$$\Delta t_{cr,2} = \frac{2\tilde{\rho}k}{\rho_L g} \tag{3.171}$$

where

$$\tilde{\rho} = \rho_{sat} + \left(\frac{1}{n} - 2\rho_L\right) \tag{3.172}$$

and k is the Darcy permeability of the soil:

$$k = \kappa \frac{\rho_L g}{\mu} \tag{3.173}$$

Thus, the calculation for the critical time step becomes, as Equation 3.156:

$$\Delta t_{cr} = \min\{\Delta t_{cr,1};\ \Delta t_{cr,2}\} \tag{3.174}$$

and in full:

$$\Delta t_{\text{crit}} = \min\left\{ \frac{l_{min}}{c_1}, \frac{l_{min}}{c_1}, \frac{2k\left[(n+\frac{1}{n}-2)\rho_L + (1-n)\rho_S\right]}{\rho_L\, g} \right\} \tag{3.175}$$

where k is the Darcy permeability of the soil. In this study, only a fraction of the calculated critical time step size is used, which means that the time increment Δt is:

$$\Delta t = \alpha_c\, \Delta t_{\text{crit}} \tag{3.176}$$

where α_c is the *Courant number*, and it is recommended to set $\alpha_c \approx 0.6 - 0.8$ to ensure numerical stability for double-point MPM calculations. This is lower than the Courant number used for single-point MPM [169].

3.4.11 Mapping procedure

The mapping procedure is used to map updated information from the grid nodes to the material points for solution during each timestep. It is implemented using shape functions. Figure 3.11 shows a 4-node tetrahedral element in the parent domain, where the node number can vary from 1 to 4, and in the global domain where the node number depends on the global mesh.

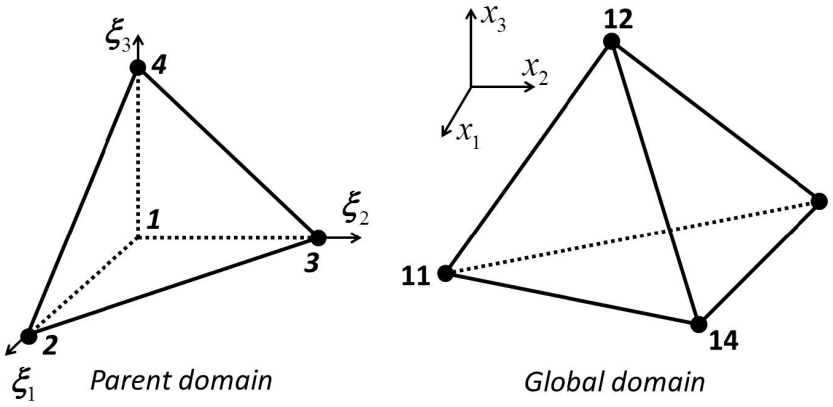

Fig. 3.11 A 4-node tetrahedral element in the parent and global domains, per [114]

For isoparametric elements, the shape functions are the same in the parent and global domains. The coordinates of a point in the global domain are determined as follows:

$$\mathbf{x}(\xi,t) = \sum_{i=1}^{4} N_i(\xi)\mathbf{x}_i(t) \tag{3.177}$$

where ξ is the vector of the parent coordinate system

$$\xi = [\xi_1\ \xi_2\ \xi_3]^T \tag{3.178}$$

The shape function is defined in the parent domain (local coordinate system) as:

$$N_1(\xi) = 1 - \xi_1 - \xi_2 - \xi_3 \tag{3.179}$$

$$N_2(\xi) = \xi_1 \tag{3.180}$$

$$N_3(\xi) = \xi_2 \tag{3.181}$$

$$N_4(\xi) = \xi_3 \tag{3.182}$$

where the subscript represents the node number in the parent domain.

The derivative of the shape function is usually required to calculate the **B** matrix (necessary to determine the internal forces of the system). The derivative is calculated using the chain rule:

$$\begin{aligned}
\frac{\partial N_i(\xi)}{\partial \mathbf{x}_1} &= \frac{\partial N_i(\xi)}{\partial \xi_1}\frac{\partial \xi_1}{\partial \mathbf{x}_1} + \frac{\partial N_i(\xi)}{\partial \xi_2}\frac{\partial \xi_2}{\partial \mathbf{x}_1} + \frac{\partial N_i(\xi)}{\partial \xi_3}\frac{\partial \xi_3}{\partial \mathbf{x}_1} \\
\frac{\partial N_i(\xi)}{\partial \mathbf{x}_2} &= \frac{\partial N_i(\xi)}{\partial \xi_1}\frac{\partial \xi_1}{\partial \mathbf{x}_2} + \frac{\partial N_i(\xi)}{\partial \xi_2}\frac{\partial \xi_2}{\partial \mathbf{x}_2} + \frac{\partial N_i(\xi)}{\partial \xi_3}\frac{\partial \xi_3}{\partial \mathbf{x}_2} \\
\frac{\partial N_i(\xi)}{\partial \mathbf{x}_3} &= \frac{\partial N_i(\xi)}{\partial \xi_1}\frac{\partial \xi_1}{\partial \mathbf{x}_3} + \frac{\partial N_i(\xi)}{\partial \xi_2}\frac{\partial \xi_2}{\partial \mathbf{x}_3} + \frac{\partial N_i(\xi)}{\partial \xi_3}\frac{\partial \xi_3}{\partial \mathbf{x}_3}
\end{aligned} \tag{3.183}$$

The compact form can be written as:

$$\begin{Bmatrix} \frac{\partial N_i(\xi)}{\partial \mathbf{x}_1} \\ \frac{\partial N_i(\xi)}{\partial \mathbf{x}_2} \\ \frac{\partial N_i(\xi)}{\partial \mathbf{x}_3} \end{Bmatrix} = \begin{bmatrix} \frac{\partial \xi_1}{\partial \mathbf{x}_1} & \frac{\partial \xi_2}{\partial \mathbf{x}_1} & \frac{\partial \xi_3}{\partial \mathbf{x}_1} \\ \frac{\partial \xi_1}{\partial \mathbf{x}_2} & \frac{\partial \xi_2}{\partial \mathbf{x}_2} & \frac{\partial \xi_3}{\partial \mathbf{x}_2} \\ \frac{\partial \xi_1}{\partial \mathbf{x}_3} & \frac{\partial \xi_2}{\partial \mathbf{x}_3} & \frac{\partial \xi_3}{\partial \mathbf{x}_3} \end{bmatrix} \begin{Bmatrix} \frac{\partial N_i(\xi)}{\partial \xi_1} \\ \frac{\partial N_i(\xi)}{\partial \xi_2} \\ \frac{\partial N_i(\xi)}{\partial \xi_3} \end{Bmatrix} \tag{3.184}$$

The derivatives of the natural coordinates ξ with respect to the global coordinates $\mathbf{x}$ are not explicitly available. The 3x3 matrix in Equation 3.184 is the inverse of the Jacobian matrix **J**:

$$\begin{bmatrix} \frac{\partial \xi_1}{\partial \mathbf{x}_1} \frac{\partial \xi_2}{\partial \mathbf{x}_1} \frac{\partial \xi_3}{\partial \mathbf{x}_1} \\ \frac{\partial \xi_1}{\partial \mathbf{x}_2} \frac{\partial \xi_2}{\partial \mathbf{x}_2} \frac{\partial \xi_3}{\partial \mathbf{x}_2} \\ \frac{\partial \xi_1}{\partial \mathbf{x}_3} \frac{\partial \xi_2}{\partial \mathbf{x}_3} \frac{\partial \xi_3}{\partial \mathbf{x}_3} \end{bmatrix} = \mathbf{J}^{-1} = \begin{bmatrix} \frac{\partial \mathbf{x}_1}{\partial \xi_1} \frac{\partial \mathbf{x}_2}{\partial \xi_1} \frac{\partial \mathbf{x}_3}{\partial \xi_1} \\ \frac{\partial \mathbf{x}_1}{\partial \xi_2} \frac{\partial \mathbf{x}_2}{\partial \xi_2} \frac{\partial \mathbf{x}_3}{\partial \xi_2} \\ \frac{\partial \mathbf{x}_1}{\partial \xi_3} \frac{\partial \mathbf{x}_2}{\partial \xi_3} \frac{\partial \mathbf{x}_3}{\partial \xi_3} \end{bmatrix} \tag{3.185}$$

3.4.12 Newtonian Fluid Model

The fluids in these simulations are universally modelled as Newtonian fluids. For weakly compressible liquids, the density is related to the liquid pressure:

$$\frac{\partial \rho_L}{\partial t} = -\frac{1}{c_p^2} \frac{\partial p_L}{\partial t};\ c_p = \sqrt{K_L/\rho_L} \tag{3.186}$$

where c_p is the acoustic wave speed, and K_L is the liquid bulk modulus. For a relatively small pressure range and an isothermal process, c_p is constant and the pressure-density relationship becomes linear:

$$p_L = p_{L,0} - c_p^2(\rho_L - \rho_{L,0}) \tag{3.187}$$

where $p_{L,0}$ are $\rho_{L,0}$ are reference values for pressure and density ($0kPa$ and $1000kg/m^3$ respectively), and $c_p = \sqrt{K_L/\rho_{L,0}}$.

The value of liquid pressure at which cavitation occurs is $p_{L,thres}$ and the corresponding density is $\rho_{L,thres}$ where

$$\rho_{L,thres} = \frac{1}{c_p^2}(p_{L,0} - p_{L,thres}) + \rho_{L,0} = \rho_{L,0}\left(1 - \frac{p_{L,thres}}{K_L}\right) \tag{3.188}$$

In the case of $\rho_L \geq \rho_{L,thres}$, the pressure can be directly calculated as a function of the volumetric strains $\varepsilon_{vol,L}$:

$$p_L = p_{L,thres} + K_L \varepsilon_{vol,L} \tag{3.189}$$

and otherwise, the pressure is set to $p_{L,thres}$

In this study, the pressure in the liquid constituent is computed incrementally:

$$\frac{dp_L}{dt} = K_L \frac{d\bar{\varepsilon}_{vol,L}}{dt} \text{ with } p_L \geq p_{L,thres} \tag{3.190}$$

For two-phase coupled analysis, the term $\frac{d\bar{\varepsilon}_{vol,L}}{dt}$ is calculated according to the mass balance equation. For a single-phase liquid, the term $\bar{\varepsilon}$ is equal to the volumetric strain of the liquid material ($\bar{\varepsilon}_{vol,L} = \varepsilon_{vol,L}$).

$$\frac{d_L \bar{\varepsilon}_{vol,L}}{dt} = \frac{1}{n}[n(\nabla \cdot \mathbf{v}_L) + (1-n)(\nabla \cdot \mathbf{v}_\mathbf{S})] \tag{3.191}$$

Finally, the deviatoric component of the stress tensor is calculated as

$$\sigma_{dev,L} = 2\mu_d \frac{D^L \varepsilon_{dev,L}}{Dt} \text{ with } p_L > p_{L,thres} \tag{3.192}$$

where μ_d is the dynamic viscosity of the water and $\varepsilon_{dev,L}$ is the deviatoric component of the strain tensor. This is only used in the case of a single-phase liquid; for a two-phase coupled analysis the shear stresses in the liquid component disappear. Further details on the development of the weakly compressible fluid model are available in Martinelli (2016) [105].

3.5 Summary of the numerical implementation of MPM

The computational cycle consists of two distinct phases: the Lagrangian phase and the convective phase [169]. During the computation, the unknown variables are always recorded by the material points, but they are interpolated onto the grid nodes at the beginning of each time step. Per Sulsky (1995) [139], to minimise division by nodal masses, momentum is used in place as of velocity as much as possible.

An MPM simulation consists of the following summarised stages:

1. The initialisation of background grid and material points
2. The material point quantities are extrapolated to the grid nodes
3. The equations of motion are solved on the grid
4. Newton's 2nd Law is solved to obtain the nodal acceleration (equation 3.86)
5. Derivative terms are extrapolated back to the material points
6. The grid is reset and the position of the material points is updated

The geometry is discretised into a collection of material points, each with its own material properties and initial conditions (velocity, stress, temperature, etc.). Since the grid is used to provide a point for gradient calculations, it is normally made large enough to cover the expected spatial extent of the computational domain.

After the derivative terms are extrapolated back to the material points, the variables on the material points (positions, velocities, strains, stresses etc.) are then updated with these rates depending on the integration scheme the choice of constitutive model.

Once the material points are fully updated at the current time step, the grid is reset to allow the next time step to begin.

These stages are summarised in Figure 3.12.

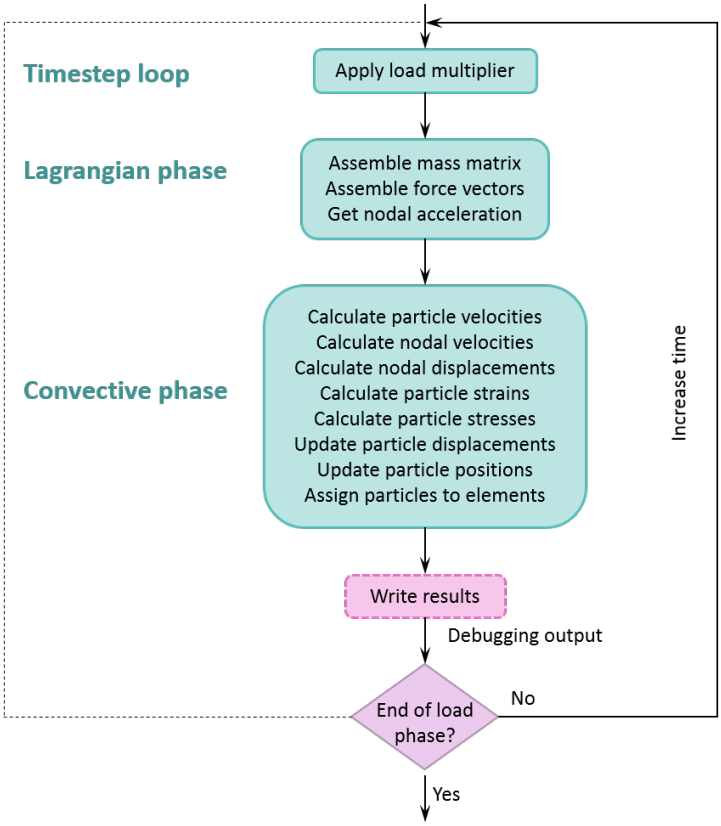

Fig. 3.12 Structure of each timestep in MPM, after [169]

3.6 MPM mesh convergence studies

Many researchers have previously undertaken convergence studies in MPM of the mesh size and particle densities. In Zhao and Liang (2010) [170], the dependencies of the results of a dam-break flow simulation, like the ones presented in this thesis, on the computational mesh size and particle density (the number of MPs per element) were investigated, and it was determined that the selections of the mesh size and the number of MPs per element did not significantly influence the dam-break flow modelling. The pilot study employed here was simulations of dam-break flows with an aspect ratio of 1.0. Two mesh sizes were employed: coarse (0.1 m) and fine (0.05 m). Three different particle densities were used: 4, 8 and 10. The results of this study are presented in Table 3.2.

From Table 3.2, it can be seen that the mesh size and the particle density do not play an important role in the results of dam-break flow simulations. Refining the mesh and increasing the particle density does produce more accurate results, but overall the results are very similar. To balance the computational costs and accuracy of the simulations, relatively coarse meshes were chosen. The particle density for all simulations was chosen as at least 4 particles per element (PPE). For the sloped beach investigated later in this thesis, up to 12 fluid material points were assigned per element, since otherwise the number of particles forming the thin layer of run-up on the slope was too few to generate a meaningful result.

Table 3.2 Convergence study for dam break flow case comparing flood front positions at different times [170]

Condition	Mesh size (m)	MPs per element	Flood front positions (m) at different time							
			0s	0.1s	0.2s	0.5s	0.8s	1.0s	1.2s	1.5s
1	0.1	4	1.00	1.10	1.40	2.86	4.55	5.80	7.05	8.92
2	0.1	8	1.00	1.10	1.40	2.86	4.62	5.83	7.10	9.00
3	0.1	10	1.00	1.10	1.40	2.82	4.58	5.81	7.05	8.92
4	0.05	4	1.00	1.10	1.41	2.85	4.58	5.80	7.05	8.98

Further mesh convergence studies in [169] indicate that frequent pressure fluctuations are observed when using finer meshes, which can be attributed to the previously discussed grid-crossing errors. Using a finer mesh causes more frequent migration of MPs between elements and therefore, the grid-crossing errors are more pronounced, discussed by Al-Kafaji (2013) [3] and Guilkey et al. (2006)[51]. The problem is more severe when the number of point per element is low and the stiffness of the material is high [3]. However, as mentioned previously, the mesh resolution plays an important role in the accuracy of the results: by decreasing the mesh size, the run up height in the numerical solution converges with the analytical results of Li and Raichlen (presented in Section 6.3). Martinelli (2016) [105] also finds that the accuracy of the results increases using a large number of liquid MPs and a fine mesh. Although it depends on the situation being modelled, Martinelli finds that increasing the number of material points per element has a greater effect on improving accuracy than refining the mesh.

Finally, Zhao finds that the nodal density oscillations are the main cause of pressure fluctuations due to the weakly compressible behaviour of the fluid. The change in calculated nodal density in this method is directly due to the proportional change in points per element in the elements surrounding the node. Therefore, by increasing the number of points per element the oscillations are reduced. The recommendation is to employ a finer mesh in situations where the resolution of the simualtion is important, and to mitigate the pressure oscillation by introducing a greater number of points per element to compensate [169]. This thesis has been informed by the work carried out previously by Zhao, using this guidance to inform the

selection of mesh size and the number of material points per element. For all the simulations recorded in this thesis, pilto studies were run to determine the appropriate parameters that balance results quality with the computational time required to run the simulation.

3.7 Comparison of MPM with the Smoothed Particle Hydrodynamics method

All numerical models require nodal connectivity to determine the spatial derivatives of field variables. This is constructed by finite elements in FEM, and by searching for neighbour particles in meshfree methods. Since nodal spacing changes very timestep, neighbour searches must be carried out every timestep in SPH. This increases the computational cost of SPH compared to MPM, where the nodal connectivity does not change.

SPH does not require a pre-defined mesh, but consequently, the computational cost of evaluating field functions and derivatives is higher than in MPM. The rectangular background grid in MPM can be used for all time steps, completely avoiding mesh distortion and element entanglement associated with FEM.

The constant and linear consistency conditions are not satisfied in SPH for particles at or near a domain boundary (where the support domain intersects) due to the irregular particle distribution. This consistency can be restored, at a significant computational cost. It may also lead to negative density or negative energy results that lead to the breakdown of the simulation. The constant and linear consistency conditions are inherently satisfied in MPM since the traditional shape functions are used.

In SPH, an integration over the support domain means that the summation happens over a finite number of particles, so insufficient sampling points may lead to numerical instability. Particles under tensile stress start to develop unstable motion and may exhibit clumping or lead to a computational blowup. By contrast, the grid nodes in MPM serve as field nodes to construct approximation functions of field variables, and the material points serve as sample points for integration. Since the number of material points is usually significantly larger than the number of grid nodes, the numerical instability from insufficient sampling points is avoided. In MPM, the time step is determined directly from the background mesh size using the Courant number, remaining constant throughout the computation. In SPH, the critical time step is related to the smallest smoothing length. Since this can decrease under compression, the time step may also shorten so that SPH typically requires more time steps in a large deformation problem.

In MPM, the boundary conditions at the free surface are satisfied automatically, and essential boundary conditions are applied at the grid nodes, as in FEM. Additional boundary conditions can be imposed at the mesh nodes or at the material points. SPH does not require the velocity field to be single-valued, so a degree of penetration and mixing may occur. MPM requires a single-value velocity field so interpenetration of material is precluded and no-slip contact between invading particles is automatically satisfied.

SPH has been widely applied to fluid dynamics problems, whereas MPM application to fluid dynamics is relatively rare. Recently, there has been a growing interest in applying MPM to fluid flow problems:

- Fluid-membrane interaction (York et al., in 1999 and 2000, Gan et al., in 2011 and Lin et al., in 2014)
- Sea-ice dynamics (Sulsky, in 2007)
- Fluid-solid interactions induced by surface tension using the generalised interpolation MPM (GIMP)
- Coupling of soil skeleton and pore water flow (Zhang et al., in 2009, Zheng et al., in 2013 and Bandara et al., in 2016)
- Seepage flow from embankments (Martinelli et al., 2017)

Overall, comparisons between SPH and MPM show a faster convergence and higher numerical accuracy and efficiency for MPM, however, the efficiency of MPM for fluid flow could be greatly enhanced using an adaptive mesh. The large number of empty background cells created in solving fluid flow problems in MPM lead to greater computational costs being incurred Sun et al. [140]

For these problems, the constitutive equations are history-dependent so material points must be followed; this is difficult to implement in a Eulerian scheme. However, modelling using purely Lagrangian methods typically results in a severe mesh distortion, leading to a poorly conditioned stiffness matrix leading to mesh lock-up or entanglement. Re-meshing can be implemented; this prevents the lock-up and tangling but then interpolation must be performed for all history-dependent variables, which can introduce errors [138]. MPM serves as an extension of the particle-in-cell method in which particles are interpreted to be material points that are followed throughout the loading process. These particles do not represent material grains but instead are pieces of a continuum solid. Each material point has a constant mass, which is conserved throughout the simulation, as well as all the other information required for the calculation. Mass conservation is therefore implicit in MPM.

A mapping and re-mapping algorithm is used to allow information to be mapped back and forth between the material points and background mesh nodes during an analysis [148]. A fixed Eulerian grid allows a spatial gradient to be determined. Since the grid can also be interpreted as an updated Lagrangian frame of reference, the usual convection term in the acceleration associated with Eulerian formulations does not appear [138]. Consequently, mesh tangling is avoided, and the spatial and temporal history of the material motion can be tracked. As for FEM, the choice of grid size can influence the results but does not carry any permanent information [41]. The background grid also reduces the cost of executing the simulation using the material point method when compared to other methods.

3.8 Summary of the advantages of MPM

In MPM, each material point is viewed as a representative volume element (RVE) rather than grains [98]; it uses a continuum based on soil constitutive models, typically the Mohr–Coulomb and the Cam Clay or Modified Cam Clay models. The material domain is discretised by a group of particles, as illustrated in Figure 3.1. Each particle carries all material variables, such as the mass, position, velocity, stress and strain. The momentum equations are solved on the predefined background mesh.

The material point method is therefore particularly convenient for modelling based on history-dependent constitutive models since information such as strain, stress, and history-dependent variables can be carried by the material points. These material points are used as integration points like the Gaussian points [148] which enables the spatial and temporal tracking of history-dependent variables [1], and allowing for error-free advection of material properties via the motion of the material points.

MPM also avoids the tensile instability that arises in SPH, where the integration over the support domain is converted into a summation for only a finite number of particles [96]. The numerical instability arises since there is an inadequate number of sampling points for the integration, particularly in materials under tensile stress. MPM avoids this by utilising grid nodes to produce approximation functions of the field variables and letting the material points serve as sampling points for integration. Since the number of material points is usually greater than the number of grid nodes, this eliminates the numerical instability [1].

Unlike FEM, MPM does not require periodical re-meshing steps and remapping of state variables and is, therefore, better suited to modelling large material deformations. This makes the MPM particularly useful for modelling dam-break flows, wave attack on coastal defences, and large land flows such as the Vaiont landslide. More recently, a 3D version of the code has been applied to hypervelocity impact problems [96]. The particle basis of MPM allows it to treat

crack propagation and other discontinuities better than FEM, where the orientation of the mesh influences crack propagation in the material. Furthermore, a no-slip, no-penetration contact algorithm is implicit to the material point method, with no associated additional computational expense.

In MPM, it is the particles and not the mesh points that store all the information on the state of the calculation. Therefore, no numerical error results from the mesh returning to its original position after each calculation cycle, and no re-meshing algorithm is required. Instead, the momentum balance equation is solved at each node of the background mesh, and then after the location of the material points has been updated, the background mesh is reset to the original position, consequently avoiding mesh-entanglement problems.

This use of a background mesh in MPM allows for the implementation of boundary conditions in a similar method to that in FEM, which is advantageous when compared to mesh-free methods. SPH requires a time-consuming neighbour particle search, whereas MPM requires only the identification of particles relative to the background mesh thus making it more computationally efficient [1]. The background grid also allows for a straightforward and efficient treatment of frictional contacts of multiple bodies [145].

Whilst the MPM offers many advantages, as with any numerical method, it has drawbacks. Each simulation requires a large amount of memory since the grid must cover the entire region occupied by both the solid and the liquid bodies. MPM also results in lower accuracy than the FEM as the material points often do not lie at the optimal position for numerical integration. Additionally, enforcement of boundary conditions can be difficult compared with FEM, although much easier than in SPH. Finally, formal analysis (convergence, error and stability) of the MPM is extremely difficult [145].

Overall, however, MPM successfully avoids the tensile instability and numerical fracture problems that occur in SPH. Numerical studies show that MPM is much more efficient than SPH, especially in large scale problems [96]. The imposition of essential boundary conditions is very simple in MPM, making the MPM more promising than SPH in the simulation of large scale hydrodynamic problems.

Chapter 4

Dam-break wave simulations

This chapter describes the effect of changing the permeability of a permeable barrier, via manipulation of the mean grain size, on the run-up response to a dam-break flood for the case of a vertical sea wall.

Initially, simulations of dam-break flows that have the same initial conditions and geometry as published results were run to verify and demonstrate the accuracy and stability of the material point method when applied to dam-break flows impacting on porous media. The results are shown to be in good agreement with validated and verified numerical methods and experimental data.

Subsequently, parametrised numerical simulations were run to establish the effect of changing the permeability of a porous vertical barrier on the maximum run-up height reached by the flood wave. The width of the wall was also varied to ensure that the permeability of the barrier was the main parameter affecting the run-up height. The permeability of the porous medium is modified by changing the grain size, in accordance with Ergun's law [40], as in Chapter 3.1:

$$\mathbf{F}_d = n^2 \left[\frac{\mu}{\kappa} + n\rho_L \frac{F}{\sqrt{\kappa}} |\mathbf{v}_L - \mathbf{v}_S| \right] (\mathbf{v}_L - \mathbf{v}_s) + \sigma_L \nabla n \tag{4.1}$$

with the first two terms representing a viscous force related to the permeability of the soil skeleton k, the liquid viscosity μ and the relative velocity between the liquid and solid phases $(\mathbf{v}_L - \mathbf{v}_s)$. The final term is contributed by the gradient of the porosity ∇n. F is a coefficient and κ is the intrinsic soil permeability, calculated from the Kozeny-Carman formula [15] such that

$$F = \frac{B}{\sqrt{A} n^{1.5}} \tag{4.2}$$

where B is a constant set to 1.75 according to Ergun [40] and

$$\kappa = \frac{D_p^2}{A} \frac{n^3}{(1-n)^2} \tag{4.3}$$

where D_p is the mean effective grain size diameter and n is the soil porosity. A is a constant and has been determined to be in the range 150 - 180, and for the situations explored here, the value of 150 will be used, after Ergun (1952) [40, 105].

4.1 Motivation

Dam-break floods are an example of free-surface flows driven by gravity. They are of significant interest to civil and environmental engineers as they represent a well-established hazard in the field of free-surface hydrodynamics. Understanding the overall response of a wave that results from a dam-break flood impacting on a permeable barrier is key to designing effective flood defences; thus minimising the risk posed by dam-break floods. The maximum water surface level reached by the impacting wave on the porous barrier should be minimised to prevent overtopping of the barrier. This investigation seeks to establish the ability of a permeable barrier to mitigate potential flooding in response to a dam-break flow by absorbing wave energy as the water infiltrates the porous medium. The permeability of the barrier is varied by changing the mean grain size of the constituent material of the barrier. The width of the permeable wall is also varied in this investigation, to establish if the run-up height is influenced more by the grain size when the thickness of the wall is also increased, therefore ensuring that the wall thickness is sufficiently large that the only variable affecting the run-up height is the permeability of the barrier.

Design parameters for permeable flood defences include the grain size of the particles forming the seawall and the width of the seawall. According to all fit equations, the risk of overtopping is primarily determined by the relative still water depth, with wave amplitude being the second main factor [60]. However, these parameters cannot be controlled by dam construction.

The material point method is applied here to the widely investigated dam-break problem as a pilot study to assess the validity of applying a method historically used in solid mechanics and soil mechanics to a problem involving hydrodynamic flow.

4.2 Methodology

4.2.1 Dam-break simulations

This section describes the setup and geometry of the numerical simulations for the dam-break flood investigations. The code employed here is the jointly developed FORTRAN code Anura3D [105]. It should be noted that the MPM model employed in these simulations is a three-dimensional model, but with a thickness such that only one layer of elements is employed to save computational cost since the width of the simulation geometry is not significant [169].

4.2.2 Simulation geometry

These simulations used the Anura3D double-point MPM code. The initial geometry for the solid wall verification case is shown in Figure 4.1. These numerical simulations are compared with published results to verify the ability of the MPM code to produce reliable results for this problem. The initial geometry for the investigation into the impact of dam-break floods on porous media is shown in Figure 4.1. In these simulations, the width of the dam-break flood column is fixed, so that the aspect ratio is governed by the height of the column. For the investigations, the height H is 0.2m so that $\alpha = \frac{0.2}{0.1} = 2$. The two variables, then, are the width of the permeable seawall w and mean grain size D_p. The width w is varied between 0.05, 0.07, 0.1, 0.12, 0.4 and 0.6m. The mean grain size D_p was varied between 0.0001m and 0.5m.

Table 4.1 Summary of parameters investigated in the dam-break simulations

Wall width w	Grain size D_p [mm]												
[m]	0.1	0.5	1	2	5	7	10	20	30	50	100	300	500
0.05	0.1	-	1	2	5	7	10	20	30	50	100	300	500
0.07	0.1	-	1	2	5	7	10	20	-	50	100	300	500
0.1	0.1	0.5	1	2	3	-	10	-	30	50	100	300	500
0.2	0.1	0.5	1	-	-	-	10	-	30	50	100	300	500
0.4	0.1	-	1	-	-	-	10	-	30	50	100	300	500
0.6	0.1	-	1	-	-	-	10	-	30	50	100	300	500

4.2.3 Simulation parameters

For all investigations, the liquid column has material parameters $\rho = 1000$, $K = 20000$, and $\mu = 1e^{-6}$, where ρ is the density $\left[\text{kg/m}^3\right]$, K is the bulk modulus [kPa], and μ is dynamic viscosity [kg/m·s]. The porous dam has material parameters $n = 0.49$, $\rho = 2650$, $k = 1.0214e^{-9}$, where n is the initial porosity [no units], ρ is the density as before, k is the intrinsic permeability

Millimeters (mm)	Micrometers (μm)	Phi (ϕ)	Wentworth size class	
4096		-12.0	Boulder	
256		-8.0	Cobble	Gravel
64		-6.0	Pebble	
4		-2.0	Granule	
2.00		-1.0	Very coarse sand	
1.00		0.0	Coarse sand	
1/2 0.50	500	1.0	Medium sand	Sand
1/4 0.25	250	2.0	Fine sand	
1/8 0.125	125	3.0	Very fine sand	
1/16 0.0625	63	4.0	Coarse silt	
1/32 0.031	31	5.0	Medium silt	
1/64 0.0156	15.6	6.0	Fine silt	Silt
1/128 0.0078	7.8	7.0	Very fine silt	
1/256 0.0039	3.9	8.0	Clay	Mud
0.00006	0.06	14.0		

Table 4.1 The Wentworth size chart, used to select values for grain size D_p [149]

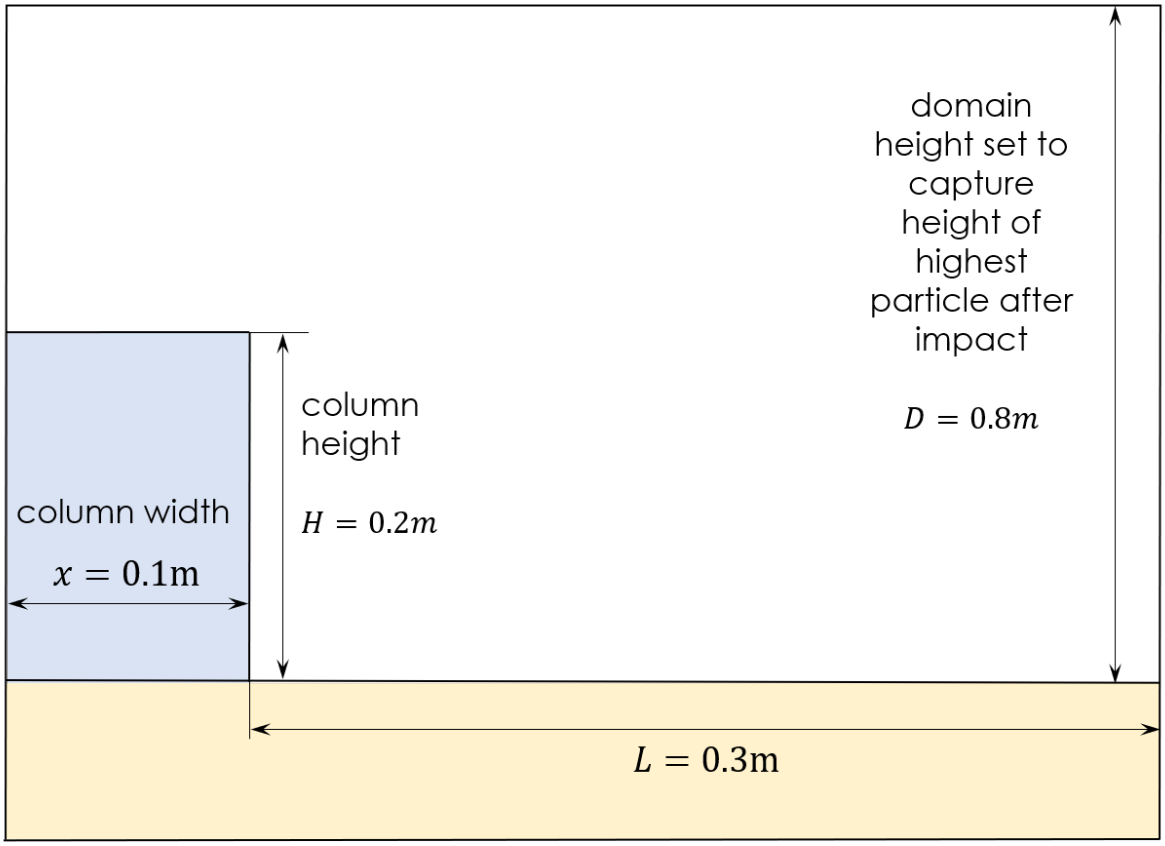

Fig. 4.1 The initial geometry used for verification of numerical simulations of dam-break floods, for the solid wall verification case

$[\mathrm{m}^2]$, and the material is modelled as a linear elastic material with $E = 10000$ and $\nu = 0.3$ where E is Young's modulus [no units] and ν is Poisson's ratio [kPa]. In order to enable the simulations to run with a relatively large timestep, the bulk modulus of water was assigned an unrealistically low value. It has been established that this increased compressibility of water does not cause any significant difference to the simulations as long as the modelled water has a sound speed over 10 times larger than the maximum flow velocity [90, 169].

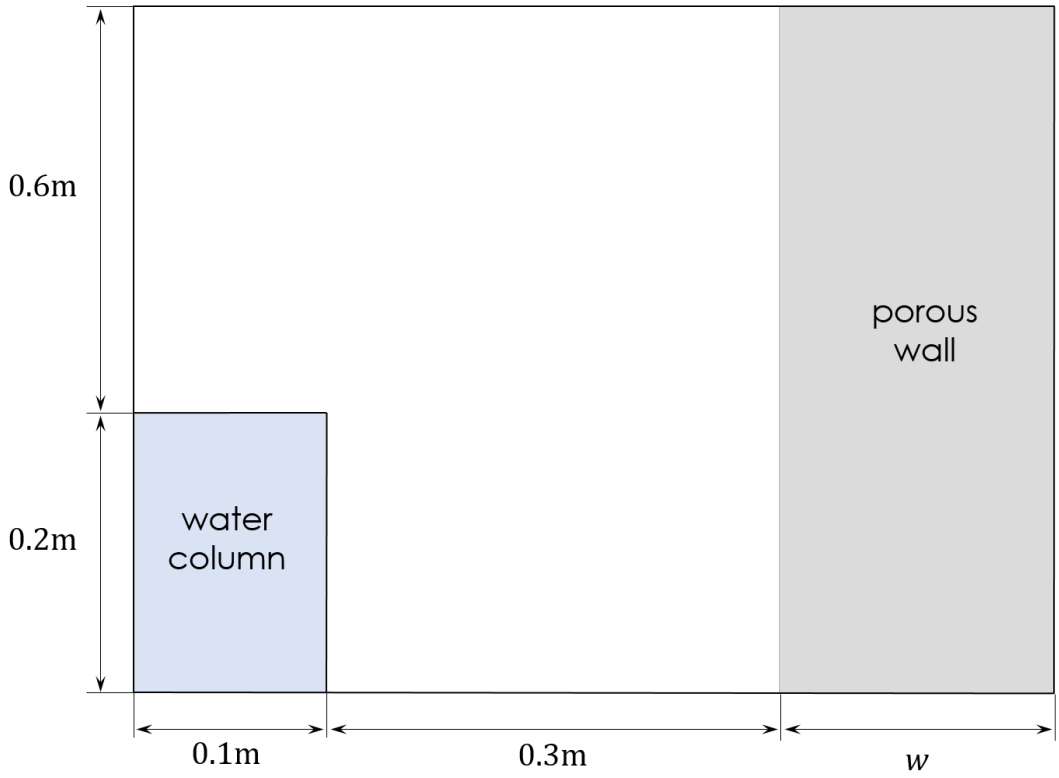

Fig. 4.2 The computational domain used for numerical simulations of dam-break floods. w is the width of the wall and is varied throughout the simulations. All dimensions are in metres.

The liquid column has 20 fluid material points specified per element, and the soil column has 4 solid material points specified per element. Since the grid spacing is specified as 0.01m, 24,000 fluid material points are initiated for each simulation. A two-phase double-point simulation type is used, with a Courant number of 0.8 to ensure stability. No smoothing is used and no damping is applied, which is recommended for the double-point code. For each case, the maximum allowable porosity is 0.7. This parameter distinguishes between the solid states and liquid states in the double-point MPM code. It must be at least larger than the initial porosity of the soil. Otherwise, the soil is liquefied when the simulation begins. This is explained in detail in Chapter 3.1, with reference particularly to Figure 3.7. The porosity of the dam is not varied

in these simulations, only the grain size is altered to modify the permeability of the material. These parameters are summarised in Table 4.2.

Table 4.2 The calculation and material parameters used in the dam-break simulations

	Parameter	*Value*	*Unit*
Mesh properties	Mesh size	0.01	m
	Number of elements	$3,200 - 8,000$	-
	MPs per element	20 fluid or 4 solid	-
Fluid properties	Density	1000	kg/m^3
	Bulk modulus	20,000	kPa
	Dynamic viscosity	$1e^{-6}$	kPa $\cdot$ s

4.2.4 Analysis of results

Centre of mass method

A significant challenge presented by this series of simulations lay in determining the most effective parameter or method by which to compare the maximum run-up height reached by the flood. We are interested in the maximum run-up height reached by the wave generated when the water column collapses so that we can identify the best possible mitigation method. However, due to the particle scattering that occurs in the MPM simulation, identifying which particle best represents the run-up height proves challenging. An example of this is shown in Figure 4.3. We could select the highest point reached by any particle (highlighted in green), but for situations where the particles are artificially scattered, this is not a good representation of the run-up height. Furthermore, for cases with a narrow porous block, some particles are observed to travel through the porous dam, reaching the solid boundary at the end of the domain, where they are reflected, travelling back through the porous dam to reach significant heights, and therefore artificially increasing the perceived run-up height. This phenomenon can be observed when watching the simulation progress over time, but even under close observation, there is a lack of certainty as to which particles this situation applies to. Any results identified using this method would be very dependent on the judgement of the researcher and would, therefore, prove challenging to defend. We could also attempt to identify the *"highest point reached by a particle in contact with the wall"* (highlighted in red), or the *"highest point reached by particles that are part of a continuous plume"* (highlighted in orange), however, both methods lack precision and are heavily subjective, requiring decisions to be made by the interpreter. This method of selecting a particle and thereby identifying the maximum run-up height was therefore deemed inadequate.

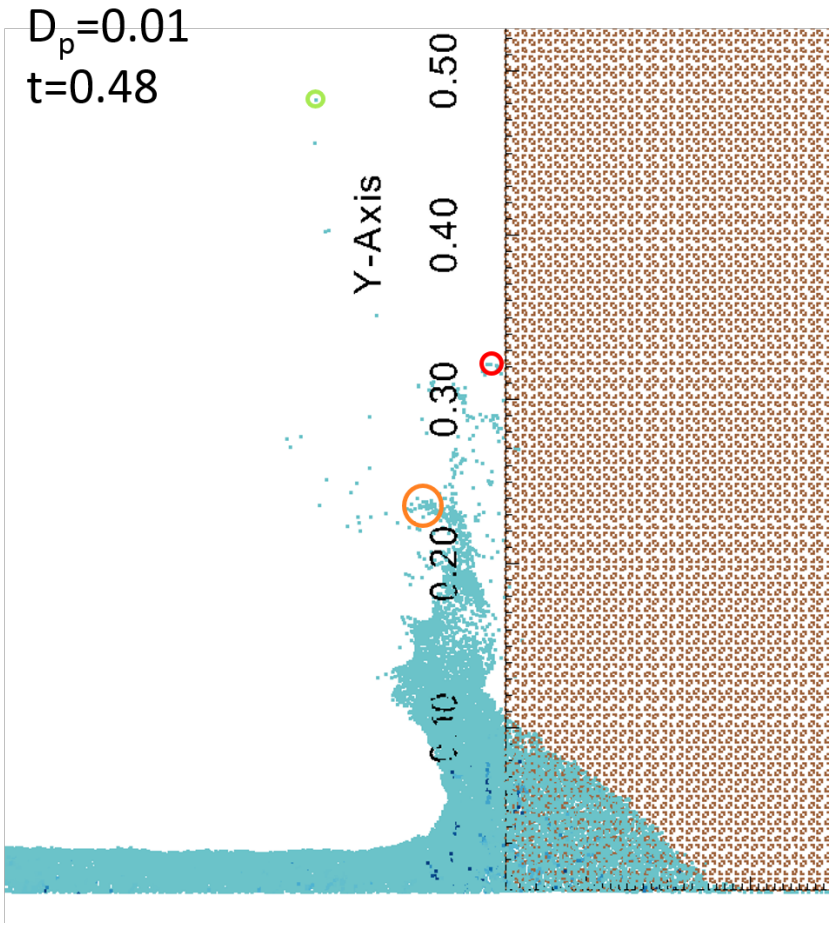

Fig. 4.3 Identifying which particle represents the run-up height of the dam-break wave is challenging. In this example, the wall width is $w = 0.2$m

To overcome this problem, we can instead take an average of the y-coordinates of the particles to find the *centre of mass* of the particles, and select the highest value of the centre of mass at any time step to compare across the simulations. This method is much more objective, and, since there are 24,000 particles in each simulation, any anomaly from a few scattered particles is naturally smoothed out. Averaging the centres of mass of the particles quickly proved to produce much more consistent results. We would intuitively expect that more porous walls would results in a lower run-up height, since more fluid can invade the porous dam, and a greater amount of energy is absorbed. However, using this method, for the more porous walls ($D_p > 0.05$) the centre of mass was observed to increase as the average grain size increased. Figure 4.4 shows an example where this is the case. When the plume is inspected, however, we can see that the run-up height is not increasing, so there is an issue, at least in part, with this

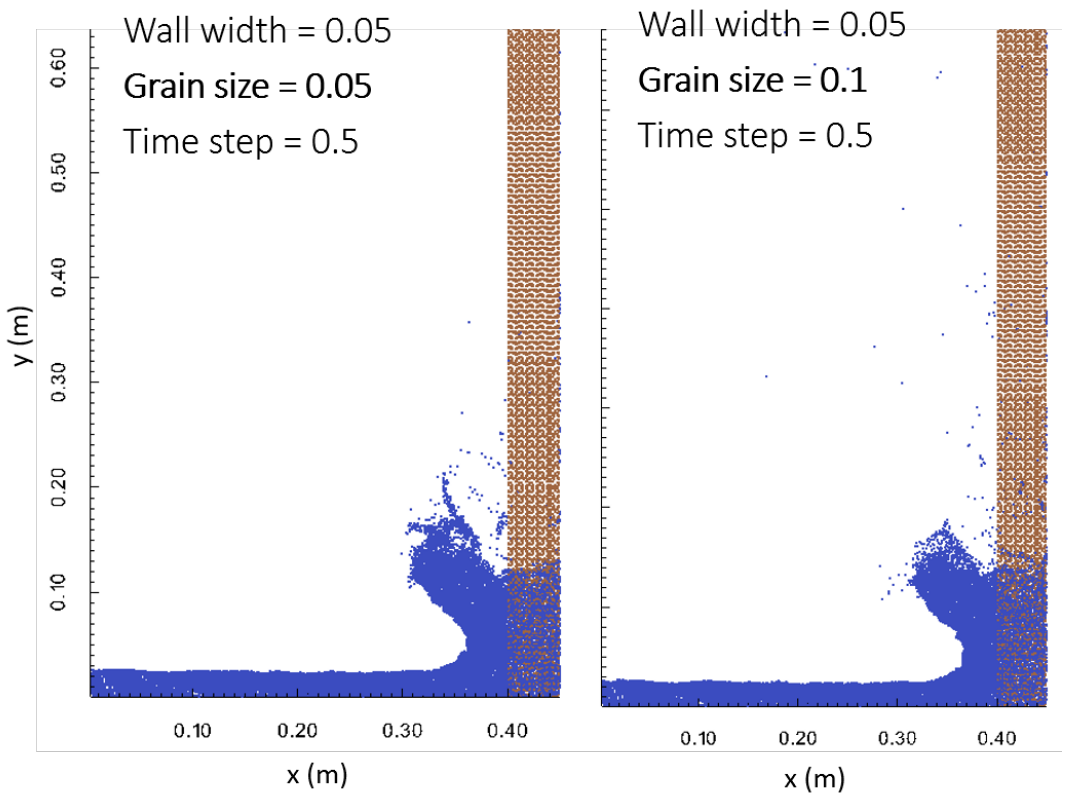

Fig. 4.4 The large number of particles not involved in the run-up height can affect the overall centre of mass, masking small changes. In this example, the wall width $w = 0.05$m.

method of identifying the run-up height. Consequently, further refinement of the method used to analyse the results is required.

One issue with averaging the y-coordinates across all of the particles is that the large number of particles that are not involved in the run-up process may skew the result. To avoid this, we can remove particles that are outside a fixed margin, as shown in Figure 4.5. Figures 4.7 and 4.8 show the two trial margins tested in two different instances. The third trial margin of width 0.02m was rejected since it is demonstrably unsuitable: by making the margin so close to the porous dam, many particles that contribute to the run-up height would not be included in the centre of mass calculations. The two margins of 0.05m and 0.1m were trialled across all of the simulation results, to determine which filter was the most suitable. It can be seen in both Figure 4.7 and Figure 4.8 that the narrower, 0.05m margin will remove a few particles that are of interest, however, the 0.1m margin removes fewer of the particles that are not of interest.

Figure 4.9 compares the two margins for the case where the wall width $w = 0.05$m, for two extremes of grain size ($D_p = 0.0001$m and 0.5m). As explained above, we would expect that when we increase the grain size, and therefore the permeability, of the porous wall, the

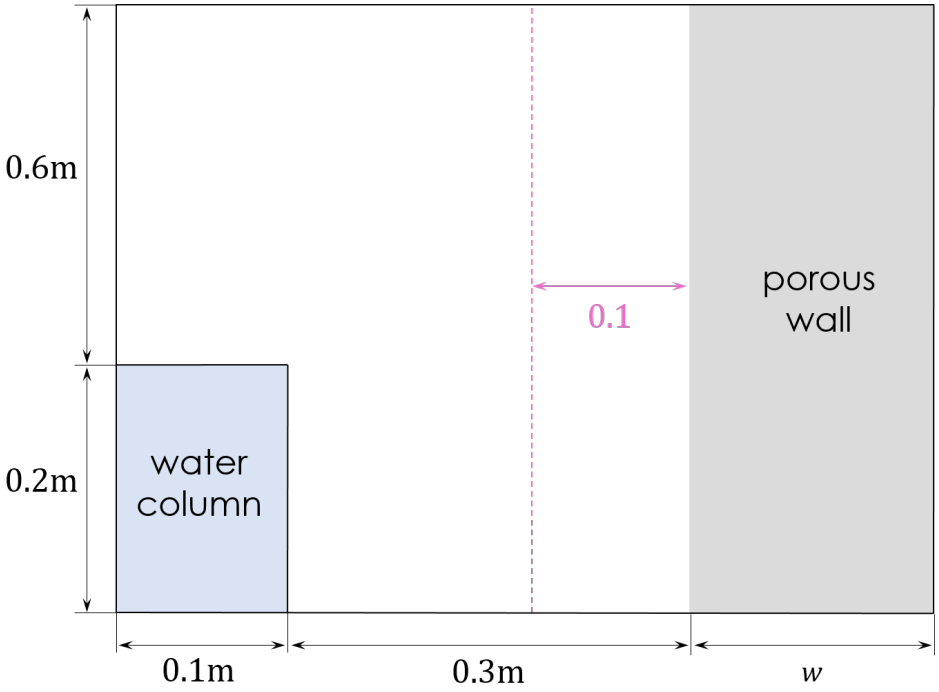

Fig. 4.5 A margin of 0.1m trialled to filter particles that did not contribute to the run-up height

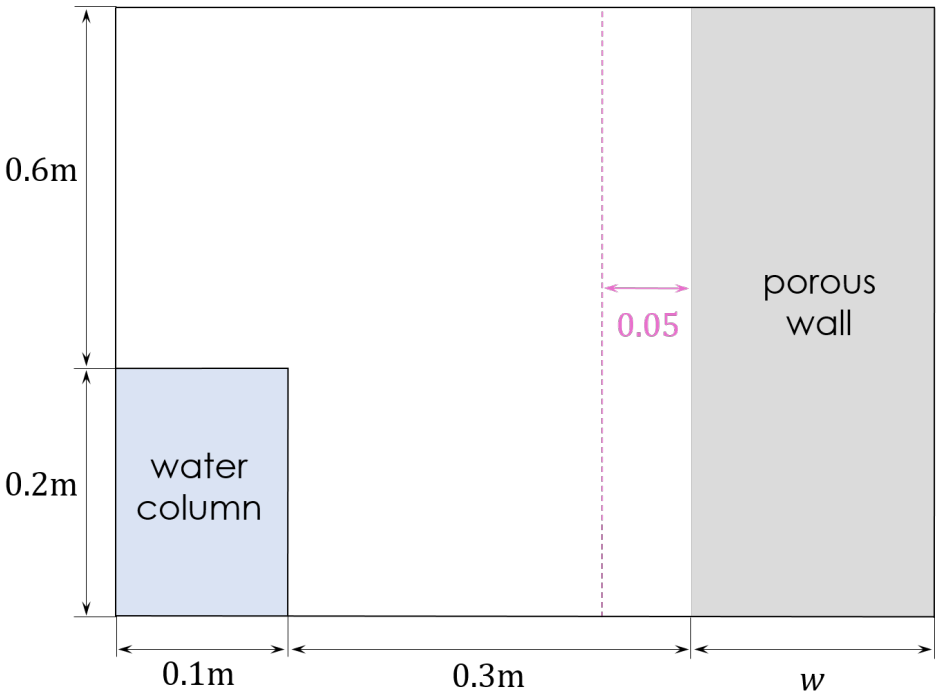

Fig. 4.6 A margin of 0.05m trialled to filter particles that did not contribute to the run-up height

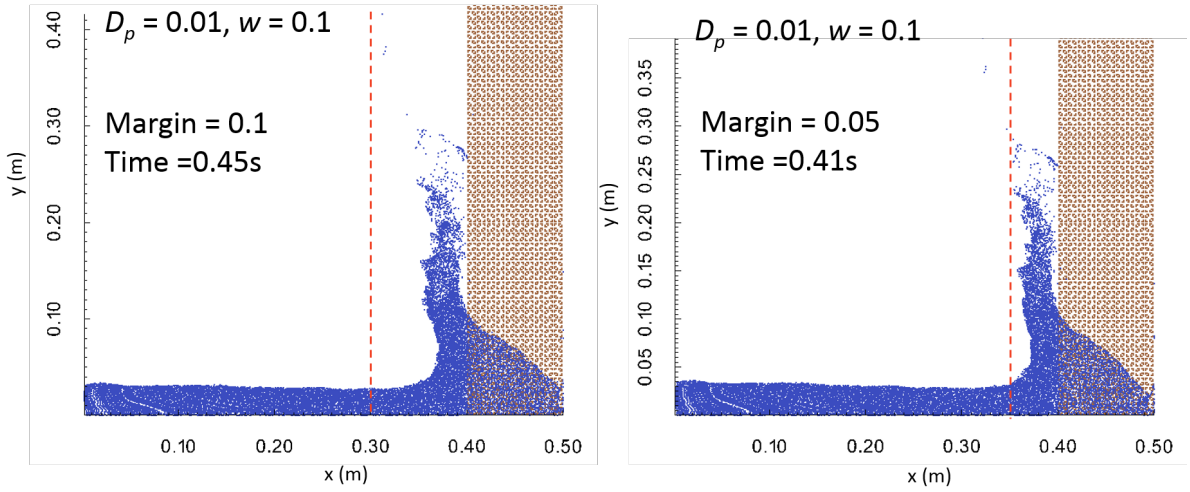

Fig. 4.7 A demonstration of the two different margins, shown for the case where D_p = 0.01m and w = 0.1m.

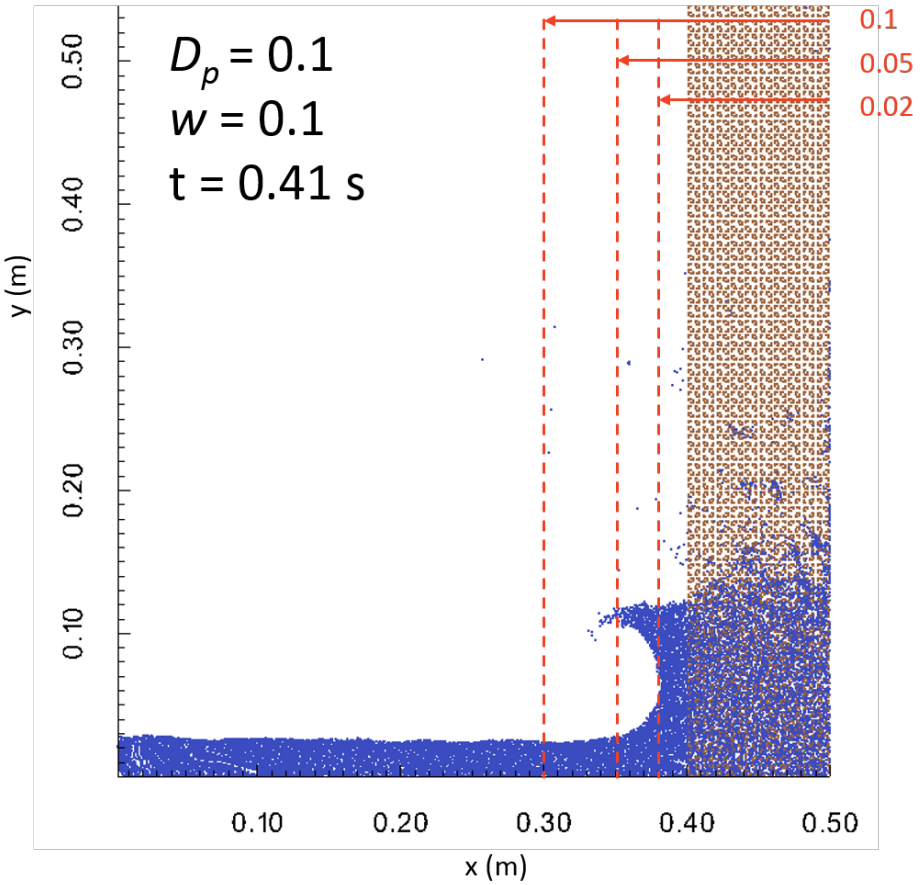

Fig. 4.8 A demonstration of three different trial margins for the case where D_p = 0.1m and w = 0.1m. The margin of width 0.02m was rejected since it was unsuitable.

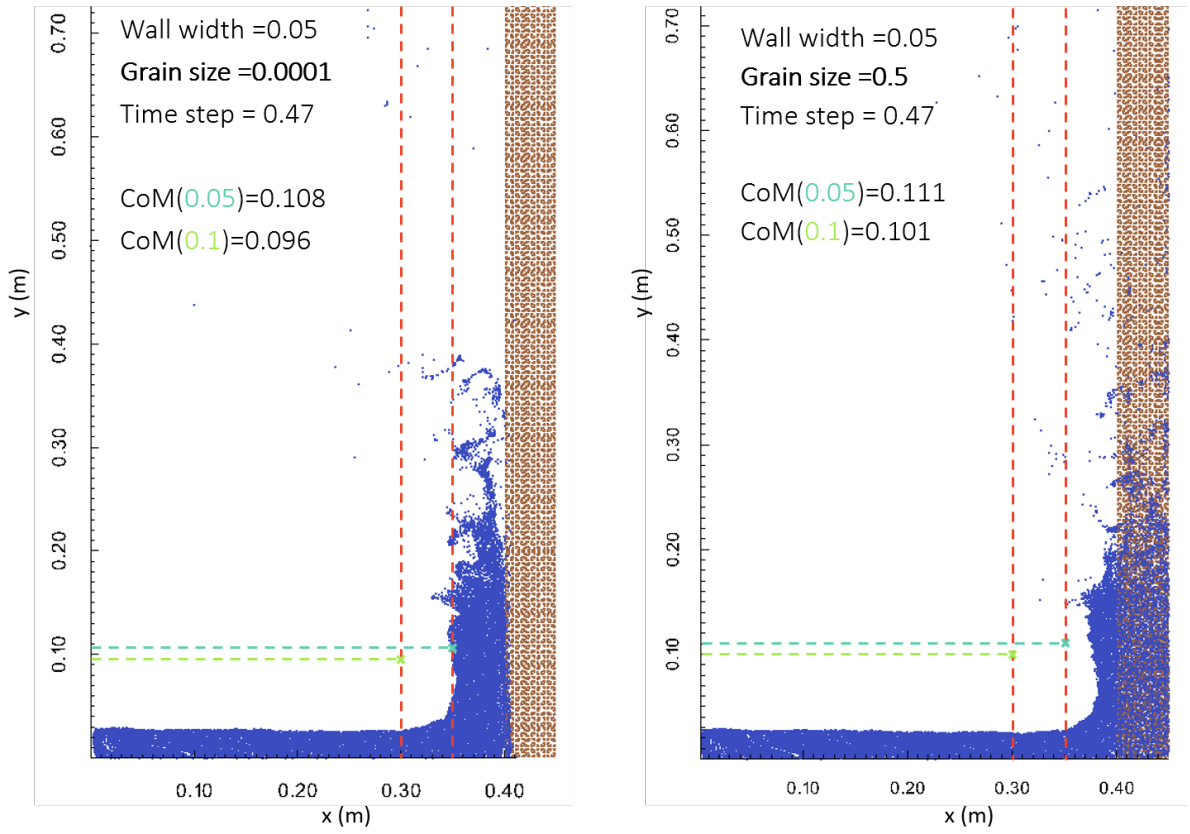

Fig. 4.9 Comparing the two margins for two cases, where $w = 0.05$ and D_p is 0.0001 and 0.5, respectively. The resulting centre of mass for each case is shown by the dashed line.

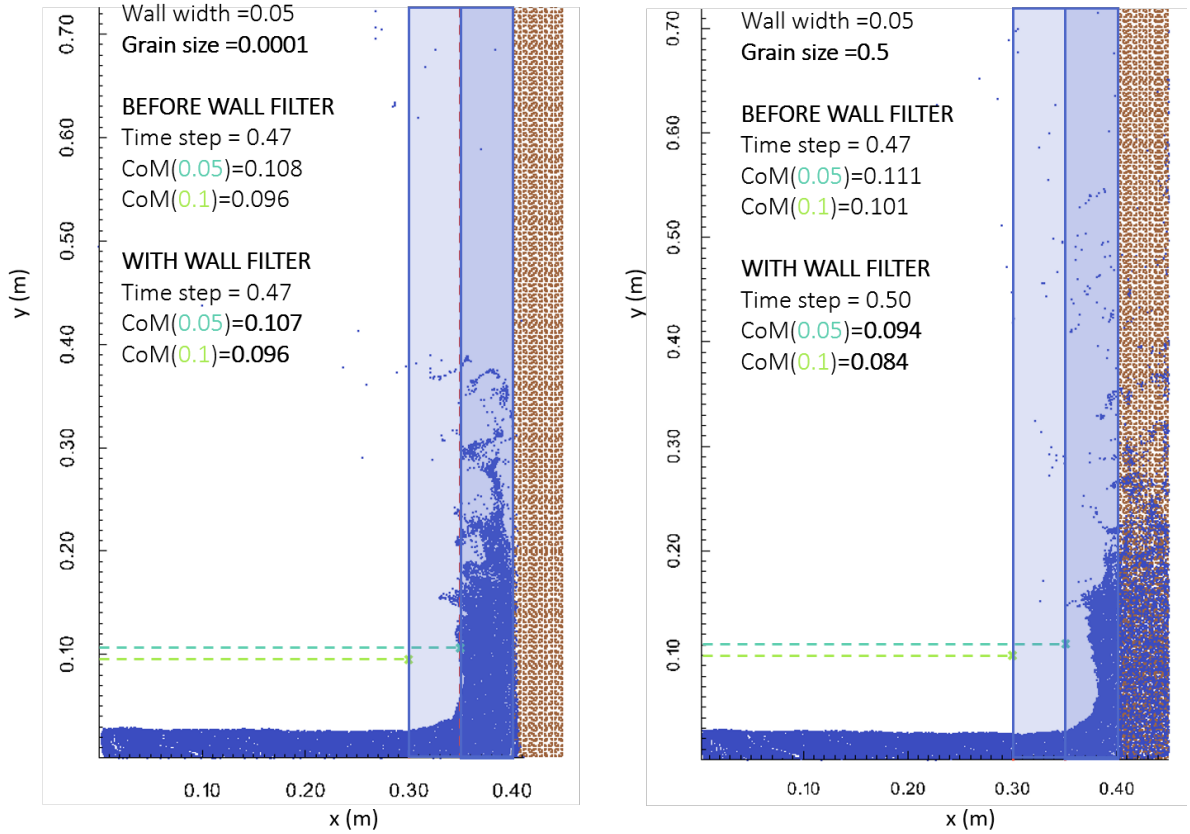

Fig. 4.10 Filtering out particles that have penetrated the porous dam for the case where w = 0.05m and D_p is 0.0001 and 0.5m, respectively. The centre of mass produced for each case is shown by the dashed line.

run-up height will decrease. Despite some particle scattering, we can see by inspection that this is indeed the case; the larger mean grain size allows more water to flow into the wall and reduces the run-up height reached by the plume. However, the centre of mass increases, even with the margins in place. Two effects are responsible for this increase in the centre of mass: firstly, the particles that have penetrated the porous dam contribute additional height to the mean, and secondly, there is an increased level of particle scattering in the more porous case. Whilst identifying and subsequently removing scattered particles is challenging, we can easily remove the particles that have penetrated the dam. This is deemed an appropriate course of action here since the investigation seeks to find the external run-up height reached by the wave.

Finally, we arrive at the version of this method used to identify the run-up height reached by the dam-break flood in this series of simulations. Figure 4.10 shows the effect of using this filter on the cases that have been previously discussed. The centre of mass for the more porous case is lower, which is a more accurate reflection of the run-up height. A comparison

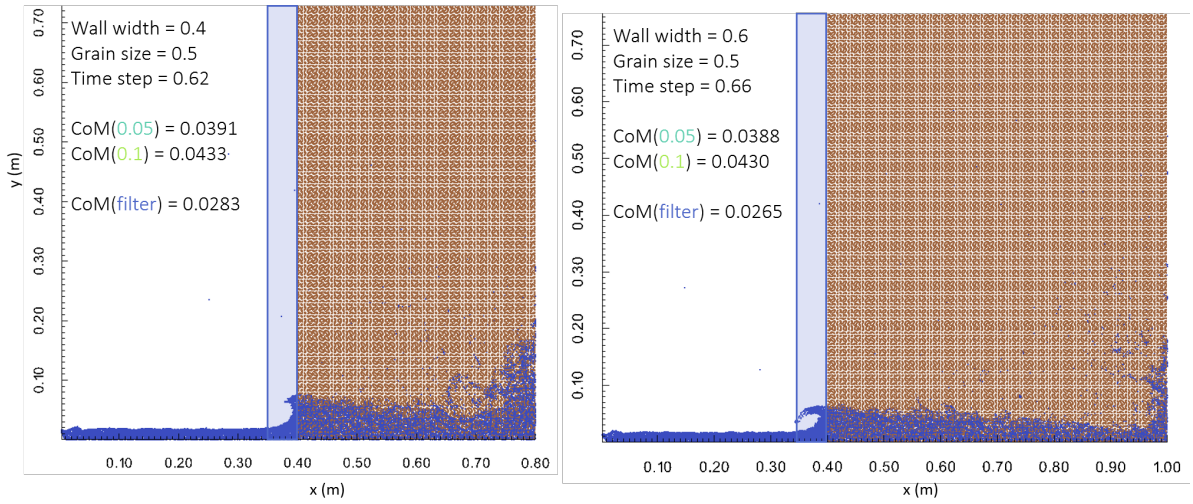

Fig. 4.11 Comparing results using a margin of 0.05m and filtering out particles that have penetrated the dam for the case where D_p is 0.5m and the wall widths w are 0.4 and 0.6m, respectively.

is also shown for the case where the grain size D_p is 0.5m and the wall widths are 0.4m and 0.6m respectively. It is clear that using the margin of 0.05m and filtering out particles that have penetrated the wall gives the best result for comparison of the run-up height across the simulations.

Statistical method

A further method of analysis was trialled, using a statistical approach whereby the 95th and 98th percentiles of the height reached by any of the particles is found and plotted. The overall aim of these techniques is to determine a reliable and objective method of recording the run-up height reached by the wave by establishing a rigorous method of eliminating the scattered particles. The results of the previously detailed method and the method described here are presented and analysed in Section 4.4.

4.3 Model Validation

4.3.1 Solid wall simulations for dam-break floods

The initial validity of the MPM results for dam-break flows was established by direct comparison with results produced using SPH published in Dongfang Liang's 2009 paper *"Evaluating shallow water assumptions in dam-break flows"* [88], and with published results in Dongfang

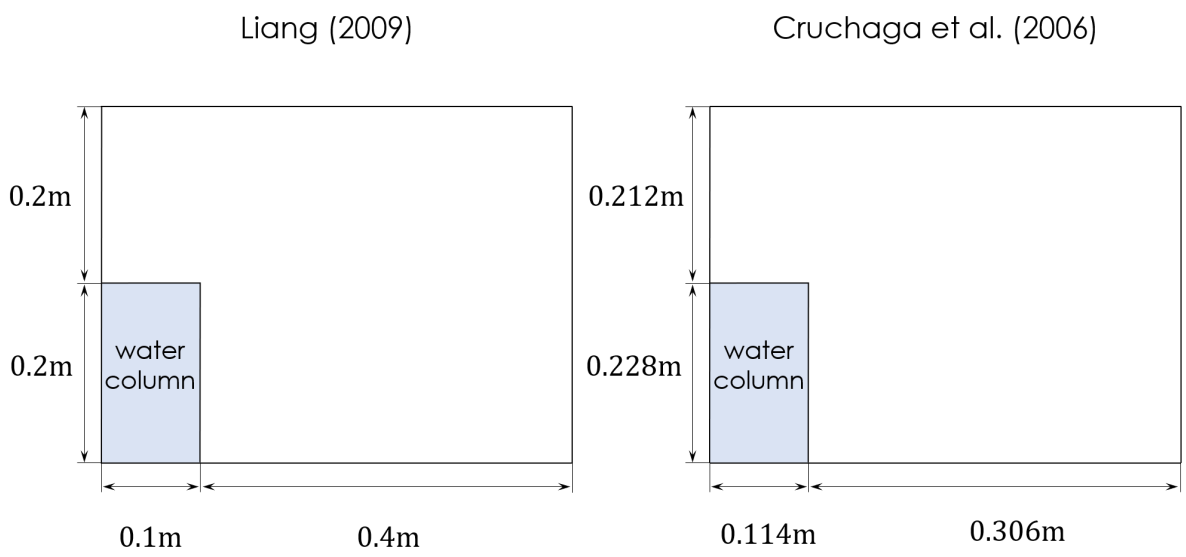

Fig. 4.12 Initial geometries of solid wall verification simulations replicating Liang (2009) [88] and Cruchaga et al. (2006) [33]

Liang and Xuanyu Zhao's 2017 paper *"Numerical simulations of dam-break floods with MPM"* [89].

The results produced are also compared to numerical and experimental results published in Cruchaga, Celentano and Tezduyar's 2006 paper *"Collapse of a liquid column: numerical simulation and experimental validation"* [33], experimental results published in Martin and Moyce (1952) *"An experimental study of the collapse of liquid columns on a rigid horizontal plane"* [104] and numerical results published in Koshizuka and Oka (1996) *"Moving-Particle Semi-Implicit Method for Fragmentation of Incompressible Fluid"* [75].

These simulations use a solid end boundary and form the basis of the simulations in section 4.3.2, on porous wall simulations. Figure 4.12 shows the initial geometry used for these validation simulations, based on the geometries used in Liang (2009) [88] and in Cruchaga et al. (2006) [33].

Figure 4.13 shows a comparison of particle distribution at different time intervals for these simulations (right-hand side) with those published by Liang (left-hand side). In both the SPH and MPM simulations, the initial pressure distribution is hydrostatic: the pressure contours are plotted for the MPM results in the first instance and the hydrostatic pressure distribution is demonstrated by the horizontal pressure contours that run parallel to the free-surface. Figures 4.13(b)-(e) show the evolution of the flood front as it propagates down the tank. The shape of the flood front produced by the MPM results is in very good agreement with those produced using the SPH model. Once the flood hits the end of the tank, it rapidly climbs the wall, reaching much higher than the initial height of the column, shown in Figure 4.13(f), as

the kinetic energy of the front is transformed into potential energy. Again, both the MPM and SPH models are in good agreement with the mechanism by which the flood evolves, however, the lack of smoothing in the MPM simulations means that particle scattering can be observed. The next phase is for the run-up water to collapse down and curl back on itself, shown in Figure 4.18(g), and finally, this body of water plunges into the wave generated by the initial column collapse, that is still moving towards the end of the tank, forming a cavity and forceful splashing, resulting in turbulent motion. Both models show the same progression, although once again particle scattering is evident in the MPM simulations. Overall, good agreement is shown with the particles following the same distribution, however, the MPM results exhibit significantly more particle scattering after the impact with the solid wall. The pressure contours are much smoother in the SPH simulation, whereas in the MPM simulations the pressure fluctuations are too high to be useful. However, when we compare the shape of the plume and the run-up height, the SPH and MPM methods show good agreement. As noted by Liang, due to the absence of the vertical acceleration, the SWEs solver cannot account for the time required to transform the kinetic energy of the wave into potential energy, for which the vertical movement is essential [88]. Consequently, the SWEs solver unsurprisingly gives very different results to the other two models, especially after the impact with the solid wall.

Figure 4.14 shows a quantitative comparison of the propagation speed of the flood front over time with results published by various research groups using both experimental and numerical methods. These results are normalised according to the Froude scaling law to allow for comparison with results from different geometries so that

$$t^* = \frac{t}{\sqrt{\frac{H_1}{g}}}, \quad x^* = \frac{x}{H_1} \tag{4.4}$$

where H_1 is the initial height of the water column. Since the SWEs results have been demonstrated to be unrealistic, these are not plotted here. As noted by Liang, the SPH results depend slightly on the kernel smoothing length, with a smaller smoothing length producing a higher speed [88]. The MPM results show the same trend with a slightly higher speed, this may be explained by a small amount of particle scattering at the leading edge making it challenging to identify the precise location of the flood front. Generally, the numerical simulations are in very good agreement with experimental results, and with results produced using other numerical methods.

Figures 4.15 and 4.16 show a comparison for the time history of the flood front and column height respectively for the MPM simulations using the geometry after the experiments published in Cruchaga et al. [33], shown in figure 4.12. Koshizuka and Oka use an aspect ratio $\alpha = 2$ and a tank length four times the width of the column for a total of 14.6cm [75]. Again, the

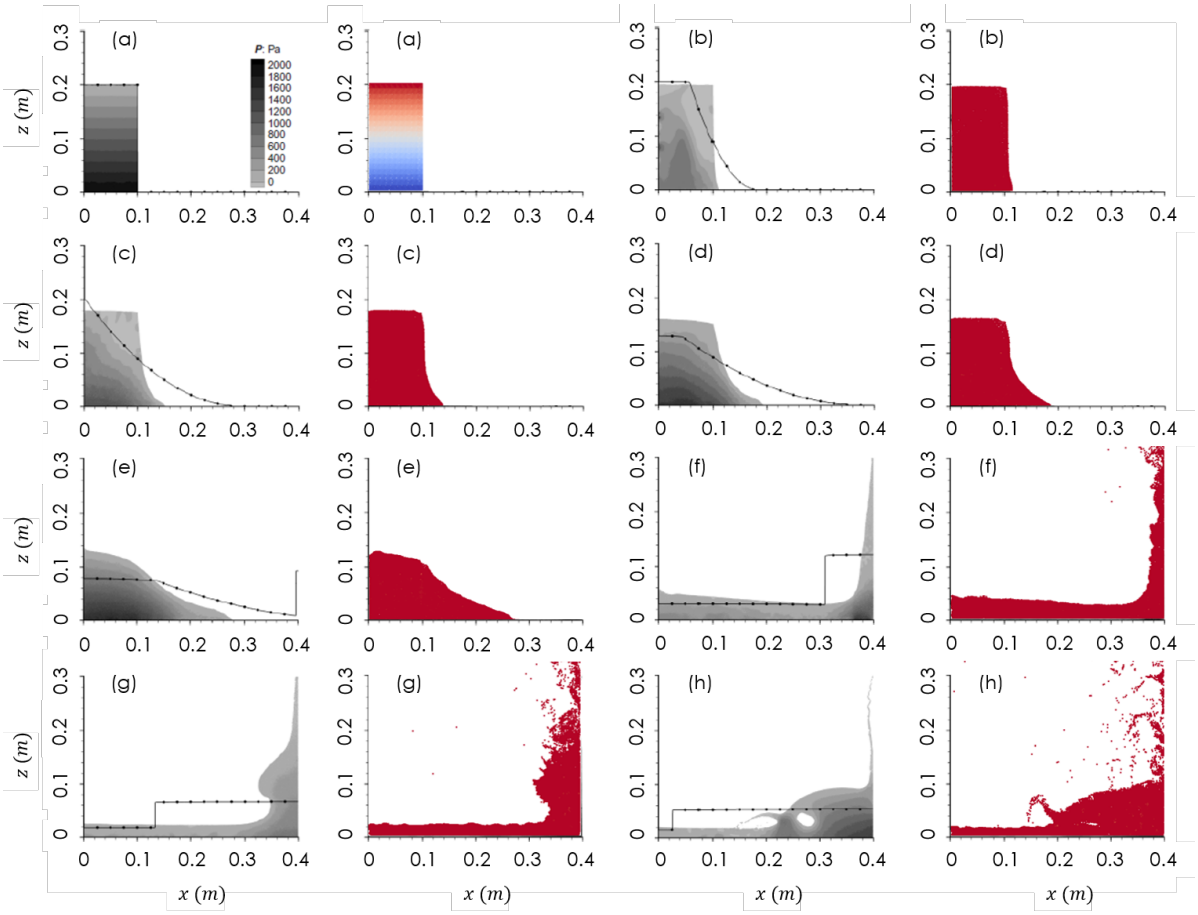

Fig. 4.13 Direct comparison of results produced using MPM with the extensively verified SPH results produced by Liang (2009) [88]. In the left column, solid lines with circles represent the shallow water equations (SWEs) results and the contours represent SPH results. The MPM results are plotted in the right columns: (a) t = 0s; (b) t = 0.03s; (c) t = 0.07s; (d) t = 0.10s; (e) t = 0.15s; (f) t = 0.35s; (g) t = 0.55s; (h) t = 0.66s

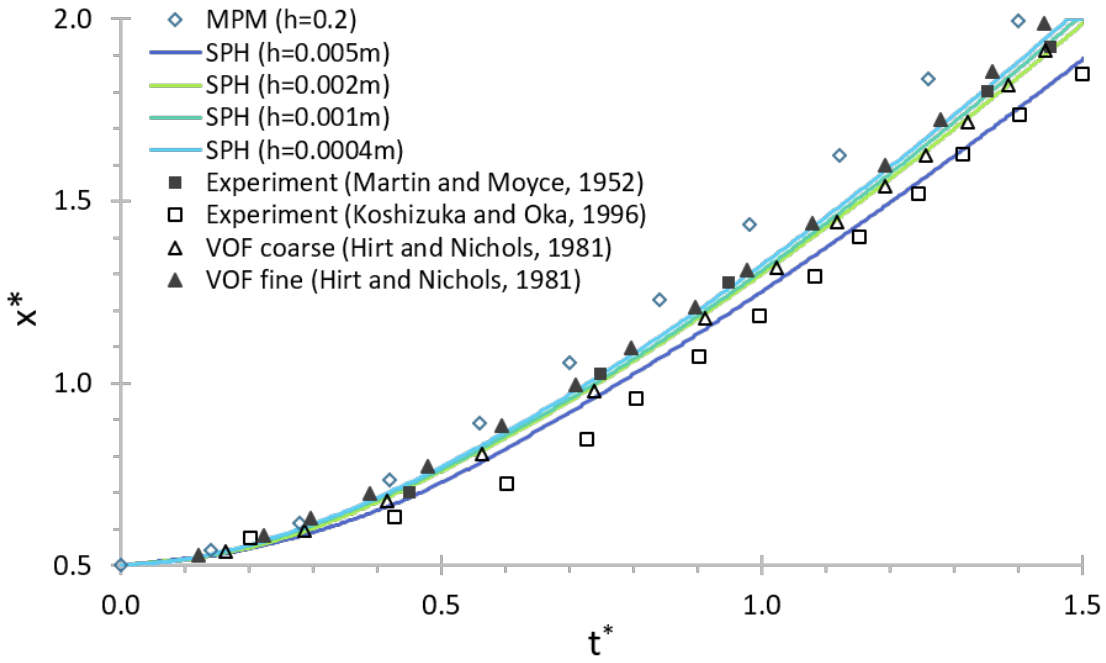

Fig. 4.14 Comparison of results from simulations using the geometry from Liang (2009) to published experiments, plotting the evolution of the position of the front over time

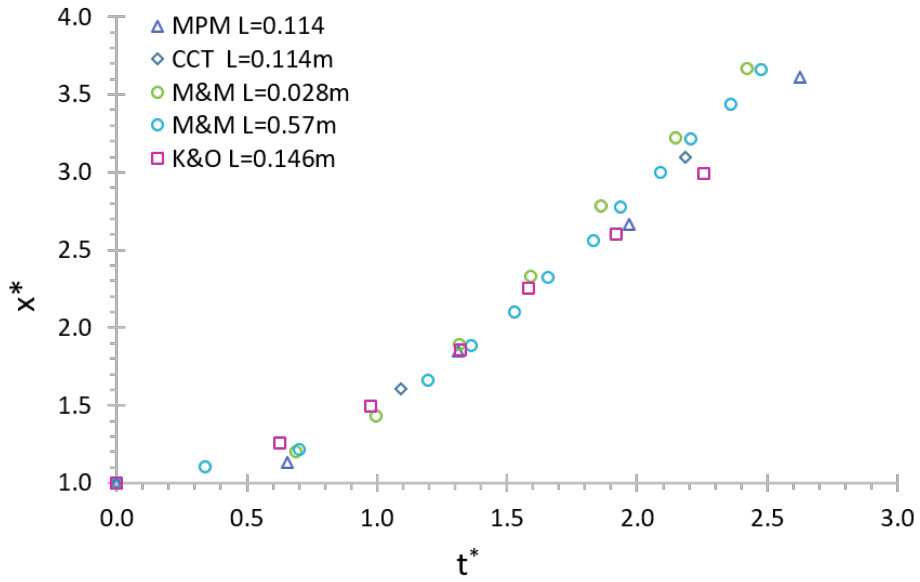

Fig. 4.15 Comparison of results from simulations using the geometry from Cruchaga et al. (2006) to published experiments, plotting the evolution of the position of the front over time

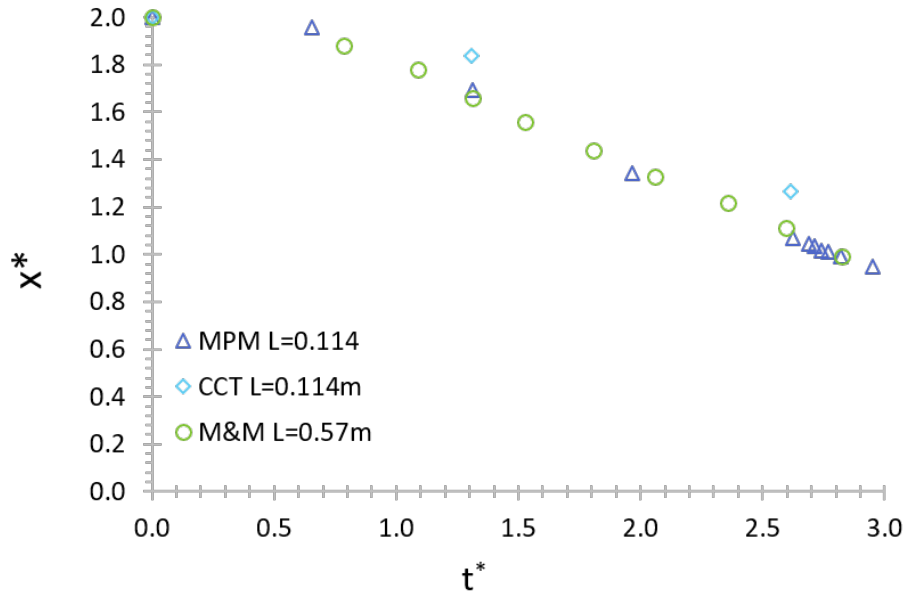

Fig. 4.16 Comparison of results from simulations using the geometry from Cruchaga et al. (2006) to published experiments, plotting the evolution of the height of the column over time

results have all been normalised according to the Froude scaling law to allow for precise comparison. The MPM results are a very close match for the numerical results published by Koshizuka and Oka (1996) [75], although the experimental results published by Martin and Moyce (1952) [104] and the experimental results published by Cruchaga et al. (2006) [33] show a slightly higher frontal propagation speed. The numerical results published by Cruchaga et al. (2006) show a noticeably initial slower propagation speed than those produced by their experiments [33]. They suggest that this occurs at least in part due to the gate opening effect; whereby the physical gate present in the experiments takes a finite amount of time to rise, affecting the initial progress of the column collapse when compared to the instantaneous gate opening of the numerical simulations. When a gate-opening parameter was included in their simulations, more advanced flood positions at early instants of the analysis are obtained at the bottom of the tank, due to the "orifice effect" induced at the beginning of the gate opening, which increases the fluid velocity at the bottom of the tank [33]. This situation quickly changes as the dam-break wave propagates and frictional effects slow the overall propagation, causing the wave to reach the end of the tank later than if no gate-opening effect is included. This would suggest that the slightly higher speed reached by the experimental results compared with the numerical results is an effect of the gate-opening in an experiment being non-instantaneous.

Investigating the evolution of the height of the water column (Figure 4.16) shows a very close match between the MPM simulations and the experimental results published in Martin and Moyce (1952), suggesting that whilst the gate opening being non-instantaneous may affect the bottom of the water column as the flow develops, there is little effect on the top of the column.

4.3.2 Parametric study of mean grain size effect on run-up height

The solid wall simulations capturing dam-break flow formed the basis for a parametric study numerically investigating the effect of changing the permeability of the porous material on the fluid-structure interaction between dam-break flood waves and a permeable flood barrier. The ability of the MPM code to produce reliable results for wave impact on porous media is validated by extensive comparison of simulation results with numerical and experimental results published in Liu et al.'s 1999 paper *"Numerical Modeling of Wave Interaction with Porous Structures"* [94], and in Ren et al. (2016) *"Improved SPH simulation of wave motions and turbulent flows through porous media"* [126].

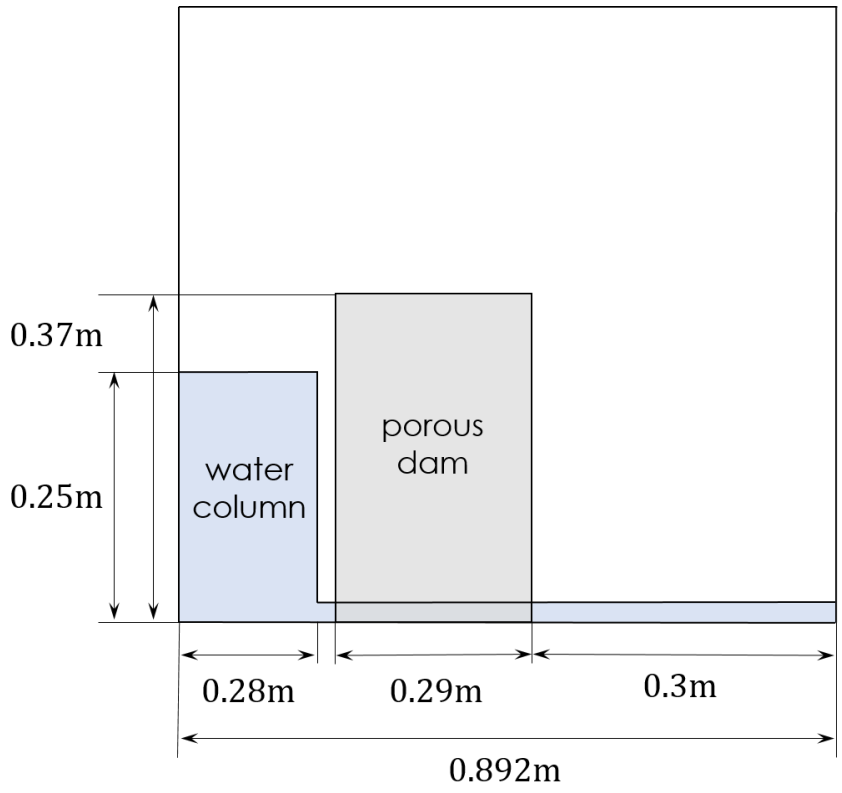

Fig. 4.17 Initial geometry of model validation simulations for wave impact on porous media, after Liu (1999) [94]. All dimensions are in metres.

The geometry of the numerical simulations used for this verification study, based on the geometry employed by Liu (1999) [94], is shown in Figure 4.17. The experiments conducted by Liu et al. (1999) used a water tank of 0.892m × 0.44m × 0.58m. A porous structure of 0.29m × 0.44m × 0.37m was built with crushed rocks ($d_{50} = 1.59$ cm, $n = 0.49$) was placed at the centre of the tank, from x = 0.3–0.59m. A gate was constructed 2cm (including the gate thickness and gap) away from the porous structure and pulled up manually within 0.1s at the beginning of the test. The initial water level d was 0.25m. The numerical set-up is the same as the experimental set-up except that there is a gap of 2cm between the water column and the near side of the porous dam, and no gate.

The permeability of the porous block based on the grain size of the material is described by the Kozeny-Carman equation:

$$\kappa = \frac{D_p^2}{A} \frac{n^3}{(1-n)^2} \tag{4.5}$$

where κ is the permeability [m^2], D_p is the effective grain size diameter [m], n is the soil porosity [no units], and A is a constant, equal to 150 (Ergun, 1952) [40]. In these simulations, the soil porosity is fixed so that the permeability is varied only by altering the grain size.

In the double-point MPM code, the permeability of the soil body is directly related to the interaction force vector between the liquid and the soil particles, resulting from the drag force exerted on the solid particles by the fluid, originating from the relationship equation developed by Ergun ([40]), and characterised by the Kozeny-Carman equation, as above. The initial geometry and permeability parameters (grain size and porosity) are the same as those of the experimental results published by Liu (1999):

$$\kappa = \frac{0.0159^2}{150} \frac{0.49^3}{(1-0.49)^2} = 7.623 \times 10^{-7} \text{m}^2 \tag{4.6}$$

where the mean grain size diameter is 0.0159m and the initial porosity, n, is 0.49, resulting in a permeability of 7.623×10^{-7}m^2.

Figure 4.18 shows a comparison of the results obtained using MPM for the time history of the free-surface displacement at $x = 0.445$m (i.e. in the centre of the porous block, as indicated in Figure 4.17) to the experimental data published in Liu et al., 1999 [94], the VOF method results also published in Liu et al., 1999 [94] as well as the ISPH method results published in Akbari and Namin, 2013 [2] and the SPH model results published in Ren et al., 2016 [126].

Liu et al. (1999) considered that the flow in the porous structure was free of turbulence if the permeability of the porous medium was very small. The turbulence effect was only found to be significant if the pore size was comparatively large (Hsu et al., 2002 [55]). Shao (2010) [131] and Akbari and Namin (2013) [2] both identified that the turbulence might be

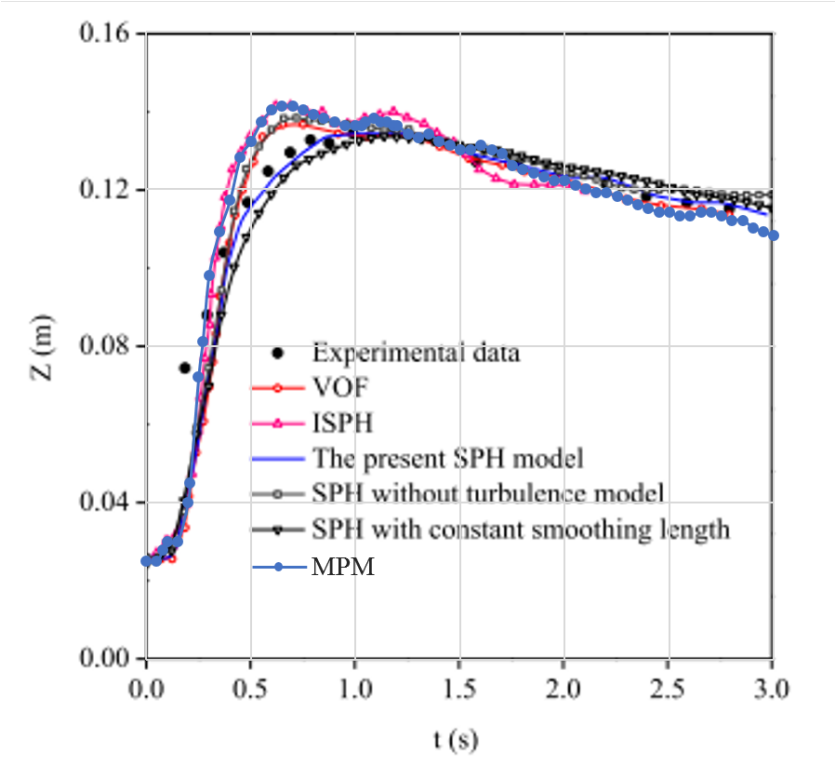

Fig. 4.18 Comparison of the MPM results for time history of free-surface displacement at $x = 0.445$m with various published data [126]

significant in the wave breaking zone, to simplify matching conditions with the porous flow region and the flow external to the porous structure, the turbulence effect was not incorporated in their ISPH models even in the flow outside the porous medium. Ren et al. (2014) [126] included a sub-particle-scale turbulence closure model in their WCSPH model in the external flow, but not in the flow inside the porous structures. Consequently, a large jump in the level of turbulence at the interface was observed. In their 2016 study, an improved WCSPH model was developed to investigate the wave motions and turbulent flow both in and around the porous structure. These results are also plotted in Figure 4.18. The results obtained using MPM are in very close agreement with published results, particularly the VOF (volume of fluid) results obtained by Liu in 1999 and the SPH results without the turbulence model that were published in Ren et al., 2016. The SPH results with the inclusion of the SPS turbulence model show the closest match for the experimental results, except for a slight under-prediction at the early stages. The MPM results closely resemble the other numerical results with no turbulence model, i.e. Liu (1999)'s use of the VOF method and Akbari and Namin (2013)'s ISPH results and Ren et al.'s "SPH without turbulence model" simulations. These all slightly

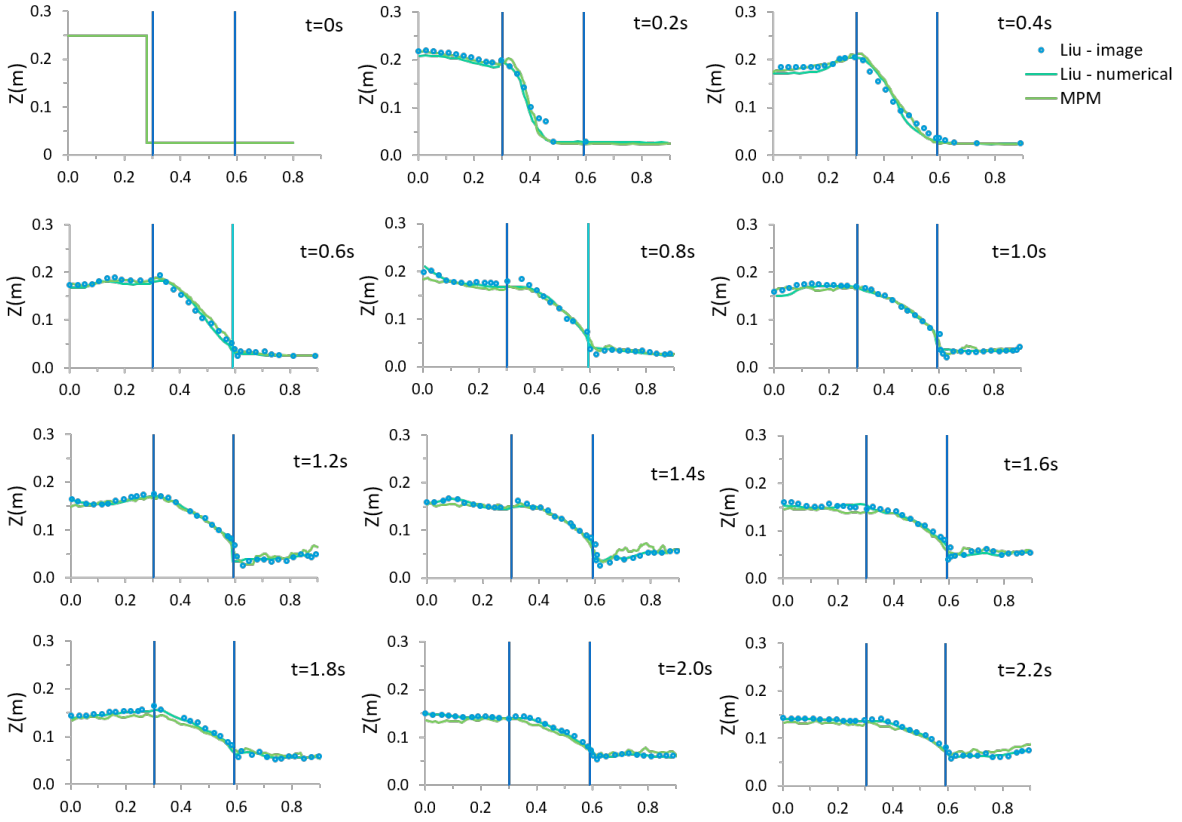

Fig. 4.19 Time history of free-surface profiles compared with experimental and numerical results published in Liu (1999) [94]

overestimate the free-surface displacement between 0.4s < t < 0.8s. This discrepancy arises since significant turbulence is generated in the porous flow zone as the particles initially rush rapidly into the dam, and this turbulence is not accounted for in the model. This overestimation of the free-surface displacement becomes much less significant later in the simulations; the much broader gap between the water column edge and the leading edge of the dam gives the flow more time to develop. The MPM simulations produce a better match to the experimental simulations after this initial peak, whereas in the period t > 1.5s, the SPH models with and without turbulent effects overestimate the displacement. Since this investigation is focused on the maximum run-up height, the initial peak is not crucial and we can consider the method robust without additional turbulence models.

Figure 4.19 shows time-history comparisons of free-surface profiles for the flow passing through the porous dam at different points in time for a direct comparison with the numerical and experimental results published in Liu (1999). After the gate is opened, or the simulation is started, the water column immediately begins to collapse and fluid particles rush towards the porous dam. After $t = 0.2$s, fluid particles have filled the gap between the initial water column and the porous dam, and a dam-break flow begins to develop. Since the porous dam offers some resistance to the flow, the particles stack up and rise to form a small upward jet develops inside the leading edge of the dam at $t = 0.4$s. This jet can be observed in both the numerical and experimental results. Some of the impacting water is reflected by the porous boundary to form a wave travelling back towards the left side of the tank, reaching the tank wall at $t = 0.8$s before being totally re-reflected by the solid boundary back towards the dam. The free fluid domain on the left side of the tank shows a free-surface oscillation driven by the gap between the initial water column and the porous dam. The frequency of this oscillation is comparable to the natural frequency of the water body contained on the left side of the tank; similar to harbour oscillations [94]. This fluctuation gradually decreases as particles pass through the porous dam. Concurrently, fluid particles escape the far boundary of the porous dam and propagate towards the right tank boundary, reaching the wall at $t = 1.0$s and reflecting to form a similar oscillation on the right side of the dam.

The largest discrepancy between numerical and experimental results occurs at $t = 0.2$s, where the experimental data indicate a faster advancement of water particles near the bottom inside the porous dam. This could be partially explained by the gate-opening phenomena whereby the manual operation of the gate is non-instantaneous, taking around 0.1s and allowing water near the bottom of the tank to be released earlier. Additionally, the higher flow rate near the bottom of the tank could be caused by the larger porosity that results from the presence of a flat glass surface [94].

As the simulation progresses, the initial discrepancy between the experimental and numerical result diminishes. The pressure difference drives fluid particles through the porous dam, and at t = 1.2s the front reaches the far wall and is reflected, breaking on the porous dam at around t = 1.6s. Close agreement between the numerical and experimental results show that this phenomenon is captured authentically, although particle scattering is observed in the MPM simulations.

Overall, a very consistent agreement between the MPM simulations and the experimental and numerical results published in Liu (1999) is obtained. The lower free-surface displacement at the early stage ($t < 0.4$s) in the numerical results is likely to be caused by gate opening effects as discussed above. Later in time, numerical results from both sets of simulations compare well with image data, suggesting that the numerical model produces an accurate representation of flow data.

4.3.3 Glass bead simulations

Also published in Liu (1999) is a set of results for a series of experiments using small glass beads in place of rocks for the porous dam. MPM simulations to replicate these experiments were also carried out, and the results are shown in Figure 4.20. These results show some agreement with the published numerical data, although the agreement is not as good for the experimental data. Liu observes that whilst his numerical results are based on van Gent coefficients of $\alpha_p = 1000$ and $\beta_p = 1.1$, the bead size for the glass beads simulations is outside the test range of van Gent (1995). These coefficients modify the van Gent equations:

$$a_p = \alpha_p \frac{(1-n)^2}{n^3} \frac{\nu}{gD_{50}^2} \tag{4.7}$$

$$b_p = \beta_p \left[1 + \frac{7.5}{KC}\right] \frac{1-n}{n^3} \frac{1}{gD_{50}^2} \tag{4.8}$$

where n is porosity, ν is the dynamic viscosity, D_{50} is the characteristic diameter (average size) of the porous medium, and KC is the Keulegan-Carpenter (1958) number, representing the ratio of the characteristic length scale of fluid motion to the characteristic length scale of the porous medium, i.e.:

$$KC = \frac{u_c T}{nD_{50}} \tag{4.9}$$

where T is a typical wave period and u_c can be estimated from $u_c = \sqrt{\bar{u}_i \bar{u}_i}$ where u_i is the ith component of the instantaneous pore velocity.

a_p and b_p are then used by Liu to describe the flow through the porous medium [94].

The coefficient β_p generated good results for the rock experiments and so the value was kept the same for the glass bead experiments [94]. The coefficient α_p was reduced by a factor of 5 so that $\alpha_p = 200$. The original coefficient was obtained in high Re tests where the viscous effects were consequently negligible. In this case, $Re \approx 100$ so the suggested value for α_p is no longer appropriate. There is no method of modifying this coefficient in the MPM code, however, the engineering applications of these simulations involve larger Re flows where the frictional force is subsequently negligible.

Liu also noted that the surface tension and capillary effects present in the laboratory scale model cause the free-surface to stick to the glass wall, meaning that the experimental data may overestimate the free-surface level at some points in the porous dam. This was not observed during the laboratory experiments with the crushed rock dam [94].

The results presented here are for high Re flows where the linear frictional force caused by the viscous effect can be neglected, so these simulations serve as an example of a situation where the method would need to be modified to produce reliable results. Overall, this is a situation where the MPM results are less applicable, and so it was determined that this is not an appropriate avenue for investigation.

4.4 Results and discussion

After the validation studies, an extensive parametric study was undertaken to ascertain the effect on the run-up response to dam-break floods waves of manipulating the mean grain size of a porous barrier to alter its permeability. The width of the permeable seawall was also changed to ensure that it was sufficiently wide enough that the full effect of manipulating the grain size was captured.

Figure 4.21 shows a comparison of the wave shape formed in response to a dam-break flood, at the point of impact, for different grain sizes. Where the permeability increases as a result of the larger grain size, the water percolates through the dam, reducing the run-up response of the wave. The particle scattering that was previously mentioned is noticeable in the last these snapshots, where the grain size is very large.

Figure 4.22 shows the results of all simulations plotted on semi-log axes, using the mean centre of mass and filtering method described in Section 4.2.4. Each simulation is represented by a point on the graph. It is clear from this graph that varying the grain size of the porous dam has a significant impact on the run-up height achieved by a dam-break flow impacting on the dam. As predicted, the overall trend shows that increasing the mean grain size of the material

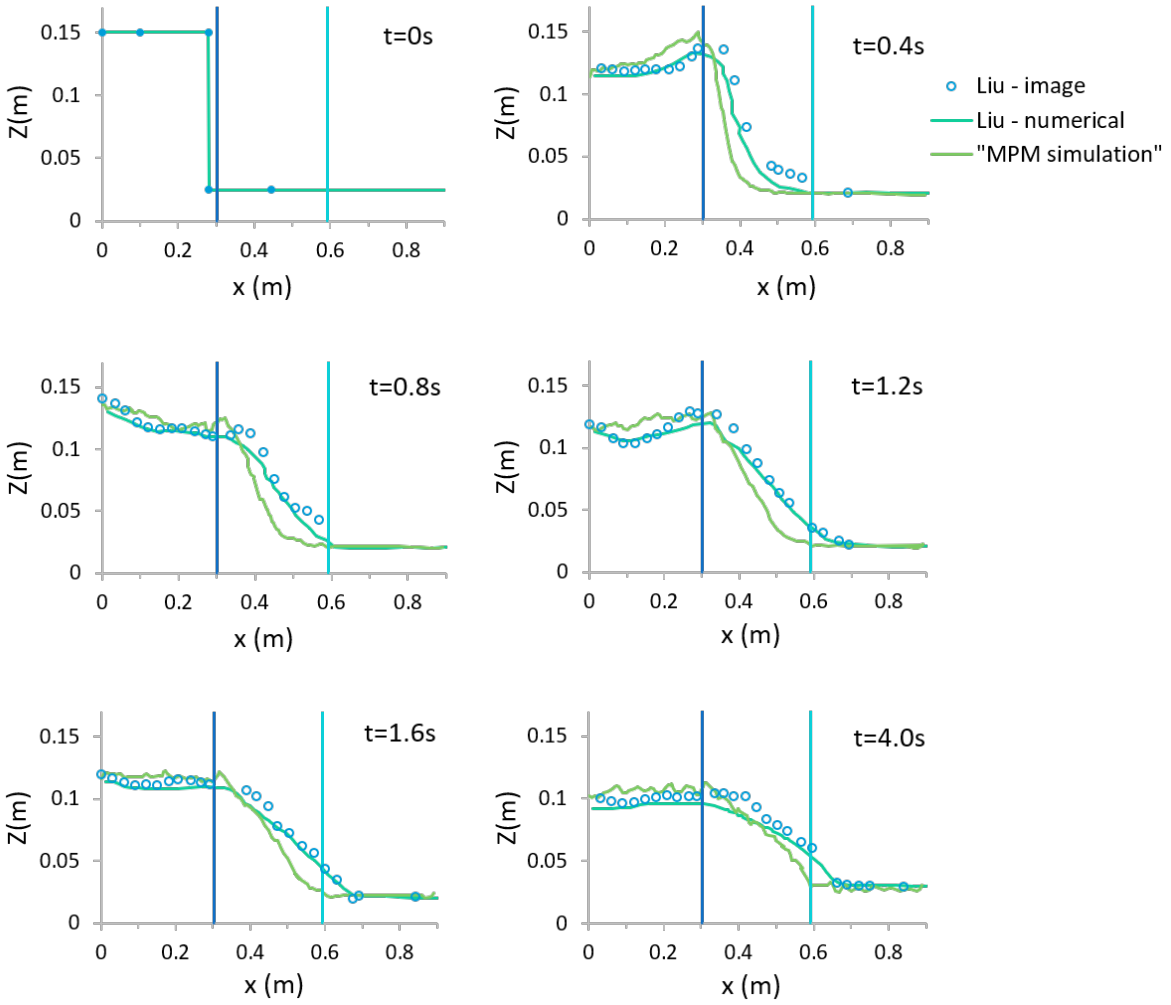

Fig. 4.20 Time history of free-surface profiles compared with experimental and numerical results published in Liu (1999) for the glass beads case [94]

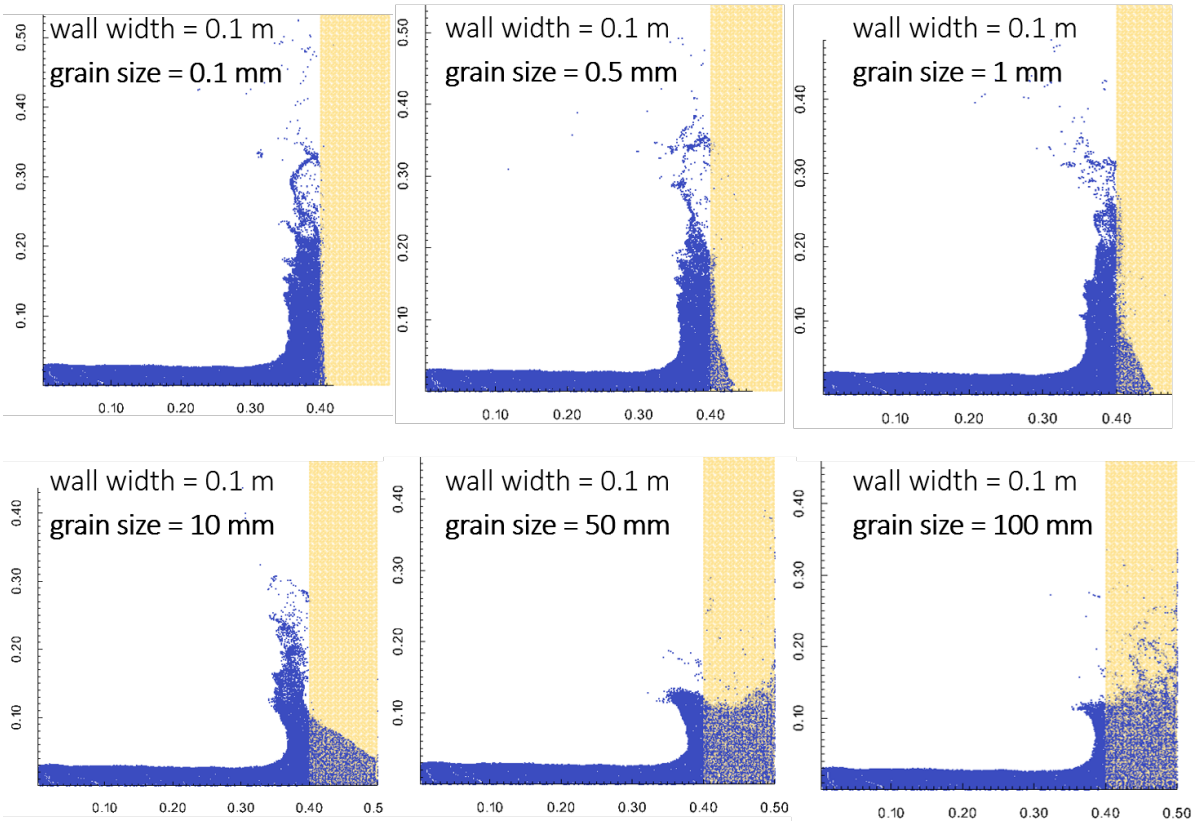

Fig. 4.21 Simulation results: comparison of free-surface shape at the time of maximum run-up for a dam-break flood wave

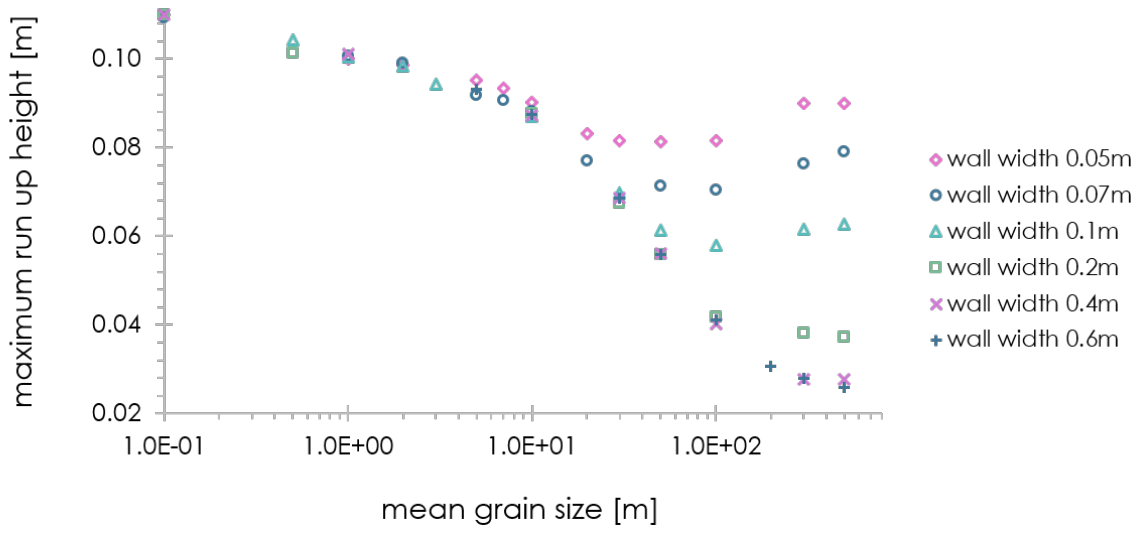

Fig. 4.22 Simulation results for dam-break flooding: plotting the highest mean centre of mass of particles 0.35m $< x <$ 0.40m, against increasing mean grain size individually, for all cases, on semi-log axes.

and therefore the permeability of the barrier reduces the run-up height response to a dam-break flood.

For the range of mean grain sizes investigated where $0.0001\text{m} < D_p < 0.005\text{m}$, all wall widths show the same results. This result can be explained by realising that porous walls made of fine sediment correspond to very low permeability so that only very few particles can penetrate the boundary of the porous medium during the run-up process, regardless of the width of the wall, so the run-up process is correspondingly rapid. Hence, for very small grain size, the width of the wall does not play an important role in determining the maximum run-up height reached by the impacting flood wave. The wall thickness begins to play a role only when the barrier is very permeable as a result of the increased grain size. In this range, therefore, the grain size is the only parameter that governs the maximum height reached by the flood wave.

The wall widths of 0.4m and 0.6m show almost identical responses, suggesting that the barrier is sufficiently wide that beyond this point, increasing the width of the wall does not affect the run-up height for the range of grain sizes investigated here ($0.0001\text{m} < D_p < 0.5\text{m}$).

For the cases with narrower walls, there is a point where increasing the grain size no longer reduces the run-up height. For the narrowest wall width, where $w = 0.05\text{m}$, this occurs at a grain size of roughly 0.05 m. For $w = 0.07\text{m}$, this occurs around $D_p = 0.1\text{m}$. For $w = 0.1\text{m}$, this minimum is at $D_p = 0.1\text{m}$, and for $w = 0.2\text{m}$, the minimum occurs around $D_p = 0.5\text{m}$. For all these cases, increasing the grain size is no longer effective once the grain size is around the same order of magnitude as the wall width.

For the three narrowest widths of the porous wall that were investigated, ($w = 0.05\text{m}$, 0.07m and 0.1m), there are still situations where the run-up height superficially appears to increase with the grain size, thus warranting a closer investigation of these results. An example of these cases is shown in Figure 4.23. Visual inspection of these results shows that although the maximum run-up height reached by the plume appears to be approximately the same for each situation, albeit with a slight visual reduction for increased grain size, the number of scattered particles dramatically increases with each increase in grain size. This particle scattering occurs in part when the fluid particles reflect off the solid wall at the end of the domain and travel back through the porous dam, artificially scattering and increasing the run-up height. Other particles may scatter in MPM as a result of cell-crossing errors. Evidence of this can be seen in the snapshots in Figure 4.23. There is no clear cut method by which to determine which particles are scattered and which represent the "true" run-up height. This investigation seeks to identify the influence of the grain size on the run-up response, but the influence is quite small with such a small wall width. The overall influence of the grain size is more significant when the porous wall thickness is bigger, further justifying removing these results. Furthermore, the narrow width of the wall compared to the large grain size of the soil particles means these results are

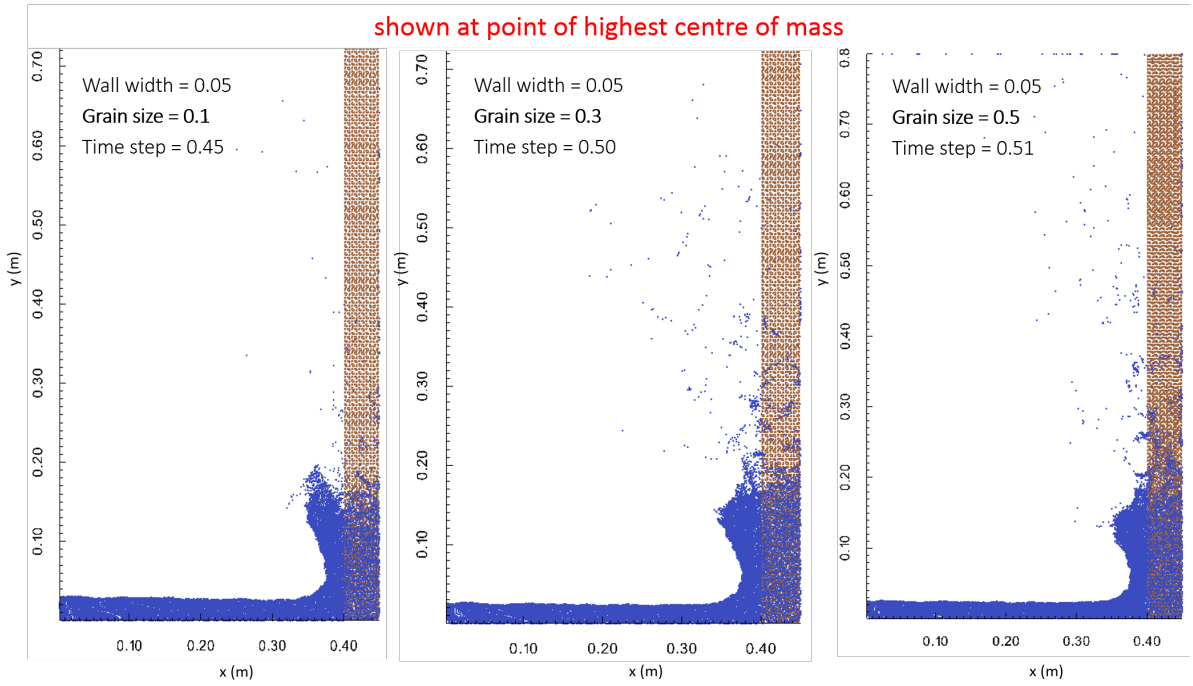

Fig. 4.23 Simulation results where the run-up height, based on the centre of mass, superficially appears to increase with increasing grain size, D_p, as a result of increased scattering.

arguably unphysical and certainly are of little interest. Finally, the porous material is modelled as a continuum, so the largest grain sizes ($D_p = 0.3$m and 0.5m) are approaching the limit of a material that can reasonably be described as continuous; so an assessment should be made as to whether or not these results are physically valid. Assessment of larger grain sizes would certainly require an alternative material model.

Figure 4.24 shows the same results as before, but with these questionable results removed. The trend is now very clear. The wall width has some influence on the overall run-height as the grain size increases. For the most extreme case, where $w = 0.05$m, the deviation from the general trend initially occurs at $D_p = 0.005$m, much less than the maximum reasonable result at $D_p = 0.05$m. This suggests that the wall width does have some influence at this point, where $0.005\text{m} < D_p < w$. However, the grain size is demonstrably the dominant parameter, and the wall widths of 0.4m and 0.6m show the same results. Figure 4.24 shows very clearly the trend that this investigation was aiming to identify: the maximum mean centre of mass of the particles decreases as the grain size is increased, provided the barrier is wide enough to allow sufficient percolation. Increasing the grain size of the permeable barrier is consequently determined to be an effective method of reducing the run-up height.

Figures 4.25 and 4.26 show the results recovered from the same set of simulations, using the statistical methods detailed in Section 4.2.4, for the 95$^{\text{th}}$ and 98$^{\text{th}}$ percentiles, respectively.

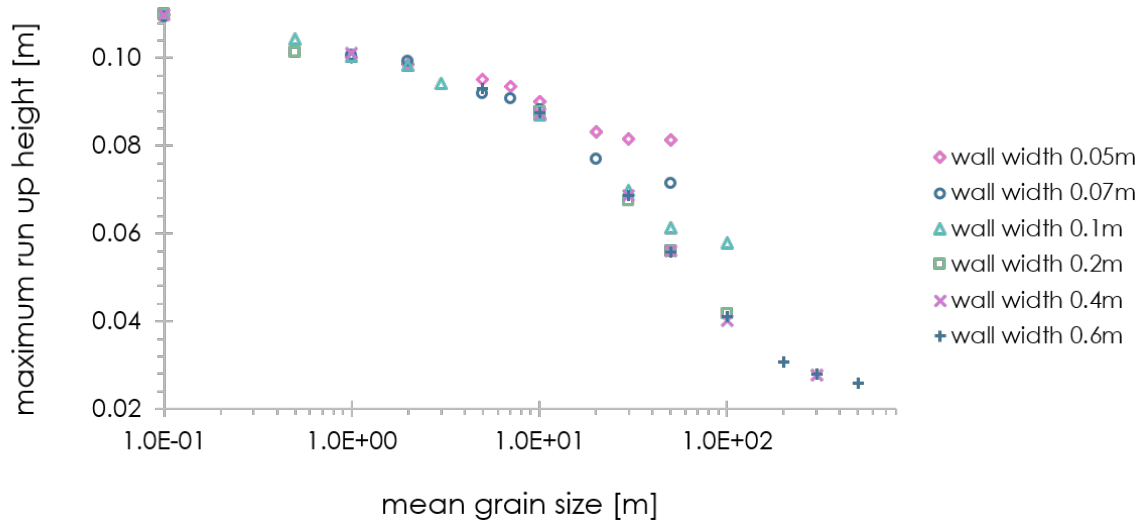

Fig. 4.24 Simulation results for dam-break flooding: plotting the highest mean centre of mass of particles 0.35m $< x <$ 0.40m against increasing mean grain size individually on semi-log axes, removing cases where $D_p > w$.

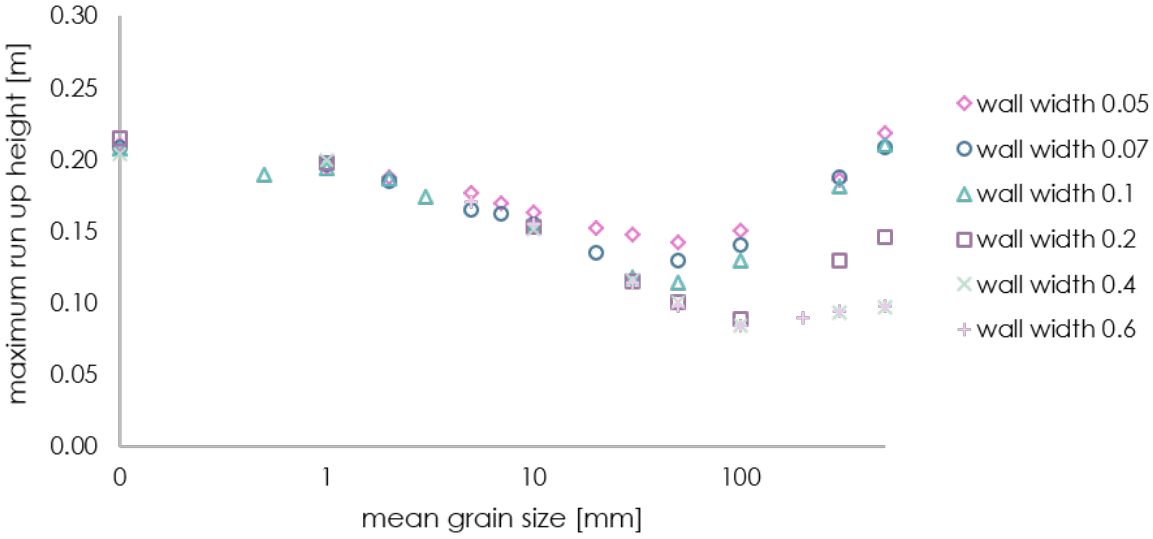

Fig. 4.25 Simulation results for dam-break flooding: plotting the 95th percentile of the centre of mass against increasing mean grain size individually, for all cases, on semi-log axes.

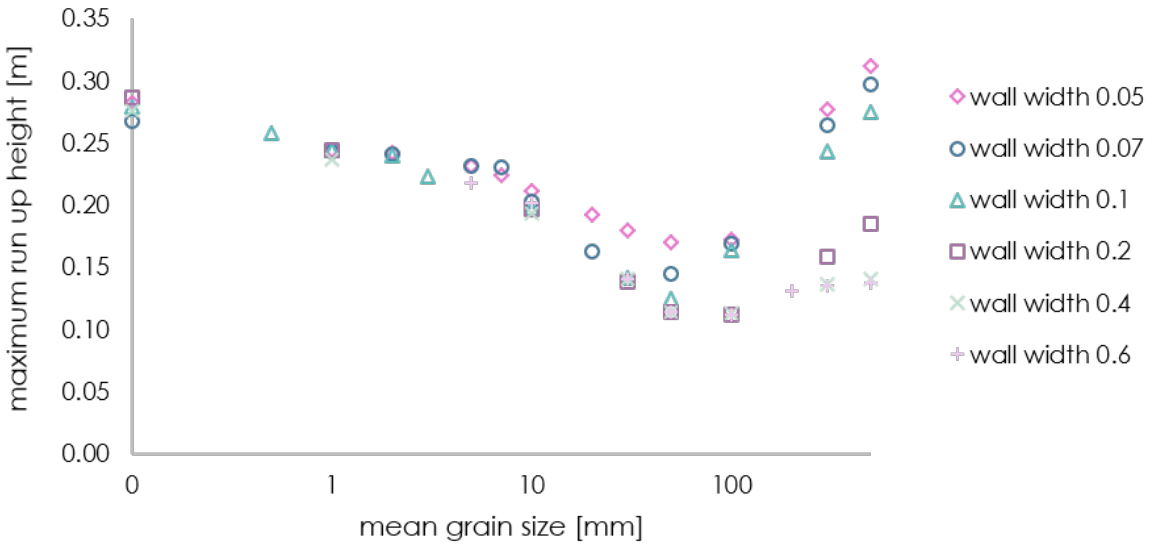

Fig. 4.26 Simulation results for dam-break flooding: plotting the 98th percentile of the centre of mass against increasing mean grain size individually, for all cases, on semi-log axes.

Every simulation is represented by a single point of the graph. Up to a grain size of around 80mm, these results show the same general trend as the previous method of interpretation: the increasing grain size tends to reduce the run-up response. However, using this method of analysis, once the grain size increases beyond approximately 80mm, the run-up height appears to increase. This unphysical result is likely a result of the particles that have reached the solid barrier at the end of the permeable wall reflecting back and combining with the incoming wave to reach greater heights. This hypothesis is supported by examining the trend displayed for the different wall widths - the "run-up height" increase is much greater for the narrower walls, where the wave will reach the solid boundary sooner. This method of analysis demonstrates that as the permeability of the wall increases, the speed with which the wave passes through also increases, so that the width of the wall becomes significant for larger grain sizes. For the widest wall investigated (0.6m), the upward slope is not significant and so the run-up results are still meaningful. The results for the two percentiles investigated show the same trend, but with a slight difference in the overall value, as might be expected.

4.5 Conclusions

In this chapter, the material point method has been applied to the traditional dam-break flow problem. The aim of this investigation was primarily to establish the validity of this code applied to the dam-break problem, and secondly, to establish the effect on the run-up height response of a dam-break flood wave impacting on a porous, permeable vertical flood defence, when the permeability of the wall is changed by modification of the mean grain size. It was anticipated that increasing the grain size, and therefore the permeability, of the porous medium would reduce the maximum height reached by the wave impacting on the permeable barrier: the increased permeability allows the water to percolate into the wall so that the barrier absorbs wave energy from the flow as friction generated by the fluid-structure interaction causes dissipation of significant energy.

When compared with experimental data and results from other verified numerical methods published by various research groups, using techniques such as SPH and VOF, the MPM simulations gave good predictions of the frontal propagation of dam-break floods, and the flow through porous media. The material point method is thus demonstrated to be an appropriate method for modelling hydraulic flows interacting with permeable barriers.

The effect of increasing the grain size for different wall widths of a porous barrier on the run-up height in response to a dam-break flood was investigated using MPM. The wall width was varied to ensure that this is not a limiting parameter when investigating the grain size. Different methods of quantifying the run-up height were trialled to overcome shortcomings in the numerical method used for quantification of the investigation results. An appropriate method was identified: the centre of mass of relevant particles is found numerically by averaging the y-coordinate so that the problem of objectively identifying the appropriate particle is overcome. Particles that do not affect the run-up height are filtered out of this mean. Any simulations results that have been skewed by large amounts of particle scattering have been removed. These are also physically unrealistic, justifying the exclusion of these results. Furthermore, the results are assessed statistically by plotting the 95^{th} and 98^{th} percentiles of the y-coordinates of all the particles in the simulation. This method of analysis offered further insight into the wave behaviour.

The wall width has some impact on the effectiveness of the permeable barrier. As the grain size increases, the wall width necessary for the increase in permeability to be effective in reducing the maximum run-up height also increases. This is because the run-up height is reduced by the water percolating into the porous medium, and a narrow barrier does not allow sufficient fluid to flow in to enable a reduction in run-up height. Furthermore, the maximum run-up height may actually be reached inside the barrier, as the wave reaches the solid far boundary and reflects, superimposing on the incoming wave. We can therefore state that there

is a minimum width required for the barrier to operate effectively and that this increases with increasing grain size and thus the permeability of the barrier. Increasing the wall width from 0.4m to 0.6m had no quantifiable impact on the run-up height, for any grain size, so a minimum achievable run-up height was identified across the range investigated. Overall, the mean centre of mass of the broken wave was reduced from 0.11m in the worst case of a solid wall to 0.026m, demonstrating that the run-up response of a dam-break flood can be significantly reduced by increasing the permeability of the barrier to absorb the maximum possible energy of the impacting wave. The influence of the grain size is more significant when the thickness of the porous wall is greater since more water is allowed to percolate. It is possible that a larger reduction in run-up is possible with larger grain sizes; however, modelling a material would such a large grain size would require an alternative material model since it could no longer be realistically described as a continuum.

In summary, increasing the grain size, and therefore the permeability, of the porous dam effectively reduces the overall run-up height in response to a dam-break flood. The mean grain size of the barrier is shown to be the dominant parameter affecting run-up height, provided the barrier is wide enough to allow percolation and to prevent the reflected wave superimposing on the incoming wave. The largest grain size investigated here was a mean grain size of 500mm; the grain size was not extended beyond this point since it falls outside the limitations of the numerical method used, which is designed to represent a continuum. All investigations show that increasing the grain size beyond 50mm had a limited effect on reducing the overall run-up response. The largest grain sizes investigated ($D_p = 0.3$m and 0.5m) are approaching the limit of a material that can reasonably be described as continuous; assessment of larger grain sizes would certainly require an alternative method.

Chapter 5

Solitary wave run-up on vertical seawalls

This chapter describes the effect of changing the permeability of a permeable barrier on the run-up response to a solitary wave flood, for the case of a vertical sea wall. As in the previous chapter, the permeability of the barrier is modified by altering the mean grain size of the material forming the barrier.

Simulations of solitary waves with the same initial conditions and geometry as published results were run to verify and demonstrate the accuracy and stability of the material point method when applied to solitary waves impacting on porous media. The results are demonstrated to be in good agreement with validated and verified data, including both results produced using numerical methods as well as experimental data, strongly suggesting that MPM is an appropriate method to employ for this case study.

The focus of the investigation is the changing wave response when the permeability of the vertical sea wall defence is changed by altering the representative mean grain size of the constituent particles forming the barrier. The run-up height, normalised by the initial still water depth, is compared to the normalised wave height to establish an empirical relationship between run-up height and grain size; and therefore to provide design guidelines for permeable flood defences. The amplitude of the impacting wave is also varied so that it can be established whether the relationship between run-up response and permeability varies for differing wave heights.

5.1 Motivation

The ability of porous barriers to absorb wave energy is of great interest in coastal engineering, as the flow friction that develops within the porous medium can be exploited to create significant wave energy dissipation, therefore reducing the effect of incoming flood waves. Familiarity with flow processes arising from wave motion through porous structures is key to ensuring both

the long-term stability and the functionality of these structures. Solitary waves are often used to model the effects of tsunamis, due to their hydraulic similarities [91, 87, 161].

In 2004, the Sumatra–Andaman earthquake triggered a devastating Indian Ocean tsunami that spread throughout the Indian Ocean, inundating coastal communities across South and Southeast Asia. Communities along the surrounding coasts of the Indian Ocean were severely affected, and the Boxing Day Tsunamis killed over 200,000 people in 14 countries [142, 43]. The earthquake was one of the deadliest natural disasters in recorded history. A similarly extreme level of damage was observed as a result of the storm surge associated with Hurricane Katrina in 2005 [161].

The primary cause of both calamities is the inundation that occurred as a direct result of tsunami and storm surge waves, respectively [64, 161]. Tsunamis, in particular, have a wave height above the normal mean water level that is comparable to that of swell but often have a substantially stronger impact [161].

Tsunami waves do not behave in the same manner as normal undersea currents or waves, because they have a much longer wavelength. Solitary waves are considered to accurately represent many important aspects of tsunamis and nearshore waves of very long wavelength [141], and consequently, solitary waves are widely used in numerical simulations to model the effect of tsunamis [73]. Tsunamis can travel inland for relatively large distances, with the potential to cause significant property damage and loss of life. Most of the damage associated with tsunamis is related to their run-up at the shoreline [87]. Consequently, understanding the free-surface flow motion and predicting the maximum run-up height that arises as a result of these seismic waves is an essential part of any coastal flood mitigation effort.

When considering run-up response to solitary wave attack, the interaction between the fluid and the structure is a key factor in determining how effective the flood defence will be, particularly in the case of permeable barriers, where the aim is to reduce the wave energy by utilising the flow friction that develops through turbulence and fluid-structure interaction as the wave propagates through the barrier. Accurately predicting the maximum run-up height reached by such waves will empower engineers to design and construct more effective coastal flood defences.

This chapter investigates the effect of manipulating the mean grain size of a permeable barrier on the run-up response to a solitary wave, using the material point method.

5.2 Methodology

This section describes the setup of the numerical simulations used to investigate a solitary wave flood impacting on a vertical sea wall.

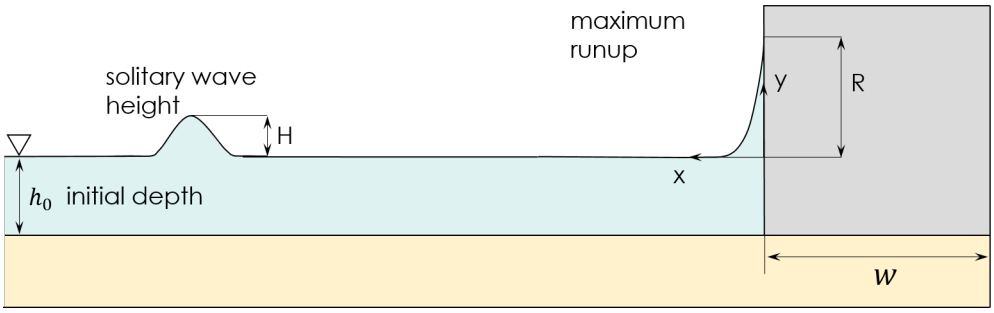

Fig. 5.1 Problem definition sketch for the case of a solitary wave impacting on a permeable vertical sea wall.

5.2.1 Simulation geometry

These simulations also used the Anura3D double-point MPM code. A problem definition sketch for the case of a vertical sea wall is shown in Figure 5.1. The grain size was again varied between 0.05mm (extremely fine sand to simulate a solid surface) and 200mm (a very large grain size, representative of large cobbles). The vertical wall has been extended sufficiently far above the height of the paddle and still water depth to allow the full extent of the run-up to be captured. Based on the investigations carried out in Chapter 4, the initial width of the vertical barrier was set reasonably wide. It was determined that walls with a width of an order of magnitude $\approx 2-3$ x the width of the wave are wide enough that the width itself is not a governing parameter since sufficient percolation is able to take place. This was not simply held as an assumption; several simulations with a wall twice as wide were run for different situation and the results were compared to prove this hypothesis. Figure 5.2 also shows the *wave generating paddle*. This paddle is accelerated to a specified velocity, to produce a solitary wave of a particular height. This wave generation is explained in Section 5.2.3.

5.2.2 Simulation parameters

For these simulations, the liquid water is modelled as a Newtonian fluid with material parameters $\rho = 1000$, $K = 20000$, and $\mu = 1e^{-6}$, where ρ is the density $\left[\text{kg/m}^3\right]$, K is the bulk modulus [kPa], and μ is dynamic viscosity [kg/m $\cdot$ s]. The dry part of the porous beach is modelled as a linear elastic material, with material parameters $n = 0.43$, $\rho = 2650$, $K_0 = 0.5$, $E = 10000$ and $\nu = 0.3$, where n is the initial porosity [no units], ρ is the density, as before, K_0 is coefficient of lateral earth pressure [no units], E is Young's modulus [kPa] and ν is Poisson's ratio [no units]. The saturated part of the porous beach is modelled as a fully coupled, saturated, linear elastic material, with material parameters $n = 0.43$, $\rho = 2650$, $K_0 = 0.5$, $\rho = 1000$, $K = 20000$, and $\mu = 1e^{-6}$, $E = 10000$, and $\nu = 0.3$. Finally, the paddle that is accelerated to generate the water

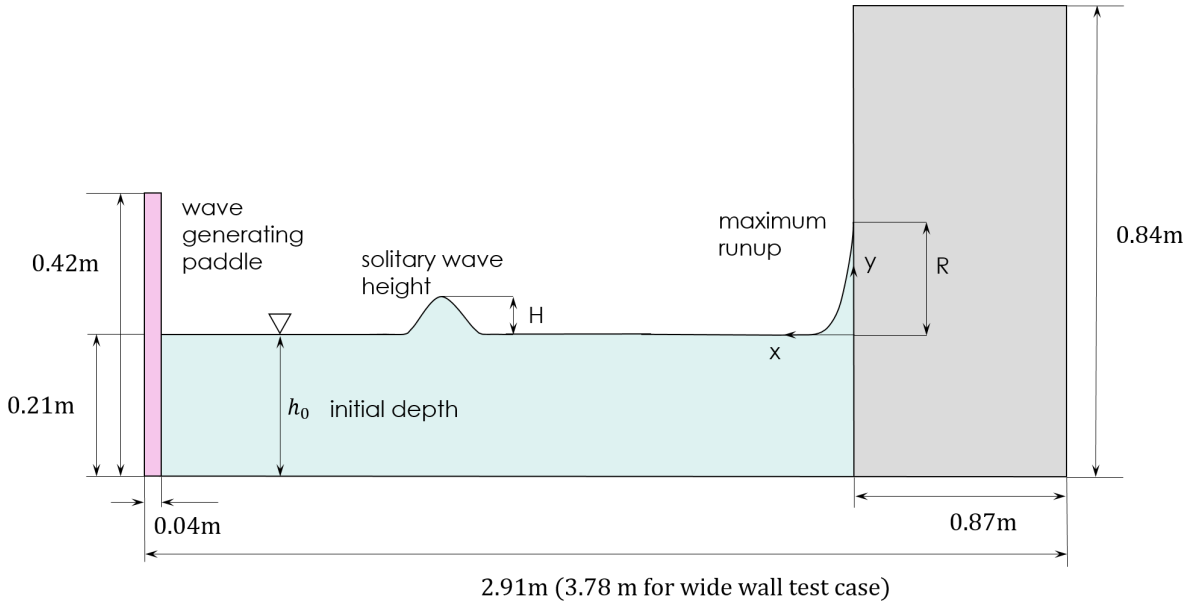

Fig. 5.2 The computational domain dimensions used for the numerical investigation of a solitary wave impacting on a vertical sea wall.

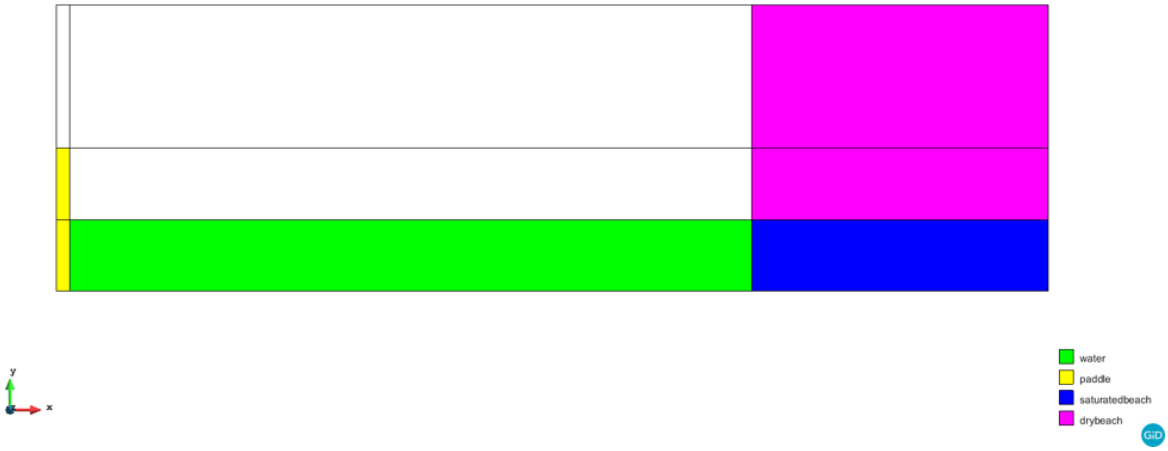

Fig. 5.3 The material assignment for the vertical sea wall case

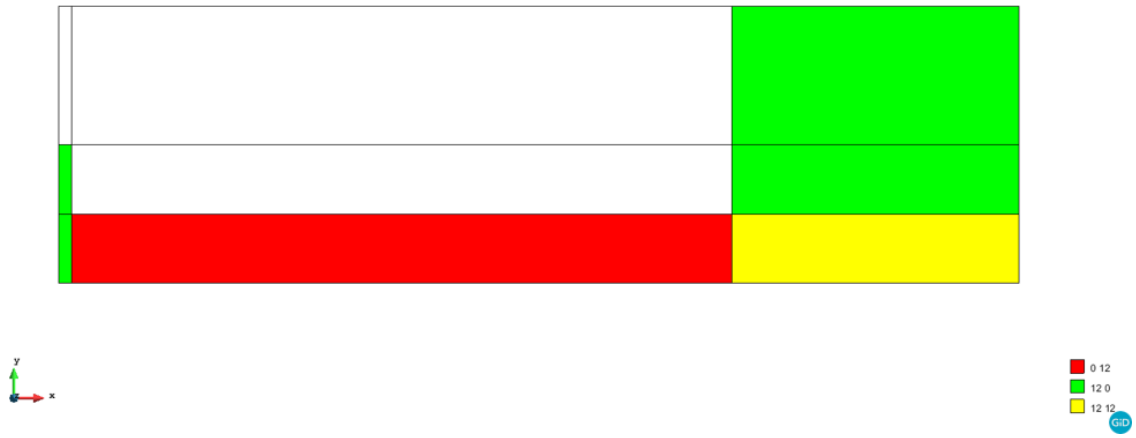

Fig. 5.4 The material point assignment indicating the number of material points initiated per element for each phase

wave is modelled as a linear elastic material, with material properties $n = 0.42$, $\rho = 2650$, $K_0 = 0.5$, $E = 10000$ and $\nu = 0.3$. The material assignment is shown in Figure 5.3. The paddle material must be differentiated from the beach material so that we can specify a velocity to all of the particles forming the paddle. This is achieved by specifying a different initial porosity: any element with an initial porosity below 0.425 is recognised as forming part of the paddle.

The material point assignment is shown in Figure 5.4. The liquid water has 12 fluid material points specified per element, and the dry beach and paddle each have 12 solid material points specified per element. The saturated beach has 12 solid material points and 12 fluid material points generated per element. The grid spacing for the vertical sea wall simulations presented here is specified as 0.02m, shown in Figure 5.5. This is twice as large as the sloped beach cases described in the next chapter. The different geometry of the vertical sea wall case compared to the sloped beach means more filled elements and therefore more material points generated for a similarly sized domain; the computation cost is correspondingly higher, hence the need to increase grid spacing. The mesh spacing of 0.01m is unsuitable in this case, as the simulations otherwise become too computationally expensive and in some cases will not even run as internal storage capacity is exceeded. The coarser mesh of 0.02m used for these simulations compared to those presented for the sloped beach case in the next chapter means that more material points per element are assigned to achieve similar results. There is no horizontal fixity is applied to the leftmost surface, so that the paddle can move freely. These parameters are summarised in Table 5.1.

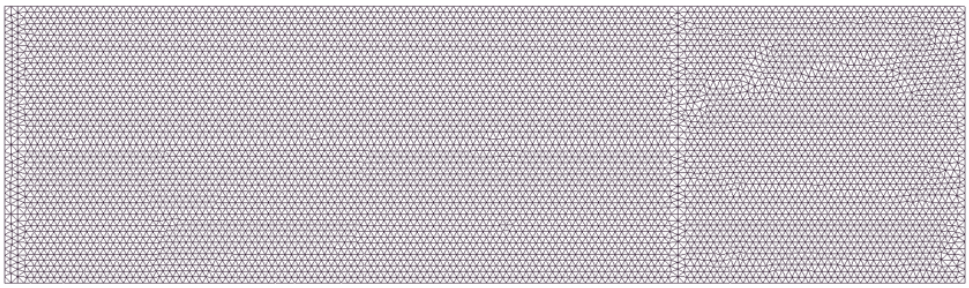

Fig. 5.5 The mesh generated for the vertical sea wall case, with grid spacing 0.02m

A two-phase double-point simulation type is used, with a Courant number of 0.8 to ensure stability. No smoothing is used and no damping is applied, which is recommended for the double-point code [169]. For each case, the maximum allowable porosity is 0.95. This parameter distinguishes the solid states and liquid states and it must at least be larger than the initial porosity of the soil. Otherwise, the soil is determined to be liquefied when the simulation begins. The porosity of the beach is not varied in these simulations, only the grain size is altered to modify the permeability of the material, as per Ergun's Law.

5.2.3 Wave generation via paddle

A novel boundary condition was developed to allow the Anura3D software to generate a solitary wave for the purposes of these investigations.

The solitary wave is generated by specifying the velocity of the material points that form the paddle. The velocity graph for the case where the wave height H is 0.03423m (so that H/h_0 is 0.163) is shown in Figure 5.6. The parameters that govern the paddle wave generation are shown in Table 5.2. These parameters are used in the wave equation:

$$U = \frac{H}{h_0} c \left(1 - tanh^2 \left(\frac{\beta c (t - t_0)}{2} \right) \right) \tag{5.1}$$

where

$$tanh\left(\frac{\beta c}{2} t \right) = \frac{e^{\beta c t} - 1}{e^{\beta c t} + 1} \tag{5.2}$$

Table 5.1 Calculation and material parameters used in the simulations of a solitary wave impacting on a vertical wall

	Parameter	*Value*	*Unit*
Mesh properties	Mesh size	0.02	m
	Number of elements	$6,111-7,938$	-
	MPs per element	12 fluid, 12 solid	-
Fluid properties	Density	1000	kg/m^3
	Bulk modulus	20,000	kPa
	Dynamic viscosity	$1e^{-6}$	kPa $\cdot$ s
Solid material properties	Density	2650	kg/m^3
	Young's modulus	10,000	kPa
	Initial porosity	0.43	[no units]
	Lateral earth pressure	0.5	[no units]
	Poisson's ratio	0.3	[no units]

Table 5.2 Parameters used for wave generation

Parameter	*Symbol*	*Value*	*Unit*
Wave amplitude	H	0.03423	m
Still water depth	h	0.21	m
Wave speed	c	1.547868	m/s
Outskirts decay coefficient	β	3.32993	[no units]

where H is the wave amplitude [m], h_0 is the initial still water depth [m], c is the wave speed [m/s], so that $c = \sqrt{g(H+h)}$, β is the outskirts decay coefficient [no units] and t is time [s].

This equation is implemented by adding a new subroutine to the Anura3D source code. These changes are shown in Figure 5.7.

5.3 Model Validation

The ability of the MPM code to produce reliable results for predicting the run-up height of solitary waves incident on vertical seawalls was established by extensive comparison of results produced using this method with published results using a variety of experimental and numerical techniques. In particular, these results were validated by comparison with numerical results produced using SPH methods published in Liang et al.'s 2016 paper *"Incompressible SPH simulation of solitary wave interaction with movable seawalls"* [89]. In this paper, the incompressible Smoothed Particle Hydrodynamics (SPH) method is applied to investigate the impact of solitary waves on seawalls. The model is used to simulate the solitary wave

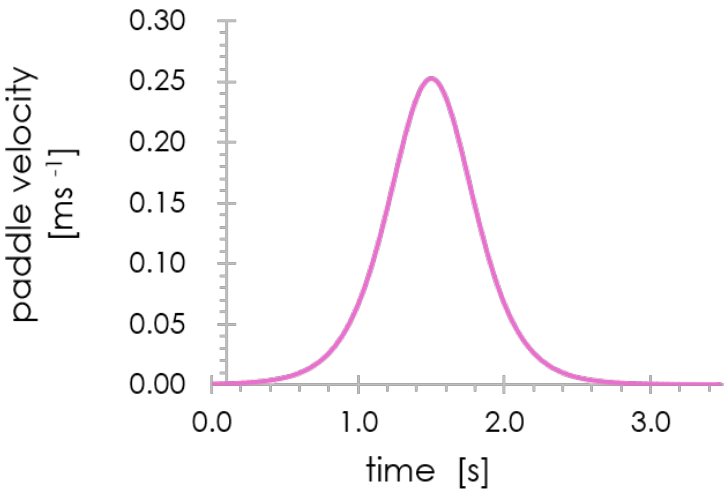

Fig. 5.6 Velocity-time graph for the paddle used for wave generation

```
subroutine UpdateParticleVelocityAndMapMomentum(Momentum)
 if (Particles(ParticleIndex)%InitialPorosity .le. 0.425)  then ! paddle particles
     if (CalParams%OverallRealTime .le. 3.0) then
         call GetPaddleMPsVelocity(ParticleVelocity)
     else
         ParticleVelocity = 0.0
     end if
 else ! NOT paddle particles
    ParticleVelocity = ParticleVelocity + ParticleIncrementalVelocity
 end if

subroutine GetPaddleMPsVelocity(PaddleMPVelocity)
in module ModDYNConvectivePhase
```

Fig. 5.7 The subroutine added to the MPM code for wave generation

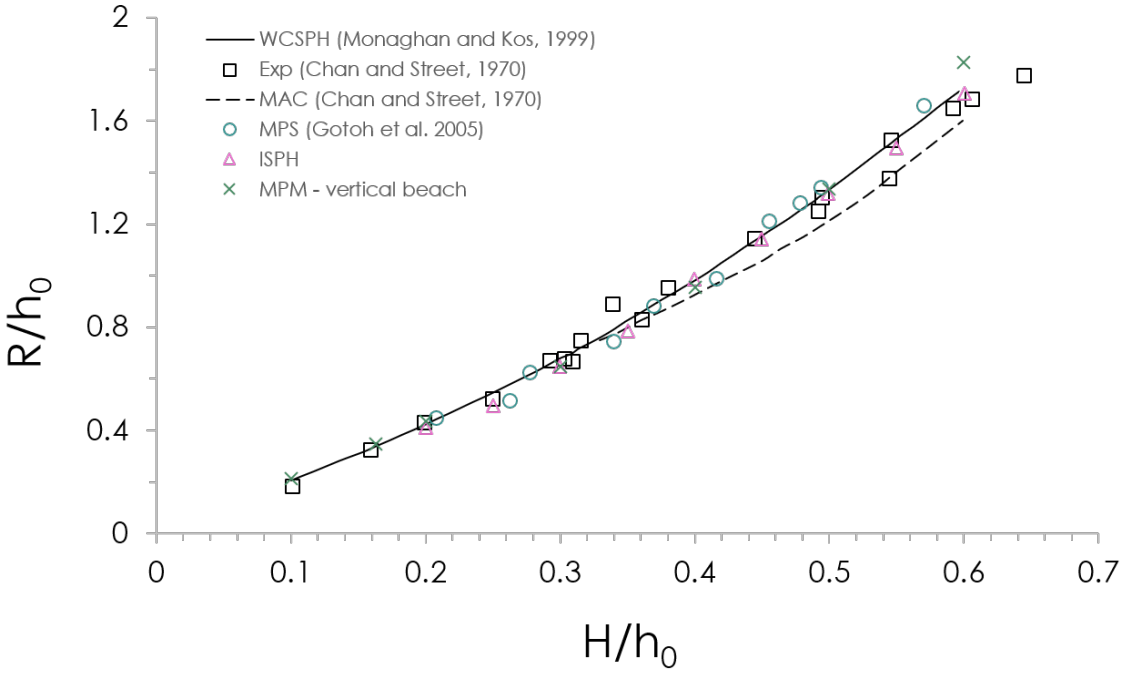

Fig. 5.8 Comparison of results produced using the material point method with numerous published experimental and numerical data for the case of solitary wave run-up on a vertical sea wall.

propagation and run-up against a fixed vertical wall, and the computations compared well with previous experimental and numerical results [89]. The incident wave height is found to be the dominant factor affecting the movement of movable seawalls. This adds weight to the hypothesis investigated here; strongly suggesting that there will also be a significant impact of the incident wave height on the maximum run-up height reached by the incoming flood wave.

A comparison of the results produced here using the material point method to the results produced by Liang et al. using the incompressible SPH method is plotted in Figure 5.8. The results are also compared to numerical results produced by Gotoh et al. in 2005 using the moving particle semi-implicit (MPS) method, Chan and Street (1970) using the marker-and-cell (MAC) method and Monaghan and Kos in (1999) using the weakly compressible SPH (WCSPH) method, as well as experimental results produced by Chan and Street (1970).

The results produced here using MPM compare very well with the published numerical and experimental data. The results fit very precisely for waves that have a lower incident height, although there is a slight overestimation of the run-up at the highest investigated wave height. There is some uncertainty in the MPM results due to the particle scattering mentioned

before, however, the results are generally a very good fit. All published results and analytical theory suggest that incident waves with a larger amplitude produce a higher run-up on the vertical wall. The correlation between run-up height and wave height is not linear due to the inherently nonlinear behaviour of the wave motion after it impacts on the barrier, causing turbulent sloshing. Based on this excellent agreement of the MPM results with those produced using different experimental and numerical techniques, it is clear that this method can be appropriately applied for predicting the maximum run-up height reached by a solitary flood wave within the height range $0.1 \leq \frac{H}{h_0} \leq 0.6$.

5.4 Results and discussion

5.4.1 Grain size influence

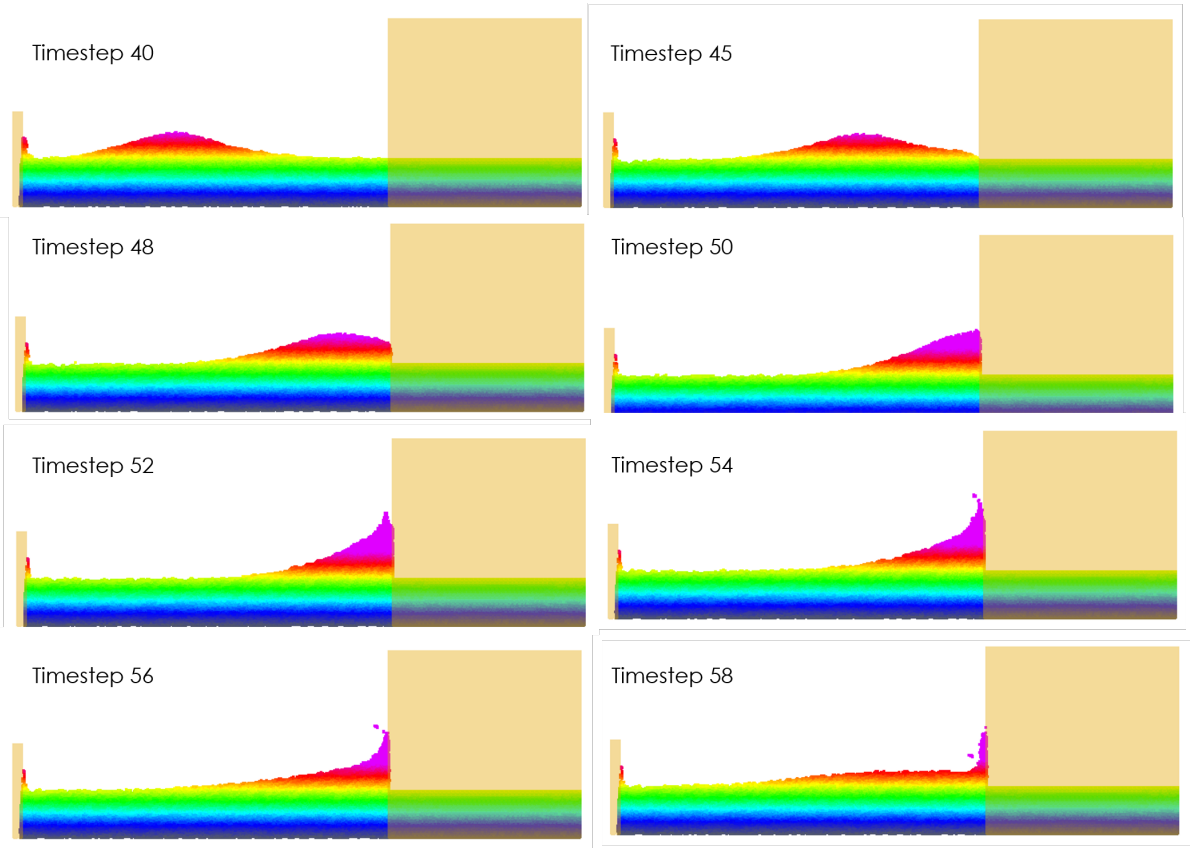

Fig. 5.9 Free-surface profile development throughout time for a small grain size ($D_p = 0.05$mm) and a wave height of H=0.105m $\left(\frac{H}{h_0} = 0.5\right)$

Figures 5.9 and 5.10 show examples of the free-surface profile development throughout time when a solitary wave interacts with a vertical sea wall, for a small grain size ($D_p = 0.05$mm),

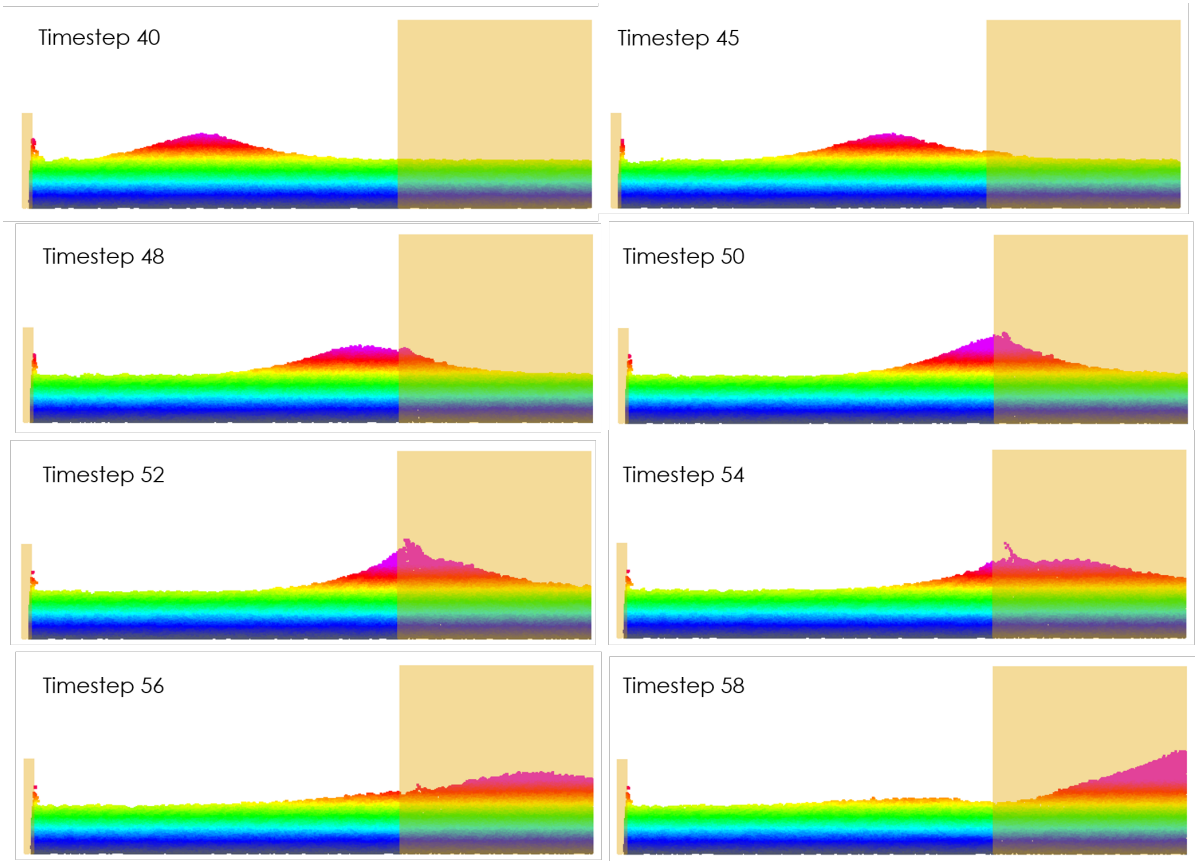

Fig. 5.10 Free-surface profile development throughout time for a large grain size ($D_p = 50$mm) and a wave height of H=0.105m $\left(\frac{H}{h_0} = 0.5\right)$

and a large grain size ($D_p = 50$mm), and an initial wave height of H=0.105m $\left(\frac{H}{h_0} = 0.5\right)$. These specific examples were selected to best illustrate the contrast as the grain size increases. On observation of these figures, it is clear that the increased mean grain size of the porous wall, by increasing the permeability of the medium, allows the incoming wave to percolate into the beach and thus reduces the maximum run-up height via frictional dissipation of the wave energy. In Figure 5.9, where the mean grain size is very fine, the wave generated by the paddle travels through the still water and on impact with the impermeable vertical sea wall, the wave rapidly climbs, reaching a maximum run-up height in timestep 54, before beginning the run-down process. By contrast, in Figure 5.10, where the grain size is very large, the wave generated by the paddle flows into the permeable barrier. This percolation is visible from timestep 45. As the wave progresses, it continues to flow into the permeable barrier, climbing the wall as friction generated by the fluid-structure interaction slows the flow in the barrier. The maximum run-up height is still reached at timestep 54, but it is now much lower. The wave continues to flow into the permeable barrier during the run-down process, and in the final slide, we observe a secondary run-up process occurring within the permeable barrier as the wave reaches the solid barrier at the end of the domain.

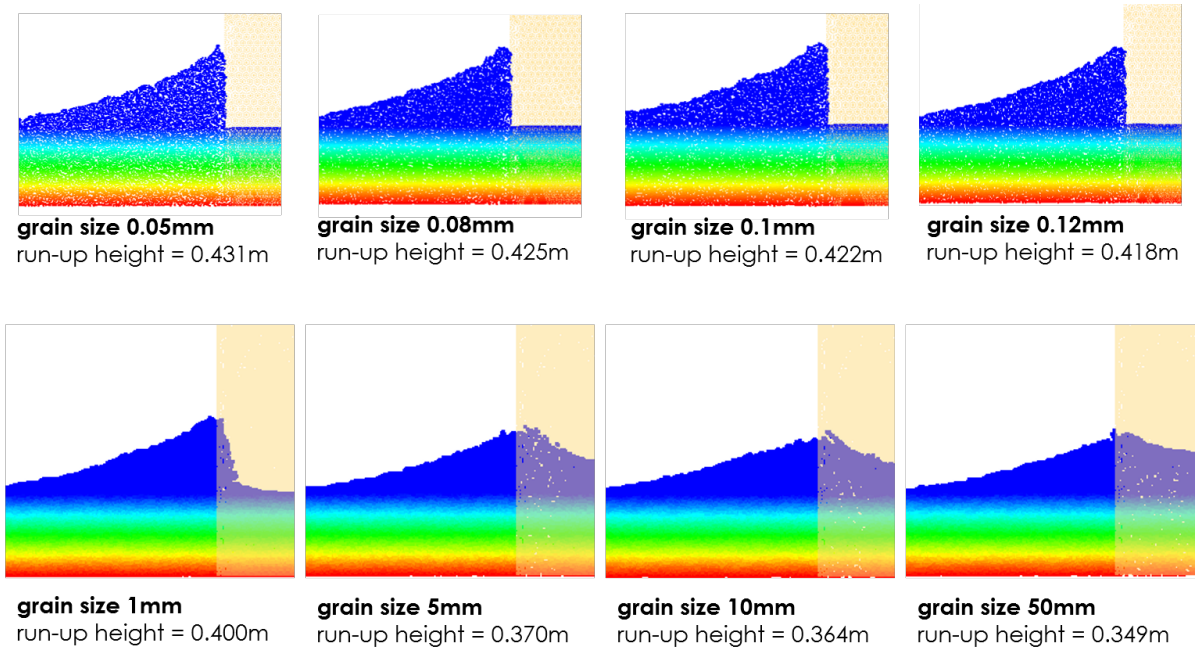

Fig. 5.11 Simulation results: comparison of free-surface shape at impact for wave height H=0.84m.

Figure 5.11 shows a comparison of the wave shape formed by the solitary wave at the point of impact with a vertical sea wall constructed from materials with different mean grain sizes. The top four diagrams show wave impact for the smallest grain sizes investigated, and the

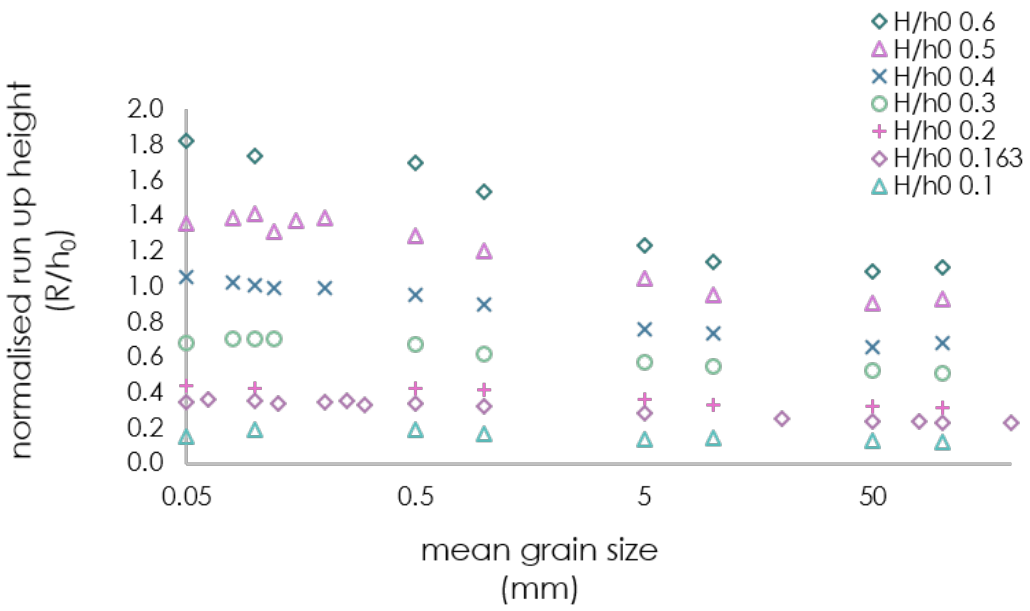

Fig. 5.12 Simulation results: maximum run-up heights for varying wave heights and grain sizes

bottom four diagrams show the shape of the wave at the point of impact for the larger grain sizes. All figures presented here are taken from the case where the initial wave height H is 0.084m, so that $H/h_0 = 0.4$. This wave height was selected for the example since the wave is sufficiently large enough that the effect of changing the grain size on the run-up response is clear to the observer, however, the wave height is not so high that the impact of the wave on the beach causes the particles to scatter. Here, "scatter" refers to an unphysical dispersion of the particles as an artefact of the calculation method used. Whilst some of the dispersion is arguably physical, non-physical dispersion also occurs. This non-physical dispersion may arise as a result of the cell-crossing error discussed in Chapter 3.

Figure 5.11 shows that when the grain size is 0.1mm or less, the permeable barrier behaves as a solid wall, which demonstrated by a complete lack of percolation of the water into the barrier. The extremely fine-grained case ($D_p = 0.05$mm) was used in the validation studies presented in the previous section as a means of studying the wave impact on a solid wall. On examination of the different studies presented, it is clear that, per the hypothesis, where the permeability of the porous medium increases as a result of the increase in mean grain size, a larger volume of water percolates into the material, thus reducing the maximum run-up height reached by the impacting wave. However, for the largest grain sizes, such as those displayed on the bottom right of Figure 5.11, although the mean grain size increases, the benefit of the increased permeability is not manifested in a reduction of the run-up height reached.

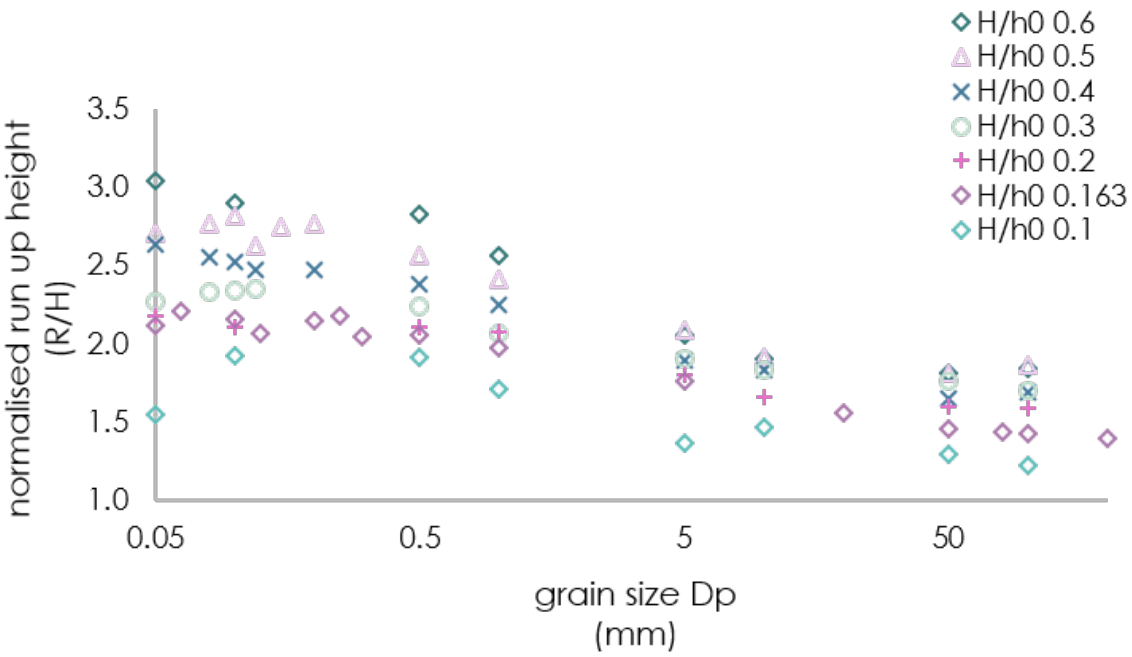

Fig. 5.13 Simulation results: maximum run-up heights for varying grain sizes, normalised by initial wave height

This behaviour can also be identified by inspection of the results plotted in Figure 5.12. The maximum run-up height, normalised by the initial still water depth, h_0, is plotted again the mean grain size (D_p), for the seven different waves heights that were investigated, so that each point on the graph represents a different simulation. For the initial set of simulations that were run $\left(\frac{H}{h_0} = 0.03423\right)$, the grain size was increased from $D_p = 0.05$mm to $D_p = 200$mm. However, subsequent simulations were only run for $0.05\text{mm} < D_p < 100\text{mm}$. The reason for this is twofold. Firstly, as highlighted in the results presented below, once D_p increased beyond 50mm, there is no observable decrease in run-up height, and secondly, as described in Chapter 4, the porous medium is modelled as a continuum, so the largest grain size investigated here are already challenging that assumption. Any increase in grain size beyond $D_p \approx 100$mm would possibly require a discrete element model to produce results that are scientifically valid. Therefore, the decision was taken to focus the investigation on the range $D_p \leq 100$mm.

Figure 5.13 shows the same simulation results, but here the maximum run-up height reached has been normalised by the initial wave height so that the respective curves collapse onto each other for easier comparison of the mitigation effect of increasing the grain size.

Inspection of Figure 5.11 suggests that the maximum run-up height does not change significantly in response to any of the wave heights until the grain size increases beyond 0.1mm. This indicates a minimum mean grain size of 0.1mm must be reached before any significant

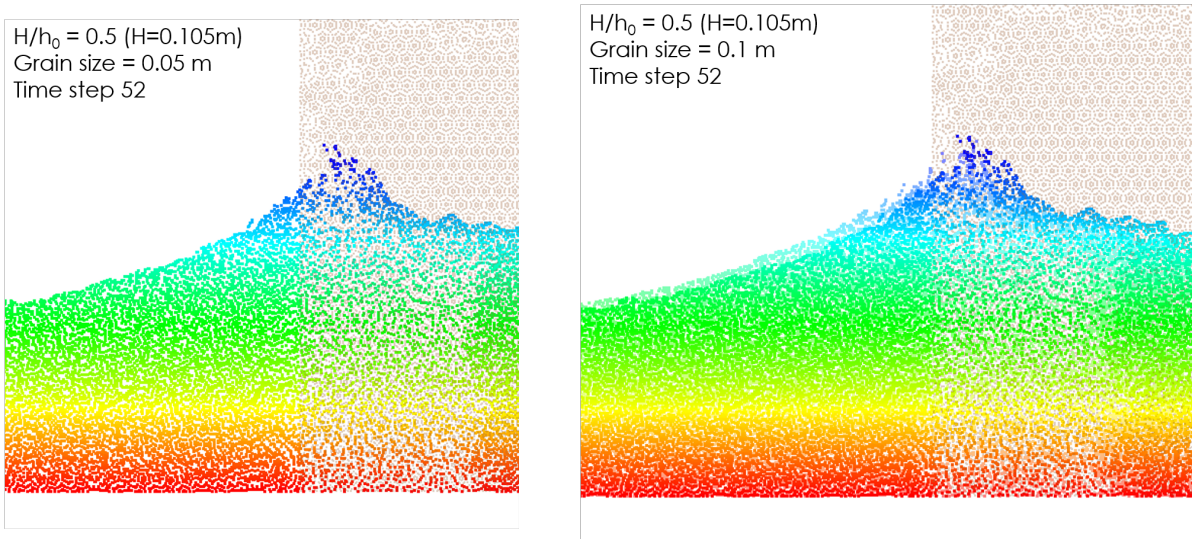

Fig. 5.14 Simulation results: comparing maximum run-up results of two large grain sizes ($D_p = 0.05$m and $D_p = 0.1$m) for $\frac{H}{h_0} = 0.5$ to show that there is only a minimal further benefit in increasing the mean grain size.

percolation occurs. Figure 5.12 suggests that a mean grain size as large as 0.5mm is necessary to see a noticeable reduction of the maximum run-up height. Figure 5.13 supports the results displayed by Figure 5.12.

Conversely, we also observe in both Figures 5.11 and 5.12 that increasing the grain size beyond 10mm does not have a significant impact on the run-up response, even when the grain size is extremely large (100 or 200mm). This is further explored in Figures 5.14 and 5.15. Figure 5.14 shows a direct comparison at the point of maximum run-up for $D_p = 0.05$m and $D_p = 1.0$m for a wave height $\frac{H}{h_0} = 0.5$. The figure on the left shows the results for $D_p = 0.5$m and the figure on the right shows the results for $D_p = 1.0$m layered on top. The contour used here represents the y-coordinate of the particle. The large wave size was selected to emphasise any difference in the two results. Despite a significant increase in the mean grain size (classed as *fine* and *medium* boulders on the Wentworth chart, respectively), the difference in the run-up response is subtle, even at this large scale. There is no practical difference in the maximum run-up height reached. Figure 5.15 shows the same two simulations as they progress through different time steps. Again, the difference between the two results is hard to perceive up to the point of impact. Although there is an observable difference in the way the wave breaks after the point of maximum run-up (timestep 54), the maximum height reached by the impacting wave remains the same. This suggests that increasing the mean grain size beyond ≈ 0.5m will have a limited effect on increasing the percolation of the wave, and thereby reducing the run-up height reached.

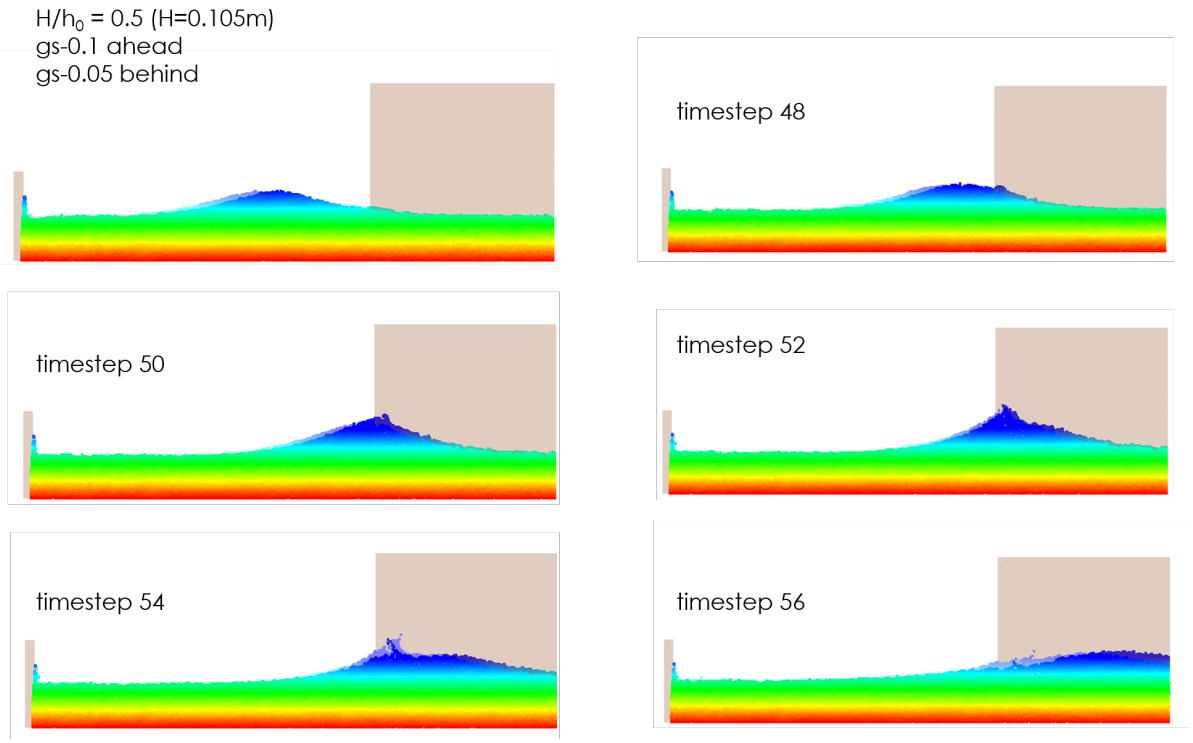

Fig. 5.15 Simulation results: comparing the progression of the wave interacting with two large grain sizes ($D_p = 0.05$ and $D_p = 0.1$m) for $\frac{H}{h_0} = 0.5$ to show that there is minimal further benefit in increasing the mean grain size.

The most significant impact on the run-up height is seen between grain sizes of 0.5mm and 5mm, where there is a sharp decrease in run-up response for all wave heights as significantly larger volumes of water percolate through the porous dam. This suggests that a mean grain size of $\approx$ 5mm is optimal for minimising the run-up response under these conditions. There is also a visible anomaly, most notable in Figure 5.12, for a wave height of $\frac{H}{h_0} = 0.5$, for $0.1m < D_p < 0.2m$, where the maximum run-up height appears to slightly increase as the grain size increases from 0.15m to 0.2m. It seems likely that this is simply due to an underestimation of the run-up height at $D_p = 0.15$m, as the method used to estimate the maximum run-up height is not precise. The overall trend indicated is not affected, and the results are broadly in agreement with the rest.

5.4.2 Wall width influence

It was demonstrated in Chapter 4 that there is a minimum wall width required for the increase in grain size to be effective in reducing the maximum run-up height reached. The simulations described above were run under the assumption that the width of the wall was sufficient for this percolation to occur. This assumption is proved here by doubling the width of the wall from 0.87m to 1.74m and re-running for a range of grain sizes and wall widths.

Figure 5.16 shows the comparison of the initial results with those where the wall width was increased. The results are in very consistent with those produced using a narrower wall, indicating that the assumption of the initial wall width being sufficiently wide to not be a limiting parameter is valid. The only result that does not sit precisely on the same curve as before is for the largest wave height investigated, and for the largest grain size. This result is also the one most likely to suffer from some unreliability due to the scattering issues that have been previously mentioned, so it seems very likely that the increase in wall width does not have an impact, but rather highlights the lack of precision in this particular result. We can, therefore, be confident that our initial assumption was valid and that increasing the width of the wall has no impact on the simulation results presented here. It also confirms the results found in Chapter 4: that the width of the wall is a limiting factor in minimising the run-up height reached by the impacting wave, rather than a dominant parameter.

5.5 Conclusions

In this chapter, the material point method has been used to investigate solitary wave interaction with a vertical sea wall constructed from porous media. The aim of this investigation was to first ratify the ability of the code to capture the interaction between a solitary wave and a permeable

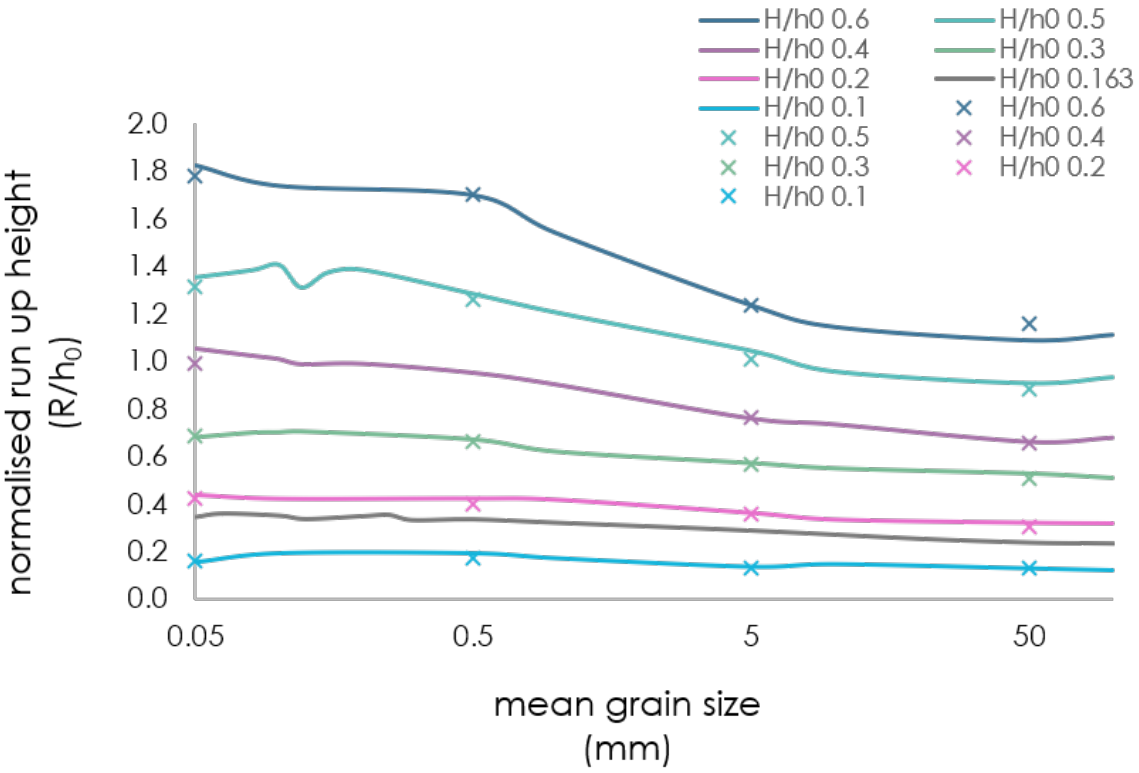

Fig. 5.16 Simulation results: maximum run-up heights for varying wave heights and grain sizes, plotted with smooth lines, with wider wall results plotted as crosses.

vertical barrier, and subsequently to determine the effect on the run-up height response of a solitary flood wave impacting on a porous vertical sea wall, when the permeability of the wall is changed via modification of the mean grain size of the constituent material. It was anticipated that increasing the grain size, and therefore the permeability, of the porous medium would reduce the maximum height reached by the flood wave since the increased permeability allows the water to percolate into the wall. This percolation allows the barrier to absorb significant wave energy via a mechanism of friction generated by the fluid-structure interaction, causing dissipation of the wave energy.

For the solitary wave case, the width of the wall is wide enough that it should not influence the run-up response, at a width of 0.87m (compared to a maximum width of 0.6m for the dam-break flood investigation). This assumption is also proved by increasing the width of the wall and comparing the results. Instead, here, the height of the impacting wave is varied as a major investigation parameter, and the run-up response is shown to follow the same form when the grain size is changed for all impacting wave heights, suggesting that the behaviour is predictable. The beneficial effect seen when increasing the grain size to approximately 50mm is proportional to the wave height, but this benefit is realised for all incoming waves. It is also clear that increasing the grain size beyond 50mm does not offer a significant benefit, regardless of the height of the impacting wave.

When compared with experimental data and results using other verified numerical methods (such as MPS, MAC, ISPH and WCSPH) published by various research groups, the MPM simulations gave good predictions of the solitary wave run-up on a vertical sea wall. The material point method is thus demonstrated to be an appropriate method for this application.

The effect of increasing the mean grain size of the constituent material, of a vertical sea wall, on the maximum run-up height reached in response to solitary waves, of varying heights, was investigated using MPM. The wall width was also increased to ensure that this is not a limiting parameter when we are investigating the effect of modifying the grain size. Increasing the width of the wall had no impact on the effectiveness of the permeable sea wall. We can, therefore, state that the dominant parameter here is the grain size.

Increasing the mean grain size of the porous medium forming the sea wall significantly reduced the maximum run-up height reached by the incoming waves. For the largest wave height investigated $\left(\frac{H}{h_0} = 0.6,\ H = 0.126\text{m}\right)$, the maximum normalised run-up height $(\frac{R}{h_0})$ reached by the broken wave was reduced from 1.83m in the worst case of a solid wall to 1.09m (for a constituent mean grain size of $D_p = 50$mm), thus demonstrating that the run-up response to an incoming solitary wave flood can be significantly reduced by increasing the permeability of the barrier to allow the water to fully percolate and dissipate the maximum possible amount

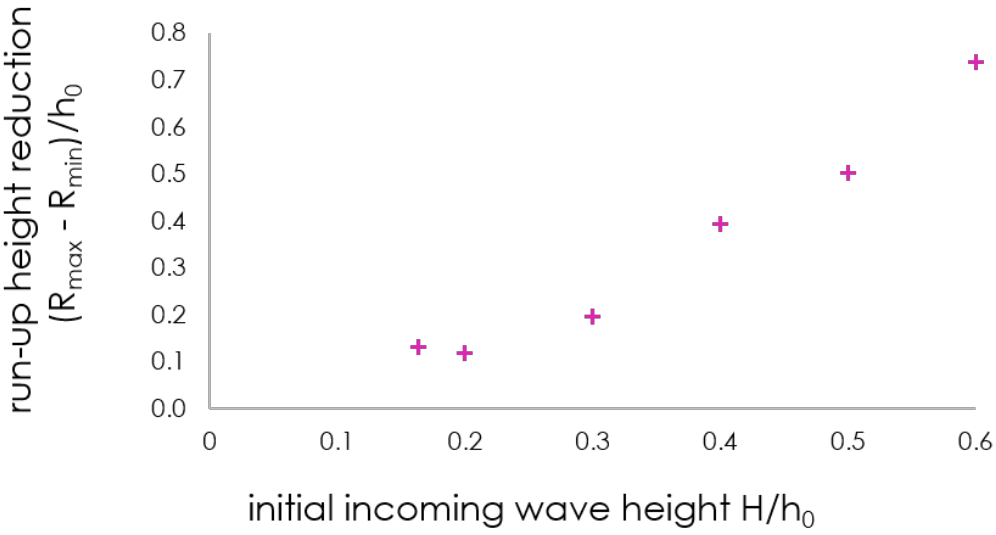

Fig. 5.17 Simulation results: reduction in maximum normalised run-up height compared to incoming wave height

of energy from the impacting wave. The benefit of increasing the mean grain size is emphasised when the incoming wave height is greater. This is demonstrated in Figure 5.17.

An even greater reduction in run-up may be possible with larger grain sizes; however, modelling a material would such a large grain size would require an alternative material model, such as the discrete element method, since a grain size greater than $\approx$ 100mm can no longer be realistically described as a continuum.

Overall, permeable vertical sea walls have been demonstrated to offer significant potential benefits to flood mitigation strategies, whether in response to dam-break floods or solitary waves. The material point method is demonstrated to be an appropriate method of capturing the flow behaviour, fluid-structure interaction, and run-up response. To be effective, the permeable sea wall should be wide enough that the maximum amount of energy can be absorbed from the wave. In these simulations, this is achieved when the width of the barrier is approximately three times the initial height of the wave. The initial height of the impacting wave does not affect the response to increasing grain size, however, larger initial wave heights will result in a higher run-up response. The most effective mitigation of the run-up response is seen when the initial wave is very large. The most beneficial response is seen at a mean constituent particle diameter of $D_p \approx$ 50mm, any increase beyond this has a negligible effect in all the situations that have been investigated thus far.

Chapter 6

Solitary wave run-up on sloped beaches

6.1 Introduction

This chapter describes parametric numerical investigations into the run-up response behaviour of a solitary wave impacting on a permeable sloped beach. The parameters investigated include waves of different initial height interacting with beaches formed of a permeable constituent material that has a varying mean grain size. The investigations in this chapter were carried out on a steep beach with slope angle $\beta = 1:2.08$. This slope is steep enough that all impacting waves remain unbroken, according to the wave breaking criterion proposed by Gjevik and Pedersen (1981) whereby the wave will break when $H/h_0 < 0.479\ \cot\beta^{-\frac{10}{9}}$ [45].

The results are compared to published data for experimental and theoretical results for the run-up of solitary waves on plane beaches to verify the results of the simulations and establish the ability of the MPM code to produce reliable results in this application. Particular attention is paid to comparing the results produced in this investigation to those published by Li and Raichlen (2002) [87], and to the analytical theory published by Synolakis (1987) [141]. It is demonstrated that the material point method is a suitable method for modelling wave run-up on plane beaches.

The focus of the investigation is the changing wave run-up response when the permeability of the beach is changed, by altering the representative mean grain size of the constituent particles forming the beach. The run-up height, normalised by the initial still water depth, is compared to the normalised wave height to establish an empirical relationship between run-up height and grain size; and to provide design guidance for coastal flood defences. The amplitude of the impacting wave is also varied, to establish if the relationship between run-up response and permeability varies for differing wave heights.

6.1.1 Motivation

The run-up level reached by incoming waves is one of the most important factors affecting the design of coastal flood defence structures such as dykes, revetments, and breakwaters [61, 144]. Many cases of coastal inundation occur during extreme events such as tsunamis or storm surges driven by strong winds when the maximum wave run-up exceeds the height of the sloped beach. These waves are generally modelled as solitary waves [141]. Wave run-up is thus one of the main physical processes accounted for during the design process of coastal flood defences [9]. Accurate and reliable prediction of the maximum run-up height is the key to successfully planning coastal flood management. Furthermore, the run-up height reached by incoming storm surge waves is a critical parameter in assessing the potential effects of the rising sea-levels and more extreme storms that are occurring as a result of anthropogenic global climate change and leading to a corresponding increase in both the frequency and severity of coastal inundation. Consequently, the interest of coastal engineers is primarily focused on the estimation of extreme run-up during storm conditions, essential for accurate predictions of the impact of storm surges on coastal areas. Successful prediction of run-up height is therefore crucial in any flood mitigation effort.

Wave run-up may be affected by many parameters, including, but not limited to geometric and structural characteristics of the sloped beach itself such as:

- Surface roughness
- Permeability
- Porosity

Hydraulic parameters of the impacting wave such as:

- Wave steepness
- Wave height
- Angle of attack

This investigation focuses on the permeability of the slope and the wave height as investigative parameters, seeking to ascertain the maximum run-up height reached by perpendicular solitary waves approaching a steep plane beach. The surface roughness is not considered here. This chapter investigates the effect of manipulating the mean grain size of a porous beach on the run-up response to unbroken solitary waves of different amplitudes, using the material point method.

6.1.2 Previous research

When considering the potential run-up response to wave attack, the interaction that occurs between the fluid and the structure is a key factor in determining how effective the flood defence will be. Whilst the process of long-wave generation and propagation is well understood, the processes involved in wave run-up are not. It is clearly understood that the run-up variation is different for breaking and non-breaking waves [141] [87] so we should consider carefully which category each situation is encompassed by. The study of the run-up of non-breaking waves has led to the development of analytic solutions for increasingly complex situations. Surface profiles developed from the nonlinear analytic theory have been shown to adequately model the climb of non-breaking waves [141].

Further, whilst previous studies have investigated solitary wave run-up on plane beaches (Monoghan and Kos (1999) [111], Kim and Ko (2008), [73], Rasoul and Kourosh (2012) [108]), many of these studies assume that the sloped beach is smooth and impermeable. In the real world, however, beaches are generally formed of porous media such as sand, soil or gravel. An accurate prediction of run-up height on sloped beaches, therefore, requires the inclusion of a material model that fully encompasses the permeable nature of the material forming the beach.

Initially, Heitner and Housner (1970) used the long wave equation, in Lagrangian coordinates, to investigate solitary wave run-up. Further analytic solutions can be grouped according to their fundamental equation base: those based on the Boussinesq equations such as Pedersen and Gjevik (1983) and Zelt (1986) who worked using Lagrangian coordinates, and the work of Kim, Liu and Ligett (1983) who solve these equations using boundary integral methods. The other group of analytic solutions have been developed from the shallow-water wave equations, two nonlinear equations that arise directly from the Boussinesq equations when the effects of dispersion and vertical accelerations are considered to be negligible. Lewy (1946) published the classic solution of the linear form of these equations for the case of periodic waves impacting on a sloped beach. Carrier and Greenspan (1958) then derived a nonlinear transformation that reduced the two nonlinear equations to a single, linear equation and solved this for several initial value problems. Keller and Keller (1964) then solved the linear problem of a periodic wave in a tank of constant depth and then impacting on a sloped beach. Regular, weak and apparent solutions of the two nonlinear equations were summarised by Meyer (1986).

Hibberd and Peregrine (1979) calculated the run-up of a uniform, fully turbulent bore on a plane beach, accounting for energy dissipation using a Lax-Wendroff scheme, but no attempt was made to model turbulent fluctuations through the bore [54]. This study also neglected the effects of bottom friction, and subsequently, the run-up heights were considerably overestimated, particularly for shallow slopes. Zelt and Raichlen (1990) [164] then developed a Lagrangian representation of the Boussinesq equation, using a finite-element model to investigate the

run-up response to solitary waves in both 2D and 3D bathymetry. Zelt (1991) then applied this model to the case of run-up for both breaking and non-breaking waves on a planar beach [163], including additional terms in the model equations to model dissipation due to both bottom friction and turbulence generated by wave breaking and bore propagation, finding that for cases where waves do not break on run-up, bottom friction does not play an important role and can, therefore, be neglected for smooth impermeable beaches with slopes greater than 20°. Wave breaking and bore propagation were modelled using an artificial viscosity technique, which smooths excessive velocity gradients in the breaking regions which otherwise lead to numerical fluctuations. Despite not attempting to model turbulent fluctuations, or flow details in the breaking region, reasonably accurate numerical predictions of run-up and reflection of breaking solitary waves on sloped beaches were obtained [163]. Grilli (1997) used boundary element techniques to solve a fully non-linear potential flow model for breaking solitary waves on steep and shallow beaches[49]. Zhang (1996) modelled run-up of ocean waves using a finite-difference scheme for the shallow water and Boussinesq equations that remaps grid points at the surface according to the instantaneous shoreline position [167].

However, there remains no analytic solution for the empirical relationships between the normalised run-up height and the normalised wave height that have been established experimentally, and there is a lack of conclusive evidence with regards to the relative importance of dispersion and non-linear effects during the run-up phase [141]. This investigation focuses on using numerical methods to determine the run-up response for a range of incident non-breaking solitary wave heights on porous media of varying permeability for the case of a steeply sloping beach.

6.2 Material parameters

For the sloped beach simulations, the liquid water is modelled as a Newtonian fluid with material parameters $\rho = 1000$, $K = 20000$, and $\mu = 1e^{-6}$, where ρ is the density $\left[\text{ kg/m }^3\right]$, K is the bulk modulus [kPa], and μ is dynamic viscosity [kg/m $\cdot$ s]. The dry porous beach is modelled as a linear elastic material, with material parameters $n = 0.43$, $\rho = 2650$, $K_0 = 0.5$, $E = 10000$ and $\nu = 0.3$, where n is the initial porosity [no units], ρ is the density, as before, K_0 is coefficient of lateral earth pressure [no units], E is Young's modulus [kPa] and ν is Poisson's ratio [no units]. The saturated porous beach is modelled as a fully coupled saturated linear elastic material, with material parameters $n = 0.43$, $\rho = 2650$, $K_0 = 0.5$ and $E = 10000$, for the solid phase, and $\rho = 1000$, $K = 20000$, and $\mu = 1e^{-6}$, and $\nu = 0.3$ for the liquid phase. Finally, the paddle is modelled as a linear elastic material, with material properties $n = 0.42$, $\rho = 2650$, $K_0 = 0.5$, $E = 10000$ and $\nu = 0.3$.

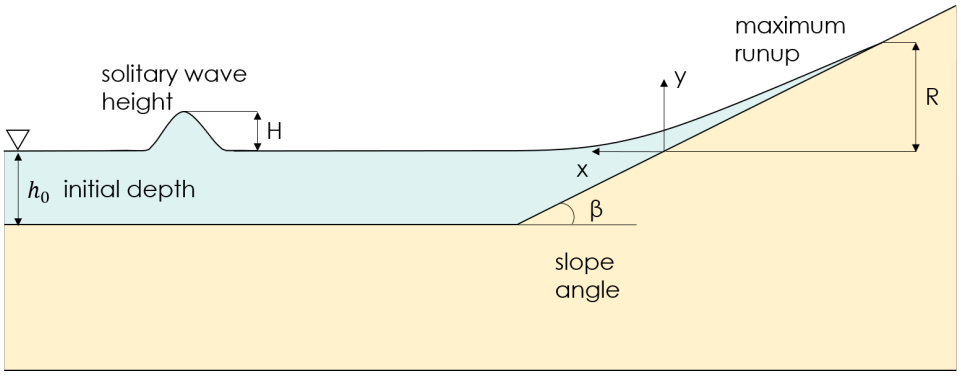

Fig. 6.1 Problem definition sketch for the case of a solitary wave climbing a steeply sloping beach

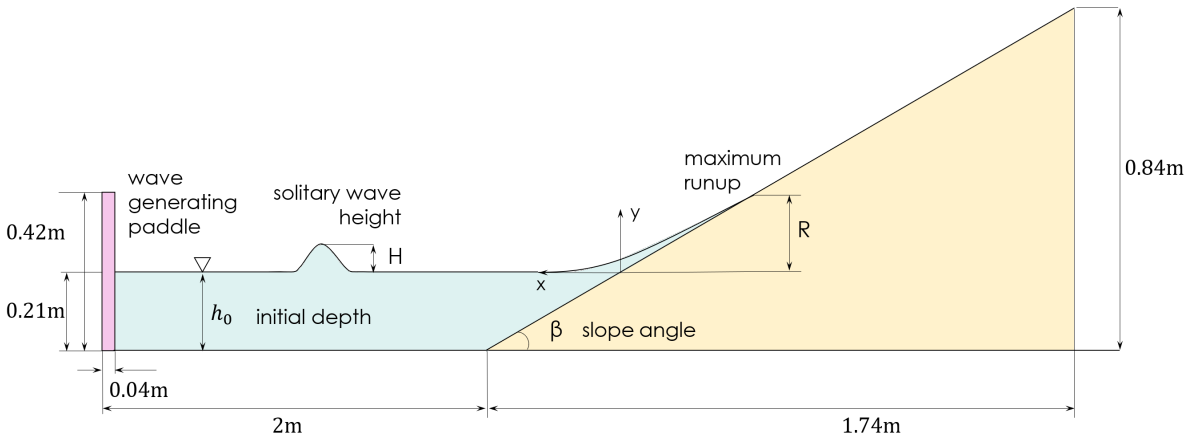

Fig. 6.2 The computational domain dimensions used for the numerical investigation of a solitary wave impacting on a steep slope.

The steeply sloping beach simulations used the Anura3D double-point MPM code. A problem definition sketch for the sloping beach case is shown in Figure 6.1. The initial depth d is 0.21m and the slope angle β is 26° so that the steepness of the slope is 1:2.08. For these initial simulations where the wave height is not varied, the initial wave height H is 0.03423m so that H/h_0 is 0.163. This wave height is chosen to match the studies used for verification. The grain size was varied between 0.05mm (extremely fine sand to simulate a solid surface) and 200mm (a very large grain size representative of large cobbles). Useful values for grain sizes to investigate were selected from the Wentworth size chart, shown in Table 4.1. The computational domain used for these investigations is shown in Figure 6.2.

The material assignment for the steeply sloped beach is shown in Figure 6.3. As described in Section 5.2.3, this includes the wave-generating paddle. The paddle material must be differentiated from the beach material so that we can specify a velocity to these material points. This is achieved by specifying a different initial porosity. Any element with an initial porosity below 0.425 is recognised as forming part of the *paddle*.

The material point assignment is shown in Figure 6.4. The liquid water has 3 fluid material points specified per element, and the dry beach and paddle have 3 solid material points specified per element. The saturated beach has 3 solid material points and 3 fluid material points generated per element. The mesh in these simulations is very fine, so fewer material points are required.

The grid spacing for the sloped beach simulations is specified as 0.02m, shown in Figure 6.5. No horizontal fixity is applied to the leftmost surface, to allow the paddle to move. These parameters are summarised in Table 6.1.

Table 6.1 Calculation and material parameters used in the simulations of a solitary wave running up on a sloped beach

	Parameter	*Value*	*Unit*
Mesh properties	Mesh size	0.02	m
	Number of elements	$6,111-7,938$	-
	MPs per element	12 fluid, 12 solid	-
Fluid properties	Density	1000	kg/m^3
	Bulk modulus	20,000	kPa
	Dynamic viscosity	$1e^{-6}$	kPa · s
Solid material properties	Density	2650	kg/m^3
	Young's modulus	10,000	kPa
	Initial porosity	0.43	[no units]
	Lateral earth pressure	0.5	[no units]
	Poisson's ratio	0.3	[no units]

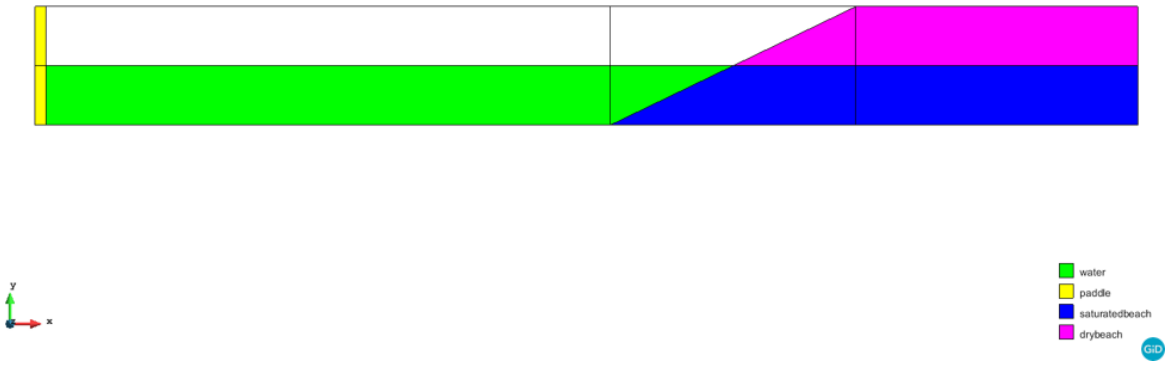

Fig. 6.3 The material assignment for the steeply sloped beach case

A two-phase double-point simulation type is used, with a Courant number of 0.8 to ensure the stability of the solution. No smoothing is used and no damping is applied, which is recommended for the double-point code. For each case, the maximum allowable porosity is 0.95. This parameter distinguishes the solid states and liquid states and it must at least be larger than the initial porosity of the soil. Otherwise, the soil is determined to be liquefied when the simulation begins. A more in-depth discussion of this porosity parameter may be found in Chapter 3.1, with particular reference to Figure 3.7. The porosity of the beach is not varied in these simulations, only the grain size is altered to modify the permeability of the material.

The solitary wave is generated using the same method described in Chapter 5: by specifying the velocity of the material points that form the paddle, as discussed in sections 5.2.3, for the case of the vertical sea wall.

6.3 Model Validation

The MPM model for establishing the run-up height of solitary waves incident on sloped beaches has been verified by extensive comparison with various published numerical and experimental data. The results produced by the MPM code were initially compared with the approximate non-linear theory developed by Synolakis (1987) [141], and subsequently with the revised non-linear theory and corresponding experimental results published by Li and Raichlen (2002) [87]. Li and Raichlen studied the run-up of non-breaking solitary waves on a uniform plane beach, finding an analytic non-linear solution to the classical shallow water equations based on the complete Carrier and Greenspan transformations (1958) [25], and thus demonstrating that the

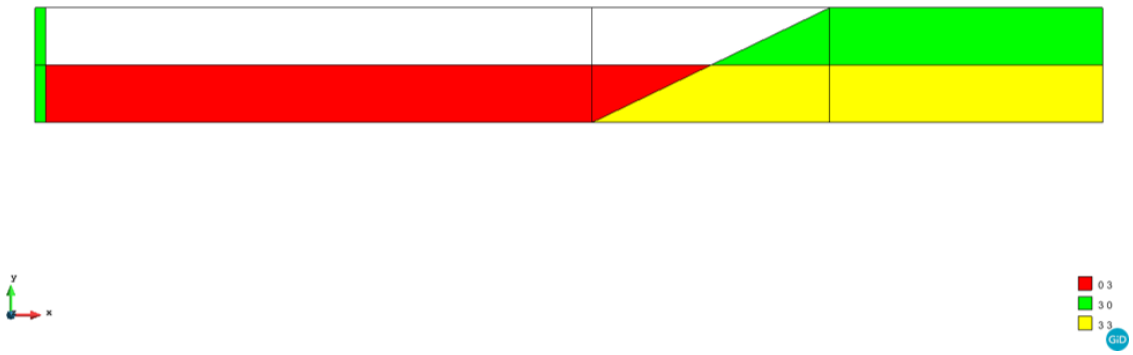

Fig. 6.4 The material point assignment for the steeply sloped beach case

Fig. 6.5 The mesh generated for the steeply sloped beach case, with grid spacing 0.02m

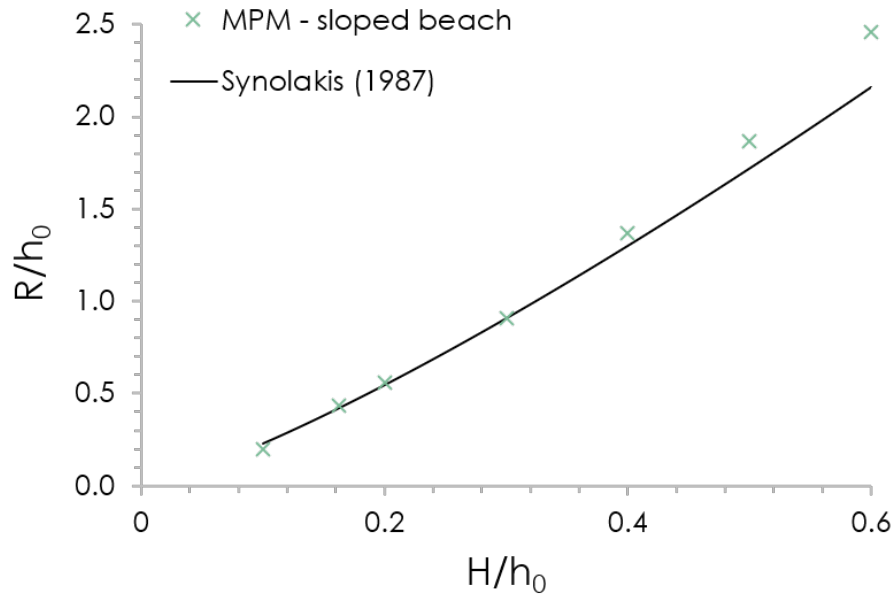

Fig. 6.6 Comparison of results produced using the material point method with the theory developed in 1987 by Synolakis for the run-up on a sloped beach for different attacking wave heights

high-order correction that they proposed to the approximate non-linear theory of Synolakis (1987) is in much better agreement with the experimental results produced for non-breaking solitary wave run-up [87].

Figure 6.6 shows a comparison of results produced using the material point method to the analytic theory developed in 1987 by Synolakis for the run-up on a sloped beach for different attacking wave heights. The theory developed by Synolakis describes the run-up height R in terms of the wave height H as

$$\frac{R_s}{h_0} = 2.831\sqrt{\cot\beta}\left(\frac{H}{h_0}\right)^{\frac{5}{4}} \tag{6.1}$$

where R_s is the run-up height according to Synolakis, h_0 is the initial still water depth and β is the slope angle, which in this case is 26° so that cot β is 2.08. This nonlinear approximation can be viewed as an extension of the linear theory developed by Carrier and Greenspan (1958), which reduces the shallow water equations to a single linear equation [25]. There is a notable difference between the MPM results and the analytical theory, particularly for larger initial wave heights.

Li and Raichlen, 2002 [87] proposed an adaptation to the approximate nonlinear theory developed by Synolakis (1987) that is one order higher, to resolve the issue of determining

accurate boundary conditions and initial conditions in the (σ, λ) space utilised by Carrier and Greenspan (1958) to reduce the shallow water wave equations to a single linear equation. Li and Raichlen (2002) suggest that the solution of the linear shallow water equations using a higher-order boundary condition should be more accurate than both linear and approximate nonlinear solutions [87]. The maximum run-up obtained from the theory developed by Li and Raichlen is obtained as

$$\frac{R}{h_0} = \frac{R_s}{h_0} + \frac{R_{cr}}{h_0} = \frac{R_s}{h_0}\left(1 + \frac{R_{cr}}{R_s}\right) \tag{6.2}$$

with R_s being the maximum run-up according to Synolakis, as before in equation 6.1, and R_{cr} is a correction factor applied to the approximate theory based on the non-linear approach presented by Li and Raichlen (2002) where

$$\frac{R_{cr}}{h_0} = 0.293 \left(\cot\beta\right)^{\frac{3}{2}} \left(\frac{H}{h_0}\right)^{\frac{9}{4}} \tag{6.3}$$

such that

$$\frac{R_{cr}}{R_s} = 0.104 \cot\beta \frac{H}{h_0} \tag{6.4}$$

and thus the non-linear run-up is differentiated from the linear run-up by the inclusion of an extra term. This extra term is a function of the initial relative incident wave height and the beach slope angle. The significance of the correction factor can be seen in Figure 6.7, where the results produced using the material point method are compared to the approximate non-linear theory of Synolakis, as well as the numerical results for the revised non-linear theory developed by Li and Raichlen, and the experimental results published in the same paper.

Figure 6.7 shows that the differences between the results of the non-linear theory of Li and Raichlen and the approximate non-linear theory of Synolakis are small, especially for smaller waves, and diverge slightly as initial wave height increases. This is expected - when the correction term R_{cr}/R_s is plotted as a function for the relative wave height H/h_0 for constant slope angle β, it can be demonstrated that the *wave breaking limit* limits the relative height of non-breaking waves for which either of the two theories can be applied [87]. The limit of relative wave height for the wave breaking during run-up is given in Synolakis (1986) as

$$\frac{H}{h_0} = 0.8183 \left(cot\beta\right)^{-\frac{10}{9}} \tag{6.5}$$

Even at the wave breaking limit, the non-linear correction term varies only from 5% to 8% for slope angles from 1:200 to 1:2, respectively, so that for any practical engineering application

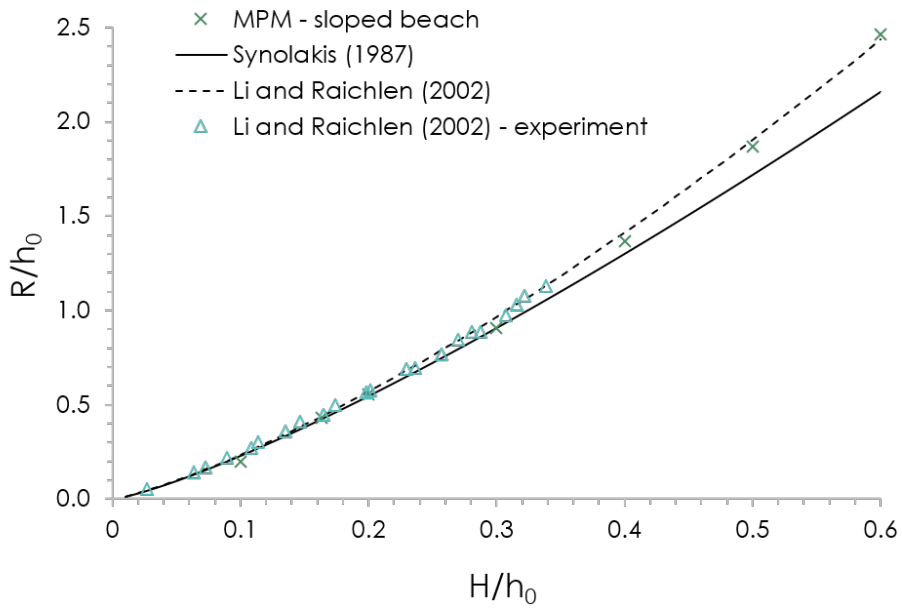

Fig. 6.7 Comparison of results produced using the material point method with the approximate nonlinear theory of Synolakis and the nonlinear theory developed by Li and Raichlen

the approach of Synolakis is sufficient to predict the maximum run-up of non-breaking solitary waves, however, it is clear from the experimental results that the revised non-linear theory presented by Li and Raichlen (2002) represents a better prediction of the run-up process than the earlier approximate non-linear theory of Synolakis (1987), at most an improvement in accuracy of around 10%. Overall, when the correction to the approximate non-linear theory proposed by Li and Raichlen (2002) is applied, very good agreement between experimental and numerical results is achieved. The results produced using the material point method closely match the experimental and numerical results of Li and Raichlen (2002), demonstrating that the material point method provides reliable results for the run-up of solitary waves on plane beaches and is, therefore, an appropriate method for this investigation.

The sloped beach simulations were further verified by comparison of the free-surface profiles with those published by Li and Raichlen in their 2002 paper *"Solitary Wave Runup on Plane Slopes"* [87]. The comparison of the free-surface profiles for four different stages of the run-up for the case where $H/h_0 = 0.163$ is shown in Figure 6.8. In the initial stages of run-up, the difference between the two theories and the experimental data is small. As the run-up proceeds, the nonlinear theory of Li and Raichlen agrees better with the experimental results than the approximate nonlinear theory of Synolakis. This is expected since the nonlinear

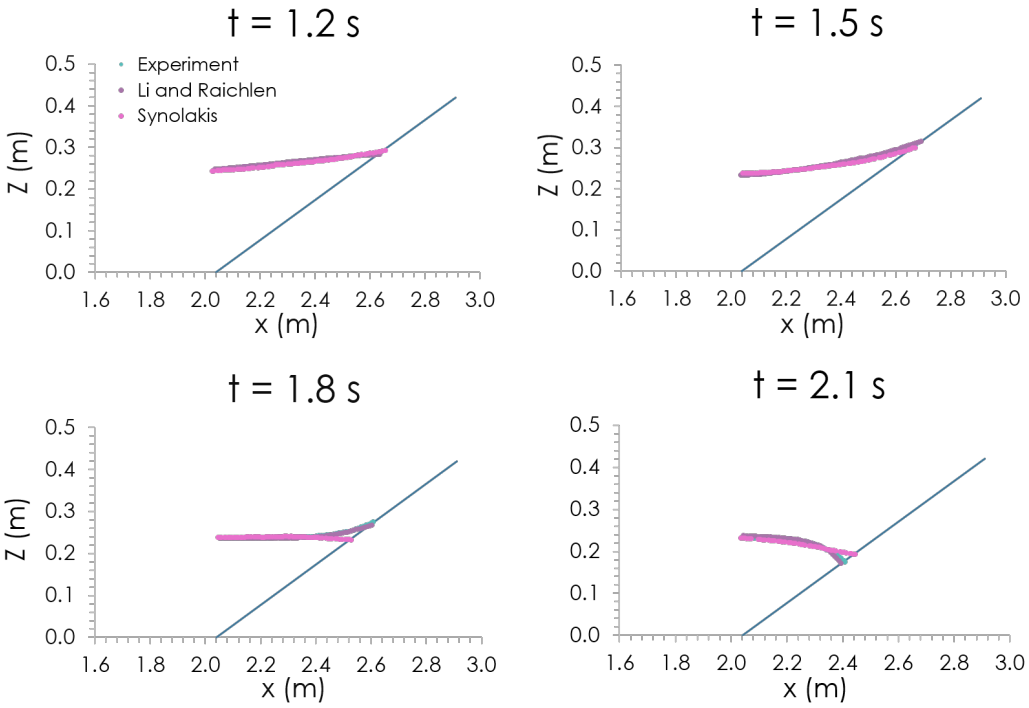

Fig. 6.8 Comparison of the run-up of a solitary wave with $H/h_0 = 0.163$ on a 1:2.08 slope with results published by Li and Raichlen (2002) and with the approximate nonlinear theory of Synolakis (1987). Normalised surface profiles are shown as a function of normalised distance at different times

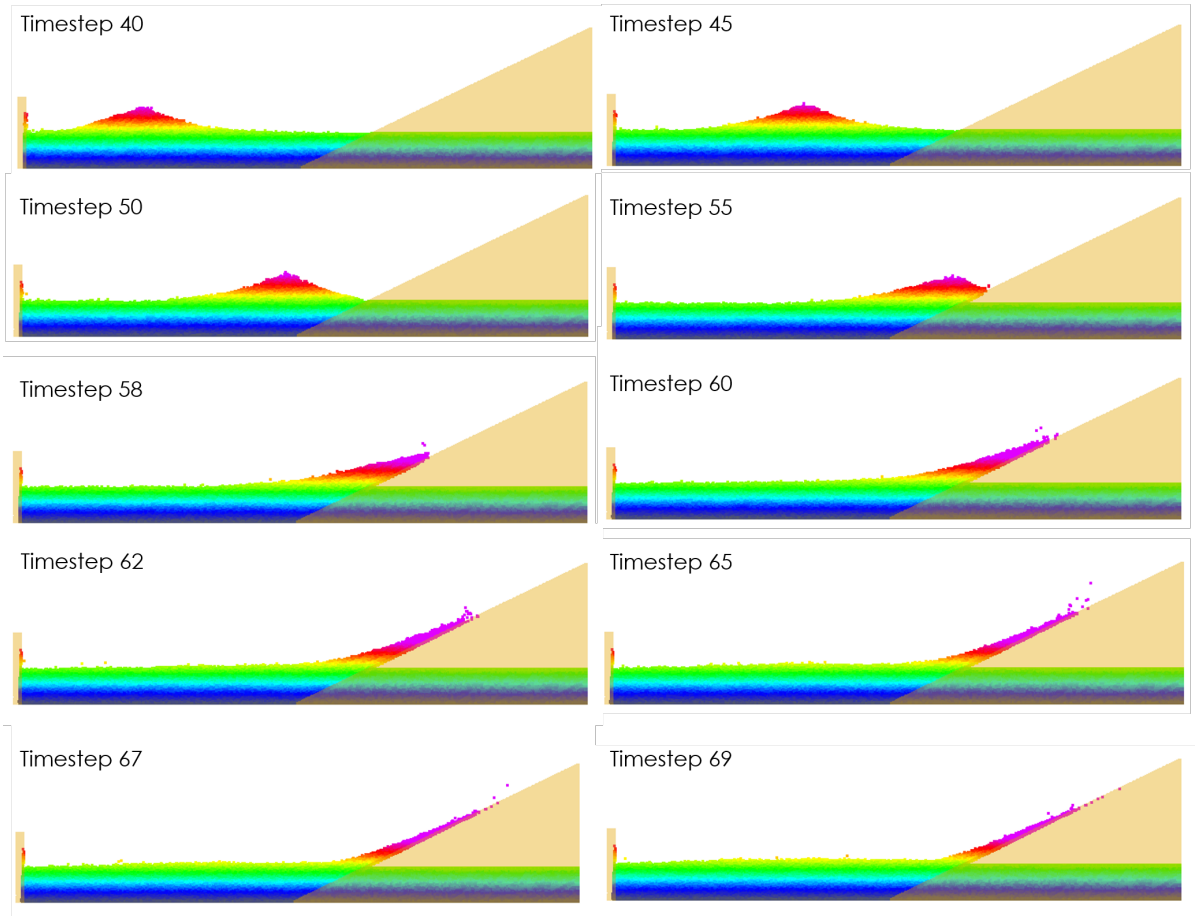

Fig. 6.9 Free-surface profile development throughout time for a small grain size ($D_p = 0.05$mm) and a wave height of H=0.105m $\left(\frac{H}{h_0} = 0.5\right)$

effects become increasingly significant as the run-up process proceeds [87]. It should also be noted that both theories agree well with experimental and numerical data as the distance offshore from the shoreline increases, supporting the assumption that nonlinear effects can be neglected offshore of the toe of the slope, and around the region of the toe. However, in the area of peak run-up, the nonlinear theory tends to overestimate the run-up amplitude, which may be due to frictional effects, or the effect of the use of the meniscus to define the peak run-up in the physical experiments [87].

6.4 Results and discussion

Figures 6.9 and 6.10 show the free-surface profile development throughout time for a small grain size ($D_p = 0.05$mm) and a large grain size ($D_p = 50$mm), for the case when the initial wave height H=0.105m $\left(\frac{H}{h_0} = 0.5\right)$. On observation of these figures, it is very clear how

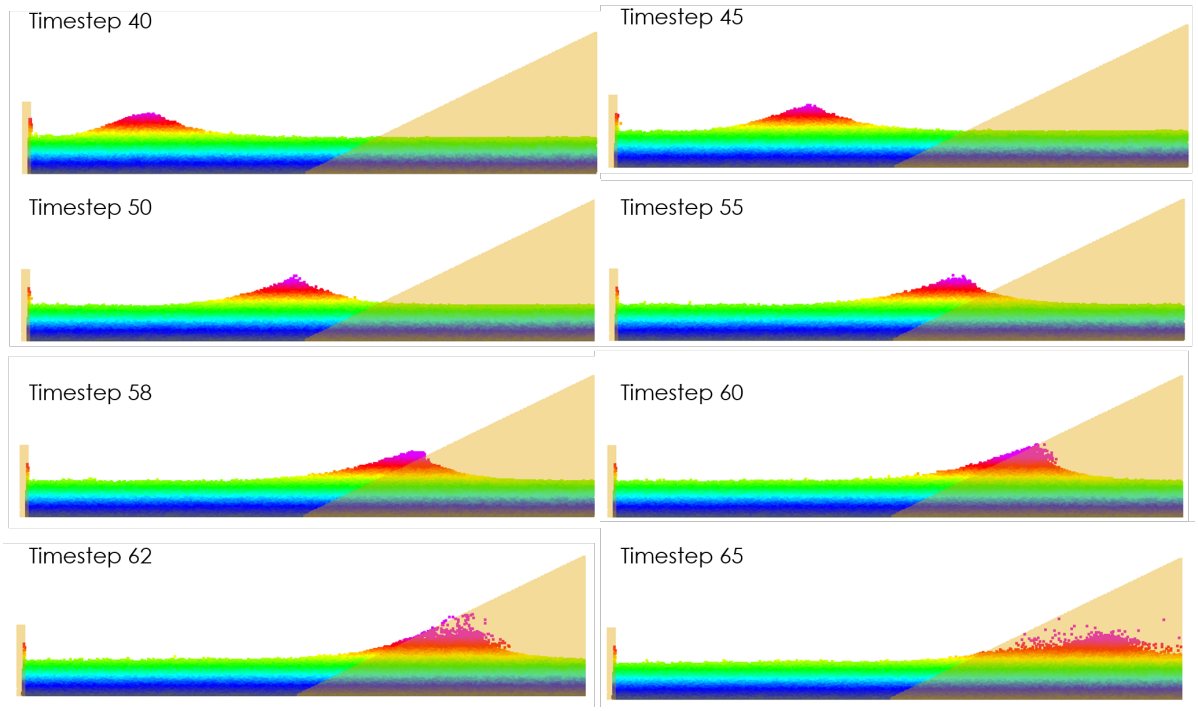

Fig. 6.10 Free-surface profile development throughout time for a large grain size ($D_p = 50$mm) and a wave height of H=0.105m $\left(\frac{H}{h_0} = 0.5\right)$

the increased mean grain size of the porous beach increases the permeability of the medium, allowing the incoming wave to percolate into the beach and thus reducing the maximum run-up height via frictional dissipation of wave energy. In Figure 6.9, where the mean grain size is very fine, the wave generated by the paddle travels through the still water and on reaching the impermeable, steeply sloping beach, the wave rapidly climbs the beach, reaching a maximum run-up height in timestep 67 where the fluid is spread in a very thin layer along the surface of the beach, before beginning the process of run-down. By contrast, in Figure 6.10, where the grain size is very large, the wave generated by the paddle flows into the permeable beach. This percolation is visible from timestep 55 onwards. As the wave progresses, it continues to flow into the beach, climbing the slope as friction generated by the soil-water interaction slows the flow within the sand. The maximum run-up height is now reached at timestep 62, at a much lower height. The wave continues to flow through the permeable beach during the run-down process, with the propagation speed significantly reduced.

Figure 6.11 shows a comparison of the wave shape formed by the solitary wave at the point of maximum run-up on a sloped beach that is constructed from a material with increasing mean grain size. The top two diagrams show wave impact for the smallest grain sizes investigated, the middle two diagrams show a medium grain size, and the final diagram shows the shape of

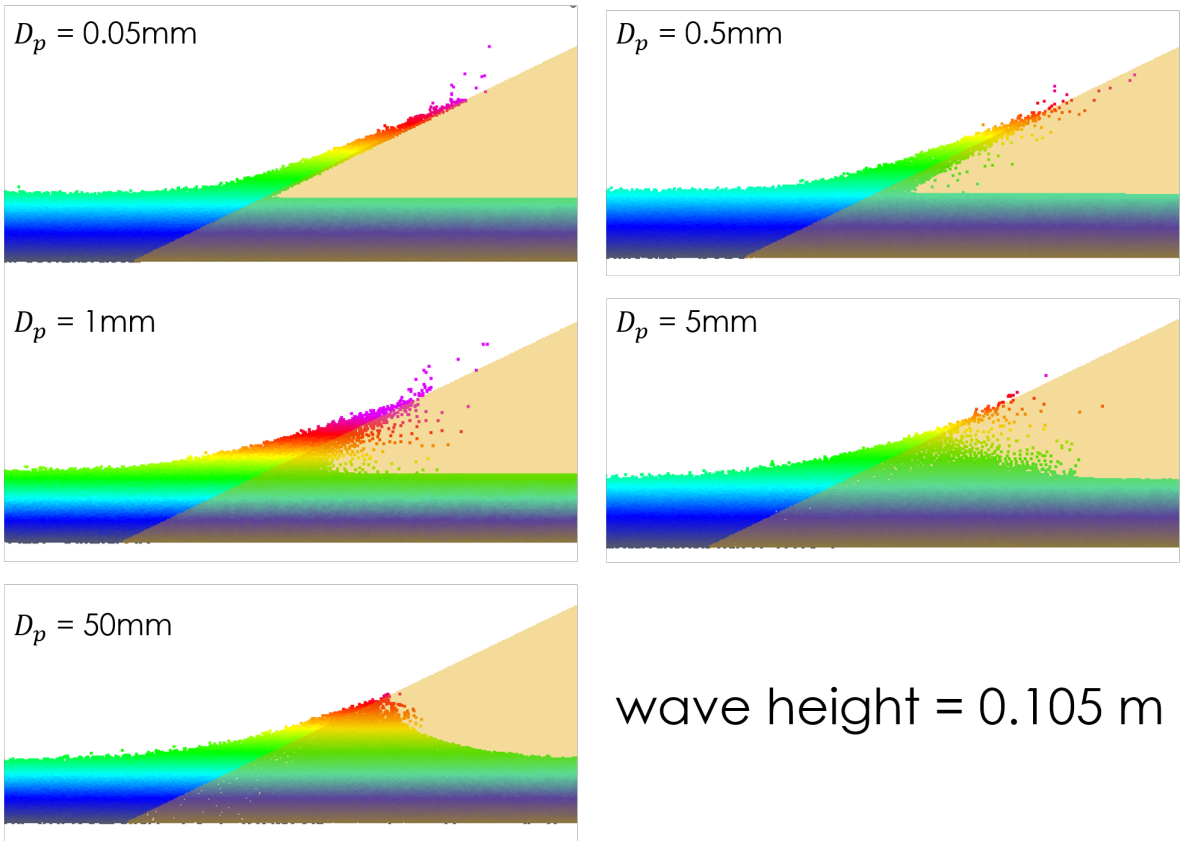

Fig. 6.11 Simulation results: maximum run-up heights at the point of impact for varying grain sizes at a wave height of H=0.105m $\left(\frac{H}{h_0} = 0.5\right)$

the wave at the point of impact for the largest grain size ($D_0 = 50$mm). All figures presented here are taken from the case where the initial wave height H is 0.105m so that $H/h_0 = 0.5$. This wave height was select for the example since the wave is sufficiently large enough that the effect of changing the grain size on the run-up response is clear to the observer, however, the wave height is not so high that the impact of the wave on the beach causes the particles to scatter.

Figures 6.12 and 6.11 show that when the grain size is 0.05mm, the permeable barrier behaves as a solid wall, which demonstrated by a complete lack of percolation of the water into the barrier. The extremely fine-grained case ($D_p = 0.05$mm) was used in the validation studies presented in the previous section as a means of studying the wave impact on a solid wall. On examination of the different studies presented, it is clear that, per the hypothesis, where the permeability of the porous medium increases as a result of the increase in mean grain size, a larger volume of water percolates into the porous beach, thus reducing the maximum run-up height reached by the impacting wave. However, for the largest grain sizes, such as those

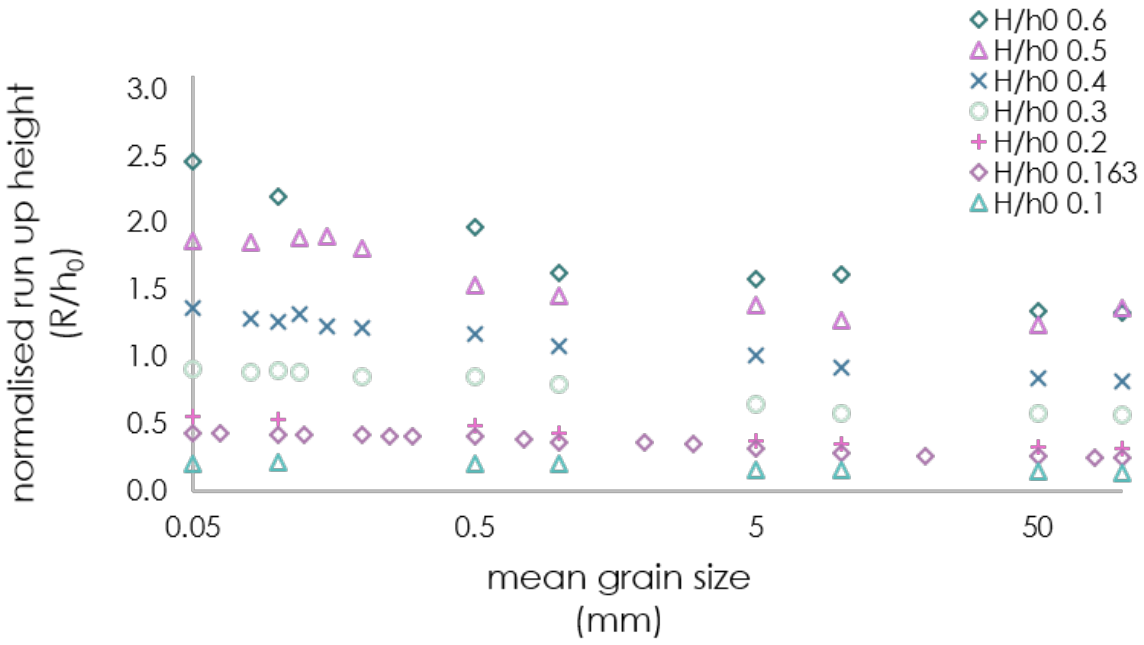

Fig. 6.12 Simulation results: maximum run-up heights for varying wave heights and grain sizes

displayed on the bottom left of Figure 6.11, although the mean grain size increases, the benefit of the increased permeability is not manifested in a reduction of the run-up height reached.

Figure 6.12 shows the maximum run-up height, normalised by the initial still water depth, h_0 plotted again the mean grain size (D_p), for the seven different waves heights that were investigated, so that each point displayed on the graph represents a different simulation. For the initial set of simulations that were run $\left(\frac{H}{h_0} = 0.03423 \right)$, the grain size was increased from $D_p = 0.05$mm to $D_p = 200$mm. However, subsequent simulations were only run for $0.05\text{mm} < D_p < 100\text{mm}$. The reason for this is twofold. Firstly, as highlighted in the results presented below, once D_p increased beyond 50mm, there is no observable decrease in run-up height, and secondly, as described in Chapters 4 and 5, the porous medium is modelled as a continuum, so the largest grain size investigated here are already challenging that assumption. Any increase in grain size beyond $D_p \approx 100$mm would realistically require a discrete element model to be scientifically valid. Therefore, the decision was taken to focus the investigation on the range $D_p \leq 100$mm.

Figure 6.13 shows the same simulation results, but here the maximum run-up height reached has been normalised by the initial wave height so that the respective curves collapse onto each other for easier comparison of the mitigation effect of increasing the grain size.

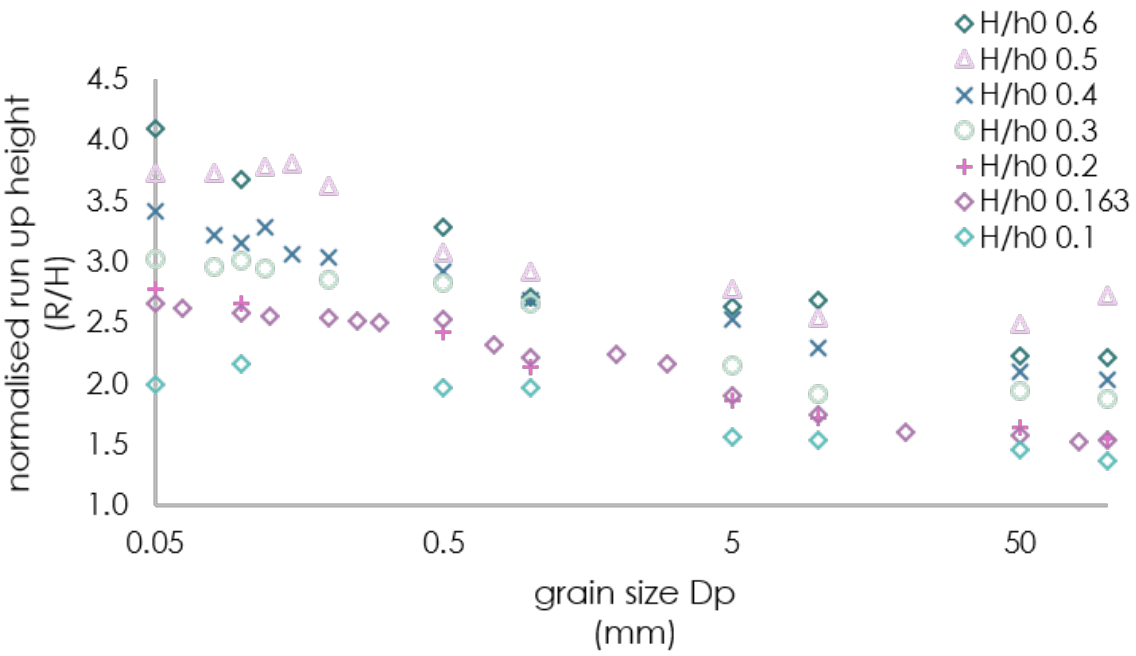

Fig. 6.13 Simulation results: maximum run-up heights for varying grain sizes, normalised by initial wave height

Inspection of both Figure 6.12 and Figure 6.13 tells us that, with the exception of the largest wave height investigated, the maximum run-up height does not change significantly in response to any of the wave heights, until the grain size increases beyond 0.1mm. This suggests a minimum mean grain size of ≈ 0.1mm before any notable percolation begins to occur for most cases. As previously mentioned, for the very large initial wave height, there is considerable particle scattering present in the results, making precise identification of the maximum run-up challenging. For this reason, it is the trend that is important, rather than the individual results, since we cannot be sure of the possible error margin here. It may be, therefore, that the initial decrease in run-up height at very small grain sizes which is observed in this instance only, is an artefact of this uncertainty rather than a true reduction in the run-up as a result of percolation. Figure 6.14 shows these two sets of simulation results at the point of maximum run-up for comparison. By inspection, there appears to be very little difference in percolation between the two situations, and the run-up height may have a trivial reduction, but it is not possible to say definitively. For the other initial wave heights, there is no reduction in the run-up height observed for these grain sizes.

Figure 6.13 suggests that a mean grain size as large as ≈ 0.5mm is necessary to see a noticeable reduction of the maximum run-up height. Conversely, we also observe in Figures 6.11,

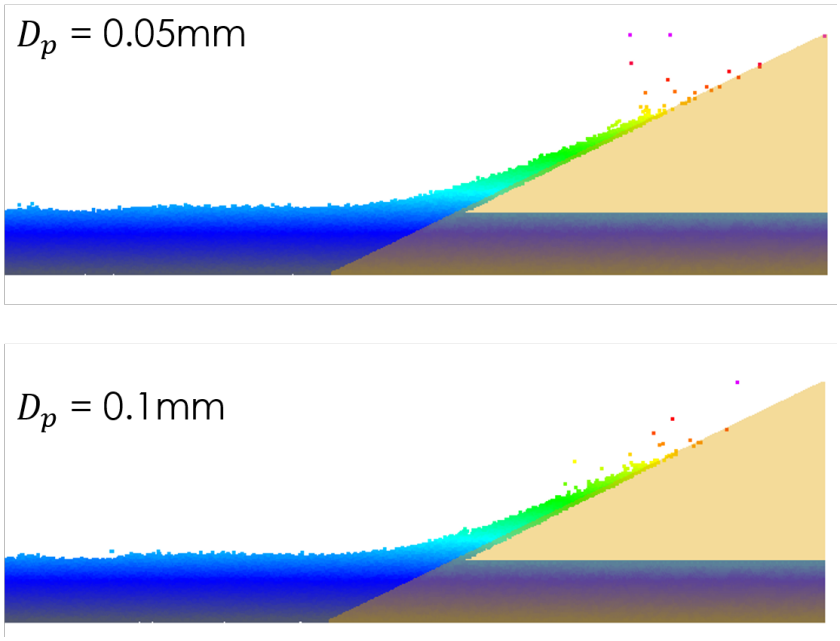

Fig. 6.14 Simulation results: comparing percolation for the two finest mean grain sizes investigated when the initial wave height H=0.126m $\left(\frac{H}{h_0} = 0.6\right)$

6.12 and 6.13 that increasing the grain size beyond approximately 10mm does not have a noticeable impact on the run-up response, even when the grain size is extremely large (100mm or 200mm). Further study would be required to determine if this is a natural limit to how much wave energy can be absorbed. If we inspect the results individually, there is a slight decrease. For a wave height of 0.126m, the run-up height $\frac{R}{h_0}$ for a grain size of 50mm is 1.34, and the run-up height for a grain size of 100mm is 1.33. However, the most significant drop in run-up height is observed in the range $0.1mm < D_p < 1mm$.

This is further explored in Figures 6.15, which shows a direct comparison at the point of maximum run-up for $D_p = 0.5$m and $D_p = 1.0$m for a wave height $H = 0.105$m or $\frac{H}{h_0} = 0.5$. The figure on the top shows the results for $D_p = 0.5$m and the figure on the bottom shows the results for $D_p = 1.0$m. The large wave size was selected to highlight any differences in the two results. Despite a significant increase in the mean grain size (classed as *fine* and *medium* boulders on the Wentworth chart, respectively), the difference in the run-up response is subtle, even at this large scale. Although there is a slight difference in the observed percolation volume, there is no practical difference in the maximum run-up height reached. Figure 6.14 shows the same initial wave height but for much finer grain sizes. Although there is little difference between the two cases shown in each of the figures, there is a very clear difference between the two figures in terms of both the volume of water that successfully percolates into the beach and the corresponding run-up height reached by the wave. This suggests that increasing the

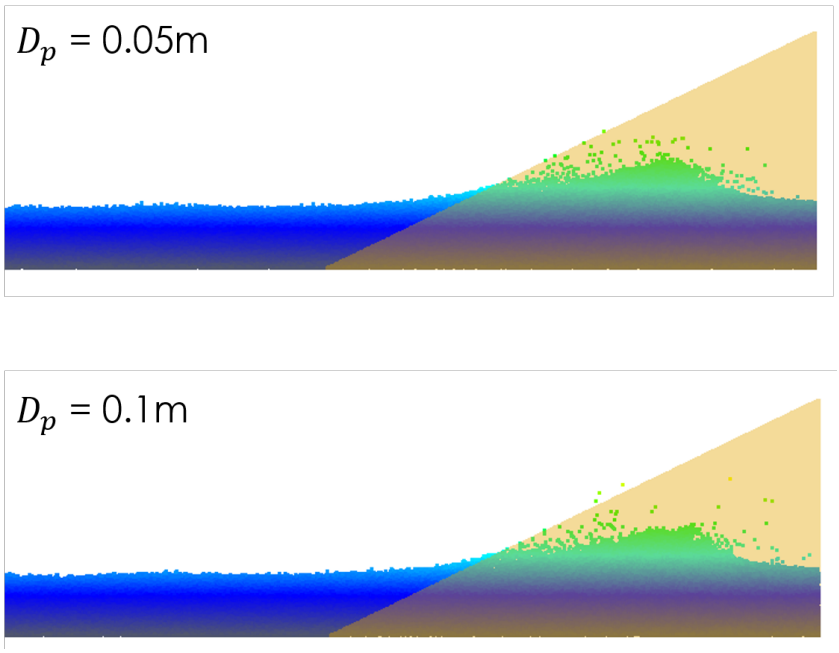

Fig. 6.15 Simulation results: comparing percolation for the two largest mean grain sizes investigated when the initial wave height H=0.105m $\left(\frac{H}{h_0} = 0.5\right)$

mean grain size is a very effective method of reducing the maximum run-up height reached by solitary waves impacting on steeply sloped beaches. However, beyond a mean grain size of $D_p \approx 0.5$m, further increasing the mean grain size will have a limited effect on increasing the percolation of the wave, and thereby reducing the run-up height reached. Furthermore, investigation of this situation would require incorporating a discrete element model into the material point method.

From Figures 6.12 and 6.13 we can see that the most significant impact on the run-up height is seen between grain sizes of 0.5mm and 5mm, where there is a sharp decrease in run-up response for all wave heights, as significantly larger volumes of water percolate through the porous dam. This suggests that a mean grain size of $D_p \approx 5$mm is optimal for minimising the run-up response under these conditions.

6.5 Pilot study: run-up on a permeable layer over a solid core

Whilst the results of the parametric studies presented previously are promising, suggesting that a seawall with larger permeability can absorb more wave energy and hence decrease the wave run-up. It is also important to acknowledge that in practice, there may adverse effects from

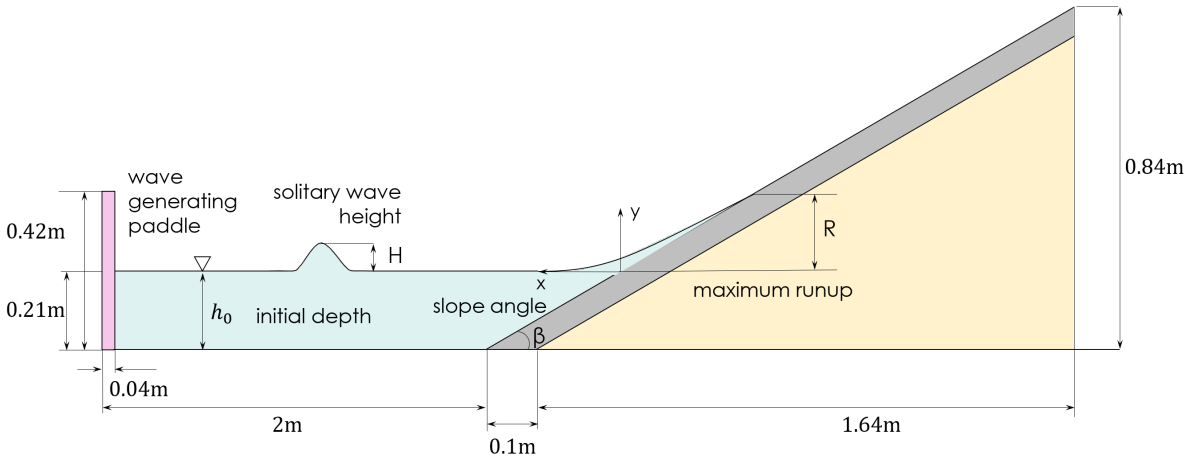

Fig. 6.16 The computational domain dimensions used for the numerical investigation of a solitary wave impacting on a solid steep slope covered by a thin permeable layer.

simply allowing the wave to flow through the barrier. To this end, a pilot study was carried out investigating the results of putting a thin permeable layer of varying grain size over a solid sloped core.

A problem definition sketch for the sloping beach case is shown in Figure 6.16. The initial depth d is 0.21m and the slope angle β is 26° so that the steepness of the slope is 1:2.08. The thickness of the permeable layer is 0.1m. This pilot study consists of an initial set of simulations where the wave height is not varied. The wave heights used for this pilot study were $H = 0.63$m and $H = 0.84$m so that H/h_0 is 0.3 and 0.4, respectively. The grain size was varied between 0.1mm (fine sand) and 100mm (a very large grain size representative of large cobbles).

For these simulations of a permeable layer sitting on a solid core, the liquid water is modelled as a Newtonian fluid with material parameters $\rho = 1000$, $K = 20000$, and $\mu = 1e^{-6}$, where ρ is the density $\left[\text{ kg/m }^3\right]$, K is the bulk modulus [kPa], and μ is dynamic viscosity [kg/m $\cdot$ s]. The dry porous beach is modelled as a linear elastic material, with material parameters $n = 0.43$, $\rho = 2650$, $K_0 = 0.5$, $E = 10000$ and $\nu = 0.3$, where n is the initial porosity [no units], ρ is the density, as before, K_0 is coefficient of lateral earth pressure [no units], E is Young's modulus [kPa] and ν is Poisson's ratio [no units]. The saturated porous beach is modelled as a fully coupled saturated linear elastic material, with material parameters $n = 0.43$, $\rho = 2650$, $K_0 = 0.5$ and $E = 10000$, for the solid phase, and $\rho = 1000$, $K = 20000$, and $\mu = 1e^{-6}$, and $\nu = 0.3$ for the liquid phase. Finally, the paddle is modelled as a linear elastic material, with material properties $n = 0.42$, $\rho = 2650$, $K_0 = 0.5$, $E = 10000$ and $\nu = 0.3$.

These simulations were also run using the Anura3D double-point MPM code. A two-phase double-point simulation type is used, with a Courant number of 0.8 to ensure the stability of

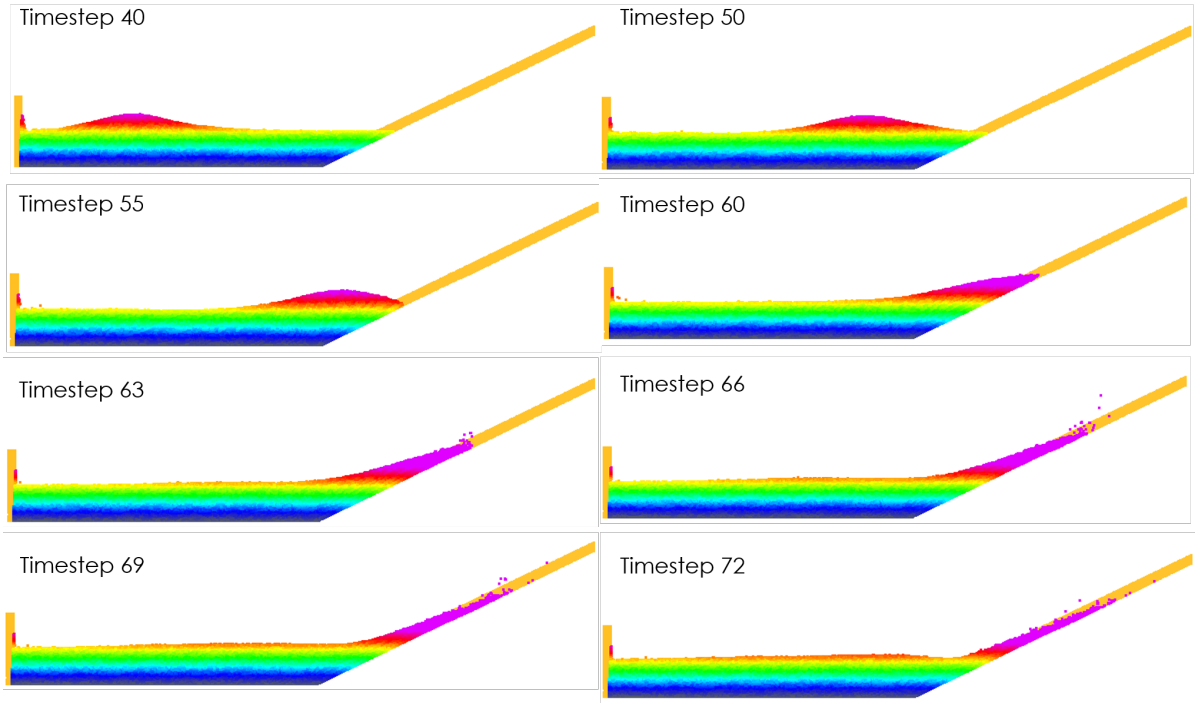

Fig. 6.17 Free-surface profile development throughout time for a large grain size ($D_p = 50$mm) and a wave height of H=0.84m $\left(\frac{H}{h_0} = 0.4\right)$

the solution. No smoothing is used and no damping is applied, which is recommended for the double-point code. For each case, the maximum allowable porosity is 0.95.

Figure 6.17 shows the free-surface profile development throughout time for for a large grain size ($D_p = 50$mm), for the case when the initial wave height H=0.84m $\left(\frac{H}{h_0} = 0.4\right)$. Since the soil layer is so thin and less wave energy is absorbed, it was difficult to produce results for very fine grain sizes, since the particles running so far up the beach tended to escape the domain, causing the simulation to stop. It is possible to mitigate this by increasing the size of the computational domain, but of course this makes the simulation much less computationally efficient. Since this is a pilot study, the results of the completed simulations are recorded and regarded and sufficient for the purposes of demonstrating the effect of a thin permeable layer over a solid core, however, it is noted that to extend this study, a larger domain is necessary.

Figure 6.18 shows a comparison of the simulation results presented at the point of maximum run-up for initial wave heights H=0.063m and H=0.084m $\left(\frac{H}{h_0} = 0.3 \text{ and } 0.4\right)$ and grain sizes of 10mm, 50mm, and 100mm. The difference between these results is very small, suggesting that a thicker layer would provide more mitigation.

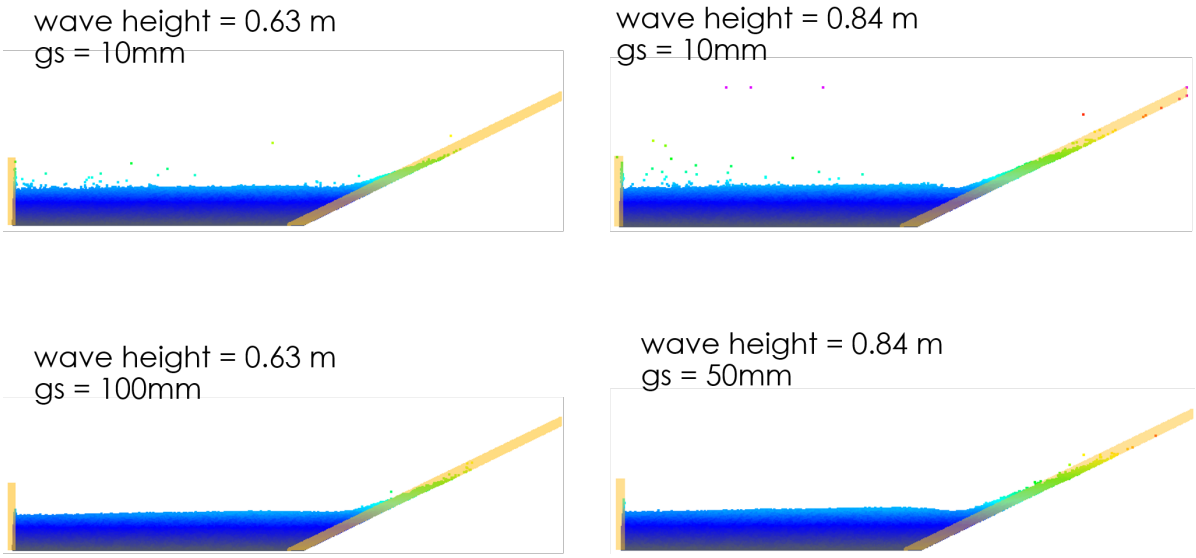

Fig. 6.18 Simulation results: comparing percolation for the permeable layer for initial wave heights H=0.063m and H=0.084m $\left(\frac{H}{h_0} = 0.3 \text{ and } 0.4\right)$ for different grain sizes, at the point of maximum run-up.

6.6 Conclusions

This chapter has employed the material point method to explore the run-up response of solitary waves impacting on steeply sloped porous beaches that vary in permeability as a result of changing the mean grain size of the constituent particles forming the beach. This investigation aimed primarily to test the ability of the code to capture the soil-water interaction between a solitary wave and a steeply sloping beach, and secondly, to determine the effect on the run-up height response of a solitary flood wave impacting on a permeable beach when the permeability of the beach is altered via modification of the mean grain size of the constituent material. It was anticipated that increasing the grain size, and therefore the permeability, of the porous beach would reduce the maximum height reached by the flood wave since the increased permeability allows the water to percolate into the beach. This percolation allows the barrier to absorb significant wave energy via a mechanism of friction generated by the soil-water interaction, causing dissipation of the wave energy.

The computed maximum run-up heights have been extensively compared to published experimental and numerical results and good agreement has been demonstrated. The applicability of the material point method to this type of hydrodynamic investigation has been ratified.

The investigations presented in this thesis consider the case of infinitely long seawalls and porous beaches, creating a two-dimensional geometry. This approach of using a simple case of a solitary wave propagating in a constant depth and encroaching on a planar beach yields

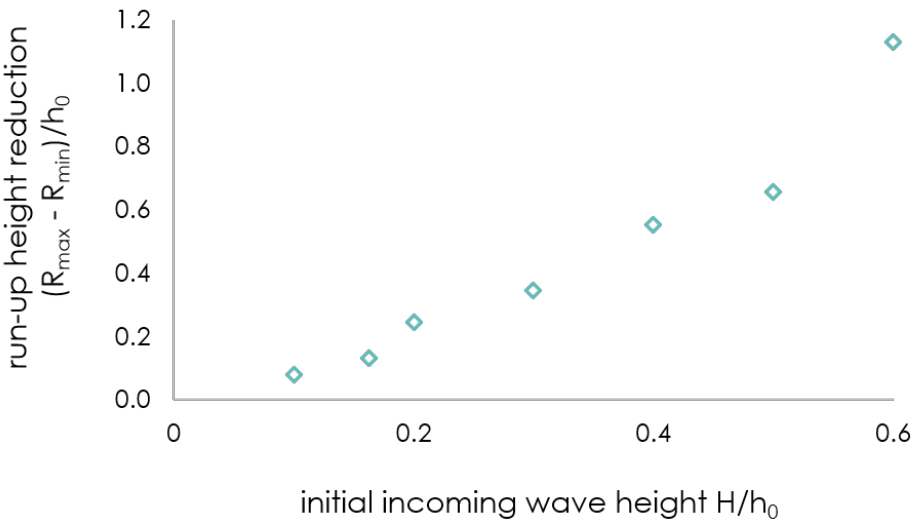

Fig. 6.19 Simulation results: reduction in maximum normalised run-up height compared to incoming wave height

results that can be applied to three-dimensional coastal structures, however, future research may be extended to encompass the three-dimensional situation so that the wave diffraction around coastal structures of finite length may be considered.

The height of the impacting wave has been varied; as has the mean grain size of the constituent particles forming the beach. These were the major investigation parameters. The run-up response is shown to follow the same form relative to the grain size, for all impacting wave heights, suggesting that the behaviour is predictable if the height of the incoming storm surge wave is known.

The beneficial effects observed when increasing the grain size to approximately 50mm is proportional to the wave height, but this benefit is realised for all incoming waves. It is also clear that increasing the grain size beyond 50mm does not offer a significant benefit, regardless of the height of the impacting wave.

When compared with experimental data and analytical results such as the approximate non-linear theory published Li and Raichlen (2002) [87], the MPM simulations gave very good predictions of the solitary wave run-up on a vertical sea wall. The material point method is thus demonstrated to be an appropriate method for this application.

The effect of increasing the mean grain size of the constituent particles forming a sloped beach, on the maximum run-up height reached, in response to solitary waves of varying heights, was then investigated using MPM. Increasing the mean grain size significantly reduced

the maximum run-up height reached by the incoming waves. For the largest wave height investigated $\left(\frac{H}{h_0} = 0.6,\ H = 0.126\text{m}\right)$, the maximum normalised run-up height $\left(\frac{R}{h_0}\right)$ reached by the broken wave was reduced from 2.46 in the worst case of an impermeable beach, to 1.33 (for a constituent mean grain size of $D_p = 100$mm), a reduction of 46%, thus demonstrating that the run-up response to an incoming solitary wave flood can be significantly reduced by increasing the permeability of the barrier to allow the water to fully percolate and dissipate the maximum possible amount of energy from the impacting wave. The benefit of increasing the mean grain size is emphasised when the incoming wave height is greater. The smallest proportional mitigation was seen for an incoming wave of height 0.021m $\left(\frac{H}{h_0} = 0.1,\ H = 0.021\text{m}\right)$, where the maximum normalised run-up was reduced from 0.22, to 0.14, a proportional reduction of 37%. This is illustrated in Figure 6.19.

An even greater beneficial reduction in run-up may possibly be achieved by exploiting even larger grain sizes; however, modelling a material would such a large grain size would require an alternative material model, such as the discrete element method, since a grain size greater than $\approx$ 100mm can no longer be realistically described as a continuum.

Overall, permeable steeply sloped beaches have been demonstrated to offer significant potential benefits to coastal flood mitigation strategies, offering protection for areas vulnerable to inundation due to solitary waves arising, for example, from tsunami waves or storm surges. The material point method is demonstrated to be an appropriate method of capturing the flow behaviour, soil-water interaction, and run-up response. The initial height of the impacting wave does not affect the shape of the response to increasing grain size, however, larger initial wave heights will result in a higher run-up response. The most effective mitigation of the run-up response is correspondingly seen when the initial wave is very large. The most beneficial response is recorded when the mean constituent particle diameter $D_p \approx 50$mm, any increase beyond this has a negligible effect in all the situations that have been investigated thus far. Further investigation of larger particles using a discrete element method may be warranted.

Chapter 7

Conclusions and future work

7.1 Summary

In recent years, MPM has come to the fore as a modelling technique in the fields of both solid mechanics and soil mechanics, due to its capability in handling large deformation problems. However, most applications thus far employ the single-point formulation, so utilisation in the field of hydrodynamic flows has been limited. There have been few published studies on the advantages and applicability of the double-point formulation. This thesis describes the development of the double-point formulation and the extension of the code to apply it to novel problems, specifically to the examples of solitary wave interaction with permeable sea walls and steep plane beaches. The purposes of this study were primarily to verify the suitability of MPM when applied to problems of hydrodynamic flow, secondly, to apply the MPM to real-world problems such as dam-break flow and wave run-up on a plane slope, and finally to modify the code to undertake parametric investigations into wave run-up on both vertical sea walls and steep plane beaches to ascertain the effect of modifying the mean grain size on the constituent material. The main outcomes of this study are summarised below:

- The double-point MPM code was applied to study dam-break flow problems and evaluate the results against previously published research. When compared with experimental data and results from other verified numerical methods, the MPM prediction of dam-break flooding was shown to be reliable.
- A parametric study of water column collapse simulations interacting with permeable dams of varying width and permeability was undertaken to ascertain the effect of altering the mean grain size on minimising the run-up height. It was found that as long as the dam is wide enough to allow sufficient water to percolate (0.4 m or $\approx$ 2x the width of the water column), the width of the wall does not influence on the maximum run-up height.

- Novel boundary conditions were developed to allow the simulation of solitary waves of different heights in the Anura3D software.
- The adapted double-point MPM code was applied to study solitary wave run-up and interaction with steeply sloped plane beaches. When compared with experimental data and results from other verified numerical methods, the MPM prediction of run-up height and soil-water interaction was shown to be reliable.
- Finally, a parametric study of solitary waves of various heights interacting with steeply sloped beaches and vertical seawalls of varying permeability was employed. This study aimed to determine the effect of altering the mean grain size on minimising the run-up height. The width of the wall was assumed to be wide enough that it does not influence the maximum run-up height. This assumption was proved by doubling the width of the wall and re-running the simulations; no discrepancy was observed, so we can be confident that this is the case. Again, it was found that increasing the mean grain size of the constituent particles and therefore the permeability reduces the maximum run-up height reached by the incoming wave. A benefit is observed for all incoming waves, regardless of height, but greater proportional mitigation is realised for larger incoming waves, highlighted in Figure 7.1.

The results of these case studies demonstrate that the double-point MPM code is a powerful tool that is applicable to many problems of hydrodynamic flows and fluid-structure interaction. However, this method is not without its drawbacks. For example, there are numerical instabilities such as the highlighted cell-crossing error, which can cause unphysical results or prevent the simulation from running entirely. Furthermore, the computational efficiency of the double-point formulation is significantly reduced compared to the single-point formulation, although each simulation of the type presented here typically still only takes between two and seven days to complete, so MPM remain computationally efficient compared to many other numerical methods. With the advent of high-performance computing (HPC), it would be possible to exploit more sophisticated computing techniques, particularly parallelisation, to further enhance the double-point MPM code and improve computational efficiency.

To conclude, there are many advantages of using MPM compared to other particle-based methods: not only the swift application of boundary conditions, and the ability to capture the history of the material, but also features developed for use with the Finite Element Method (FEM) can be adopted directly, both of which are of particular relevance in the field of soil mechanics where the history-dependent nature of soil behaviour requires specific, complex constitutive models. The double-point MPM code, by allowing separate modelling of the solid and liquid phases, has many potential applications in the field of hydrodynamics. By separating

the velocity fields of the solid and liquid phases, we can model the movement of the water entirely separately to the soil skeleton, allowing accurate modelling of complex soil-water and fluid-structure interactions. By applying the double-point MPM code to the case studies in this research (dam-break flow interaction with permeable media, solitary wave interaction with permeable media, and solitary wave run-up on permeable plane slopes), the double-point MPM code has been established as an advantageous method for studying problems involving large free-surface deformations and the interaction of these hydrodynamic flows with porous media of varying permeability.

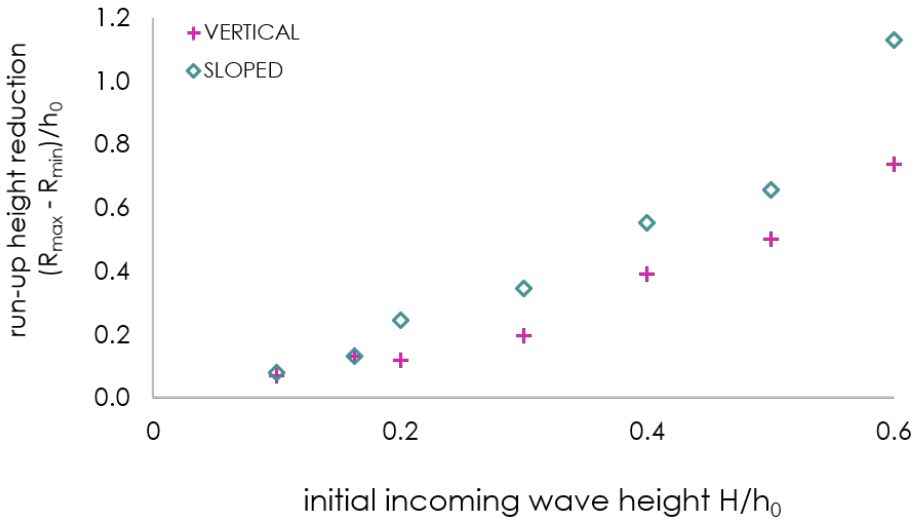

Fig. 7.1 Simulation results: reduction in maximum normalised run-up height compared to incoming wave height for a sloped beach and a vertical sea wall

7.2 Recommendations for future work

7.2.1 Effect of vegetation

Figure 7.2 shows a simple schematic of how a permeable barrier could be added to the sloped beach simulations to assess the potential protective benefits of a vegetation layer in minimising wave run-up. The material parameters of such a representative vegetation layer could be tuned against experimental results to match different types of vegetation. For example, they could represent mangrove forests, or simply grasses of different types and lengths, to identify the

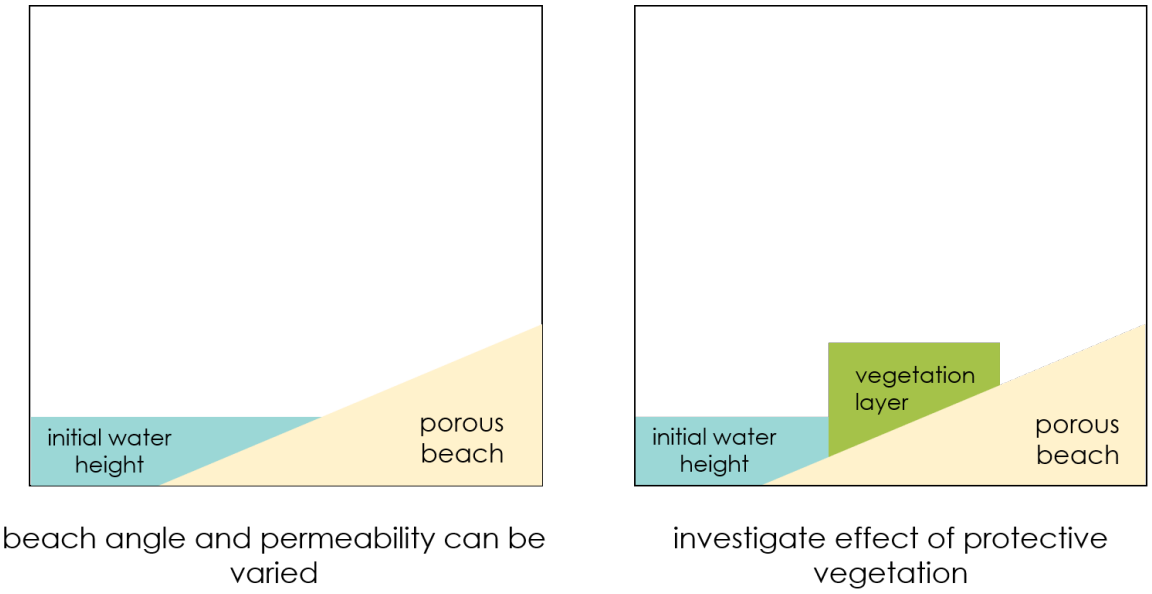

Fig. 7.2 Using an additional layer to assess the protective effects of vegetation

optimum parameters for flood defence. Significant experimental studies would be required to assess and tune the parameters representing the vegetation.

7.2.2 Three-dimensional problems

The investigations presented in this thesis consider the case of infinitely long seawalls and beaches, creating a two-dimensional geometry. This approach of using a simple case of a solitary wave propagating in a constant depth and encroaching on a planar beach yields results that apply to the three-dimensional coastal structures, future research may be extended to encompass the three-dimensional situation so that the wave diffraction around coastal structures of finite length may be considered.

7.2.3 Turbulence and surface roughness

This study has not explicitly considered the effect of turbulence. Although turbulence is generated when the incoming flow interacts with porous media, these effects are not directly resolved. Turbulence effects of flow inside the structure could also be considered. As Sakakiyama and Liu (2001) observed, there is a significant turbulence intensity inside breakwaters [128]. Turbulence is also crucial when investigating the effects of changing porosity on wave pressures. Turbulence effects play an important role in the wave breaking zone [126], [131], [2]. If the study were extended to much larger pore sizes, it would, therefore, be recommended to consider

the turbulent effects. It may also be useful to consider wave pressure and impact force, as well as run-up height, for which the turbulence would certainly need to be considered.

7.2.4 Modifications to the MPM code

Currently, the Anura3D software uses a double set of material points to represent the solid and the liquid phases, but no representation is made for the gas phases and the soil is assumed to be either dry or fully saturated, and never partially saturated. The current Anura3D code could be extended to a three-point formulation, modelling the gas phase separately to the liquid and solid phases, to better model unsaturated soil behaviours.

Pressure oscillations are evident in the two-point MPM. These can be somewhat mitigated by introducing the mixed integration scheme to reduce grid-crossing errors and by applying the pressure smoothing technique employed in the one-point formulation. Also, the fully incompressible implicit solver, as proposed by Kularathna (2017) [77] and Zhang et al. (2017) [168], could be integrated to the Anura3D solver to improve the pressure calculation.

As highlighted in Section 3.4, in the current explicit two-point MPM formulation, the size of the timestep is restricted by the permeability criteria and the stiffness criteria. For porous media with very low permeability, or when incompressibility is approached, the timestep size reduces so dramatically that it can become too expensive or even computationally infeasible to run [169]. Kularathna and Soga (2017) [77] demonstrated that although adopting implicit MPM increases the computational cost for a single timestep, the step size can be maintained at a reasonable value, which can subsequently have the overall effect of reducing the computational cost. Therefore, implicit implementations of MPM have the potential for further research.

Currently, in the Anura3D code, the interaction forces between the soil skeleton and the liquid phase are described by a drag force term, which accounts for the viscous force and the gradient of porosity [105]. This is suitable for describing forces arising as a result of seepage flows. However, it is not sufficient for describing the interaction between free water and the soil skeleton. An accurate description of this interaction is fundamental to modelling phenomena including sediment transport and scour. This has direct relevance to the applications in this thesis since significant scour is well-known to occur at the base of sea walls.

References

[1] Abe, K., Soga, K., and Bandara, S. (2014). Material Point Method for coupled hydromechanical problems. *Journal of Geotechnical Engineering*, 140(3).

[2] Akbari, H. and Namin, M. M. (2013). Moving particle method for modeling wave interaction with porous structures. *Coastal Engineering*, 74:59–73.

[3] Al-Kafaji, I. K. J. (2013). *Formulation of a dynamic material point method (MPM) for geomechanical problems*. PhD thesis, Stuttgart University, Germany.

[4] Altomare, C., Crespo, A., Rogers, B., Dominguez, J., Gironella, X., and Gómez-Gesteira, M. (2014). Numerical modelling of armour block sea breakwater with smoothed particle hydrodynamics. *Computers & Structures*, 130:34 – 45.

[5] America's Climate Choices: Panel on Advancing the Science of Climate Change; National Research Council (2010). *Advancing the Science of Climate Change*. The National Academies Press.

[6] Amicarelli, Kocak, Sibilla, , and Grabe (2017). A 3D smoothed particle hydrodynamics model for erosional dam-break floods. *International Journal of Computational Fluid Dynamics*, 31:413–434.

[7] Andersen, S. M. (2009). *Material-point analysis of large-strain problems: modelling of landslides*. PhD thesis, Aalborg University.

[8] Antoci, C., Gallati, M., and Sibilla, S. (2007). Numerical Simulation of Fluid-Structure Interaction by SPH. *Computational Structures*, 85(11–14):879–890.

[9] Arana, A. H. (2017). *Wave run-up on beaches and coastal structures*. PhD thesis, UCL.

[10] Ataie-Ashtiani, B. and Shobeyri, G. (2008). Numerical Simulation of Landslide Impulsive Waves by Incompressible Smoothed Particle Hydrodynamics. *International Journal for Numerical Methods in Fluids*, 56:209 – 232.

[11] Bandara, S. (2013). *Material Point Method to simulate large deformation problems in fluid-saturated granular medium*. PhD thesis, University of Cambridge.

[12] Bandara, S. and Soga, K. (2015). Coupling of soil deformation and pore fluid flow usingMaterial Point Method. *Computers and Geotechnics*, 63:199 – 214.

[13] Bardenhagen, S. and Kober, E. (2004). The Generalized Interpolation Material Point Method. *Computer Modeling in Engineering and Sciences*, 5:477–495.

[14] Bayas, J. C. L., Marohn, C., Dercon, G., Dewi, S., Piepho, H. P., Joshi, L., van Noordwijk, M., and Cadischa, G. (2011). Influence of coastal vegetation on the 2004 tsunami wave impact in west Aceh. In *Proceedings of the National Academy of Sciences of the United States of America*, volume 108, page 18612–18617.

[15] Bear, J. (1988). *Dynamics of fluids in porous media*. Dover Publications Inc.

[16] Benz, W. (1990). Smooth Particle Hydrodynamics: A Review. *The Numerical Modelling of Nonlinear Stellar Pulsations*, 302:3837–3870.

[17] Beuth, L. (2012). *Formulation and Application of a Quasi-Static Material Point Method*. PhD thesis, Stuttgart University, Germany.

[18] Beuth, L., Benz, T., Vermeer, P., and Więckowski, Z. (2007). Large deformation analysis using a quasi-static Material Point Method. *Journal of Theoretical and Applied Mechanics*, 38:45–60.

[19] Biot, M. (1962). Mechanics of Deformation and Acoustic Propagation in Porous Media. *Journal of Applied Physics*, 33:1482–1498.

[20] Bouscasse, B., Colagrossi, A., Marrone, S., and Antuono, M. (2013). Nonlinear water wave interaction with floating bodies in SPH. *Journal of Fluids and Structures*, 42:112–129.

[21] Brackbill, J., Kothe, D., and Ruppel, H. (1988). Flip: A low-dissipation, particle-in-cell method for fluid flow. *Computer Physics Communications*, 48:25 – 38.

[22] Bullock, G., Obhrai, C., Peregrine, D., and Bredmose, H. (2007). Violent breaking wave impacts. part 1: Results from large-scale regular wave tests on vertical and sloping walls. *Coastal Engineering*, 54(8):602 – 617.

[23] Canelas, R., Crespo, A., Domínguez, J., Ferreira, R., and Gómez-Gesteira, M. (2016). SPH-DCDEM model for arbitrary geometries in free surface solid-fluid flows. *Computer Physics Communications*, 202:131–140.

[24] Capone, T., Panizzo, A., and Monaghan, J. (2010). SPH modelling of water waves generated by submarine landslides. *Journal of Hydraulic Research*, 48:80–84.

[25] Carrier, G. and Greenspan, H. (1958). Water waves of finite amplitude on a sloping beach. *Journal of Fluid Mechanics*, 4:97–109.

[26] Cascini, L., Cuomo, S., Pastor, M., Sorbino, G., and Piciullo, L. (2014). SPH run-out modelling of channelised landslides of the flow type. *Geomorphology*, 214:502–513.

[27] Ceccato, F. (2015). *Study of large deformation geomechanical problem with the Material Point Method*. PhD thesis, Universit'a degli Studi di Padova.

[28] Ceccato, F., Yerro, A., and Martinelli, M. (2018). Modelling soil-water interaction with the Material Point Method. Evaluation of single-point and double-point formulations. In *In Numerical Methods in Geotechnical Engineering IX, Volume 1: Proceedings of the 9th European Conference on Numerical Methods in Geotechnical Engineering (NUMGE 2018)*.

[29] Chwang, A. T. (1983). A porous-wavemaker theory. *Journal of Fluid Mechanics*, 132:395–406.

[30] Colagrossi, A. and Landrini, M. (2003). Numerical Simulation of Interfacial Flows by Smoothed Particle Hydrodynamics. *Journal of Computational Physics*, 191:448–475.

[31] Courant, R., Friedrichs, K., and Lewy, H. (1967). On the partial difference equations of mathematical physics. *IBM Journal of Research and Development*, 11:215–234.

[32] Crespo, A., Gómez-Gesteira, M., and Dalrymple, R. (2008). Modeling Dam Break Behavior over a Wet Bed by a SPH Technique. *Journal of Waterway, Port, Coastal, and Ocean Engineering*, 134:313–320.

[33] Cruchaga, M., Celentano, D., and Tezduyar, T. (2007). Collapse of a Liquid Column: Numerical Simulation and Experimental Validation. *Computational Mechanics*, 39:453–476.

[34] Cummins, S. J. and Rudman, M. (1999). An SPH projection method. *Journal of Computational Physics*, 152(2):584 – 607.

[35] Cundall, P. (1971). A computer model for simulating progressive, large-scale movements in blocky rock systems. *Proceedings of the International Symposium on Rock Mechanics*, pages 129–136.

[36] Dalrymple, R. and Rogers, B. (2006). Numerical Modeling of Water Waves with the SPH Method. *Coastal Engineering*, 53:141–147.

[37] Dalrymple, R. A., Losada, M. A., and Martin, P. A. (1991). Reflection and transmission from porous structures under oblique wave attack. *Journal of Fluid Mechanics*, 224:625–644.

[38] del Jesus, M., Lara, J., and Losada, I. (2012). Three-dimensional interaction of waves and porous coastal structures: Part I: Numerical model formulation. *Coastal Engineering*, 64:57 – 72.

[39] Dhakal, T. and Zhang, D. (2016). Material point methods applied to one-dimensional shock waves and dual domain material point method with sub-points. *Journal of Computational Physics*, 325:301–313.

[40] Ergun, S. (1952). Fluid Flow Through Ppacked Columns. *Journal of Chemical Engineering Progress*, pages 89–94.

[41] Fern, E. J. and Soga, K. (2016). The role of constitutive models in MPM simulations of granular column collapses. *Acta Geotechnica*, 11(3):659–678.

[42] Fern, J., Rohe, A., Soga, K., and Eduardo, A. (2019). *Material Point Method for Geotechnical Engineering: A Practical Guide*. CRC PRESS.

[43] Geist, E. L., Titov, V. V., and Synolakis, C. E. (2006). Tsunami: wave of change. *Scientific American*, 294:56–63.

[44] Gingold, R. A. and Monaghan, J. J. (1977). Smoothed particle hydrodynamics: theory and application to non-spherical stars. *Monthly Notices of the Royal Astronomical Society*, 181:375–389.

[45] Gjevik, B. and Pedersen, G. (1981). Run-up of long waves on an inclined plane. *Journal of Fluid Mechanics*, 135:283–299.

[46] Goda, Y., Kishara, Y., and Kamiyama, Y. (1975). Laboratory investigation on the overtopping rate of seawalls by irregular waves. *Report of the Port and Harbour Research Institute*, 14.

[47] Gotoh, H. and Sakai, T. (1999). Lagrangian simulation of breaking waves using particle method. *Coastal Engineering Journal*, 41:303–326.

[48] Grenier, N., Le Touzé, D., Colagrossi, A., Antuono, M., and Colicchio, G. (2013). Viscous bubbly flows simulation with an interface SPH model. *Ocean Engineering*, 69:88–102.

[49] Grilli, S., Svendsen, I., and Subramanya, R. (1997). Breaking criterion and characteristics for solitary waves on slopes. *Journal of Waterway, Port, Coastal and Ocean Engineering*, 123:102–112.

[50] Gui, Q., Dong, P., Shao, S., and Chen, Y. (2015). Incompressible SPH simulation of wave interaction with porous structure. *Ocean Engineering*, 110:126 – 139.

[51] Guilkey, J., Hoying, J., and Weiss, J. (2006). Computational modeling of multicellular constructs with the material point method. *Journal of Biomechanics*, 39:2074–2086.

[52] Harlow, F. H. (1964). The particle-in-cell computing method in fluid dynamics. *Methods in Computational Physics*, 3:319 – 343.

[53] Hattori, M., Arami, A., and Yui, T. (1994). Wave impact pressure on vertical walls under breaking waves of various types. *Coastal Engineering*, 22:79 – 114.

[54] Hibberd, S. and Peregrine, D. (1979). Surf and run-up on a beach: A uniform bore. *Journal of Fluid Mechanics*, 95:323–345.

[55] Hsu, T.-J., Sakakiyama, T., and Liu, P. L.-F. (2002). A numerical model for wave motions and turbulence flows in front of a composite breakwater. *Coastal Engineering*, 46(1):25 – 50.

[56] Huang, C.-J., Chang, H.-H., and Hwung, H.-H. (2003). Structural permeability effects on the interaction of a solitary wave and a submerged breakwater. *Coastal Engineering*, 49(1):1 – 24.

[57] Huang, C.-J., Shen, M.-L., and Chang, H.-H. (2008). Propagation of a solitary wave over rigid porous beds. *Ocean Engineering*, 35(11):1194 – 1202.

[58] Huang, L. and Chao, H. (1992). Reflection and transmission of water wave by porous breakwater. *Journal of Waterway, Port, Coastal and Ocean Engineering*, 118(5):437–452.

[59] Huang, Y., Zhang, W., Xu, Q., Xie, P., and Hao, L. (2012). Run-out analysis of flow-like landslides triggered by the Ms 8.0 2008 Wenchuan earthquake using smoothed particle hydrodynamics. *Landslides*, 9:275–283.

[60] Huber, L. E., Evers, F. M., and Hager, W. H. (2017). Solitary wave overtopping at granular dams. *Journal of Hydraulic Research*, 55(6):799–812.

[61] Hughes, S. A. (2004). Estimation of wave run-up on smooth, impermeable slopes using the wave momentum flux parameter. *Coastal Engineering*, 51:1085–1104.

[62] Hughes, T. J., Liu, W. K., and Zimmermann, T. K. (1981). Lagrangian-Eulerian finite element formulation for incompressible viscous flows. *Computer Methods in Applied Mechanics and Engineering*, 29:329–349.

[63] Hwang, S.-C., Khayyer, A., Gotoh, H., and Park, J.-C. (2014). Development of a fully lagrangian MPS-based coupled method for simulation of fluid–structure interaction problems. *Journal of Fluids and Structures*, 50:497–511.

[64] I., R., H.R., R., S.C., Y., and Y.L., Y. (2007). Lessons from hurricane katrina storm surge on bridges and buildings. *Journal of Waterway, Port, Coastal, and Ocean Engineering*, 133:463–483.

[65] Ijima, T., Chou, C. R., and Yoshida, A. (1976). Method of analyses for two-dimensional water wave problems. In *Proceedings of the Coastal Engineering Conference (Honolulu)*, pages 2717–2736.

[66] Iryanto, I. and Gunawan, P. H. (2016). Simulation of wave mitigation by coastal vegetation using smoothed particle hydrodynamics method. *Journal of Physics: Conference Series*, 693.

[67] Jassim, I., Stolle, D., and Vermeer, P. (2013). Two-phase dynamic analysis by Material Point Method. *International Journal for Numerical and Analytical Methods in Geomechanics*, 37(15):2502–2522.

[68] Jing, L. and Hudson, J. (2002). Numerical methods in rock mechanics. *International Journal of Rock Mechanics and Mining Sciences*, 39:409–427.

[69] Karunarathna, S. and Lin, P. (2006). Numerical simulation of wave damping over porous seabeds. *Coastal Engineering*, 53(10):845 – 855.

[70] Khayyer, A., Gotoh, H., and Shao, S. (2008). Corrected incompressible SPH method for accurate water-surface tracking in breaking waves. *Coastal Engineering*, 55(3):236 – 250.

[71] Khayyer, A., Gotoh, H., and Shao, S. (2009). Enhanced predictions of wave impact pressure by improved incompressible SPH methods. *Applied Ocean Research*, 31(2):111 – 131.

[72] Khayyer, A., Gotoh, H., Shimizu, Y., Gotoh, K., and Shao, S. (2017). An Enhanced Particle Method for Simulation of Fluid Flow Interactions with Saturated Porous Media. *Journal of Japan Society of Civil Engineers, Ser. B2 (Coastal Engineering)*, 73(2).

[73] Kim, N. and Ko, H. S. (2008). Numerical Simulation on Solitary Wave Propagation and Run-up by SPH Method. *KSCE Journal of Civil Engineering*, 12:221–226.

[74] Koraim, A., Heikal, E., and Zaid, A. A. (2014). Hydrodynamic characteristics of porous seawall protected by submerged breakwater. *Applied Ocean Research*, 46:1 – 14.

[75] Koshizuka and Oka (1996). Moving-Particle Semi-Implicit Method for Fragmentation of Incompressible Fluid. *Nuclear Science and Engineering*, 123:421–434.

[76] Koshizuka, S. Nobe, A. and Oka, Y. (1998). Numerical analysis of breaking waves using the moving particle semi-implicit method. *International Journal for Numerical Methods in Fluids*, 26:751–769.

[77] Kularathna, S. (2017). *Splitting solution scheme for material point method*. PhD thesis, University of Cambridge.

[78] Kumar, K. (2015). *Multi-scale multiphase modelling of granular flows*. PhD thesis, University of Cambridge.

[79] Lara, J., del Jesus, M., and Losada, I. (2012). Three-dimensional interaction of waves and porous coastal structures: Part II: Experimental validation. *Coastal Engineering*, 64:26 – 46.

[80] Lara, J., Garcia, N., and Losada, I. (2006). Rans modelling applied to random wave interaction with submerged permeable structures. *Coastal Engineering*, 53(5):395 – 417.

[81] Lara, J. L., Losada, I. J., Maza, M., and Guanche, R. (2011). Breaking solitary wave evolution over a porous underwater step. *Coastal Engineering*, 58(9):837 – 850.

[82] Lean, G. H. (1967). A simplified theory of permeable wave absorbers. *Journal of Hydraulic Research*, pages 15–30.

[83] LeVeque, R. J. (2002). *Finite Volume Methods for Hyperbolic Problems*, page 1–12. Cambridge Texts in Applied Mathematics. Cambridge University Press.

[84] L.H., H. (1991). The inertial effect of a finite thickness porous wave-maker. *Journal of Hydraulic Research*, 29:417–432.

[85] L.H., H., Hseih, P. C., and Chang, G. Z. (1993). Study on porous wave-makers. *Journal of Engineering Mechanics*, 119:1600–1614.

[86] Li, S. and Liu, W. K. (2002). Meshfree and particle methods and their applications. *Applied Mechanics Reviews*, 55.

[87] Li, Y. and Raichlen, F. (2002). Solitary Wave Runup on Plane Slopes. *Journal of Waterway Port Coastal and Ocean Engineering*, 33.

[88] Liang, D. (2009). Evaluating shallow water assumptions in dam-break flows. In *Proceedings of the Institution of Civil Engineers - Water Management*, volume 163, pages 227–237.

[89] Liang, D., Jian, W., Shao, S., Chen, R., and Yang, K. (2017). Incompressible SPH simulation of solitary wave interaction with movable seawalls. *Journal of Fluids and Structures*, 69:72 – 88.

[90] Liang, D., Thusyanthan, I., Madabhushi, G., and Tang, H. (2010). Modelling solitary waves and its impact on coastal houses with SPH method. *China Ocean Engineering*, 24:353–368.

[91] Lin, P., Chang, K.-A., and Liu, P. L.-F. (1999). Runup and Rundown of Solitary Waves on Sloping Beaches. *Journal of Waterway, Port, Coastal, and Ocean Engineering*, 125:247–255.

[92] Liu, M. and Liu, G. (2010a). Smoothed Particle Hydrodynamics (SPH): an Overview and Recent Developments. *Archives of Computational Methods in Engineering*, 17:25–76.

[93] Liu, M. B. and Liu, G. (2010b). Smoothed Particle Hydrodynamics (SPH): an overview and recent developments. *Archives of Computational Methods in Engineering*, 17:25–76.

[94] Liu, P.-F., Lin, P., Chang, K.-A., and Sakakiyama, T. (1999). Numerical modeling of wave interaction with porous structures. *Journal of Waterway, Port, Coastal and Ocean Engineering*, 125(6):322–330.

[95] Lucy, L. B. (1977). A numerical approach to the testing of the fission hypothesis. *Astronomical Journal*, 83:1013–1024.

[96] Ma, S. and Zhang, X. (2009). Comparison of MPM and SPH in hypervelocity impact simulation. *International Journal of Impact Engineering*, pages 272–282.

[97] Ma, Z. T., Zhang, X., and Huang, P. (2010). An Object-Oriented MPM Framework for Simulation of Large Deformation and Contact of Numerous Grains. *Computer Modeling in Engineering and Sciences*, 55:61–87.

[98] Mackenzie-Helnwein, P., Arduino, P., Shin, W., Moore, J. A., and Miller, G. R. (2010). Modelling strategies for multiphase drag interactions using the Material Point Method. *International Journal for Numerical Methods in Engineering*, 83(3).

[99] Madsen, O. (1974). Wave transmission through porous structures. *Journal of the Waterways, Harbors, and Coastal Engineering Division*, 3:69–188.

[100] Madsen, P. (1983). Wave reflection from a vertical permeable wave absorber. *Coastal Engineering*, 7:381–396.

[101] Mallayachari, V. and Sundar, V. (1994). Reflection characteristics of permeable seawalls. *Coastal Engineering*, 23:135–150.

[102] Mamouri, S. J., Fatehi, R., and Manzari, M. T. (2015). A consistent incompressible SPH method for internal flows with fixed and moving boundaries. *International Journal for Numerical Methods in Fluids*, 81(10):589–610.

[103] Margolin, L. (1997). Introduction to "An Arbitrary Lagrangian–Eulerian Computing Method for All Flow Speeds". *Journal of Computational Physics*, 135:198–202.

[104] Martin, J. C. and Moyce, W. (1952). Part IV. An experimental study of the collapse of liquid columns on a rigid horizontal plane. *Philosophical Transactions of The Royal Society A: Mathematical, Physical and Engineering Sciences*, 244:312–324.

[105] Martinelli, M. (2016). Soil-water interaction with Material Point Method. Double-Point Formulation. *Report on EU-FP7 research project MPM-Dredge*.

[106] Martinelli, M. and Rohe, A. (April 2015). Modelling fluidisation and sedimentation using the Material Point Method. *Pan-American Congress on Computational Mechanics*.

[107] Martinelli, M., Rohe, A., and Soga, K. (2017). Modelling dike failure using the Material Point Method. *Procedia Engineering*, 175:341 – 348. Proceedings of the 1st International Conference on the Material Point Method (MPM 2017).

[108] Memarzadeh, R. and Hejazi, K. (2012). ISPH Numerical Modelling of Nonlinear Wave Run-up on Steep Slopes. *Journal of the Persian Gulf (Marine Science)*, 3:17–26.

[109] Mieremet, M. M. J. (2015). *Numerical stability for velocity-based 2-phase formulation for geotechnical dynamic analysis*. PhD thesis, Delft University of Technology.

[110] Monaghan, J. (1985). Smooth Particle Hydrodynamics: A Review. *Computer Physics Reports*, 3:71–124.

[111] Monaghan, J. and Kos, A. (1999). Solitary waves on a Cretan beach. *Journal of Waterway, Port, Coastal and Ocean Engineering*, 125(3):145–154.

[112] Monaghan, J. J. (1992). Smoothed Particle Hydrodynamics. *Annual Review of Astronomy and Astrophysics*, 30:543–574.

[113] Monaghan, J. J. (1994). Simulating free surface flows with SPH. *Journal of Computational Physics*, 110:399–406.

[114] MPM Research Community (2019). *Anura3D MPM Software Scientific Manual Version 2019.1 - Tinctorius*. Anura3D MPM Research Community.

[115] Nicholas Perrone, R. K. (1975). A general finite difference method for arbitrary meshes. *Computers & Structures*, 5:45–57.

[116] NOAA (National Oceanic and Atmospheric Administration) (2016a). 2016 update to data originally published in 2009: Sea level variations of the United States 1854–2006. *NOAA Technical Report NOS CO-OPS 053*.

[117] NOAA (National Oceanic and Atmospheric Administration) (January 2017). Global and regional sea level rise scenarios for the United States. *NOAA Technical Report NOS CO-OPS 083*.

[118] NOAA (National Oceanic and Atmospheric Administration) (March 2016b). Extended reconstructed sea surface temperature. *NOAA Technical Report NOS CO-OPS 053*.

[119] Özhan, E. and Shi-Igai, H. (1977). On the development of solitary waves on a horizontal bed with friction. *Coastal Engineering*, pages 167–184.

[120] Pastor, M., Blanc, T., Haddad, B., Petrone, S., Sanchez, M., Drempetic, V., Issler, D., Crosta, G., Cascini, L., Sorbino, G., and Cuomo, S. (2014). Application of a SPH depth-integrated model to landslide run-out analysis. *Landslides*, 11:793–812.

[121] Pastor, M., Haddad, B., Sorbino, G., Cuomo, S., and Drempetic, V. (2009). A depth-integrated, coupled SPH model for flow-like landslides and related phenomena. *International Journal for Numerical and Analytical Methods in Geomechanics*, 33:143 – 172.

[122] Popa, H. and Batali, L. (2010). Using Finite Element Method in geotechnical design. comparison between soil constitutive laws and case study. *Proceedings of the 3rd WSEAS Int. Conference on Finite differences - finite elements - finite volumes - boundary elements*.

[123] Pu, J. H., Shao, S., Huang, Y., and Hussain, K. (2013). Evaluations of SWEs and SPH Numerical Modelling Techniques for Dam Break Flows. *Engineering Applications of Computational Fluid Mechanics*, 7:544–563.

[124] Rafiee, A. and Thiagarajan, K. (2009). An SPH projection method for simulating fluid-hypoelastic structure interaction. *Computer Methods in Applied Mechanics and Engineering*, 198:2785–2795.

[125] Rao, S. (2017). *The Finite Element Method in Engineering, 6th Edition*. Butterworth-Heinemann.

[126] Ren, B., Wen, H., Dong, P., and Wang, Y. (2016). Improved SPH simulation of wave motions and turbulent flows through porous media. *Coastal Engineering*, 107:14 – 27.

[127] Rogers, B. D., Dalrymple, R. A., and Stansby, P. K. (2009). Simulation of caisson breakwater movement using 2-D SPH. *Journal of Hydraulic Research*, 48:135–141.

[128] Sakakiyama, T. and Liu, P. L. F. (2001). Laboratory experiments for wave motions and turbulence flows in front of a breakwater. *Coastal Engineering*, pages 117–139.

[129] Savage, R. P. and Fairchild, J. C. (1953). Laboratory study of wave energy losses by bottom friction and percolation. *Coastal Engineering Research Centre, Vicksburg*.

[130] Sawaragi, T. and Deguchi, I. (1992). Waves on permeable layers. *Coastal Engineering*, pages 1531–1544.

[131] Shao, S. (2010). Incompressible SPH flow model for wave interactions with porous media. *Coastal Engineering*, 57(3):304 – 316.

[132] Shao, S. and Lo, E. Y. (2003). Incompressible SPH method for simulating Newtonian and non-Newtonian flows with a free surface. *Advances in Water Resources*, 26(7):787 – 800.

[133] Solenthaler, B., Schläfli, J., and Pajarola, R. (2007). A unified particle model for fluid-solid interactions. *Journal of Visualization and Computer Animation*, 18:69–82.

[134] Sollitt, C. K. and Cross, R. H. (1972). Wave transmission through permeable breakwaters. In *Proceedings of the 13th Coastal Engineering Conference (Vancouver)*, volume 3, pages 1827–1846.

[135] Stasch, J., Avci, B., and Wriggers, P. (2016). Numerical simulation of fluid-structure interaction problems by a coupled SPH-FEM approach: FSI using SPH and FEM. *PAMM*, 16:491–492.

[136] Straub, L., Bowers, C., and Herbich, J. (1957). Laboratory studies of permeable wave absorbers. In *Proceedings of 6th Conference on Coastal Engineering*, pages 729–742.

[137] Sulisz, W. (1985). Wave reflection and transmission at permeable breakwaters of arbitrary cross-section. *Coastal Engineering*, 9(4):371–386.

[138] Sulsky, D., Chen, Z., and Schreyer, H. (1994). A particle method for history-dependent materials. *Computer Methods in Applied Mechanics and Engineering*, 118:179 – 196.

[139] Sulsky, D., Zhou, S.-J., and Schreyer, H. L. (1995). Application of a particle-in-cell method to solid mechanics. *Computer Physics Communications*, 87:236 – 252.

[140] Sun, Z., Li, H., Gan, Y., Liu, H., Huang, Z., and He, L. (2018). Material Point Method and Smoothed Particle Hydrodynamics simulations of fluid flow problems: A comparative study. *Progress in Computational Fluid Dynamics, An International Journal*, 18.

[141] Synolakis, C. E. (1987). The Runup of Solitary Waves. *Journal of Fluid Mechanics*, 185:523–545.

[142] Synolakis, C. E. and Bernard, E. N. (2006). Tsunami science before and beyond boxing day 2004. *Philosophical Transactions of the Royal Society A: Mathematical, Physical and Engineering Sciences*, 364.

[143] van der Giessen, E. and Aref, H. (2003). Advances in Applied Mechanics. *Advanced Academic Press*, pages 86–87.

[144] van der Meer, J. and M. Stam, C.-J. (1992). Runup on smooth and rock slopes of coastal structures. *Journal of Waterway Port Coastal and Ocean Engineering*, 118:534–550.

[145] Vaucorbeil, A. d., Sinaie, S., Wu, J.-Y., and Nguyen, V. P. (2019). *Material point method after 25 years: theory, implementation, applications*. Monash University.

[146] Verruijt, A. (2010). *An introduction to soil dynamics*. Springer.

[147] Wallstedt, P. and Guilkey, J. (2008). n evaluation of explicit time integration schemes for use with the generalized interpolation material point method. *Journal of Computational Physics*, 227:9628–9642.

[148] Wang, B., Vardon, P. J., Hicks, M. A., and Chen, Z. (2016). Development of an implicit Material Point Method for Geotechnical applications. *Computers and Geotechnics*, 71:159 – 167.

[149] Wentworth, C. K. (1922). A Scale of Grade and Class Terms for Clastic Sediments. *The Journal of Geology*.

[150] Więckowski, Z. (1998). A particle-in-cell method in analysis of motion of a granular material in a silo. *International Journal for Computational Mechanics: New Trends and Applications, CIMNE, Barcelona*.

[151] Więckowski, Z. (2003). Modelling of silo discharge and filling problems by the Material Point Method. *Task Quarterly*, 4:701–721.

[152] Więckowski, Z. (2013). Two-phase numerical model for soil-fluid interaction problems. In *Proceedings of ComGeoIII, Krakow*, pages 410–419.

[153] Więckowski, Z., Youn, S.-K., and Yeon, J.-H. (1999). A particle-in-cell solution to the silo discharging problem. *International Journal for Numerical Methods in Engineering*, 45:1203–1225.

[154] Williams, G., Pande, G., and Beer, J. (1990). *Numerical Methods in Rock Mechanics*. Wiley.

[155] Williams, J. R., Hocking, G., and Mustoe, G. G. W. (1985). The Theoretical Basis of the Discrete Element Method. *NUMETA 1985, Numerical Methods of Engineering, Theory and Applications*.

[156] Wu, Y.-T. and Hsiao, S.-C. (2013). Propagation of solitary waves over a submerged permeable breakwater. *Coastal Engineering*, 81:1–18.

[157] Yerro, A. (2015). *MPM modelling of landslides in brittle and unsaturated soils*. PhD thesis, Universitat Politècnica de Catalunya (UPC Barcelona).

[158] Yerro, A., Alonso, E. E., and Pinyol, N. (2015). The Material Point Method for unsaturated soil. *Géotechnique*, 65(3):201–217.

[159] Yerro, A., Rohe, A., and Soga, K. (2017). Modelling internal erosion with the Material Point Method. *Procedia Engineering*, 175:365 – 372.

[160] Yu, X. (1995). Diffraction of water waves by porous breakwaters. *Journal of Waterway, Port, Coastal and Ocean Engineering*, 121(6):275–282.

[161] Yu-Hsuan, C., Hwang, K., and Hwung, H.-H. (2009). Large-scale laboratory measurements of solitary wave inundation on a 1:20 slope. *Coastal Engineering*, 56:1022–1034.

[162] Zabala, F. and Alonso, E. E. (2011). Progressive failure of Aznalcóllar dam using the Material Point Method. *Géotechnique*, 61(9):795–808.

[163] Zelt, J. (1991). The run-up of nonbreaking and breaking solitary waves. *Coastal Engineering*, 15:205–246.

[164] Zelt, J. and Raichlen, F. (1990). A Lagrangian model for wave induced harbour oscillations. *Journal of Fluid Mechanics*, 213:203–228.

[165] Zhang, D., Ma, X., and Giguere, P. (2011). Material point method enhanced by modified gradient of shape function. *Journal of Computational Physics*, 230:6379–6398.

[166] Zhang, H. W., Wang, K. P., and Zhang, Z. (2009). Material Point Method for Numerical Simulation of Failure Phenomena in Multiphase Porous Media. In *Computational Mechanics*, pages 36–47. Springer Berlin Heidelberg.

[167] Zhang, J. (1996). *Run-up of ocean waves on beaches*. PhD thesis, California Institute of Technology.

[168] Zhang, X., Chen, Z., and Liu, Y. (2017). *The Material Point Method: A Continuum Based Particle Method for Extreme Loading Cases*. Tsinghua University Press.

[169] Zhao, X. (2019). *Improvements of MPM and Its Applications in Modelling Rapid Soil/Water Movements*. PhD thesis, University of Cambridge.

[170] Zhao, X. and Liang, D. (June 2016). MPM Modelling of Seepage Flow through Embankments. *International Society of Offshore and Polar Engineers*.

[171] Zhao, X., Liang, D., and Martinelli, M. (2017). MPM simulations of dam-break floods. *Journal of Hydrodynamics, Ser. B*, 29(3):397 – 404.

[172] Zheng, X., Ma, Q., and Duan, W. (2014). Incompressible SPH method based on rankine source solution for violent water wave simulation. *Journal of Computational Physics*, 276:291–314.